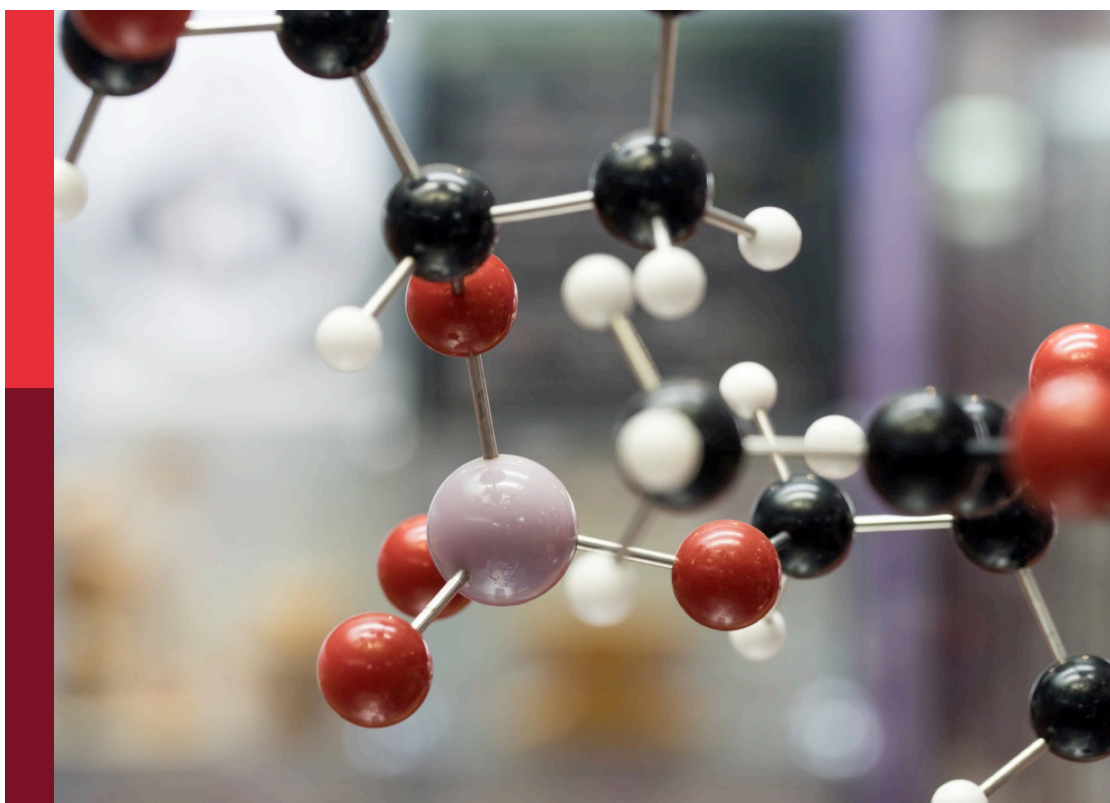


Chemical biology editor's pick 2024

Edited by
John D. Wade

Published in
Frontiers in Chemistry



FRONTIERS EBOOK COPYRIGHT STATEMENT

The copyright in the text of individual articles in this ebook is the property of their respective authors or their respective institutions or funders. The copyright in graphics and images within each article may be subject to copyright of other parties. In both cases this is subject to a license granted to Frontiers.

The compilation of articles constituting this ebook is the property of Frontiers.

Each article within this ebook, and the ebook itself, are published under the most recent version of the Creative Commons CC-BY licence. The version current at the date of publication of this ebook is CC-BY 4.0. If the CC-BY licence is updated, the licence granted by Frontiers is automatically updated to the new version.

When exercising any right under the CC-BY licence, Frontiers must be attributed as the original publisher of the article or ebook, as applicable.

Authors have the responsibility of ensuring that any graphics or other materials which are the property of others may be included in the CC-BY licence, but this should be checked before relying on the CC-BY licence to reproduce those materials. Any copyright notices relating to those materials must be complied with.

Copyright and source acknowledgement notices may not be removed and must be displayed in any copy, derivative work or partial copy which includes the elements in question.

All copyright, and all rights therein, are protected by national and international copyright laws. The above represents a summary only. For further information please read Frontiers' Conditions for Website Use and Copyright Statement, and the applicable CC-BY licence.

ISSN 1664-8714
ISBN 978-2-8325-5763-1
DOI 10.3389/978-2-8325-5763-1

About Frontiers

Frontiers is more than just an open access publisher of scholarly articles: it is a pioneering approach to the world of academia, radically improving the way scholarly research is managed. The grand vision of Frontiers is a world where all people have an equal opportunity to seek, share and generate knowledge. Frontiers provides immediate and permanent online open access to all its publications, but this alone is not enough to realize our grand goals.

Frontiers journal series

The Frontiers journal series is a multi-tier and interdisciplinary set of open-access, online journals, promising a paradigm shift from the current review, selection and dissemination processes in academic publishing. All Frontiers journals are driven by researchers for researchers; therefore, they constitute a service to the scholarly community. At the same time, the *Frontiers journal series* operates on a revolutionary invention, the tiered publishing system, initially addressing specific communities of scholars, and gradually climbing up to broader public understanding, thus serving the interests of the lay society, too.

Dedication to quality

Each Frontiers article is a landmark of the highest quality, thanks to genuinely collaborative interactions between authors and review editors, who include some of the world's best academicians. Research must be certified by peers before entering a stream of knowledge that may eventually reach the public - and shape society; therefore, Frontiers only applies the most rigorous and unbiased reviews. Frontiers revolutionizes research publishing by freely delivering the most outstanding research, evaluated with no bias from both the academic and social point of view. By applying the most advanced information technologies, Frontiers is catapulting scholarly publishing into a new generation.

What are Frontiers Research Topics?

Frontiers Research Topics are very popular trademarks of the *Frontiers journals series*: they are collections of at least ten articles, all centered on a particular subject. With their unique mix of varied contributions from Original Research to Review Articles, Frontiers Research Topics unify the most influential researchers, the latest key findings and historical advances in a hot research area.

Find out more on how to host your own Frontiers Research Topic or contribute to one as an author by contacting the Frontiers editorial office: frontiersin.org/about/contact

Chemical biology editor's pick 2024

Topic editor

John D. Wade — University of Melbourne, Australia

Citation

Wade, J. D., ed. (2024). *Chemical biology editor's pick 2024*.
Lausanne: Frontiers Media SA. doi: 10.3389/978-2-8325-5763-1

Table of contents

- 04 **Chemically diverse activity-based probes with unexpected inhibitory mechanisms targeting trypsin-like serine proteases**
Alba Ramos-Llorca, Lisse Decraecker, Valérie M. Y. Cacheux, Irena Zeiburlina, Michelle De bruyn, Louise Battut, Carlos Moreno-Cinos, Davide Ceradini, Eric Espinosa, Gilles Dietrich, Maya Berg, Ingrid De Meester, Pieter Van Der Veken, Guy Boeckstaens, Anne-Marie Lambeir, Alexandre Denadai-Souza and Koen Augustyns
- 21 **A novel insulin delivery system by β cells encapsulated in microcapsules**
Zongjie Luo, Yutong Dong, Mengyu Yu, Xiao Fu, Yudong Qiu, Xitai Sun and Xuehui Chu
- 28 **Overview of myelin, major myelin lipids, and myelin-associated proteins**
Alexander Kister and Ilya Kister
- 37 **A highly sensitive colorimetric approach based on tris (bipyridine) Ruthenium (II/III) mediator for the enzymatic detection of phenylalanine**
Maria Anna Messina, Ludovica Maugeri, Giuseppe Forte, Martino Ruggieri and Salvatore Petralia
- 43 **Beyond binding change: the molecular mechanism of ATP hydrolysis by F_1 -ATPase and its biochemical consequences**
Sunil Nath
- 65 **Chemical stability of active ingredients in diluted veterinary disinfectant solutions under simulated storage conditions**
Chae Hong Rhee, Hye-sook Lee, Hyeong-jun Yun, Ga-Hee Lee, Su-Jeong Kim, Sok Song, Myoung-Heon Lee, Moon Her and Wooseog Jeong
- 80 **Heterologous expression, purification and structural features of native *Dictyostelium discoideum* dye-decolorizing peroxidase bound to a natively incorporated heme**
Özlem Kalkan, Sravya Kantamneni, Lea Brings, Huijong Han, Richard Bean, Adrian P. Mancuso and Faisal H. M. Koua
- 93 **Chirality-enhanced transport and drug delivery of graphene nanocarriers to tumor-like cellular spheroid**
Hyunsu Jeon, Runyao Zhu, Gaeun Kim and Yichun Wang
- 105 **Preparation and structural analysis of fucomannogalactan and β -1,6-glucan from *Grifola frondosa* mycelium**
Jie Geng, Guining Wang, Jiao Guo, Xiao Han, Yunhe Qu, Yifa Zhou, Guihua Tai, Lin Sun and Hairong Cheng
- 116 **Advancement of regulating cellular signaling pathways in NSCLC target therapy via nanodrug**
Wenqiang Li, Mei Li, Qian Huang, Xiaoyu He, Chen Shen, Xiaoming Hou, Fulai Xue, Zhiping Deng and Yao Luo



OPEN ACCESS

EDITED BY

Adán Pinto Fernández,
University of Oxford, United Kingdom

REVIEWED BY

Matthew Bogyo,
Stanford University, United States
Marcin Poreba,
Wrocław University of Science and
Technology, Poland

*CORRESPONDENCE

Koen Augustyns,
✉ koen.augustyns@uantwerpen.be

SPECIALTY SECTION

This article was submitted
to Chemical Biology,
a section of the journal
Frontiers in Chemistry

RECEIVED 04 November 2022

ACCEPTED 19 December 2022

PUBLISHED 05 January 2023

CITATION

Ramos-Llorca A, Decraecker L,
Cacheux VMY, Zeiburlina I, De bruyn M,
Battut L, Moreno-Cinos C, Ceradini D,
Espinosa E, Dietrich G, Berg M,
De Meester I, Van Der Veken P,
Boeckxstaens G, Lambeir A-M,
Denadai-Souza A and Augustyns K (2023),
Chemically diverse activity-based probes
with unexpected inhibitory mechanisms
targeting trypsin-like serine proteases.
Front. Chem. 10:1089959.
doi: 10.3389/fchem.2022.1089959

COPYRIGHT

© 2023 Ramos-Llorca, Decraecker,
Cacheux, Zeiburlina, De bruyn, Battut,
Moreno-Cinos, Ceradini, Espinosa,
Dietrich, Berg, De Meester, Van Der Veken,
Boeckxstaens, Lambeir, Denadai-Souza
and Augustyns. This is an open-access
article distributed under the terms of the
[Creative Commons Attribution License](#)
(CC BY). The use, distribution or
reproduction in other forums is permitted,
provided the original author(s) and the
copyright owner(s) are credited and that
the original publication in this journal is
cited, in accordance with accepted
academic practice. No use, distribution or
reproduction is permitted which does not
comply with these terms.

Chemically diverse activity-based probes with unexpected inhibitory mechanisms targeting trypsin-like serine proteases

Alba Ramos-Llorca¹, Lisse Decraecker², Valérie M. Y. Cacheux¹,
Irena Zeiburlina², Michelle De bruyn³, Louise Battut⁴,
Carlos Moreno-Cinos¹, Davide Ceradini⁵, Eric Espinosa⁴,
Gilles Dietrich⁴, Maya Berg¹, Ingrid De Meester³,
Pieter Van Der Veken¹, Guy Boeckxstaens², Anne-Marie Lambeir³,
Alexandre Denadai-Souza² and Koen Augustyns^{1*}

¹Laboratory of Medicinal Chemistry, Department of Pharmaceutical Sciences, Faculty of Pharmaceutical, Biomedical and Veterinary Sciences, University of Antwerp, Antwerp, Belgium, ²Laboratory for Intestinal Neuroimmune Interactions, Translational Research Center for Gastrointestinal Disorders, Department of Chronic Diseases, Metabolism and Ageing, KU Leuven, Leuven, Belgium, ³Laboratory of Medical Biochemistry, Department of Pharmaceutical Sciences, Faculty of Pharmaceutical, Biomedical and Veterinary Sciences, University of Antwerp, Antwerp, Belgium, ⁴IRSD, Université de Toulouse, INSERM, INRA, ENVT, UPS, Toulouse, France, ⁵Latvian Institute of Organic Synthesis, Riga, Latvia

Activity-based probes (ABP) are molecules that bind covalently to the active form of an enzyme family, making them an attractive tool for target and biomarker identification and drug discovery. The present study describes the synthesis and biochemical characterization of novel activity-based probes targeting trypsin-like serine proteases. We developed an extensive library of activity-based probes with “clickable” affinity tags and a diaryl phosphonate warhead. A wide diversity was achieved by including natural amino acid analogs as well as basic polar residues as side chains. A detailed enzymatic characterization was performed in a panel of trypsin-like serine proteases. Their inhibitory potencies and kinetic profile were examined, and their IC₅₀ values, mechanism of inhibition, and kinetic constants were determined. The activity-based probes with a benzyl guanidine side chain showed the highest inhibitory effects in the panel. Surprisingly, some of the high-affinity probes presented a reversible inhibitory mechanism. On the other hand, probes with different side chains exhibited the expected irreversible mechanism. For the first time, we demonstrate that not only irreversible probes but also reversible probes can tightly label recombinant proteases and proteases released from human mast cells. Even under denaturing SDS-PAGE conditions, reversible slow-tight-binding probes can label proteases due to the formation of high-affinity complexes and slow dissociation rates. This unexpected finding will transform the view on the required irreversible nature of activity-based probes. The diversity of this library of activity-based probes combined with a detailed enzyme kinetic characterization will advance their applications in proteomic studies and drug discovery.

KEYWORDS

activity-based probe, serine protease, inhibitors, mast cells (MCs), irreversible inhibition

1 Introduction

In recent years, many efforts have been carried out to study the expression and function of proteins in biological organisms. This provided new insights into the pathophysiology of different diseases and disorders. Activity-based protein profiling (ABPP) is a proteomics technique that uses activity-based probes (ABPs) to visualize and characterize enzyme activity within a complex proteome. These chemical probes are designed to react covalently with the active form of a target enzyme and allow their detection or isolation. Thus, ABPs give information about the activity level of an enzyme rather than its expression level (Cravatt et al., 2008; Fang et al., 2021). This feature represents a considerable advantage since protease activity is tightly regulated. All ABPs share a similar structure consisting of four parts: 1) a warhead or reactive group; 2) a selectivity enhancing group that targets a specific enzyme family; 3) a reporter tag used for visualization or isolation, and 4) a linker or spacer to connect the three other components (Jessani and Cravatt, 2004; Berger et al., 2012).

ABPs have the potential for target and biomarker identification in different pathologies (Carvalho et al., 2015). The most common application for ABPs is detecting and visualizing active enzymes in biological samples, including *in vitro* samples, and visualization in animal models *in vivo*. However, the uptake of the ABPs by living organisms can be problematic due to their bulkiness. Alternatively, conjugation with the reporter tag can be done *in situ* by click chemistry. The probe precursors are added to living cells or tissues and then undergo the reaction with a fluorophore or affinity label to yield the ABP. Subsequently, the probes can be visualized or identified by different techniques (Sanman and Bogoy, 2014; Yao et al., 2021).

Different analytical tools can detect the complex enzyme-ABP. The method used depends on the reporter tag of choice. Fluorescent or radioactive labels could be detected by SDS-PAGE gel, imaging by microscopy, or flow cytometry (Herrera Moro Chao et al., 2015; Poreba et al., 2018; Elvas et al., 2019). Whereas, Western blots are used for biotinylated probes (Sadaghiani et al., 2007; Edgington et al., 2011). The latter can also be used to isolate or purify the targeted enzyme before detection. The strong interaction of biotin with immobilized avidin makes it a good strategy for enzyme affinity purification and mass spectrometry (MS) detection, thereby allowing the unambiguous identification of active proteases (Fonović and Bogoy, 2008; Li et al., 2013). Unfortunately, the conditions needed to dissociate the biotin-avidin interaction are harsh and sometimes unsuitable for the analysis. Alternatively, desthiobiotin, an analog of biotin which does not contain sulfur, can be used. Desthiobiotin has a lower affinity with avidin, therefore, the ABPs and enzymes can better tolerate the dissociation conditions (Hirsch et al., 2002; Ngo et al., 2019).

ABPs have been designed for various enzyme families (Yee et al., 2005; Kalesh et al., 2010; Kallemeijn et al., 2012). Specifically, they have been widely studied for many proteases (Serim et al., 2012), such as cysteine (Wang et al., 2003; Kato et al., 2005), metalloproteases (Geurink et al., 2010) and serine proteases (Shannon et al., 2012). Serine proteases represent one of the largest classes of proteases expressed in the human degradome. Unlike cysteine proteases, which are predominantly intracellular, most serine proteases are secreted enzymes, thereby active players in cell-to-cell communication in health and disease. Unambiguous identification of active serine proteases released by cells has been hindered by the

limitations of classical studies based on enzymatic substrates and inhibitors due to the catalytic overlap among proteases, while the use of ABPs for this purpose has made its proof (Denadai-Souza et al., 2018).

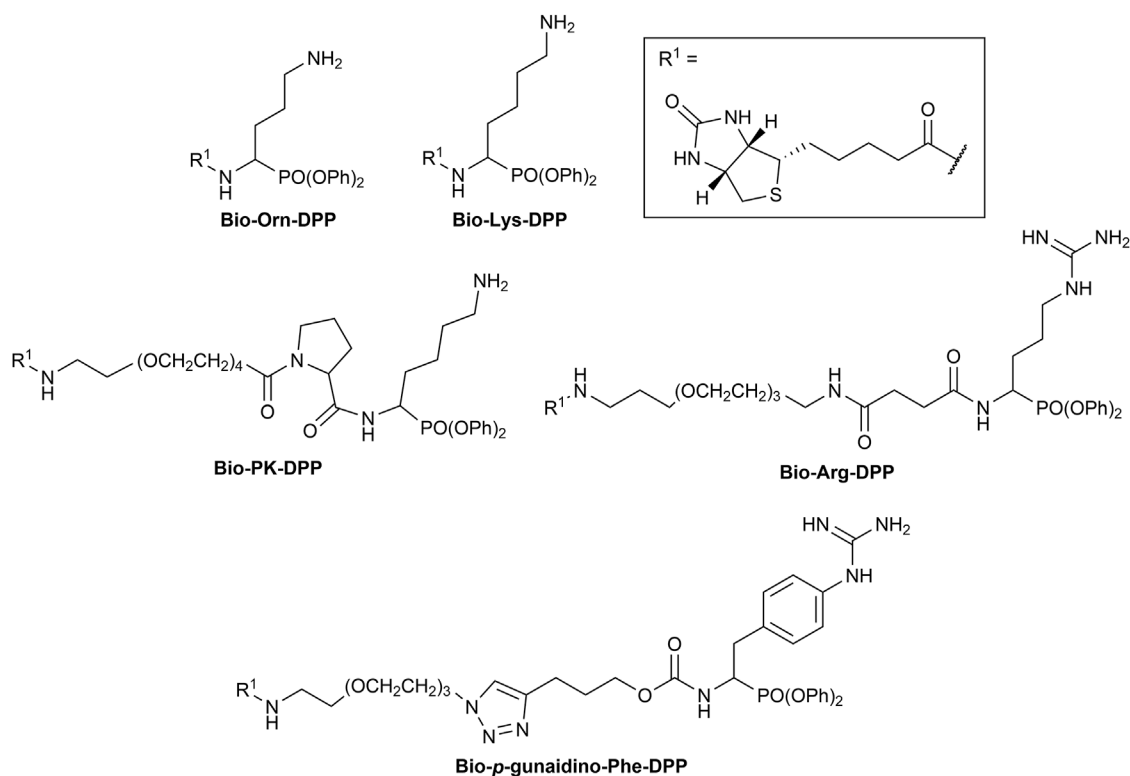
The first probe targeting serine proteases was based on a fluorophosphonate warhead, designed to react covalently with the active site serine residue on serine hydrolases. However, it has a wide-ranging reactivity and did not show selectivity towards serine proteases (Liu et al., 1999). Other warheads reported for this enzyme family include isocoumarins (Kam et al., 1993), sulfonyloxyphtalimides (Schulz-Fincke et al., 2018), and diphenyl phosphonates (Ides et al., 2014).

Diphenyl phosphonate (DPP) is a well-studied reactive group. The phosphorus can react with the serine hydroxyl on the active site to form a covalent bond. Thus, it has the required characteristics to design selective and irreversible ABPs. Therefore, it was previously used to develop irreversible inhibitors and ABPs targeting serine proteases (Oleksyszyn and Powers, 1991; Jackson et al., 1998; Joossens et al., 2007).

Within the human degradome, serine proteases can be divided into three main subfamilies known as trypsin-, chymotrypsin-, and elastase-like, depending on their substrate specificity. The specificity of a protease is determined by the preferred amino acid sequence that will fit into the specificity pocket of the active site (Perona and Craik, 2008). In this study, we focus on trypsin-like serine proteases. These have an aspartic acid residue at the bottom of the primary substrate binding pocket (S1). Thus their preference is shifted towards basic and polar residues such as lysine or arginine (Drag and Salvesen, 2010).

The first synthesized *α*-aminoalkyl diphenyl phosphonate ABPs targeting trypsin-like proteases were described by Hawthorne et al. (2004). These were based on lysine (Biotin-Lys-DPP) and ornithine (Bio-Orn-DPP) as a selectivity enhancing group. Similarly, Pan et al. (2006) described a lysine ABP by adding a pegylated linker. Additionally, they described a promising ABP with two residues, lysine in P1 and proline in P2 (Biotin-PK-DPP). More recently, Reihill et al. described an arginine probe (Biotin-Arg-DPP) as an inhibitor for channel activating proteases (Martin and Walker, 2011; Reihill et al., 2016; Ferguson et al., 2022). Moreover, several “clickable” benzyl guanidine probes conjugated with different reporter tags were reported, for instance, biotin (Biotin-*p*-guanidino-Phe-DPP) (Augustyns et al., 2012). This was proven to be a potential Positron emission tomography (PET) imaging agent if coupled with a radioactive label (Ides et al., 2014) (Figure 1).

Driven by the need to identify new biomarkers in pathologies where serine proteases are upregulated and inspired by previously reported irreversible serine protease inhibitors and ABPs, this study reports the synthesis and characterization of a library of ABPs for trypsin-like serine proteases. The idea was to move away from the ABPs mimicking the natural basic amino acids lysine and arginine and to design several different synthetic analogs to improve potency and selectivity. The ABPs described are based on a DPP warhead with a biotin or desthiobiotin tag attached by click chemistry. We performed an extensive biochemical characterization and demonstrated the ability of these ABPs to differently label trypsin-like serine proteases, both recombinant enzymes and also from degranulated mast cells. Thus, these ABPs have the potential to be used in more complex pathological samples to identify active trypsin-like proteases participating in physiological processes as well as dysregulated enzymes potentially promoting disease. Therefore, these could

**FIGURE 1**

Chemical structure of published biotinylated ABPs targeting trypsin-like serine proteases.

represent a valuable tool with translational prospects for target identification and biomarker discovery.

2 Materials and methods

2.1 Chemistry

Reagents were obtained from commercial sources and were used without further purification. Characterization of all compounds was done with ¹H and ¹³C NMR and mass spectrometry. ¹H and ¹³C NMR spectra were recorded on a 400 MHz Bruker Avance III Nanobay spectrometer with Ultrashield working at 400 and 100 MHz, respectively, and analyzed by use of MestReNova or TopSpin analytical chemistry software. Chemical shifts (δ) are in parts per million (ppm), and coupling constants (*J*) are in hertz (Hz). The signal splitting patterns were described as s = singlet, d = doublet, t = triplet, q = quartet, p = pentuplet, dd = doublet of doublet, dt = doublet of triplet, td = triplet of doublet, tt = triplet of triplet, ddd = doublet of doublet of doublet, br = broad, and m = multiplet. The LC–MS analysis was performed on a Waters UPLC–MS system equipped with a TUV and QDa detector; the column used is an Acquity UPLC BEH C18 (1.7 μm, 2.1 × 50 mm), and as eluent, a mixture of .1% FA in H₂O, .1% FA in CH₃CN, H₂O, and MeCN. The wavelengths for UV detection were 254 and 214 nm.

When necessary, flash chromatography separations were carried out using a Biotage Isolera One purification system equipped with an internal variable dual-wavelength diode array detector (200–400 nm).

Silica gel columns were used for normal phase purifications, and reverse-phase purifications were done using C18 cartridges, both from Büchi or Biotage. Dry sample loading was done by self-packing sample cartridges using Celite 545. Gradients used varied for each purification.

HRMS involved the following: the dry samples of final compounds were dissolved in CH₃CN to a concentration of .1 mM and then diluted x10 in a solution 50:50 of CH₃CN:H₂O.

The synthetic procedures and analytical data for all compounds reported in this manuscript can be found in the [Supplementary Material](#). Additional data, including schemes for the synthesis of intermediates en route to final compounds, can also be found in the [Supplementary Material](#).

2.2 Determination of IC₅₀ values

The IC₅₀ value is defined as the concentration of inhibitor required to reduce the enzyme activity to 50% after a 15 min preincubation with the enzyme at 37°C before the addition of the substrate. The IC₅₀ values were determined using a spectrophotometric assay. All the experiments were conducted in duplicate. The readout consisted of evaluating the protease-mediated release of the chromophore *para*-nitroaniline (pNA) or fluorophore 7-amino-4-methyl coumarin (AMC) moieties from the respective substrates. Enzymatic activity was measured for 30 min at 37°C. All compounds were initially screened at three concentrations (10, 1, and .1 μM) to estimate the range of the IC₅₀ value. Those which were able to reduce protease

activity by at least 50% at a concentration of 10 μM were submitted to an exact IC_{50} determination. The final IC_{50} values of the most potent inhibitors were the average of two independent experimental results. A third independent experiment was performed when the standard deviation of the two independent experiments was higher than three times the IC_{50} value. IC_{50} values were obtained by fitting the data with the four-parameter logistics equation using GraphPad Prism 9.

The conditions for each protease are described as follows, the concentration of substrate used was at the corresponding K_m .

Trypsin-3 (recombinant trypsin-3, R&D) and fluorogenic substrate tosyl-Gly-Pro-Arg-AMC ($K_m = 22.5 \mu\text{M}$) were used in Tris buffer (100 mM Tris, 1 mM CaCl_2) at pH 8.0 (25°C). Trypsase (recombinant trypsinase β -2, EnzoLife Sciences) and fluorogenic substrate Boc-Gln-Ala-Arg-AMC ($K_m = 250 \mu\text{M}$) were used in Tris buffer (50 mM Tris, 120 mM NaCl, .1 mg/ml BSA, .1 mg/ml heparin) at pH 8.0 (25°C). Thrombin (recombinant thrombin, R&D) and fluorogenic substrate Boc-Val-Pro-Arg-AMC ($K_m = 15 \mu\text{M}$) were used in TRIS buffer (50 mM Tris HCl, 50 mM Tris base, 10 mM CaCl_2 , 150 mM NaCl) at pH 8.3 (25°C). uPA (recombinant urokinase plasminogen activator, HYPHEN BioMed) and chromogenic substrate *pyro*-Glu-Gly-Arg-pNA ($K_m = 80 \mu\text{M}$) were used in HEPES buffer (50 mM HEPES) at pH 8.1 (25°C). Cathepsin G (cathepsin G human neutrophil, Sigma-Aldrich) and fluorogenic substrate Suc-Ala-Ala-Pro-Phe-AMC ($K_m = 130 \mu\text{M}$) were used in Tris buffer (50 mM Tris, 120 mM NaCl) at pH 8.0 (25°C). TLCK-treated pancreatic bovine chymotrypsin (Sigma-Aldrich) and fluorescent substrate Suc-Ala-Ala-Pro-Phe-AMC ($K_m = 58 \mu\text{M}$) were used in Tris buffer (50 mM Tris, 20 mM CaCl_2) at pH 8.3 (25°C). Neutrophil Elastase (recombinant neutrophil elastase, Enzo LifeSciences) and fluorogenic substrate Suc-Ala-Ala-Pro-Val-AMC ($K_m = 500 \mu\text{M}$) were used in Tris buffer (50 mM Tris, 120 mM NaCl) at pH 8.0 (25°C).

2.3 Kinetic experiments and determination of k_{app} , K_1 and K_i^*

Because the compounds described in this paper were previously described as irreversible inhibitors, the IC_{50} value is inversely correlated with the second-order rate constant of inactivation. For a simple pseudo-first-order inactivation process, the activity after incubation with inhibitor (v_i) varies with the inhibitor concentration (i), as described in the following equation:

$$v_i = v_0 \cdot e^{-kit}$$

where v_0 is the activity in the absence of an inhibitor, k is the second-order rate constant of inactivation, and t is the time. The inactivation rate constant was determined from the time course of inhibition.

Kinetic assays were performed in the following manner. The inhibitor was mixed with the substrate, and the buffer solution with the enzyme was added at the time zero. The progress curves show the release of pNA or AMC as a function of time. Initially, no inhibitor is bound to the enzyme, and the tangent to the progress curve (dA/dt) is proportional to the free enzyme concentration. The free enzyme concentration decreases over time due to inhibitor binding kinetics, as described above. Progress curves

were recorded in pseudo-first-order conditions ($[I]_0 \gg [E]_0$) and with less than 10% conversion of the substrate during the entire time course. In these conditions, dA/dt decreases exponentially with time. The progress curves were fitted with the integrated rate equation with GraFit7 to yield a value for k_{obs} , a pseudo-first-order rate constant.

$$A_t = A_0 + v_s \cdot t + (v_i - v_s) \cdot (1 - e^{-k_{\text{obs}}t}) / k_{\text{obs}}$$

where A_t is the absorbance at time t , A_0 is the absorbance at time zero, v_i is the initial rate and v_s is the velocity at the steady-state.

The apparent second-order rate constant (k_{app}) was calculated from the slope of the linear part of the plot of k_{obs} vs. the inhibitor concentration ($[I]_0$). In the case of competition between the inhibitor and the substrate, k_{app} is smaller than the “real” second-order rate constant k discussed above because a certain fraction of the enzyme is present as an enzyme-substrate complex. k_{app} depends on the substrate concentration used in the experiment, as described by Lambeir et al. (1996).

The apparent equilibrium constants were obtained from the following equations,

$$\frac{v_i}{v_0} = \frac{1}{1 + \frac{[I]}{K_i}}; \quad \frac{v_s}{v_0} = \frac{1}{1 + \frac{[I]}{K_i}}$$

where v_i is the initial rate, v_s is the steady-state velocity and v_0 is the uninhibited initial rate.

2.4 Determination of inhibition type

To monitor the dissociation of the inhibitor-enzyme, aliquots of the enzyme were incubated at 37°C without and with the inhibitor at a concentration 10 times higher than its IC_{50} . The enzyme concentration was 2.5 times higher than the concentration used for the IC_{50} determinations. After 15 min, the aliquots were diluted 10-fold or 100-fold into the substrate concentration and assay buffer used for the IC_{50} determination. The dissociation of the enzyme-inhibitor complex was monitored by substrate hydrolysis over time (Joossens et al., 2006).

2.5 Labeling and detection of recombinant proteases

Recombinant proteases (100 ng) were labeled with 1 μM ABP in reaction buffer in a final volume of 40 μL for 30 min at 37°C. After the addition of 4X Laemmli buffer (Bio-Rad, GmbH) supplemented with Bond-Breaker Tris (2-CarboxyEthyl)Phosphine (TCEP) Solution (Thermo Scientific, United States), the samples were heated at 95°C for 5 min and loaded into 4%–20% Mini-Protean TGX precast gels (Bio-Rad, GmbH). After electrophoresis, the proteins were blotted onto nitrocellulose membranes using the Trans-Blot Transfer Turbo System (Bio-Rad). Membranes were incubated with NeutrAvidin-HRP (1:50,000), and bands were visualized with ECL Select Western Blot Detection Reagent (GE Healthcare Life Sciences) by chemiluminescence (Chemidoc XRS; Bio-Rad). The molecular weight of each band was determined with the Image Lab Software v5 (Bio-Rad).

2.6 Primary human mast cells culture

Peripheral blood mononuclear cells (PBMCs) were obtained from buffy coats (Etablissement Français du Sang). CD34⁺ precursors cells were isolated from PBMCs (EasySep™ Human CD34 Positive Selection Kit, STEMCELL Technologies) and grown under serum-free conditions using StemSpan™ medium (STEMCELL Technologies) supplemented with recombinant human IL-6 (50 ng/ml; Peprotech), human IL-3 (10 ng/ml; Peprotech) and 3% supernatant of CHO transfectants secreting murine SCF (a gift from Dr. P. Dubreuil, Marseille, France, 3% correspond to ~50 ng/ml SCF) for 1 week. Cells were next grown in IMDM Glutamax I, sodium pyruvate, 2-mercaptoethanol, .5% BSA, Insulin-transferrin selenium (all from Invitrogen), penicillin (100 U/ml), streptomycin (100 µg/ml) and 3% supernatant of CHO transfectants secreting murine SCF for 8 weeks then tested phenotypically (CD117+, FcεRI+) and functionally (β-hexosaminidase release in response to FcεRI crosslinking) before use for experiments. Only primary cell lines showing more than 95% CD117+/FcεRI+ cells were used for experiments.

2.7 Mast cell degranulation assay

1 × 10⁵ mast cells were distributed in 50 µl Tyrode's Buffer and adapted to 37°C for 30 min. Mast cells were next stimulated with DNP-BSA (200 ng/ml) after sensitization with 1 µg/ml of IgE anti DNP (Sigma-Aldrich) overnight. Supernatants were harvested and stored at -80°C. (β-hexosaminidase was assayed by measuring the release of p-nitrophenol from the substrate p-nitrophenyl N-acetyl-β-D-glucosaminide).

2.8 Measurement of protein concentration

The concentration of protein in supernatants was determined using the Pierce Protein BCA Assay Kit, according to instructions (Thermo Scientific).

2.9 Measurement of proteolytic activity

Tryptase-like activity in mast cell supernatants was measured with .075 mM Boc-Gln-Ala-Arg-AMC hydrochloride as substrate in 50 mM Tris 120 mM NaCl + .1 mg/ml BSA + 50 µg/ml heparin pH = 8 at 25°C (Sigma-Aldrich). Substrate cleavage was calculated by the change in fluorescence (excitation: 355 nm, emission: 460 nm), measured over 30 min at 37 °C on a FLUOstar Omega microplate reader (BMG Labtech). Sample values were interpolated into a linear regression generated with a standard curve of AMC (Sigma-Aldrich). Data were expressed as U of tryptase-like activity per L (U defined as 1 µmol/min).

2.10 Functional proteomic profiling of mast cell supernatants

Mast cell supernatants (10 µg of total protein) were labeled with 1 µM individual ABPs (46b, 52b, or 57b) in 50 mM Tris, 120 mM

NaCl, .1 mg/ml BSA, 50 µg/ml heparin, pH 8 at 25°C (Sigma-Aldrich) in a final volume of 500 µL. As a control, supernatants were pre-incubated for 60 min at 37°C under stirring (1,000 rpm) in 4 mM AEBSE (Sigma), and 1X complete EDTA-free inhibitor cocktail (Roche) before incubation with a mixture containing the 3 ABPs mentioned above. The pre-incubation with protease inhibitors allows the identification of active proteases since enzyme inhibition abrogates their interaction with the ABP. The reaction product was then precipitated in 15% trichloroacetic acid at 4°C overnight. The pellet was washed twice in cold acetone (-20°C) and solubilized in 45 µL of Laemmli buffer (Bio-Rad) supplemented with Bond-Breaker TCEP Solution (Thermo Scientific). Samples were then heated at 95°C for 5 min, clarified by centrifugation at 12,000 g for 5 min, and the solubilized sample was loaded into 4%–20% Mini-Protean TGX precast gels (Bio-Rad, GmbH). After electrophoresis, the proteins were blotted onto nitrocellulose membranes using the Trans-Blot Transfer Turbo System (Bio-Rad). Membranes were incubated with NeutrAvidin-HRP, and bands were visualized with ECL Select Western Blot Detection Reagent (GE Healthcare Life Sciences) by chemiluminescence (Chemidoc XRS; Bio-Rad). The molecular weight of each band was determined with the Image Lab Software v5 (Bio-Rad) with Dual Color Protein Precision Plus Standard (10–250 kDa; Bio-Rad) as reference. The bands corresponding to active proteases were identified by their sensitivity to the pre-incubation with protease inhibitors.

2.11 Detection of tryptase in mast cell supernatants

Protein in the mast cell supernatants (75 µg of total protein) was precipitated in 15% trichloroacetic acid at 4°C overnight. The pellet was washed twice in cold acetone (-20°C) and solubilized in 75 µL of Laemmli buffer protein supplemented with TCEP (Bio-Rad). Samples were then heated at 95°C for 5 min, clarified by centrifugation at 12,000 g for 5 min, and 5 µg of the solubilized sample was loaded into 4%–20% Mini-Protean TGX precast gels (Bio-Rad, GmbH). After electrophoresis, the proteins were blotted onto a nitrocellulose membrane using the Trans-Blot Transfer Turbo System (Bio-Rad). The membrane was incubated with primary anti-mast cell tryptase antibody (sc-32889, Santa Cruz Biotechnology) at 1:1,000 dilution overnight at 4°C. Subsequently, the membrane was labeled with the secondary HRP-conjugated antibody (1:10,000; P0448, Dako) for 1 h at room temperature. Bands were visualized with ECL Select Western Blot Detection Reagent (GE Healthcare Life Sciences) by chemiluminescence (Chemidoc XRS; Bio-Rad). The molecular weight of each band was determined with the Image Lab Software v5 (Bio-Rad).

3 Results

3.1 Chemical synthesis

With the aim to achieve a range of chemical tools able to identify different trypsin-like serine proteases in complex proteomes, the first goal of this study was to obtain an extensive and diverse library of ABPs. Trypsin-like serine proteases interact favorably with basic and polar residues in the S1 pocket (Perona and Craik, 2008). Previously

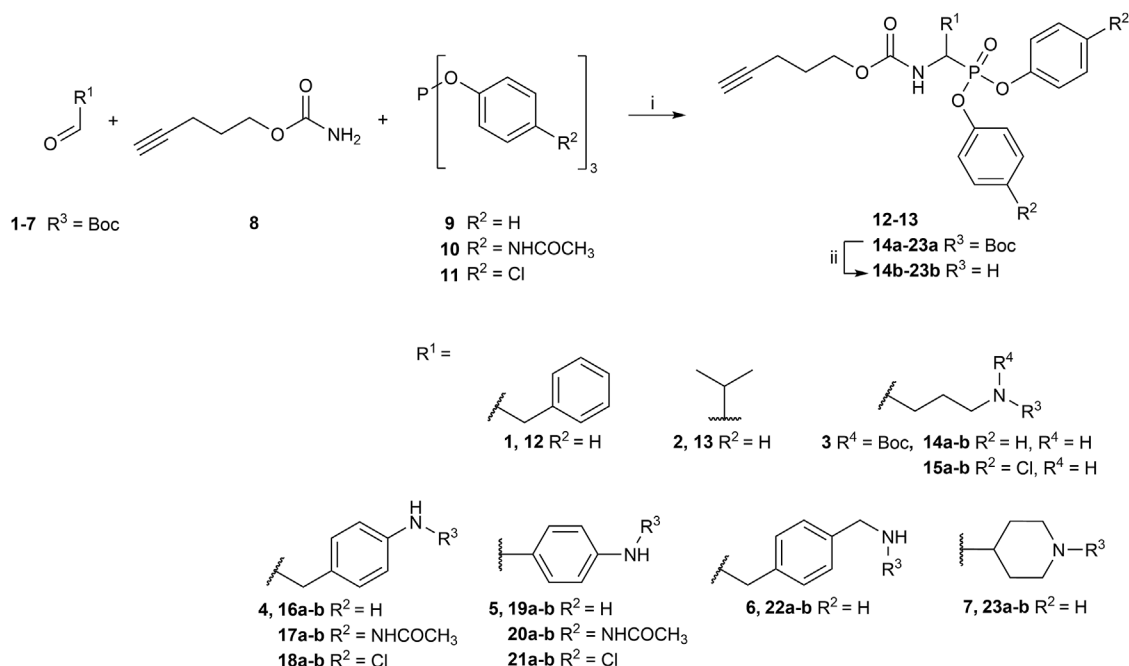


FIGURE 2

General synthesis of diaryl phosphonate alkyne probes by the Birum-Oleksyszyn reaction; (i) Lewis acid, solvent, rt, 16 h; (ii) TFA, DCM, rt, 2–5 h or HCl (4M, dioxane), rt, 2–5 h.

reported diaryl phosphonate ABPs targeting this family incorporated ornithine and the trypsin-like natural substrate, lysine (Pan et al., 2006). Other studies included benzyl guanidine as the selectivity enhancing moiety (Ides et al., 2014). Pan et al. (2006) described a promising ABP for trypsin with a two amino acid diphenyl phosphonate with proline and lysine. To broaden the probe library, not only amino acids lysine and arginine were included but also other non-natural amino acid analogs with different polar and basic moieties and a two amino acid probe with proline and lysine. In addition to residues targeting the trypsin-like family, phenylalanine and valine were introduced to target chymotrypsin and elastase-like serine proteases.

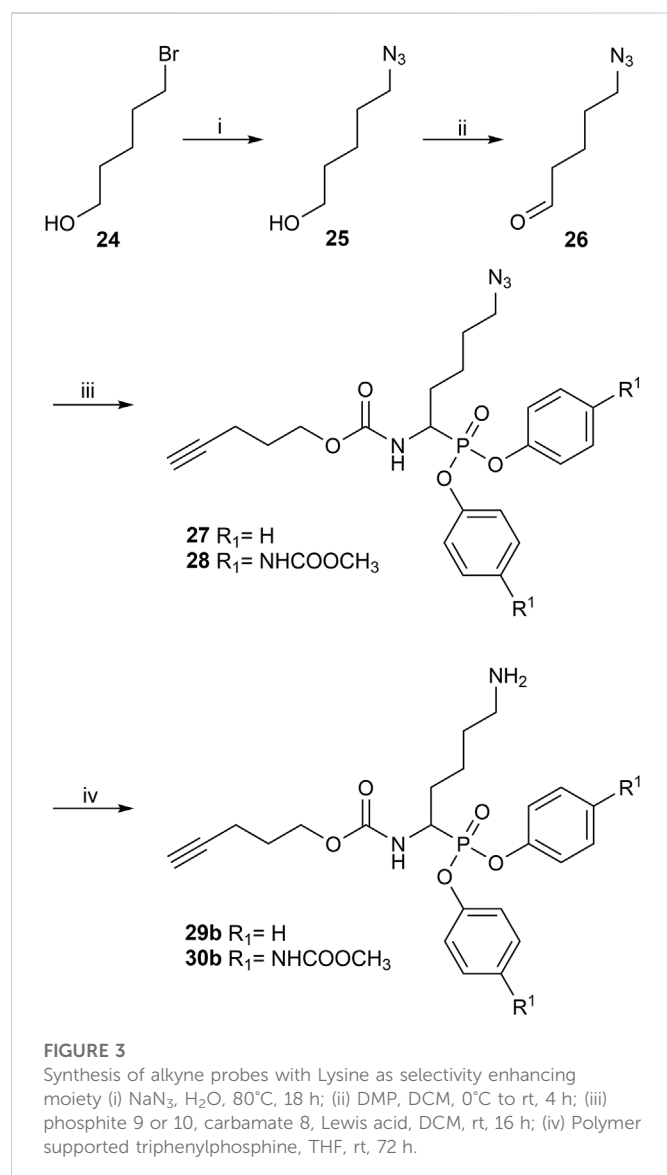
Although diaryl phosphonate ABPs targeting serine proteases have been reported in the literature, this study aimed to develop a common and accessible synthetic strategy for a wide-ranging library. Therefore, instead of adding the reporter tag by commonly used peptidic coupling (Pan et al., 2006; Reihill et al., 2016), the pegylated linker was added by click-chemistry. More specifically, the Huisgen 1,3-dipolar cycloaddition between an azide and an alkyne to form a 1,2,3-triazole moiety (Breugst and Reissig, 2020). This approach requires an initial probe bearing the warhead with a terminal alkyne. The synthetic strategy depicted in Figure 2 was inspired by the previously described route used for benzyl guanidine ABPs synthesis (Augustyns et al., 2012; Ides et al., 2014).

The primary step of the diaryl phosphonate probe synthesis is the Birum-Oleksyszyn reaction, first described by Oleksyszyn et al. (1979) in 1979 and later optimized by van der Veken et al. (2004) in 2005. This is a three-component reaction involving an aldehyde, a carbamate, and a triaryl phosphite, catalyzed by an acid (Figure 2). The product can contain an acid-labile Boc-protecting group if a Lewis acid is used as the catalyst instead of a Brønsted acid. The aldehyde

carries the selectivity enhancing group targeting the enzyme S1 pocket. Thus, various aldehydes were used to extend the chemical space (1–7). The pent-4-yn-1-yl carbamate (8) was prepared from the corresponding alcohol to conjugate the precursor with the reporting tag (Supplementary Figure S1). To add further diversity, triaryl phosphites (9–11) with two different substituents in the *para*-position were prepared from phosphorus trihalides (Supplementary Figures S2, S3).

The Birum-Oleksyszyn step required protected nitrogen aldehydes. Thus, for most products, the commercial alcohols were first protected with a Boc group, followed by Dess Martin periodinane (DMP) oxidation to achieve the desired aldehyde (4–5, 7) (Supplementary Figure S4). However, other protecting or oxidation strategies were needed for the aliphatic amines and the benzyl methyl amine.

The synthesis of 4-aminobutanol (3) required a double Boc protection of the corresponding alcohol before a Swern oxidation (Supplementary Figure S5). In contrast, the double Boc protection of 5-aminopentanol was insufficient to achieve yields higher than 5% in the Birum-Oleksyszyn reaction. It is suggested that the catalytic quantity of Lewis acid is enough to deprotect one of the Boc groups. Since Boc protection was not adequate, other synthetic strategies were assessed. The described synthesis of a diphenyl phosphonate probe with lysine and proline-lysine by Pan et al. (2006) was achieved by phthalimide protection. Unfortunately, in our hands, the phosphonate was readily hydrolyzed when deprotecting with hydrazine. A study by Hamilton et al. (1993) also postulated that they experienced inconsistency with hydrazine-mediated phthalimide deprotection. Therefore, we explored a novel synthetic strategy with the use of an azide group instead of the primary amine. Hence, the desired lysine alkyne probes (29b–30b) were



obtained from 5-azidopentanal (26), and the further reduction to a primary amine was best achieved with polymer-supported triphenylphosphine in THF (Figure 3). The same synthetic strategy was used for the proline-lysine alkyne probe (31b). The proline and the alkyne were introduced by peptidic coupling (Supplementary Figure S6). A similar approach was used to obtain the benzylmethylamine aldehyde (6), as the corresponding alcohol was not commercially available (Supplementary Figure S7).

The Boc protecting groups of the diarylphosphonates were removed using acid treatment with hydrogen chloride in dioxane or trifluoroacetic acid in dichloromethane (DCM).

The previously reported synthesis of benzylamine alkyne probes 16 and 17 used $\text{Cu}(\text{OTf})_2$ as a catalyst in DCM and tetrahydrofuran (THF), respectively. However, for the synthesis of benzylamine 4-acetamidophendiphenyl phosphonate (17), low yields were reported (<5%) (Augustyns et al., 2012). For the synthesis of this library, these catalyst and solvent combinations were kept. However, other Lewis acids and solvents were assessed when low yielding. A summary of the conditions used is shown in Table 1. For example, for the synthesis of 17, the yield was increased from 5% to 19% when using $\text{BF}_3(\text{OEt})_2$ in

acetonitrile (CH_3CN). For the benzylamine alkyne probe with unsubstituted diphenyl phosphonate (16), the combination of $\text{Cu}(\text{OTf})_2$ in DCM worked in a similar yield range as reported (Augustyns et al., 2012). These conditions were used for all the unsubstituted products ($\text{R}^2 = \text{H}$). However, for substituted diaryl phosphonates, either $\text{Bi}(\text{OTf})_3$ in THF (15), $\text{BF}_3(\text{OEt})_2$ in CH_3CN (17–18, 28), or $\text{Cu}(\text{OTf})_2$ in THF (20–21) were more successful. Interestingly, $\text{Bi}(\text{OTf})_3$ has recently been reported as one of the best-performing catalysts for the Birum-Oleksyszyn reaction in an extensive optimization of the synthesis of inhibitor UAMC-00050 (Joossens et al., 2007; Ceradini and Shubin, 2021).

All the alkyne probes with a basic amine, except all the lysine analogs, were elongated for further chemical space exploration by adding a guanidine moiety. The protected guanidine was inserted with *N*, *N'*-bis(*tert*-butoxycarbonyl)-1-guanylpurazole in a mixture of 1:1 of $\text{CH}_3\text{CN}/\text{DCM}$, reducing the previously reported reaction time from 3 days to 16 h (Augustyns et al., 2012). Later, the guanidine was deprotected by acid treatment before biochemical characterization (32b–41b) (Figure 4).

The obtained alkyne probes can be conjugated to different visualization tags such as rhodamine, biotin, BODIPY, or radiolabeled 4-fluorobenzamide. In this study, we used the affinity tags biotin and desthiobiotin. For the synthesis of the biotin and desthiobiotin probes, the alkyne probe reacted with an azide attached to the reporting tag by click chemistry (Figure 5). This produced full-conversion reactions with easy purifications. When the precursors presented basic nitrogens, these had to be Boc-protected before the cycloaddition to allow easier purifications (29a–39a). In the last step, the clicked probes were deprotected by acid treatment (45b–59b).

TABLE 1 Birum-Oleksyszyn reaction conditions.

#	R^1	R^2	Lewis acid	Solvent	Yield, % ^a
12		H	$\text{Cu}(\text{OTf})_2$	DCM	62
13		H	$\text{Cu}(\text{OTf})_2$	DCM	55
14		H	$\text{Cu}(\text{OTf})_2$	DCM	5
15		Cl	$\text{Bi}(\text{OTf})_3$	THF	10
16		H	$\text{Cu}(\text{OTf})_2$	DCM	29
17		NHCOCH_3	$\text{BF}_3(\text{OEt})_2$	CH_3CN	19
18		Cl	$\text{BF}_3(\text{OEt})_2$	CH_3CN	10
19		H	$\text{Cu}(\text{OTf})_2$	DCM	50
20		NHCOCH_3	$\text{Cu}(\text{OTf})_2$	THF	34
21		Cl	$\text{Cu}(\text{OTf})_2$	THF	41
22		H	$\text{Cu}(\text{OTf})_2$	DCM	45
23		H	$\text{Cu}(\text{OTf})_2$	DCM	46
27		H	$\text{Cu}(\text{OTf})_2$	DCM	71
28		NHCOCH_3	$\text{BF}_3(\text{OEt})_2$	CH_3CN	59

^aIsolated yield.

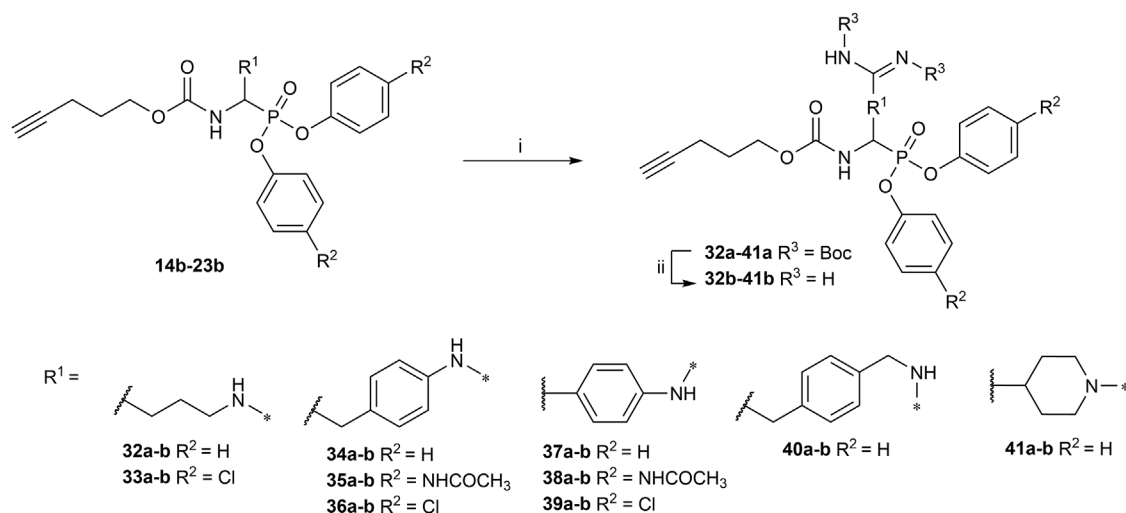


FIGURE 4

Guanylation of alkyne probes; (i) N, N'-Bis-Boc-1-Guanylpurazole, Et₃N, DCM/CH₃CN (1:1), rt, 16 h; (ii) TFA, DCM, rt, 2–5 h or HCl (4M, dioxane), rt, 2–5 h.

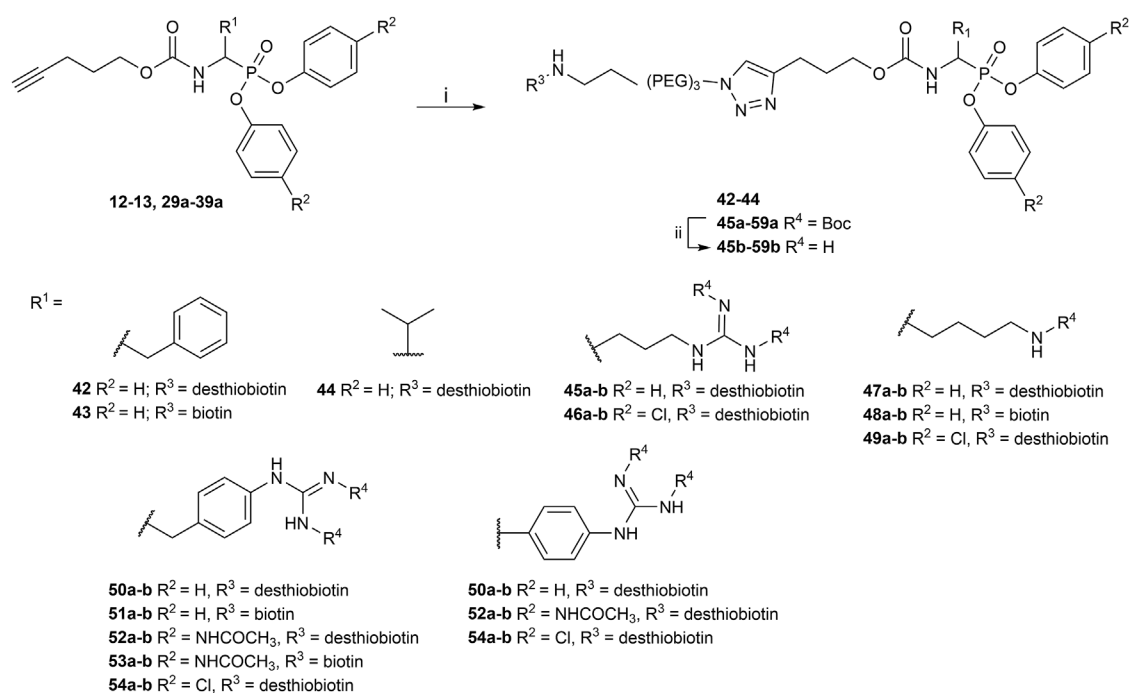


FIGURE 5

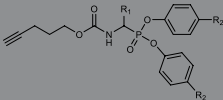
Synthesis of biotin and desthiobiotin probes by click chemistry with reporter tag azide; (i) Biotin/Desthiobiotin-(PEG)₃-Azide, CuSO₄·5H₂O, Ascorbic acid (Na salt), THF/H₂O (1:1), rt, 16 h; (ii) TFA, DCM, rt, 2–5 h or HCl (4M, dioxane), rt, 2–5 h.

3.2 Biochemical characterization

The alkyne, biotin, and desthiobiotin probes were tested in a panel of different proteases. The probes were designed to target irreversibly different families of trypsin-like serine proteases. In addition, to test their selectivity, chymotrypsin and elastase-like proteases were also

assessed. The panel included four trypsin-like proteases, as well as cathepsin G (CatG), which shares characteristics with chymotrypsin and trypsin-like proteases, and finally, chymotrypsin (ChTryp) and neutrophil elastase (NE).

The IC₅₀ values of the alkyne probes were used as a first screening cut-off. All the alkyne probes were initially screened at three

TABLE 2 IC₅₀ values of diarylphosphonate alkyne probes against a panel of serine proteases.


#	R ¹	R ²	Trypsin-3	β-tryptase	Thrombin	uPA ^a	CatG ^a	ChTryp ^a	NE ^a
IC ₅₀ (μM) ^b									
12		H	>10	>10	>10	>10	>10	1.54 ± 1.34	>10
13		H	>10	>10	>10	>10	>10	>10	>10
14b		H	>10	>10	>10	>10	>10	>10	>10
16b		H	6.85 ± 0.80	>10	>10	>10	3.74 ± 0.27	2.67 ± 0.57	>10
17b		NHCOCH ₃	3.71 ± 0.71	>10	2.97 ± 0.07	>10	0.37 ± 0.008	0.49 ± 0.28	>10
18b		Cl	1.72 ± 0.19	>10	7.88 ± 0.61	6.38 ± 0.52	0.36 ± 0.01	0.19 ± 0.14	>10
19b		H	9.06 ± 1.10	>10	6.59 ± 3.90	>10	>10	8.52 ± 1.81	>10
20b		NHCOCH ₃	N.D. ^c	>10	N.D. ^c	>10	>10	N.D. ^c	N.D. ^c
21b		Cl	N.D. ^c	>10	N.D. ^c	>10	>10	N.D. ^c	N.D. ^c
22b		H	3.82 ± 0.19	>10	>10	2.30 ± 0.10	5.26 ± 0.68	>10	>10
23b		H	>10	>10	>10	>10	>10	>10	>10
29b		H	0.07 ± 0.02	3.96 ± 0.50	7.36 ± 0.25	5.27 ± 0.15	>10	5.87 ± 3.39	>10
30b		NHCOCH ₃	0.006 ± 0.0006	0.68 ± 0.05	1.18 ± 0.07	2.44 ± 0.35	0.56 ± 0.002	>10	>10
31b	Pro-Lys	H	0.09 ± 0.03	2.98 ± 0.05	0.18 ± 0.003	2.52 ± 0.29	>10	>10	>10
32b		H	0.03 ± 0.007	3.74 ± 0.53	0.85 ± 0.13	4.80 ± 0.08	7.57 ± 0.58	>10	>10
33b		Cl	0.04 ± 0.008	0.17 ± 0.01	0.11 ± 0.007	0.25 ± 0.03	2.76 ± 0.05	>10	N.D. ^c
34b		H	0.001 ± 0.0003	0.63 ± 0.03	8.49 ± 2.25	0.008 ± 0.0003	0.45 ± 0.02	>10	>10
35b		NHCOCH ₃	<0.001	0.05 ± 0.003	1.11 ± 0.05	0.005 ± 0.001	0.06 ± 0.006	>10	>10
36b		Cl	<0.001	0.07 ± 0.02	1.77 ± 0.05	0.005 ± 0.0003	0.34 ± 0.008	3.23 ± 1.21	>10
37b		H	0.23 ± 0.01	0.90 ± 0.10	>10	1.79 ± 0.003	0.64 ± 0.03	>10	>10
38b		NHCOCH ₃	0.04 ± 0.015	0.12 ± 0.02	>10	1.52 ± 0.4	0.13 ± 0.01	>10	N.D. ^c
39b		Cl	0.09 ± 0.009	0.07 ± 0.004	>10	0.22 ± 0.06	0.09 ± 0.022	>10	N.D. ^c
40b		H	>10	>10	>10	>10	6.16 ± 0.48	>10	>10
41b		H	0.04 ± 0.002	8.37 ± 0.44	0.03 ± 0.001	>10	>10	>10	>10

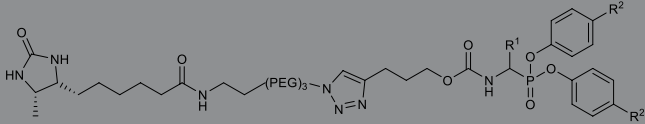
^aPanel of serine proteases abbreviations: uPA, urokinase plasminogen activator; catG, cathepsin G; ChTryp, chymotrypsin; NE, neutrophil elastase.

^bHalf maximal inhibitory concentration (IC₅₀) value is the concentration of inhibitor required to reduce the enzyme activity to 50% after a 15 min preincubation with the enzyme at 37°C and activity measurements. IC₅₀ are calculated from two independent experiments; when SD was higher than three times the average value, a third independent experiment was run (mean ± SD).

^cN.D., not determined.

concentrations (10, 1, and .1 μM). The probes with an IC₅₀ higher than 10 μM were not analyzed further, whereas the rest were submitted to an exact IC₅₀ determination. The results of this first screening are presented in Table 2. Based on these results, only the most promising alkyne probes (29–39) were clicked to biotin or desthiobiotin (45–59).

These were analyzed in the same manner. Since the alkyne probes share the same warhead and selectivity enhancing group (R¹) with the biotin and desthiobiotin probes, inhibitory potencies were similar (Table 3), as could be expected. Considering that biotin presents a strong interaction with avidin and may present challenges during the

TABLE 3 IC₅₀ values of diarylphosphonates desthiobiotin probes against a panel of serine proteases.


#	R ¹	R ²	Trypsin-3	β-tryptase	Thrombin	uPA ^a	CatG ^a	ChTryp ^a	NE ^a
IC ₅₀ (μM) ^b									
42		H	>10	>10	>10	>10	3.23 ± 0.29	2.07 ± 0.85	>10
44		H	>10	>10	>10	>10	>10	>10	4.70 ± 0.20
45b		H	0.22 ± 0.02	0.80 ± 0.05	0.61 ± 0.17	>10	>10	>10	N.D. ^c
46b		Cl	0.07 ± 0.002	0.04 ± 0.006	0.04 ± 0.006	0.42 ± 0.05	>10	>10	N.D. ^c
47b		H	0.52 ± 0.24	2.49 ± 0.19	3.55 ± 0.17	4.62 ± 0.17	>10	>10	>10
49b		NHCOCH ₃	0.09 ± 0.005	1.11 ± 0.05	1.18 ± 0.04	6.75 ± 0.52	4.47 ± 0.51	>10	>10
50b		H	0.03 ± 0.01	0.36 ± 0.07	3.52 ± 0.39	0.02 ± 0.0001	0.36 ± 0.004	1.64 ± 0.50	>10
52b		NHCOCH ₃	0.01 ± 0.001	0.07 ± 0.003	0.76 ± 0.02	0.01 ± 0.003	0.05 ± 0.007	>10	>10
54b		Cl	0.008 ± 0.002	0.11 ± 0.009	0.20 ± 0.02	0.006 ± 0.0001	0.12 ± 0.01	5.60 ± 1.06	>10
55b		H	0.24 ± 0.01	0.37 ± 0.09	>10	2.22 ± 0.07	1.62 ± 0.09	>10	N.D. ^c
56b		NHCOCH ₃	0.22 ± 0.004	0.39 ± 0.10	>10	5.19 ± 0.08	0.62 ± 0.009	>10	N.D. ^c
57b		Cl	0.18 ± 0.07	0.02 ± 0.0002	>10	0.16 ± 0.04	0.12 ± 0.04	>10	N.D. ^c
58b	Pro-Lys	H	0.16 ± 0.004	6.41 ± 0.15	0.16 ± 0.004	6.51 ± 1.15	2.90 ± 0.15	>10	N.D. ^c

^aPanel of serine proteases abbreviations: uPA, urokinase plasminogen activator; catG, cathepsin G; ChTryp, chymotrypsin; NE, neutrophil elastase.

^bHalf maximal inhibitory concentration (IC₅₀) value is the concentration of inhibitor required to reduce the enzyme activity to 50% after a 15 min preincubation with the enzyme at 37°C and activity measurements as mentioned in the Experimental section. IC₅₀ are calculated from two independent experiments; when SD was higher than three times the average value, a third independent experiment was run (mean ± SD).

^cN.D., not determined.

ABP profiling, we have based our study primarily on the desthiobiotin probes. The results of the four biotin probes analyzed are shown in the [Supplementary Table S1](#).

Because ABPs are designed to be irreversible serine protease inhibitors, the IC₅₀ is exclusively used as a first discriminatory evaluation. When an inhibitor is irreversible, its IC₅₀ value not only depends on the substrate and enzyme concentration but also on the time of incubation with the enzyme before the reaction is started by adding the substrate. Kinetic progress curves can show whether an inhibitor displays time-dependent inhibition. The progress curve in the presence of an irreversible inhibitor will show final velocities equal to zero ([Figure 6C](#)). In contrast, for a reversible inhibitor, progress curves have a non-zero final steady-state velocity ([Figure 6A](#)) ([McWhirter, 2021](#)). To corroborate the inhibitory mechanism of the compounds, jump-dilution assays were performed. These use an inhibitor concentration of 10-fold the IC₅₀ for the incubation, and *a posteriori*, the reaction mixture is diluted 10-fold or 100-fold before adding the substrate. In the case of an irreversible inhibitor, enzymatic activity is not regained ([Figure 6D](#)), whereas, in the case of a reversible compound, a slow release of the inhibitor and a gradual increase of the enzymatic activity rate is observed ([Figure 6B](#)) ([Copeland, 2013](#); [McWhirter, 2021](#)). The jump-dilution assays confirmed the behavior described by the

progress curves. The results for all probes and proteases are presented in the [Supplementary Table S2](#).

The apparent second-order rate constants (k_{app}) were derived from the kinetic progress curves. The results of the kinetic assays resemble those expected for a two-step reversible slow-binding or irreversible mechanism. Thus, the rate constant k_{app} accounts for the initial reversible enzyme-inhibitor complex (E-I) affinity and the formation rate of the reversible high-affinity complex (E*I) or the irreversible enzyme-inhibitor complex (EI). As k_{app} describes the affinity and the reactivity of the inhibitors it is the best metric to discriminate between the different inhibitors. The k_{app} values are shown in [Table 4](#).

The equilibrium association constants were derived from the progress curves of trypsin-3, β-tryptase, and thrombin to better describe the affinity of the reversible compounds. The equilibrium constant K_I describes the formation of E-I, whereas the overall process is defined by K_I* ([Copeland, 2013](#)). The equilibrium constants are shown in [Table 5](#).

Since the alkyne probes and their corresponding biotin/desthiobiotin analogs behave similarly, we will limit the discussion on the relationship between structure and activity to the alkyne probes. The IC₅₀ values ([Table 2](#)) of the benzyl guanidine probes (34b–36b) show their preference for trypsin-3 and uPA (nanomolar range) and,

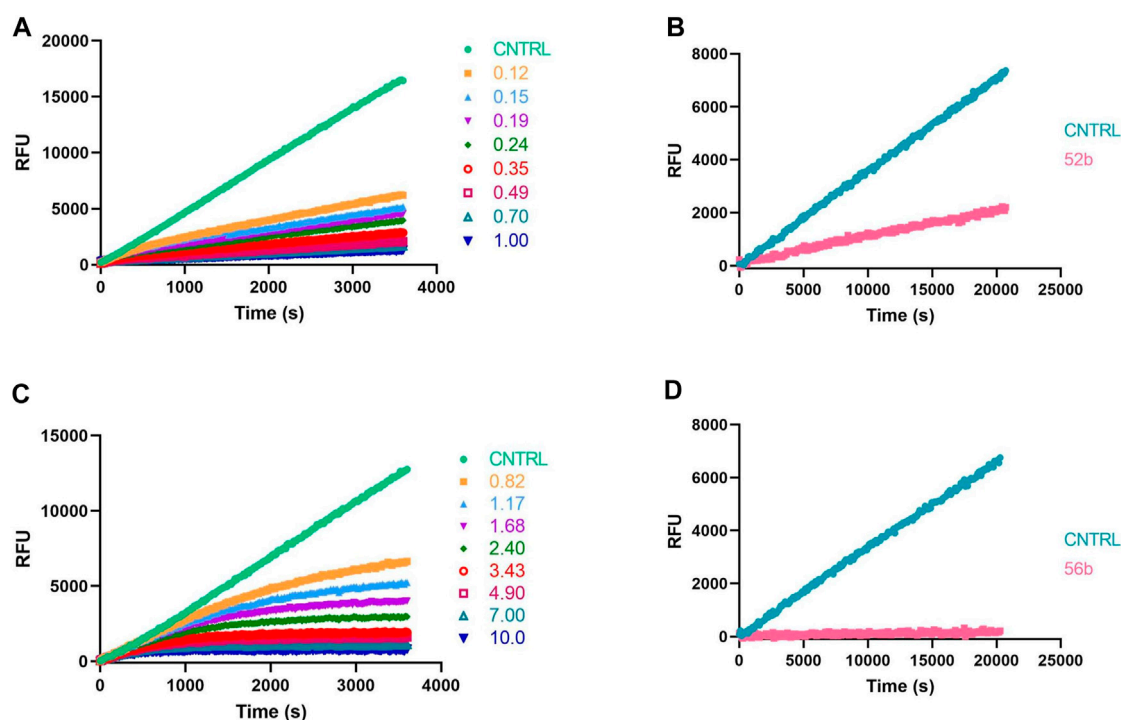


FIGURE 6

Kinetic progress curves; legend concentrations in μM (A,C) and jump dilutions (B,D) of β -tryptase; (A,B) Reversible compound 52b; (C,D) Irreversible compound 56b.

to a lesser extent, for β -tryptase and CatG, whereas the inhibition of thrombin is negligible. Despite the lower potency against β -tryptase and CatG, compound 35b is the most potent probe of the library for β -tryptase ($\text{IC}_{50} = .05 \pm .003 \mu\text{M}$) and CatG ($\text{IC}_{50} = .06 \pm .006 \mu\text{M}$). On the other hand, for thrombin, the benzyl guanidine probes were only in the micromolar range.

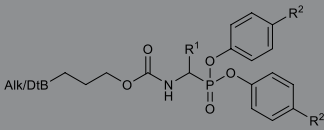
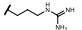
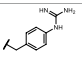
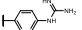
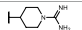
Despite being the most potent compounds, the progress curves of the benzyl guanidines show an unexpected reversible inhibition of all trypsin-like proteases tested, except for uPA, where the inhibition is irreversible (Table 4). The irreversible inhibition of uPA correlates with previous studies on similar diphenyl phosphonates inhibitors (Joossens et al., 2006). The unexpected reversible inhibition is not related to the chemical properties of the probes, such as low stability or low reactivity, but is dependent on their interaction with the protease (van Soom et al., 2015). Diphenyl phosphonates have been previously described as transition state analogs due to the resemblance with the transition state of peptide hydrolysis. For this type of inhibitor, very high-affinity interactions are expected (Oleksyszyn and Powers, 1991). A reason for not being irreversible might be that the warhead proximity and the geometry toward the serine residue on the active site are not ideal for the nucleophilic attack (Borsari et al., 2022). Alternatively, the compounds could behave as reversible covalent inhibitors where a covalent bond is formed and subsequently hydrolyzed (Tuley and Fast, 2018; McWhirter, 2021).

The k_{app} values of the benzyl guanidines derived from the progress curves correlate with the trends observed for the IC_{50} values. The benzyl guanidine probes show strong inhibition of trypsin-3, β -tryptase, and uPA, weaker for CatG and much weaker for thrombin. For trypsin-3, these probes are at least 10-fold more

potent than any of the other probes. The same occurs for β -tryptase, where the k_{app} of the bis(4-chlorophenyl)phosphonate probe 36b ($k_{\text{app}} = 61 \times 10^3 \pm 6860 \text{ M}^{-1} \text{ s}^{-1}$) is 10-fold higher than the second best probes, arginine 33b, and phenyl guanidine 39b. Noteworthy, for uPA, the probe 36b with $k_{\text{app}} = 32 \times 10^4 \pm 29 \times 10^3 \text{ M}^{-1} \text{ s}^{-1}$ is at least 100-fold more potent than the other probes with different side chains. For all reversible benzyl guanidine probes, the values of K_i^* are at least 10-fold lower than the corresponding K_i for trypsin-3 and β -tryptase (Table 5). This is consistent with high-affinity E^*I complexes and slow dissociation off-rates. For example, the bis(4-acetamidophenyl)phosphonate alkyne probe (35b) and the bis(4-chlorophenyl)phosphonate desthiobiotin probes (54b) presented a sub-nanomolar affinity for trypsin-3 with $K_i^* = 1 \times 10^{-4} \pm 1 \times 10^{-5}$ and $8 \times 10^{-4} \pm 3 \times 10^{-5} \mu\text{M}$, respectively. The rest of the benzyl guanidine probes showed nanomolar affinities for trypsin-3. On β -tryptase, sub-micromolar affinities are achieved with bis(4-chlorophenyl)phosphonate alkyne probe (36b) and both substituted diphenyl phosphonate desthiobiotin probes (52b, 54b).

The phenyl guanidine probes (37b–39b) also demonstrated strong sub-micromolar inhibitory potencies (Table 2). For β -tryptase and CatG, the IC_{50} values are in the same range as for the benzyl guanidine probes (34b–36b). For instance, the IC_{50} for β -tryptase and CatG for the bis(4-chlorophenyl)phosphonate alkyne probe (39b) are $.07 \pm .004$ and $.09 \pm .022 \mu\text{M}$, respectively, which is in the same range as for the best-performing benzyl guanidine probe 35b. For trypsin-3 and uPA, the phenyl guanidine probes lost about 100-fold potency compared to the benzyl guanidine analogs. At the concentrations tested, there was no inhibition of thrombin.

TABLE 4 k_{app} values of selected alkyne and desthiobiotin probes against a panel of trypsin-like serine proteases and the description of the mechanism of inhibition defined by the progress curves: slow-binding (Rev.) or irreversible (Irrev.).

<div></div>									
#	R ¹	R ²	Alk/DtB ^a	Trypsin-3	β-trypcase	Thrombin	uPA ^b	CatG ^b	
				k _{app} (M ⁻¹ s ⁻¹) ^c					
32b		H	Alk	18 × 10 ² ± 66 Irrev.	41 ± 5 Irrev.	64 ± 8 Rev.	41 ± 4 Irrev.	* ^d Rev.	
45b			DtB	17 × 10 ² ± 122 Irrev.	237 ± 42 Irrev.	19 ± 2 Rev.	N.D.	N.D.	
33b		Cl	Alk	35 × 10 ² ± 40 Irrev.	28 × 10 ² ± 82 Irrev.	11 × 10 ² ± 42 Rev.	15 × 10 ² ± 12 Irrev.	* ^d Rev.	
46b			DtB	92 × 10 ² ± 349 Irrev.	75 × 10 ² ± 1475 Irrev.	63 × 10 ² ± 290 Rev.	940 ± 37 Irrev.	N.D.	
34b		H	Alk	40 × 10 ³ ± 2642 Rev.	712 ± 41 Rev.	17 ± 1 Rev.	75 × 10 ² ± 725 Irrev.	* ^d Rev.	
50b			DtB	49 × 10 ³ ± 2979 Rev.	32 × 10 ² ± 613 Rev.	47 ± 5 Rev.	33 × 10 ³ ± 12 × 10 ³ Irrev.	* ^d Rev.	
35b		NHCOCH ₃	Alk	* ^d Rev.	70 × 10 ² ± 582 Rev.	128 ± 5 Rev.	13 × 10 ⁴ ± 30 × 10 ³ Irrev.	477 ± 67 Rev.	
52b			DtB	86 × 10 ³ ± 8250 Rev.	18 × 10 ³ ± 1184 Rev.	49 ± 5 Rev.	38 × 10 ³ ± 4175 Irrev.	* ^d Rev.	
36b		Cl	Alk	29 × 10 ³ ± 6499 Rev.	61 × 10 ³ ± 6860 Rev.	251 ± 16 Rev.	32 × 10 ⁴ ± 29 × 10 ³ Irrev.	* ^d Rev.	
54b			DtB	* ^d Rev.	* ^d Rev.	* ^d Rev.	23 × 10 ⁴ ± 36 × 10 ³ Irrev.	* ^d Rev.	
37b			H	Alk	293 ± 34 Irrev.	375 ± 34 Irrev.	N.D.	124 ± 23 Irrev.	582 ± 2 Irrev.
55b				DtB	231 ± 18 Irrev.	347 ± 19 Irrev.	N.D.	77 ± 1 Irrev.	301 ± 85 Irrev.
38b	NHCOCH ₃		Alk	358 ± 6 Irrev.	20 × 10 ² ± 54 Irrev.	N.D.	215 ± 7 Irrev.	14 × 10 ² ± 52 Irrev.	
56b			DtB	334 ± 85 Irrev.	321 ± 2 Irrev.	N.D.	62 ± 2 Irrev.	420 ± 37 Irrev.	
39b	Cl		Alk	11 × 10 ² ± 164 Irrev.	45 × 10 ² ± 547 Irrev.	N.D.	25 × 10 ² ± 86 Irrev.	23 × 10 ² ± 347 Rev.	
57b			DtB	13 × 10 ² ± 340 Irrev.	65 × 10 ² ± 1,203 Irrev.	N.D.	25 × 10 ² ± 11 Irrev.	11 × 10 ² ± 117 Rev.	
41b		H	Alk	17 × 10 ² ± 142 Irrev.	27 ± 2 Irrev.	41 × 10 ² ± 38 Irrev.	N.D.	N.D.	
31b	Pro-Lys	H	Alk	13 × 10 ² ± 28 Irrev.	136 ± 3 Irrev.	13 × 10 ² ± 5 Irrev.	188 ± 1 Irrev.	N.D.	

^aAlk, alkyne probe; DtB, desthiobiotin probe.

^bPanel of serine proteases abbreviations: uPA, urokinase plasminogen activator; catG, cathepsin G.

^k k_{app} are calculated from two independent experiments; when SD was higher than three times the average value, a third independent experiment was run (mean \pm SD).

^dk_{ann} determination is not possible by curve fitting.

N.D.: IC₅₀ is greater than 10 μM, and progress curves were not performed.

However, in contrast to the benzyl guanidine probes that were only irreversible for uPA, the compounds with phenyl guanidine as a side chain demonstrate irreversible inhibition for all proteases evaluated, excluding the bis(4-chlorophenyl)phosphonate probes (39b, 57b), which, surprisingly, act reversibly on CatG (Table 4).

For this series of compounds, the phosphonate aryl substituents (R^2) have a significant influence on the k_{app} , with the bis(4-chlorophenyl) phosphonate probe 39b as the best-performing for all the proteases. This probe has k_{app} values around $20 \times 10^2 \text{ M}^{-1} \text{ s}^{-1}$ for trypsin-3, β -tryptase, uPA, and CatG.

TABLE 5 Apparent equilibrium constants of the first step of slow-binding (K_1) and the overall process (K_i^*) for the reversible probes.

#	Trypsin-3		β -trypase		Thrombin	
	K_1 (μM) ^a	K_i^* (μM) ^a	K_1 (μM) ^a	K_i^* (μM) ^a	K_1 (μM) ^a	K_i^* (μM) ^a
32b	N.D. ^b	N.D. ^b	N.D. ^b	N.D. ^b	22.6 \pm 5	0.45 \pm 0.03
45b	N.D. ^b	N.D. ^b	N.D. ^b	N.D. ^b	9.97 \pm 1.0	1.14 \pm 0.11
33b	N.D. ^b	N.D. ^b	N.D. ^b	N.D. ^b	4.13 \pm 0.7	0.28 \pm 0.04
46b	N.D. ^b	N.D. ^b	N.D. ^b	N.D. ^b	0.95 \pm 0.2	0.07 \pm 0.009
34b	0.029 \pm 0.005	0.003 \pm 0.0003	15.8 \pm 5	1.11 \pm 0.09	134 \pm 26	4.93 \pm 0.51
50b	0.098 \pm 0.022	0.003 \pm 0.0002	3.28 \pm 0.5	0.41 \pm 0.03	* ^c	1.55 \pm 0.25
35b	0.001 \pm 0.0001	1 $\times 10^{-4}$ \pm 1 $\times 10^{-5}$	3.20 \pm 1.8	0.12 \pm 0.01	32.7 \pm 4	0.63 \pm 0.04
52b	0.017 \pm 0.0005	0.001 \pm 7 $\times 10^{-5}$	0.68 \pm 0.07	0.06 \pm 0.003	* ^c	0.62 \pm 0.08
36b	0.008 \pm 0.0008	0.001 \pm 0.0001	0.34 \pm 0.07	0.09 \pm 0.01	9.03 \pm 0.5	0.03 \pm 0.002
54b	0.006 \pm 0.0005	8 $\times 10^{-4}$ \pm 3 $\times 10^{-5}$	0.13 \pm 0.03	0.02 \pm 0.001	* ^c	0.06 \pm 0.006

^a K_1 and K_i^* are calculated from two independent experiments; when SD was higher than three times the average value, a third independent experiment was run (mean \pm SD).

^bN.D.: compounds have an irreversible mechanism of inhibition, K_1 was not calculated.

^c K_1 determination is not possible by curve fitting.

Whereas the benzyl and phenyl guanidine probes did not show potency towards thrombin, the piperidine-1-carboximidamide 41b is the most potent thrombin inhibitor with an $\text{IC}_{50} = .03 \pm .001 \mu\text{M}$. It is an equipotent inhibitor for trypsin-3 and has weak inhibition for β -trypase. There is no inhibition for uPA and CatG. This is also reflected in the k_{app} values obtained from the progress curves with irreversible inhibition of thrombin, trypsin-3, and β -trypase (Table 4).

Among the probes mimicking the natural amino acids, the arginine side chain proved to be the more interesting for most proteases. In particular, the bis(4-chlorophenyl)phosphonate probes 33b showed high potency and irreversibility for trypsin-3, β -trypase, and uPA. A similar k_{app} value was obtained for thrombin, although with a reversible inhibition. The lysine-mimicking probes (29b, 30b) had nanomolar inhibition for trypsin-3 but were less potent for β -trypase, thrombin, uPA, and CatG. The ornithine probe (14b) was inactive in all the proteases tested.

In previous studies, the Pro-Lys mimicking probe was reported to be promising for trypsin-3 with higher inhibitory potency than the Lys probe, but it was less active on β -trypase (Pan et al., 2006). In our study, the proline-lysine diphenyl phosphonate alkyne (31b) probe was used as a reference compound. This probe showed indeed potent, irreversible inhibition of trypsin-3 and thrombin, whereas the inhibition of β -trypase and uPA was also irreversible but less potent. However, compared to this reference compound, it is possible to select a more potent probe from our library for each investigated protease.

In general, our results demonstrate that compounds with a terminal guanidine showed significantly higher potencies than their amine analogs. For example, the less basic aniline probes 16b–18b and 19b–21b were inactive or presented IC_{50} higher than 1 μM . The only exceptions are the submicromolar IC_{50} values of 17b and 18b for CatG and chymotrypsin, reflecting the preference of these proteases for aromatic amino acids. In addition, the optimal length of the selectivity enhancing group (R^1) for this panel of trypsin-like proteases lies between 6 and 8 atoms from the α -carbon. Generally, compounds with shorter or longer R^1 groups significantly have reduced inhibitory

potency. For instance, the benzyl methyl guanidine alkyne probe (40b) only showed affinity for uPA with an $\text{IC}_{50} = 6.16 \pm .48 \mu\text{M}$.

The compounds were tested in chymotrypsin and neutrophil elastase to test selectivity over other protease families. All compounds were not potent for neutrophil elastase, including compound 13, designed to target elastase-like proteases. Likewise, most compounds were not potent or only slightly potent for chymotrypsin, with the exception of the above mentioned 17b and 18b.

Concludingly, under these assay conditions, the most potent alkyne probe for trypsin-3 based on the k_{app} values is the benzyl guanidine 34b, with a 5-fold selectivity for uPA, 55-fold over β -trypase and over 2000-fold for thrombin. Noteworthy, this probe shows a reversible slow-binding inhibitory mechanism. In case that an irreversible probe would be needed, the arginine 32b combines high potency with at least 30-fold selectivity over the other tested proteases. For β -trypase, several potent reversible probes, such as 36b were obtained, but these probes are not selective for trypsin-3 and uPA. In contrast, probes 33b and 39b are also potent for β -trypase and show an irreversible mechanism of inhibition. The preferred probe for thrombin is the 4-piperidine-1-carboximidamide (41b), with potent irreversible inhibition and excellent selectivity over β -trypase, uPA, and CatG. All the probes described in this study are irreversible with uPA. Furthermore, this enzyme has a clear preference for the benzyl guanidine side chain. Last, CatG does not have a clear preference between benzyl guanidine and phenyl guanidine probes. However, benzyl guanidine probes have a reversible mechanism, whereas phenyl guanidine probes are generally irreversible.

3.3 Labeling and detection of recombinant proteases

To further characterize the newly synthesized compounds and their potential to be used as ABPs, nine desthiobiotin probes were used for the labeling and detection of recombinant proteases. The arginine

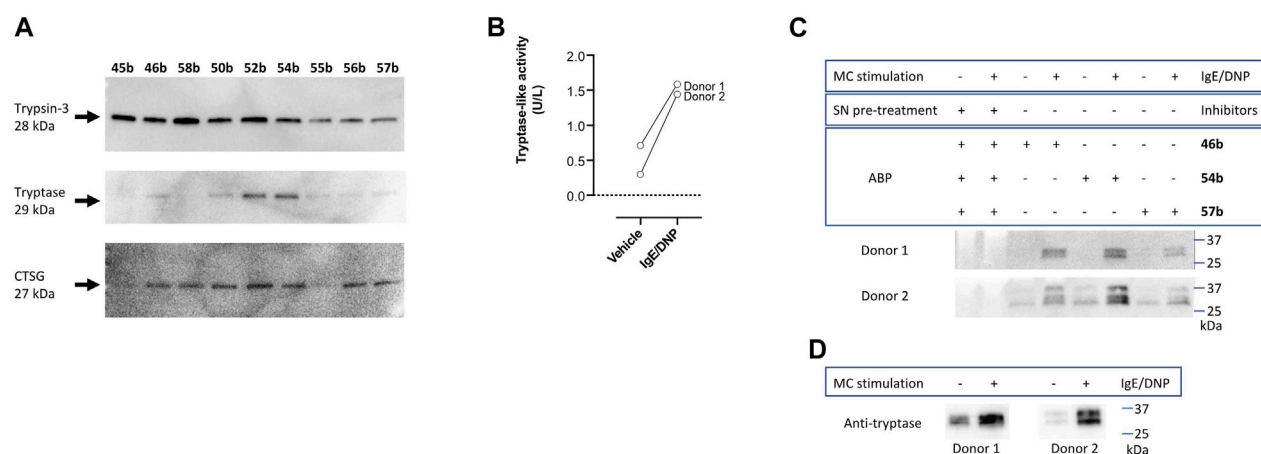


FIGURE 7
Validation of newly synthesized desthiobiotin probes for detection of trypsin-like proteases. (A) Labeling and detection of recombinant proteases in a SDS-PAGE-Blot. (B) Tryptase-like activity was measured from the stimulated mast cells of two donors by a spectrophotometric assay with a fluorogenic substrate. IgE/DNP stimulated mast cells were used. The tryptase-like activity is expressed as U/L. (C) Labeling of mast cell supernatants and identification of proteases. (D) Detection of tryptase in mast cell supernatants with anti-mast cell tryptase antibody, visualized by Western blot.

(45b–46b) and the proline-lysine (58b) desthiobiotin probes were used as reference compounds. Whereas the benzyl guanidine (50b, 52b, 54b) and phenyl guanidine probes (55b–57b) were used to determine whether the mechanism of inhibition (reversible or irreversible) is an obstacle to visualize the proteases. Samples of human recombinant proteases (trypsin-3, β -tryptase, and CatG) were incubated with the different probes before electrophoresis and detection with NeutrAvidin-HRP on a Western blot. **Figure 7A** illustrates the ability of the desthiobiotin probes to indicate the presence of the corresponding trypsin-like enzyme. Surprisingly, the reversible probes with benzyl guanidine as a side-chain (50b, 52b, 54b) can label trypsin-3, β -tryptase, and CatG under denaturing conditions. This effect can be explained due to the strong interactions between the active site of the protease and the probes. The high affinity and the slow off-rates were described in **Table 5** by the equilibrium constants K_I^* . Assuming that there is an excess of inhibitor over enzyme, the free inhibitor concentration must be very low, lower than the K_I^* , in order for the complex to dissociate. Therefore, the high affinity complex E*I survives during the whole process of labeling, gel electrophoresis, and visualization.

All the probes tested can label recombinant trypsin-3. However, the phenyl guanidine side chain is the least promising for this enzyme (55b–57b). For β -tryptase, the probes with natural amino acids as a side chain (45b, 46b, 58b) are not good ABP candidates. Both benzyl guanidine and phenyl guanidine show similar labeling intensity. Nevertheless, the probes with bis(4-chlorophenyl)phosphonate (54b, 57b) showed a slightly better resolution for the β -tryptase bands. Last, CatG could be labeled by most of the probes, except for the arginine (45b) and phenylguanidine (55b) unsubstituted diphenyl phosphonate probes.

In summary, the benzyl guanidine probes are compounds with a high affinity for trypsin-like serine proteases. Although they showed a reversible mechanism of inhibition for trypsin-3, β -tryptase, and CatG, surprisingly, these can label the recombinant proteases in a Western blot assay.

3.4 Labeling of mast cell supernatants and functional proteomic profiling

The last step to characterize the newly synthesized compounds as potential ABPs was to perform an experiment on biological samples and exemplify the ability of these ABPs to label proteases within a complex proteome. Human mast cells from two donors were stimulated to degranulate with IgE/DNP. Mast cells are immune cells that, upon degranulation, release mediators and play pivotal roles in allergic and inflammatory diseases (**Benoist and Mathis, 2002; Theoharides et al., 2012; Aguilera-Lizarraga et al., 2021**). Mast cell granules predominantly contain histamine and tryptase. Other serine proteases that are associated with mast cell degranulation, include soluble and transmembrane chymases and CatG (**Pejler et al., 2007; Caughey, 2016**). First, tryptase-like activity was measured from the stimulated mast cells by a spectrophotometric assay with a fluorogenic substrate (**Figure 7B**), which was increased compared to the vehicle. Then, mast cell supernatants were labeled with arginine (46b), benzyl guanidine (54b), and phenyl guanidine (57b) bis(4-chlorophenyl) phosphonate desthiobiotin probes. Probes 54b and 57b were chosen due to the good labeling of recombinant tryptase. Again, arginine probe 46b was used as a reference compound. **Figure 7C** shows that the three probes can label proteases in a complex proteome. The absence of bands when the samples are pre-treated with a cocktail of protease inhibitors indicates that the probes only target active proteases. It is worth noticing that samples from non-stimulated mast cells also can be labeled. Thereby, these probes are also successful at highlighting the constitutive release of proteases, which is relevant in a physiological setting (**Caughey, 2016**). For both donors, there are two overlapping bands around 30 kDa. The second donor shows an extra band at 37 kDa. After staining with an anti-tryptase antibody, only the lower bands are observed (**Figure 7D**). These most likely represent α - and β -tryptase (**Le et al., 2019**). The additional band at 37 kDa might be related to another protease. The benzyl guanidine bis(4-chlorophenyl)phosphonate desthiobiotin (54b) which is the most

potent probe for β -tryptase, displayed the best resolution, even though it shows a reversible slow-binding mechanism.

4 Discussion

ABPP is a powerful proteomic tool which enables researchers to detect and visualize active enzymes within a complex proteome. ABPP uses chemical probes designed to react covalently with the target enzyme. This tool is attractive in target and biomarker identification and drug discovery programs.

This study focuses on the serine protease family, specifically trypsin-like serine proteases. Most ABPs previously reported targeting this family used a diphenyl phosphonate as a warhead. However, there is a lack of chemical diversity as most of the reported probes contain natural amino acid mimetics as selectivity enhancing moieties. This study aimed to develop an extensive library of ABPs targeting trypsin-like serine proteases with a wide-ranging chemical diversity.

An efficient synthetic route has been implemented for probes bearing a diphenyl phosphonate warhead. A combination of different side chains targeting trypsin-like proteases and the modification of the electrophilicity of the diphenyl phosphonate warhead achieved the desired extensive library of probes. First, the alkyne probes were synthesized, and then the most promising ones were clicked to biotin and desthiobiotin as reporter tags. Furthermore, this synthetic route allows a straightforward approach to couple diverse reporter tags. Thus, alternative tags will enable other applications, such as visualization by fluorescence or PET.

To determine the inhibitory potency of the synthesized probes, their IC_{50} values were determined as a first measurement. However, since the probes were designed to be irreversible inhibitors, the IC_{50} value is not a good parameter to describe their potency. Therefore, kinetic progress curves were measured to determine the mechanism and the kinetic constants of inhibition.

For trypsin-3, β -tryptase, and uPA, the benzyl guanidine probes presented the highest inhibitory activities. Surprisingly, only for uPA, the interaction was irreversible, whereas a reversible slow-binding mechanism with trypsin-3, β -tryptase, thrombin, and CatG was observed. The phenyl guanidines, on the other hand, are good irreversible probes for trypsin-3, β -tryptase, and CatG. The preferred probe for thrombin is the 4-piperidine-1-carboximidamide, with potent irreversible inhibition and excellent selectivity over β -tryptase, uPA, and CatG.

Last, we demonstrated that our probes can label recombinant proteases and tryptase released from mast cell degranulation. Surprisingly, not only the irreversible ABPs but also the probes that presented a reversible slow-binding mechanism can label proteases under denaturing conditions.

Concludingly, these new probes for trypsin-like proteases offer significant advantages in terms of potency over the traditional probes mimicking the natural amino acids arginine and lysine. Detailed enzyme kinetic studies learn that, surprisingly, not all diaryl phosphonates show irreversible inhibition and that the inhibitory mechanism of a specific probe can differ from one protease to another. Even more surprising is the observation that irreversible binding is not needed to maintain protease labeling under denaturing conditions but that also reversible slow-tight binding is sufficient.

Data availability statement

The original contributions presented in the study are included in the article/**Supplementary Material**, further inquiries can be directed to the corresponding author.

Author contributions

Conceptualization, methodology, writing-review and editing, AR-L, LD, VC, IZ, MD, LB, CM-C, DC, EE, GD, MB, ID, PV, GB, A-ML, AD-S, and KA; validation, AR-L, LD, IZ, MD, and AD-S; investigation, AR-L, LD, VC, IZ, MD, LB, CM-C, DC, and AD-S; formal analysis, AR-L, LD, VC, IZ, MD, CM-C, DC, AD-S, and KA; resources, GD, ID, PV, GB, AD-S, and KA; data curation, AR-L; visualization, AR-L, AD-S, and KA; supervision, EE, GD, ID, PV, GB, AD-S, and KA; project administration, MB and KA; funding acquisition, MB, ID, GB, and KA; writing-original draft, AR-L, AD-S, A-ML, and KA. All authors have read and agreed to the published version of the manuscript.

Funding

This project has received funding from the European Union's Horizon 2020 research and innovation program under the Marie Skłodowska-Curie grant agreement No 765608, from the Research Fund Flanders grant agreement FWO-SBO S 001017N and the University of Antwerp SEP-BOF grant number 44875.

Acknowledgments

We would like to thank Glenn Van Haesendonck from the chemistry department of the University of Antwerp for the High-Resolution Mass Spectroscopy (HRMS) analysis of the final compounds.

Conflict of interest

The authors declare that the research was conducted in the absence of any commercial or financial relationships that could be construed as a potential conflict of interest.

Publisher's note

All claims expressed in this article are solely those of the authors and do not necessarily represent those of their affiliated organizations, or those of the publisher, the editors and the reviewers. Any product that may be evaluated in this article, or claim that may be made by its manufacturer, is not guaranteed or endorsed by the publisher.

Supplementary material

The Supplementary Material for this article can be found online at: <https://www.frontiersin.org/articles/10.3389/fchem.2022.1089959/full#supplementary-material>

References

- Aguilera-Lizarraga, J., Florens, M. v., Viola, M. F., Jain, P., Decraecker, L., Appeltans, I., et al. (2021). Local immune response to food antigens drives meal-induced abdominal pain. *Nature* 590, 151–156. doi:10.1038/s41586-020-03118-2
- Augustyns, K., van der Veken, P., Messagie, J., Joossens, J., and Lambeir, A.-M. (2012). Activity-based probes for the urokinase plasminogen activator. WO2012152807 A1.
- Benoist, C., and Mathis, D. (2002). Mast cells in autoimmune disease. *Nature* 420, 875–878. doi:10.1038/nature01324
- Berger, A. B., Vitorino, P. M., and Bogoy, M. (2012). Activity-based protein profiling. *Am. J. Pharmacogenomics* 4, 371–381. doi:10.2165/00129785-200404060-00004
- Borsari, C., Keles, E., McPhail, J. A., Schaefer, A., Sriramaratnam, R., Goch, W., et al. (2022). Covalent proximity scanning of a distal cysteine to target PI3Kα. *J. Am. Chem. Soc.* 144, 6326–6342. doi:10.1021/jacs.1c13568
- Breugst, M., and Reissig, H. (2020). The huisgen reaction: Milestones of the 1, 3-dipolar cycloaddition. *Angew. Chem. Int. Ed.* 59, 12293–12307. doi:10.1002/anie.202003115
- Carvalho, L. A. R. R., Ruivo, E. F. P. P., Lucas, S. D., and Moreira, R. (2015). Activity-based probes as molecular tools for biomarker discovery. *Medchemcomm* 6, 536–546. doi:10.1039/C4MD00417E
- Caughy, G. H. (2016). Mast cell proteases as pharmacological targets. *Eur. J. Pharmacol.* 778, 44–55. doi:10.1016/j.ejphar.2015.04.045
- Ceradini, D., and Shubin, K. (2021). One-pot synthesis of α-aminophosphonates by yttrium-catalyzed Birum–Oleksyszyn reaction. *RSC Adv.* 11, 39147–39152. doi:10.1039/D1RA07718J
- Copeland, R. A. (2013). *Evaluation of enzyme inhibitors in drug discovery A guide for medicinal chemists and pharmacologists*. Hoboken, NJ: Wiley.
- Cravatt, B. F., Wright, A. T., and Kozarich, J. W. (2008). Activity-based protein profiling: From enzyme chemistry to proteomic chemistry. *Annu. Rev. Biochem.* 77, 383–414. doi:10.1146/annurev.biochem.75.101304.124125
- Denadai-Souza, A., Bonnart, C., Tapias, N. S., Marcellin, M., Gilmore, B., Alric, L., et al. (2018). Functional proteomic profiling of secreted serine proteases in health and inflammatory bowel disease. *Sci. Rep.* 8, 7834. doi:10.1038/s41598-018-26282-y
- Drag, M., and Salvesen, G. S. (2010). Emerging principles in protease-based drug discovery. *Nat. Rev. Drug Discov.* 9, 690–701. doi:10.1038/nrd3053
- Edgington, L. E., Verdoes, M., and Bogoy, M. (2011). Functional imaging of proteases: Recent advances in the design and application of substrate-based and activity-based probes. *Curr. Opin. Chem. Biol.* 15, 798–805. doi:10.1016/j.CBPA.2011.10.012
- Elvas, F., vanden Berghe, T., Adriaenssens, Y., Vandenabeele, P., Augustyns, K., Staelens, S., et al. (2019). Caspase-3 probes for PET imaging of apoptotic tumor response to anticancer therapy. *Org. Biomol. Chem.* 17, 4801–4824. doi:10.1039/C9OB00657E
- Fang, H., Peng, B., Ong, S. Y., Wu, Q., Li, L., and Yao, S. Q. (2021). Recent advances in activity-based probes (ABPs) and affinity-based probes (A f BPs) for profiling of enzymes. *Chem. Sci.* 12, 8288–8310. doi:10.1039/D1SC01359A
- Ferguson, T. E. G., Reihill, J. A., Martin, S. L., and Walker, B. (2022). Novel inhibitors and activity-based probes targeting trypsin-like serine proteases. *Front. Chem.* 10, 782608. doi:10.3389/fchem.2022.782608
- Fonović, M., and Bogoy, M. (2008). Activity-based probes as a tool for functional proteomic analysis of proteases. *Expert Rev. Proteomics* 5, 721–730. doi:10.1586/14789450.5.721
- Geurink, P. P., Klein, T., Prèly, L., Paal, K., Leeuwenburgh, M. A., van der Marel, G. A., et al. (2010). Design of peptide hydroxamate-based photoreactive activity-based probes of zinc-dependent metalloproteases. *Eur. J. Org. Chem.* 2010, 2100–2112. doi:10.1002/ejoc.200901385
- Hamilton, R., Walker, B. J., and Walker, B. (1993). A convenient synthesis of N-protected diphenyl phosphonate ester analogues of ornithine, lysine and homolysine. *Tetrahedron Lett.* 34, 2847–2850. doi:10.1016/S0040-4039(00)73578-7
- Hawthorne, S., Hamilton, R., Walker, B. J., and Walker, B. (2004). Utilization of biotinylated diphenyl phosphonates for disclosure of serine proteases. *Anal. Biochem.* 326, 273–275. doi:10.1016/j.AB.2003.12.002
- Herrera Moro Chao, D., Kallemijn, W. W., Marques, A. R. A., Orre, M., Ottenhoff, R., van Roomen, C., et al. (2015). Visualization of active glucocerebrosidase in rodent brain with high spatial resolution following *in situ* labeling with fluorescent activity based probes. *PLoS One* 10, e0138107. doi:10.1371/journal.pone.0138107
- Hirsch, J. D., Eslamizar, L., Filanoski, B. J., Malekzadeh, N., Haugland, R. P., Beechem, J. M., et al. (2002). Easily reversible desthiobiotin binding to streptavidin, avidin, and other biotin-binding proteins: Uses for protein labeling, detection, and isolation. *Anal. Biochem.* 308, 343–357. doi:10.1016/S0003-2697(02)00201-4
- Ides, J., Thomae, D., Wyffels, L., Vangestel, C., Messagie, J., Joossens, J., et al. (2014). Synthesis and *in vivo* preclinical evaluation of an 18F labeled uPA inhibitor as a potential PET imaging agent. *Nucl. Med. Biol.* 41, 477–487. doi:10.1016/j.nucmedbio.2014.03.019
- Jackson, D. S., Fraser, S. A., Ni, L.-M., Kam, C.-M., Winkler, U., Johnson, D. A., et al. (1998). Synthesis and evaluation of diphenyl phosphonate esters as inhibitors of the trypsin-like granzymes A and K and mast cell tryptase. *J. Med. Chem.* 41, 2289–2301. doi:10.1021/jm970543s
- Jessani, N., and Cravatt, B. F. (2004). The development and application of methods for activity-based protein profiling. *Curr. Opin. Chem. Biol.* 8, 54–59. doi:10.1016/j.cbpa.2003.11.004
- Joossens, J., van der Veken, P., Surpateanu, G., Lambeir, A.-M., El-Sayed, I., Ali, O. M., et al. (2006). Diphenyl phosphonate inhibitors for the urokinase-type plasminogen activator: Optimization of the P4 position. *J. Med. Chem.* 49, 5785–5793. doi:10.1021/jm060622g
- Joossens, J., Ali, O. M., El-Sayed, I., Surpateanu, G., Van der Veken, P., Lambeir, A.-M., et al. (2007). Small, potent, and selective diaryl phosphonate inhibitors for urokinase-type plasminogen activator with *in vivo* antitumorigenic properties. *J. Med. Chem.* 50, 6638–6646. doi:10.1021/jm700962j
- Kalesh, K. A., Tan, L. P., Lu, K., Gao, L., Wang, J., and Yao, S. Q. (2010). Peptide-based activity-based probes (ABPs) for target-specific profiling of protein tyrosine phosphatases (PTPs). *Chem. Commun.* 46, 589–591. doi:10.1039/B919744C
- Kallemijn, W. W., Li, K.-Y., Witte, M. D., Marques, A. R. A., Aten, J., Scheij, S., et al. (2012). Novel activity-based probes for broad-spectrum profiling of retaining β-exoglucosidases *in situ* and *in vivo*. *Angew. Chem.* 124, 12697–12701. doi:10.1002/ange.201207771
- Kam, C. M., Abuelyaman, A. S., Li, Z., Hudig, D., and Powers, J. C. (1993). Biotinylated isocoumarins, new inhibitors and reagents for detection, localization, and isolation of serine proteases. *Bioconjug Chem.* 4, 560–567. doi:10.1021/bc00024a021
- Kato, D., Boatright, K. M., Berger, A. B., Nazif, T., Blum, G., Ryan, C., et al. (2005). Activity-based probes that target diverse cysteine protease families. *Nat. Chem. Biol.* 1, 33–38. doi:10.1038/nchembio707
- Lambeir, A., Borloo, M., De Meester, I., Belyaev, A., Augustyns, K., Hendriks, D., et al. (1996). Dipeptide-derived diphenyl phosphonate esters: Mechanism-based inhibitors of dipeptidyl peptidase IV. *Biochimica Biophysica Acta (BBA) - General Subj.* 1290, 76–82. doi:10.1016/0304-4165(96)00012-8
- Le, Q. T., Lyons, J. J., Naranjo, A. N., Olivera, A., Lazarus, R. A., Metcalfe, D. D., et al. (2019). Impact of naturally forming human α/β-tryptase heterotetramers in the pathogenesis of hereditary α-tryptasemia. *J. Exp. Med.* 216, 2348–2361. doi:10.1084/jem.20190701
- Li, N., Kuo, C.-L., Paniagua, G., van den Elst, H., Verdoes, M., Willems, L. I., et al. (2013). Relative quantification of proteasome activity by activity-based protein profiling and LC-MS/MS. *Nat. Protoc.* 8, 1155–1168. doi:10.1038/nprot.2013.065
- Liu, Y., Patricelli, M. P., and Cravatt, B. F. (1999). Activity-based protein profiling: The serine hydrolases. *PNAS* 96, 14694–14699. doi:10.1073/PNAS.96.26.14694
- Martin, S. L., and Walker, B. (2011). Preparation of protease-specific probes containing succinyl moiety for use in complex biological samples for diagnostic applications. WO2011024006A1.
- McWhirter, C. (2021). Kinetic mechanisms of covalent inhibition. *Annu. Rep. Med. Chem.* 56, 1–31. doi:10.1016/BS.ARM.2020.11.001
- Ngo, C., Mehta, R., Aggarwal, K., Fikes, A. G., Santos, I. C., Greer, S. M., et al. (2019). Pull-down of metalloproteins in their native states by using desthiobiotin-based probes. *ChemBioChem* 20, 1003–1007. doi:10.1002/CBIC.201800613
- Oleksyszyn, J., and Powers, J. C. (1991). Irreversible inhibition of serine proteases by peptide derivatives of (α-aminoalkyl)phosphonate diphenyl esters. *Biochemistry* 30, 485–493. doi:10.1021/bi00216a026
- Oleksyszyn, J., Subotkowska, L., and Mastalerz, P. (1979). Diphenyl 1-aminoalkane phosphonates. *Synth. (Stuttg)* 1979, 985–986. doi:10.1055/s-1979-28903
- Pan, Z., Jeffery, D. A., Chehade, K., Beltman, J., Clark, J. M., Grothaus, P., et al. (2006). Development of activity-based probes for trypsin-family serine proteases. *Bioorg Med. Chem. Lett.* 16, 2882–2885. doi:10.1016/j.bmcl.2006.03.012
- Pejler, G., Åbrink, M., Ringvall, M., and Wernersson, S. (2007). Mast cell proteases. *Adv. Immunol.* 95, 167–255. doi:10.1016/S0065-2776(07)95006-3
- Perona, J. J., and Craik, C. S. (2008). Structural basis of substrate specificity in the serine proteases. *Protein Sci.* 4, 337–360. doi:10.1002/pro.560040301
- Poreba, M., Rut, W., Vizovisek, M., Grobicz, K., Kasperkiewicz, P., Finlay, D., et al. (2018). Selective imaging of cathepsin L in breast cancer by fluorescent activity-based probes. *Chem. Sci.* 9, 2113–2129. doi:10.1039/C7SC04303A
- Reihill, J. A., Walker, B., Hamilton, R. A., Ferguson, T. E. G., Elborn, J. S., Stutts, M. J., et al. (2016). Inhibition of protease-epithelial sodium channel signaling improves mucociliary function in cystic fibrosis airways. *Am. J. Respir. Crit. Care Med.* 194, 701–710. doi:10.1164/rccm.201511-2216OC
- Sadaghiani, A. M., Verhelst, S. H., and Bogoy, M. (2007). Tagging and detection strategies for activity-based proteomics. *Curr. Opin. Chem. Biol.* 11, 20–28. doi:10.1016/j.CBPA.2006.11.030
- Sanman, L. E., and Bogoy, M. (2014). Activity-based profiling of proteases. *Annu. Rev. Biochem.* 83, 249–273. doi:10.1146/annurev-biochem-060713-035352
- Schulz-Fincke, A.-C., Tikhomirov, A. S., Braune, A., Girbl, T., Gilberg, E., Bajorath, J., et al. (2018). Design of an activity-based probe for human

neutrophil elastase: Implementation of the lossen rearrangement to induce Förster resonance energy transfers. *Biochemistry* 57, 742–752. doi:10.1021/acs.biochem.7b00906

Serim, S., Haedke, U., and Verhelst, S. H. L. (2012). Activity-based probes for the study of proteases: Recent advances and developments. *ChemMedChem* 7, 1146–1159. doi:10.1002/CMDC.201200057

Shannon, D. A., Gu, C., McLaughlin, C. J., Kaiser, M., van der Hoorn, R. A. L., and Weerapana, E. (2012). Sulfonyl fluoride analogues as activity-based probes for serine proteases. *ChemBioChem* 13, 2327–2330. doi:10.1002/cbic.201200531

Theoharides, T. C., Alysandratos, K. D., Angelidou, A., Delivanis, D. A., Sismanopoulos, N., Zhang, B., et al. (2012). Mast cells and inflammation. *Biochim. Biophys. Acta* 1822, 21–33. doi:10.1016/j.bbadis.2010.12.014

Tuley, A., and Fast, W. (2018). The taxonomy of covalent inhibitors. *Biochemistry* 57, 3326–3337. doi:10.1021/acs.biochem.8b00315

van der Veken, P., el Sayed, I., Joossens, J., Stevens, C., Augustyns, K., and Haemers, A. (2004). Lewis acid catalyzed synthesis of N-protected diphenyl 1-aminoalkylphosphonates. *Synth. (Stuttg)* 2005, 634–638. doi:10.1055/s-2004-837307

van Soom, J., Cuzzucoli Crucitti, G., Gladysz, R., van der Veken, P., di Santo, R., Stuyver, I., et al. (2015). The first potent diphenyl phosphonate KLK4 inhibitors with unexpected binding kinetics. *Medchemcomm* 6, 1954–1958. doi:10.1039/C5MD00288E

Wang, G., Mahesh, U., Chen, G. Y. J., and Yao, S. Q. (2003). Solid-phase synthesis of peptide vinyl sulfones as potential inhibitors and activity-based probes of cysteine proteases. *Org. Lett.* 5, 737–740. doi:10.1021/ol0275567

Yao, T., Xu, X., and Huang, R. (2021). Recent advances about the applications of click reaction in chemical proteomics. *Molecules* 26, 5368. doi:10.3390/molecules26175368

Yee, M., Fas, S. C., Stohlmeyer, M. M., Wandless, T. J., and Cimprich, K. A. (2005). A cell-permeable, activity-based probe for protein and lipid kinases. *J. Biol. Chem.* 280, 29053–29059. doi:10.1074/jbc.M504730200



OPEN ACCESS

EDITED BY

Tong Li,
City University of Hong Kong, Hong Kong
SAR, China

REVIEWED BY

Xiao Yang,
Hong Kong Centre for Cerebro-
cardiovascular Health Engineering
(COCHE), Hong Kong SAR, China
Fan Yang,
Shanghai Jiao Tong University, China
Long Gu,
Xidian University, China
Fei Jin,
Nanjing University of Science and
Technology, China

*CORRESPONDENCE

Xitai Sun,
✉ sunxitai@vip.qq.com
Xuehui Chu,
✉ dxuehuic@163.com

SPECIALTY SECTION

This article was submitted to Chemical
Biology,
a section of the journal
Frontiers in Chemistry

RECEIVED 22 November 2022

ACCEPTED 19 December 2022

PUBLISHED 05 January 2023

CITATION

Luo Z, Dong Y, Yu M, Fu X, Qiu Y, Sun X and
Chu X (2023), A novel insulin delivery
system by β cells encapsulated
in microcapsules.
Front. Chem. 10:1104979.
doi: 10.3389/fchem.2022.1104979

COPYRIGHT

© 2023 Luo, Dong, Yu, Fu, Qiu, Sun and
Chu. This is an open-access article
distributed under the terms of the [Creative
Commons Attribution License \(CC BY\)](#).
The use, distribution or reproduction in
other forums is permitted, provided the
original author(s) and the copyright
owner(s) are credited and that the original
publication in this journal is cited, in
accordance with accepted academic
practice. No use, distribution or
reproduction is permitted which does not
comply with these terms.

A novel insulin delivery system by β cells encapsulated in microcapsules

Zongjie Luo, Yutong Dong, Mengyu Yu, Xiao Fu, Yudong Qiu,
Xitai Sun* and Xuehui Chu*

Department of General Surgery, Nanjing Drum Tower Hospital Clinical College of Traditional Chinese and Western Medicine, Nanjing University of Chinese Medicine, Nanjing, China

Introduction: Diabetes is a growing epidemic worldwide and requires effective clinical therapies. In recent years, β -cell transplantation has emerged as a promising treatment for diabetes, and an encapsulation approach has been proposed to ameliorate this treatment.

Methods: Microfluidic technology had been used to generate microcapsules using a porous sodium alginate shell and a core containing β cells. The microcapsules were transplanted into diabetic mice and the therapeutic effect was measured.

Results: Porous hydrogel shell allows exchange of small molecules of nutrients while protecting beta cells from immune rejection, while the core ensures high activity of the encapsulated cells. The glucose control effect of the microcapsules were more durable and better than conventional methods.

Discussion: We believe that this system, which is composed of biocompatible porous hydrogel shell and enables highly activity of encapsulated β cells, can enhance therapeutic efficacy and has promising clinical applications.

KEYWORDS

β cells, insulin delivery system, microfluidic, microcapsules, diabetes

1 Introduction

Diabetes is a serious endocrine system disease worldwide, causing secondary damage to several organs of the body ([The Prevention of Diabetes Mellitus, 2021](#); [Cloete, 2022](#)). Both type 1 diabetes and late-onset type 2 diabetes manifest as absolute insulin deficiency ([DiMeglio et al., 2018](#)). Recently, several treatments for this condition have been used, such as oral medications, insulin injections, and islet transplants ([Shahjalal et al., 2018](#); [Yoshihara et al., 2020](#); [Cloete, 2022](#)). Oral medications and insulin injections increase the burden on diabetic patients and require frequent medication. Islet transplantation has been performed for many years and has been proven to be effective, but the duration and survival rate of islet transplantation are greatly reduced after a long period due to the attack of immune cells ([Aguayo-Mazzucato and Bonner-Weir, 2018](#); [Bourgeois et al., 2021](#); [Brusko et al., 2021](#)). Therefore, biocompatible hydrogels were applied to protect β cells from the immune cells ([Espona-Noguera et al., 2019](#); [Reys et al., 2022](#)). Three main methods of cell encapsulation have been put forward: hydrogel encapsulation, utilizing porous devices, and thin polymer coating ([van Bochove and Grijpma, 2019](#); [Khayambashi et al., 2021](#); [Peng et al., 2021](#)). Despite some successes, these methods lead to either suboptimal viability of the encapsulated cells or a fibrotic response. In addition, they lack the ability to exchange substances, making it difficult for the encapsulated cells to survive in the long term. Therefore, there is an urgent need for a novel drug delivery method that enables both long-term cell survival *in vivo* and a good exchange of substances ([Wong et al., 2018](#)).

In our research, we fabricated a novel microcapsule that encapsulates β cells using microfluidic technology to treat diabetes. Microcapsules are core-shell particles with a diameter of 1–1,000 μm made using natural or synthetic polymeric materials (Zhao et al., 2019; Huang et al., 2022). Various functional microcapsules have been developed by different technological applications, such as microfluidics, spray drying, and interfacial polymerization (Chen et al., 2019). Among them, microfluidics is a well-known strategy for rapidly preparing microcapsules with the desired morphology (Kim et al., 2022). The obtained microcapsules can effectively encapsulate the cells, but the cell viability in them is usually not adequate because the hydrogel shell reduces cell viability and intercellular communication and the compact shell restricts the internal cells from accessing external nutrients and limits insulin exiting the enclosure (Khanmohammadi et al., 2020; Liu et al., 2021; Kim et al., 2022). Therefore, the creation of a microcapsule that encapsulates highly active cells for diabetes treatment is imminent.

Here, we used a facile microfluidic electrospray device with double coaxial capillaries to prepare the microcapsules. The microcapsule shell is made of a mixture of sodium alginate (ALG) and cellulose nanocrystal (CNC). The shell with CNC endows the system with enough mechanical strength and a unique porous structure, which facilitates the exchange of substances between the cells and the external environment. The shell also avoids immune damage during treatment. The core is composed of carboxymethyl cellulose (CMC) solution and β cells. The liquid core of the microcapsules provides the encapsulated β cells with a 3D culture environment, while the shell protects these cells from immune cells after transplantation. Moreover, the encapsulated β cells are exposed to body fluid through the pores of the microcapsules, and insulin is released according to the current blood glucose status. Insulin can be released directly into the body through the pores. All these features suggest that β cells encapsulated in porous microcapsules show unique potential in diabetes therapy, which makes them a promising candidate for further clinical studies.

2 Materials and methods

2.1 Materials

ALG, CMC, and CaCl_2 were bought from Sigma. CNC was obtained from Beike 2D Materials. Cell counting kit-8 and calcein/PI were purchased from KeyGene. The insulin-producing β -cell line was obtained from ATCC. Seven-week-old female C57BL/6 mice weighing 20–22 g were acquired from the Model Animal Research Center of Nanjing University. All animal treatments were performed in strict compliance with the guidelines approved by the Animal Ethics Committee of Nanjing Drum Tower Hospital.

2.2 Design of the microfluidic device

The microfluidic electrospray tip device was set by assembling two circular capillaries coaxially. The diameters of the inner and outer capillaries, respectively, were 100 and 300 μm . The inner capillary was inserted coaxially into the outer capillary. The attachment points of the device were then sealed with clear glue.

2.3 Fabrication and characterization of porous microcapsules

In a typical experiment, two syringe pumps were used to push the shell fluid of 1.5% (w/v) ALG with .5% (w/v) CNC and the core fluid of 2% (w/v) CMC through the concentric outer (300 μm) and inner (100 μm) lumens in the coaxial needle. A 5 KV electrostatic potential was applied to the microfluidic device to generate droplets. Then, the droplets were collected in 2% (w/v) CaCl_2 solution. The microcapsules were generated by rapid crosslinking between Ca^{2+} and ALG.

2.4 Biocompatibility evaluation

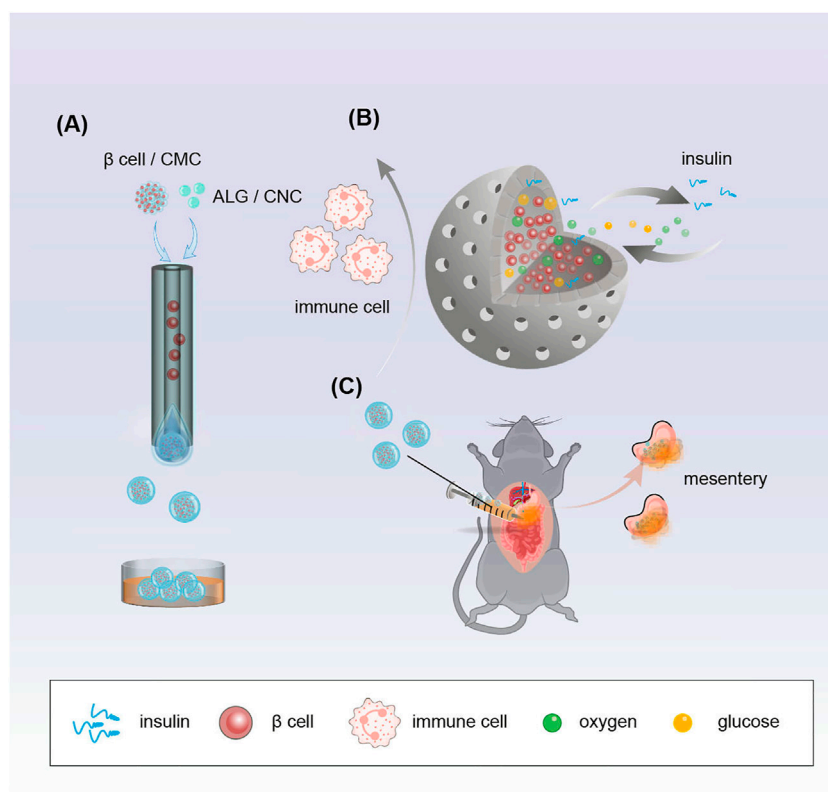
The viability of β cells was measured by cell counting kit-8 (CCK-8) assay. The prepared porous microcapsules with uniform dimensions were selected under the microscope. The β cells were planted in a 96-well plate. β cells co-cultured with microcapsules were regarded as the experimental group, and β cells cultured alone were regarded as the control group. After 72 h, the CCK-8 experiment was conducted.

2.5 Cell encapsulations and culture

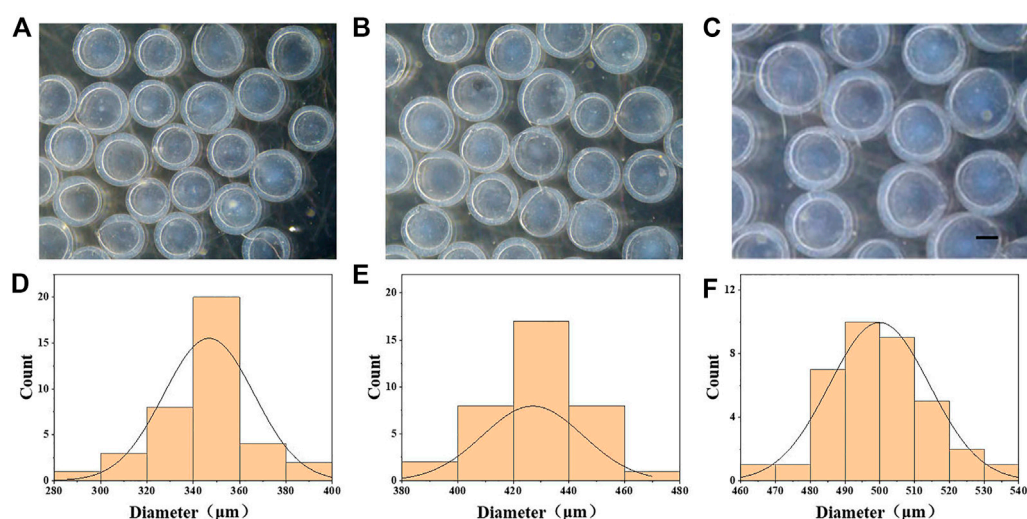
β cells (2×10^6 cells/ml) in CMC (2%, w/v) were used as the core fluid, and 1.5% (w/v) ALG and .5% (w/v) CNC were used as the shell fluid. After encapsulation, the microcapsules were washed three times with a culture medium and preserved in a culture medium.

2.6 Animal experiment

Female C57 mice were intraperitoneally injected with streptozotocin (STZ) (150 mg/kg) to establish a diabetic model. Blood glucose levels were measured every day after the administration of STZ. The level of blood glucose greater than 16.7 mmol/L showed the successful establishment of the diabetic model. Diabetic mice transplanted with microcapsules containing β cells were designated as the β -cell-Mi group. Mice that received dispersed β cells were designated as the β -cell group. Sham-operated animals were designated as the control group. For the implantation surgery, diabetic mice were injected intraperitoneally with sodium pentobarbital 60 mg/kg. A total of 300 microcapsules were placed into the mesenteric pouch, which was subsequently placed back into the mouse's abdominal cavity, and the mouse skin was carefully sutured. The mice's body weight and blood glucose levels were tracked and recorded every other day. A week after transplantation, the mice were injected intraperitoneally with 15% glucose after fasting for 12 h. The blood glucose levels were then measured at 0, 15, 30, 60, 90, and 120 min. The mice were executed after 21 days of treatment. Blood count and liver function were measured. The heart, liver, spleen, lungs, and kidneys were fixed for 24 h. The cells were then stained with hematoxylin and eosin (H&E) and were observed under the microscope and photographed.

**FIGURE 1**

Schematic demonstrating the fabrication of porous microcapsules encapsulating β cells for diabetes treatment after mesentery transplantation in diabetic mice. (A) Porous microcapsules fabricated via the microfluidic electrospay system. (B) β -cell-encapsulated microcapsules isolate immune cells, release insulin, and exchange oxygen and glucose. (C) β -cell-encapsulated porous microcapsules were applied to treat diabetes in diabetic mice after mesentery transplantation.

**FIGURE 2**

Generation of CMC-ALG microcapsules via microfluidic electrospay technology. (A-C) Bright-field microscopic images of the CMC-ALG core-shell microcapsules with different voltages. Scale bar represents 200 μm . (D-F) Diameter distribution of microparticles under different voltages. (A) 6 kV, (B) 7 kV, and (C) 8 kV.

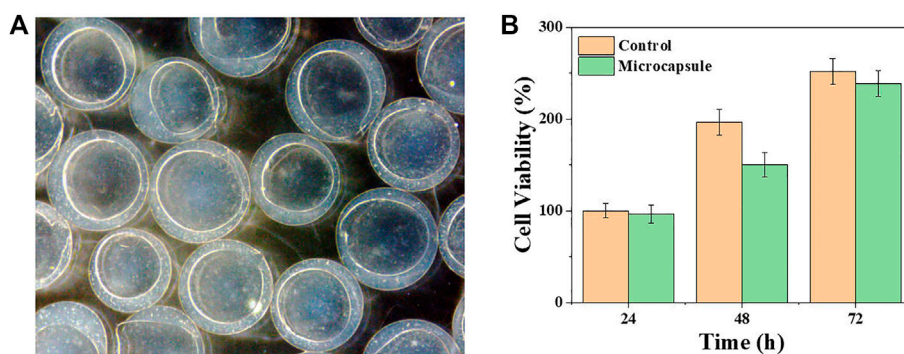


FIGURE 3
Viability and proliferation of β cells encapsulated in porous microcapsules. (A) Microscopic images of β cells after microencapsulation. (B) CCK-8 results of β cells of the control and microcapsule groups.

3 Results and discussion

3.1 Synthesis of the porous microcapsules

In a typical experiment, β -cell-encapsulated microcapsules were achieved as shown in Figure 1. The outer phase of the device consists of 1.5% ALG and .5% CNC. The inner phase consists of β cells in a culture medium with 2% CMC. The droplets were collected in CaCl_2 solution. ALG was instantly solidified to form microcapsules by the fast diffusion of Ca^{2+} . Cell-encapsulated microcapsules were rapidly collected and washed with the culture medium. Then, the microcapsules were photographed using the optical microscope. The size and structure of the microcapsules were controlled by pulsed electric field voltage, collection distance, the consistency of the biomass solution, and flow rates of internal and external phases (Figures 2A–F). The size of the microcapsules decreases with the increasing voltage, decreasing collecting distance, and decreasing biomass solution concentration. The decreasing flow rate of the internal phase led to decreasing diameters of cores, increasing shell thickness, and a slightly decreasing diameter of the entire capsule. Furthermore, the decreasing flow rate of the outer phase led to the diminishing diameter of the microcapsule and the shell thickness, while increasing the core diameter.

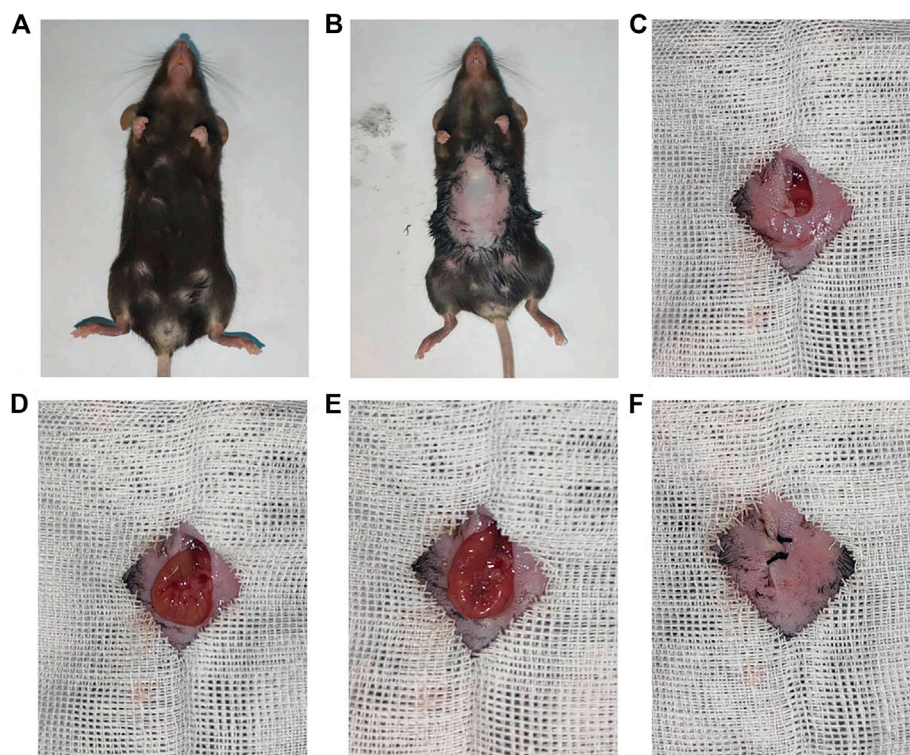
3.2 Preparation of the porous microcapsules and *in vitro* culture

The biocompatibility of microcapsules was tested to investigate their biomedical application potential. The viability of the β cells was measured when cultured with or without the microcapsules. Specifically, β cells were co-cultured with (regarded as the microcapsule group) or without (regarded as the control group) the microcapsules in 96-well plates for 3 days. The OD values were detected, depending on the amount of cells per well, and the number of live cells were counted by CCK8 to analyze the growth status (Figure 3B). The results showed that the cell viability between the two groups was not noticeably different during 3 days of cultivation. These results demonstrated great biocompatibility of the microcapsules. Then, β cells were wrapped inside the microcapsules

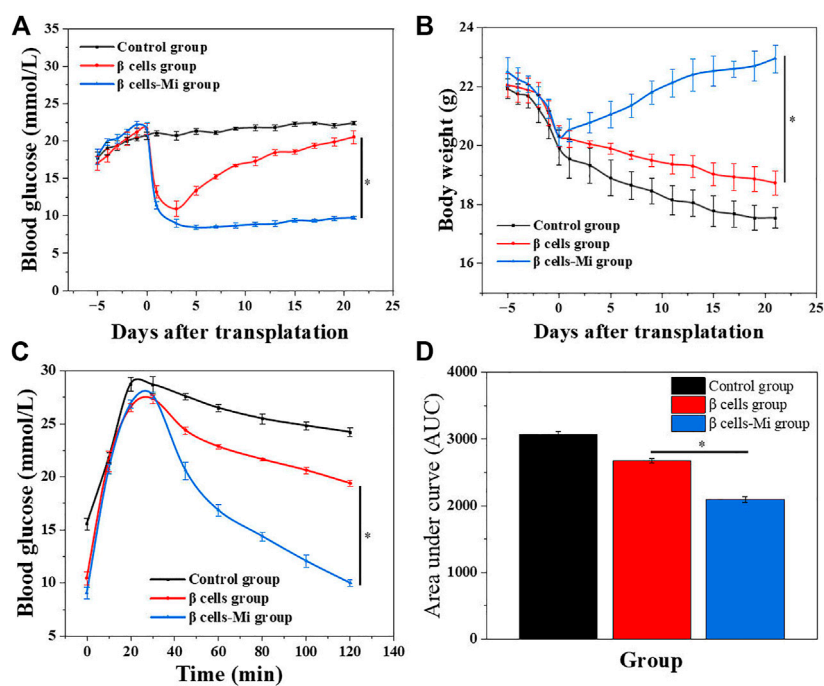
and kept sterile throughout. The cells were incubated in an incubator at a constant temperature, observed daily using a microscope, and photographed. In Figure 3A, it is obvious that the cells inside the microcapsules proliferate with time.

3.3 Animal experiment

In the end, these porous microcapsules encapsulating β cells were transplanted into diabetic mice to examine the therapeutic effects of treating diabetes. First, C57 mice were injected intraperitoneally with streptozotocin to establish a diabetic mouse model. The mice were divided randomly into the β -cell-Mi group, β -cell group, and control group. The process of transplanting the microcapsules is shown in Figure 4. Then, the blood glucose levels and body weight of the diabetic mice were recorded every other day (Figures 5A, B). The mice in the β -cell-Mi group returned to normal blood glucose levels and showed a slight increase in their body weight. The blood glucose level of the β -cell group also recovered. After 5 days, the blood glucose level gradually increased and the weight of the mice began to reduce. In addition, a mouse died on the 10th day. The mice in the control group maintained their diabetic status with a high blood glucose level and loss of weight. These measurements suggested that the direct transplantation of β cells may lead to a serious immune response. In contrast, the β cells encapsulated in microcapsules were protected by the shell and showed a long-term therapeutic effect. The intraperitoneal glucose tolerance test was performed on the seventh day (Figure 5C). The blood glucose levels of mice in the β -cell-Mi group returned to normal levels within 2 h. The blood glucose levels of mice in the β -cell group decreased significantly compared to those in the control group (Figure 5D). However, the normal blood glucose level was not decreased. These results demonstrated that the mice treated with β -cell microcapsules had great tolerance to glucose, which should be attributed to the continuous insulin release from the microcapsules. Finally, the mice were executed after 21 days of treatment. The complete blood count and liver function examination were in normal scope (Figures 6A–E). The organs were removed for H&E staining and were photographed (Figure 7). HE staining showed no obvious damage to the organs of all groups of mice, demonstrating the excellent biocompatibility of the microcapsules.

**FIGURE 4**

Procedure of β -cell-encapsulated microcapsules transplanted to the mesentery. (A,B) General pictures of a mouse. (C–F) Intraperitoneal delivery of microcapsules to the mouse with diabetes.

**FIGURE 5**

In vivo anti-diabetic efficiency of the β -cell-encapsulated microcapsules. (A,B) Blood glucose levels and body weights after transplantation. (C) Glucose tolerance tests in diabetic mice in different groups 2 h post-administration. (D) Responsiveness was calculated based on the area under the curve (AUC) at 120 min.

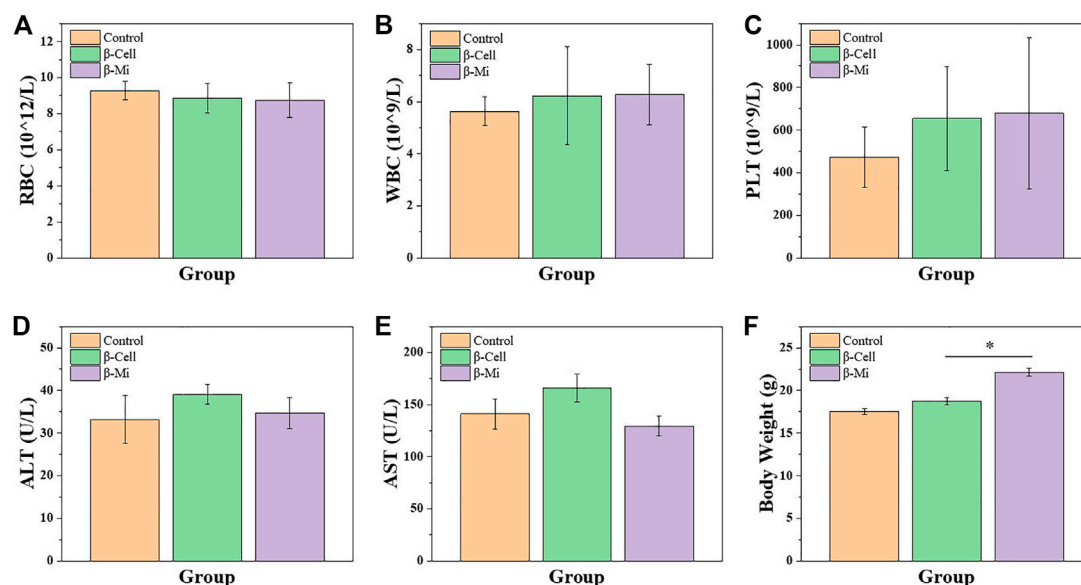


FIGURE 6
Biosafety analysis of β -cell-Mi therapy *in vivo*. (A–E) Hematology results of mice after treatments. (F) Body weight of mice before sacrifice.

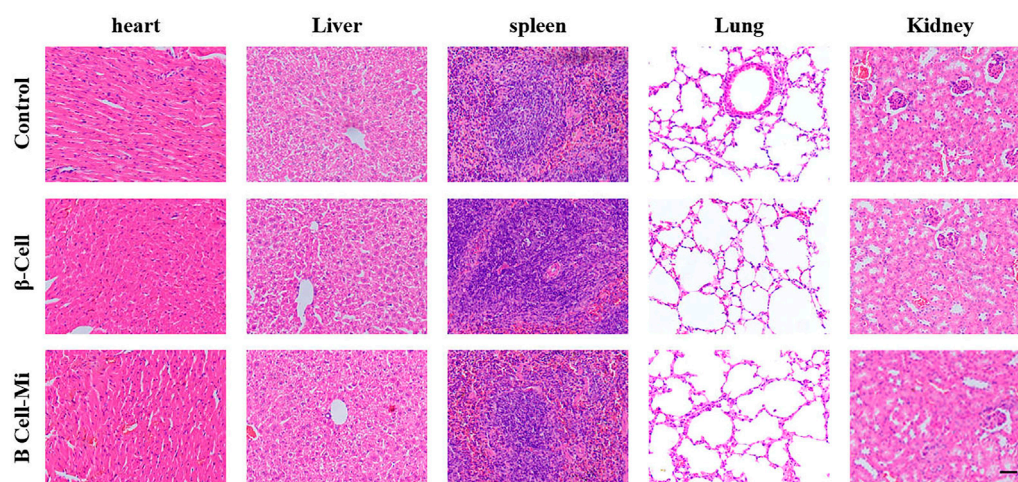


FIGURE 7
H&E staining of the main organs. Scale bar represents 200 μ m.

4 Conclusion

In summary, we presented novel porous microcapsules using microfluidic electrospray technology to encapsulate β cells to treat diabetes. In the preparation process, microcapsules containing a porous hydrogel shell and a β -cell core were prepared using a coaxial capillary device. The shell of porous hydrogel was made of a mixture of ALG and CNC, and the internal core was made of CMC solution with β cells. Driven by an external electric field, the co-current was disintegrated into droplets and falls into $CaCl_2$ solution. Since gelation of ALG occurs rapidly, the porous shell of the microcapsule was immediately obtained,

which protects the packaged β cells from immune attack after transplantation and allows the exchange of small molecules required for β -cell survival. In addition, the insulin secreted by β cells dispersed through the shell efficiently. The internal fluid core provides β cells a three-dimensional culture environment that preserves perfect cell function. Using a microfluidic electrospray method, microcapsules with tunable morphology allow for the controlled release of insulin. The released insulin from the microcapsules showed satisfactory antidiabetic function. Specifically, the blood glucose of mice in the microcapsule group was significantly lower than that in the β -cell transplantation group. Meanwhile, the body weight of mice in the

microcapsule group was significantly regained to the normal level. These characteristics suggest that microcapsules encapsulating β cells in the porous form are effective in the treatment of diabetes. Therefore, we believe that this approach will have the potential to replace conventional β -cell transplantation in clinical use.

Data availability statement

The raw data supporting the conclusion of this article will be made available by the authors, without undue reservation.

Ethics statement

The animal study was reviewed and approved by the Ethics Committee of Nanjing Drum Tower Hospital.

Author contributions

XC and XS designed the experiment. ZL and YD wrote the manuscript. MY, XF, and YQ revised the manuscript.

References

- Aguaño-Mazzucato, C., and Bonner-Weir, S. (2018). Pancreatic β cell regeneration as a possible therapy for diabetes. *Cell Metab.* 27, 57–67. doi:10.1016/j.cmet.2017.08.007
- Bourgeois, S., Sawatani, T., van Mulders, A., de Leu, N., Heremans, Y., Heimberg, H., et al. (2021). Towards a functional cure for diabetes using stem cell-derived beta cells: Are we there yet? *Cells* 10, 191. doi:10.3390/cells10010191
- Brusko, T. M., Russ, H. A., and Stabler, C. L. (2021). Strategies for durable β cell replacement in type 1 diabetes. *Science* 373, 516–522. doi:10.1126/science.abh1657
- Chen, G., Yu, Y., Wu, X., Wang, G., Gu, G., Wang, F., et al. (2019). Microfluidic electrospray niacin metal-organic frameworks encapsulated microcapsules for wound healing. *Research* 2019, 1–11. doi:10.34133/2019/6175398
- Cloete, L. (2022). Diabetes mellitus: An overview of the types, symptoms, complications and management. *Nurs. Stand* 37, 61–66. doi:10.7748/ns.2021.e11709
- DiMeglio, L. A., Evans-Molina, C., and Oram, R. A. (2018). Type 1 diabetes. *Lancet* 391, 2449–2462. doi:10.1016/S0140-6736(18)31320-5
- Espona-Noguera, A., Ciriza, J., Cañibano-Hernández, A., Orive, G., Hernández, R. M., del Burgo, L. S., et al. (2019). Review of advanced hydrogel-based cell encapsulation systems for insulin delivery in type 1 diabetes mellitus. *Pharmaceutics* 11, 597. doi:10.3390/pharmaceutics11110597
- Huang, D., Zhao, C., Wen, B., Fu, X., Shang, L., Kong, W., et al. (2022). Oxygen-carrying microfluidic microcapsules for enhancing chemo-sonodynamic therapy on patient-derived tumor organoid models. *Chem. Eng. J.* 435, 134871. doi:10.1016/j.cej.2022.134871
- Khanmohammadi, M., Zolfaghazadeh, V., Bagher, Z., Soltani, H., and Ai, J. (2020). Cell encapsulation in core-shell microcapsules through coaxial electrospinning system and horseradish peroxidase-catalyzed crosslinking. *Biomed. Phys. Eng. Express* 6, 015022. doi:10.1088/2057-1976/ab6035
- Khayambashi, P., Iyer, J., Pillai, S., Upadhyay, A., Zhang, Y., and Tran, S. D. (2021). Hydrogel encapsulation of mesenchymal stem cells and their derived exosomes for tissue engineering. *Int. J. Mol. Sci.* 22, 684. doi:10.3390/ijms22020684
- Kim, J.-W., Han, S. H., Choi, Y. H., Hamonangan, W. M., Oh, Y., and Kim, S.-H. (2022). Recent advances in the microfluidic production of functional microcapsules by multiple-emulsion templating. *Lab. Chip* 22, 2259–2291. doi:10.1039/d2lc00196a
- Liu, Z., Zhang, H., Zhan, Z., Nan, H., Huang, N., Xu, T., et al. (2021). Mild formation of core-shell hydrogel microcapsules for cell encapsulation. *Biofabrication* 13, 025002. doi:10.1088/1758-5090/abd076
- Peng, H., Chelvarajan, L., Donahue, R., Gottipati, A., Cahall, C. F., Davis, K. A., et al. (2021). Polymer cell surface coating enhances mesenchymal stem cell retention and cardiac protection. *ACS Appl. Bio Mater* 4, 1655–1667. doi:10.1021/acsabm.0c01473
- Reys, L. L., Silva, S. S., Soares da Costa, D., Reis, R. L., and Silva, T. H. (2022). Fucoidan-based hydrogels particles as versatile carriers for diabetes treatment strategies. *J. Biomater. Sci. Polym. Ed.* 33, 1939–1954. doi:10.1080/09205063.2022.2088533
- Shahjalal, H. M., Abdal Dayem, A., Lim, K. M., Jeon, T.-I., and Cho, S.-G. (2018). Generation of pancreatic β cells for treatment of diabetes: Advances and challenges. *Stem Cell Res. Ther.* 9, 355. doi:10.1186/s13287-018-1099-3
- The Prevention of Diabetes Mellitus (2021). The prevention of diabetes mellitus. *JAMA* 325, 190. doi:10.1001/jama.2020.17738
- Van Bochove, B., and Grijpma, D. W. (2019). Photo-crosslinked synthetic biodegradable polymer networks for biomedical applications. *J. Biomater. Sci. Polym. Ed.* 30, 77–106. doi:10.1080/09205063.2018.1553105
- Wong, C. Y., Al-Salami, H., and Dass, C. R. (2018). Microparticles, microcapsules and microspheres: A review of recent developments and prospects for oral delivery of insulin. *Int. J. Pharm.* 537, 223–244. doi:10.1016/j.ijpharm.2017.12.036
- Yoshihara, E., O'Connor, C., Gasser, E., Wei, Z., Oh, T. G., Tseng, T. W., et al. (2020). Immune-evasive human islet-like organoids ameliorate diabetes. *Nature* 586, 606–611. doi:10.1038/s41586-020-2631-z
- Zhao, C., Yu, Y., Zhang, X., Wu, X., Ren, J., and Zhao, Y. (2019). Biomimetic intestinal barrier based on microfluidic encapsulated sucralose microcapsules. *Sci. Bull. (Beijing)* 64, 1418–1425. doi:10.1016/j.scib.2019.07.020

Funding

This work was funded by the Natural Science Foundation of Nanjing University of Chinese Medicine (XZR2020058) and Nanjing Medical Science and Technology Development Project (YKK22067).

Conflict of interest

The authors declare that the research was conducted in the absence of any commercial or financial relationships that could be construed as a potential conflict of interest.

Publisher's note

All claims expressed in this article are solely those of the authors and do not necessarily represent those of their affiliated organizations, or those of the publisher, the editors, and the reviewers. Any product that may be evaluated in this article, or claim that may be made by its manufacturer, is not guaranteed or endorsed by the publisher.



OPEN ACCESS

EDITED BY
Francisco Solano,
University of Murcia, Spain

REVIEWED BY
Chenglong Xia,
University of California, Berkeley,
United States
Zhaowei Zhu,
The First Affiliated Hospital of Sun Yat-sen
University, China
Carlos Puebla,
Universidad de O'Higgins, Chile

*CORRESPONDENCE
Ilya Kister,
✉ ilya.kister@nyulangone.org

[†]These authors have contributed equally to
this work and share senior authorship

SPECIALTY SECTION
This article was submitted to Chemical
Biology,
a section of the journal
Frontiers in Chemistry

RECEIVED 12 September 2022
ACCEPTED 23 December 2022
PUBLISHED 21 February 2023

CITATION
Kister A and Kister I (2023), Overview of
myelin, major myelin lipids, and myelin-
associated proteins.
Front. Chem. 10:1041961.
doi: 10.3389/fchem.2022.1041961

COPYRIGHT
© 2023 Kister and Kister. This is an open-
access article distributed under the terms
of the [Creative Commons Attribution
License \(CC BY\)](#). The use, distribution or
reproduction in other forums is permitted,
provided the original author(s) and the
copyright owner(s) are credited and that
the original publication in this journal is
cited, in accordance with accepted
academic practice. No use, distribution or
reproduction is permitted which does not
comply with these terms.

Overview of myelin, major myelin lipids, and myelin-associated proteins

Alexander Kister[†] and Ilya Kister^{*†}

Department of Neurology, New York University Grossman School of Medicine, New York, NY, United States

Myelin is a modified cell membrane that forms a multilayer sheath around the axon. It retains the main characteristics of biological membranes, such as lipid bilayer, but differs from them in several important respects. In this review, we focus on aspects of myelin composition that are peculiar to this structure and differentiate it from the more conventional cell membranes, with special attention to its constituent lipid components and several of the most common and important myelin proteins: myelin basic protein, proteolipid protein, and myelin protein zero. We also discuss the many-fold functions of myelin, which include reliable electrical insulation of axons to ensure rapid propagation of nerve impulses, provision of trophic support along the axon and organization of the unmyelinated nodes of Ranvier, as well as the relationship between myelin biology and neurologic disease such as multiple sclerosis. We conclude with a brief history of discovery in the field and outline questions for future research.

KEYWORDS

myelin, myelin protein, lipid membrane, myelination, glia

1 Introduction

Myelin sheath is a modified cell membrane that wraps multiple times around the nerve axon (Figure 1). Tight, layer-by-layer packing allows for reliable electrical insulation of axons and thereby ensures rapid propagation of nerve impulses—electromagnetic waves driven by electric potential - along the axon and reduce axonal energy consumption. Compact multilayered myelin sheath allows an increase in the velocity of propagation from less than 1 m/s to 50–100 m/s without an increase in the diameter of axons. Myelin sheath is an exclusive innovation of vertebrate organisms and may explain the larger size of vertebrates relative to nearly all other animals (Zalc, 2006).

Optimum insulation depends on the types and ratios of myelin constituent lipids and proteins and myelin water fraction. If the myelin sheath is damaged, axonal insulation is disrupted, and nerve impulses along the axon slow down or fail to conduct, resulting in neurologic dysfunction. Myelin-related pathology underlies several neurogenetic diseases, such as leukodystrophies and inherited demyelinating neuropathies, and acquired neurologic diseases, such as multiple sclerosis (MS) and subacute combined degeneration (Harayama & Riezman, 2018). Myelin degradation also contributes to age-related cognitive decline (Bonetto et al., 2021). It is, therefore, important to understand at the molecular level the processes that underlie the formation of the myelin sheath (myelination) and the replacement of damaged areas of the sheath (remyelination).

In this review, we will discuss the general properties of myelin, focusing on the features of its composition, formation, structure, and function that differentiate it from the more conventional cell membranes. We will also address differences in myelin formation and properties in the central nervous system (CNS) and the peripheral nervous system (PNS).

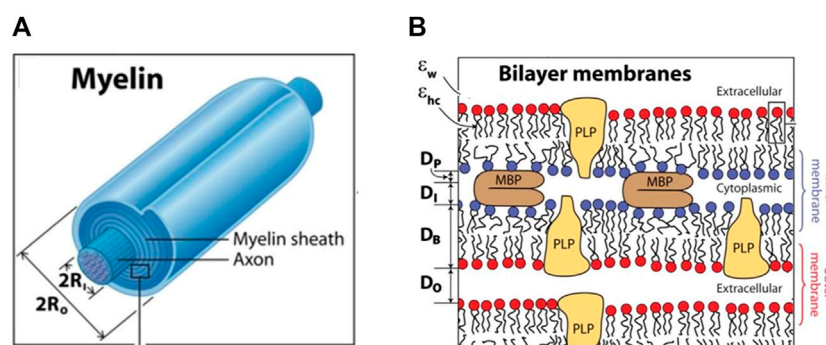


FIGURE 1

The structure of the myelin sheath. The myelinated axon (A), bilayer membranes (B). (A): The ratio of $2xRo$ to $2xRi$ (in A) is the g-ratio. Ri —inner radius; Ro —outer radius (B): Each bilayer of thickness DB is separated by cytoplasmic and extracellular water gaps of thicknesses DI and DO , and effective protein thickness DP is occupied by the fraction of MBP constituting the cytoplasmic water gap. Adapted from Min Y, et al. Proc Natl Acad Sci U S A. 106(9): 3154–3159.

2 Myelin sheath and the g-ratio

The myelin sheath is typically made of up to 100 layers tightly wound on top of each other around the axon (Figure 1A) (Simons and Nave, 2015). Two characteristic periodic morphological features of the myelin sheath are alternating major dense lines and intraperiod lines. The major dense lines are ~two to three nm wide and are formed by the closely condensed intracellular (cytoplasmic) surfaces between the inner membranes of the two lipid bilayers, as shown in Figure 1B. The intraperiod lines are wider—4 nm - and are formed by tightly apposed extracellular surfaces of myelin sheaths.

The number of myelin layers determines the thickness of the sheath, which depends on the axon diameter: the larger the axon, the thicker the myelin sheath. The relative thickness of a myelin sheath is conventionally measured as the ratio between the inner diameter and the outer diameter of the myelin sheath—so-called the g-ratio—as shown in Figure 1A. Thus, the thinner the myelin sheath, the closer the g-value is to 1. The optimal g-ratio depends on the requirement to optimize conduction speed and minimize conduction delays, as well as other properties of the system as a whole, such as the need to conserve volume, especially within the intracranial space. The optimal g-ratio was estimated to be ~0.77 for CNS and ~0.6 for PNS (Chomiak and Hu, 2009). Deviations from the optimal g-ratio may result in abnormal neural development and neurologic disease (York et al., 2021).

Quantitative determination of the g-ratio of myelin is done using electron microscopy; recent developments have made this less time-consuming (Kaiser et al., 2021). It is also possible to estimate g-ratio in the brain *in vivo* using advanced magnetic resonance imaging (MRI) techniques (Stikov et al., 2015; West et al., 2016). In healthy subjects, the g-ratio varies by brain region, with higher myelin content in the highly interconnected 'hub regions' than in the peripheral connections (Mancini et al., 2018). In patients with MS, an acquired demyelinating disorder, g-ratio-weighted nodal strength in motor, visual, and limbic regions correlates with disease severity (Kamagata et al., 2019). However, wide application of g-ratio estimation to clinical practice is hindered by the large variability of g-values obtained using various MRI techniques (Ellerbrock, Mohammadi, 2018). Comparisons of five different methods of g-ratio estimation in healthy subjects and multiple sclerosis patients showed high variability of g-values,

mostly in MS lesions, and two MRI methods did not correctly predict the degree of demyelination in MS lesions (Berg et al., 2022).

3 Glial cells and myelinogenesis in the central and the peripheral nervous system

The nervous system is traditionally divided into CNS and PNS. The CNS is comprised of the brain, spinal cord, olfactory and optic nerves, and is myelinated by oligodendrocytes. The PNS is comprised of nerves outside of the CNS—the remaining ten pairs of cranial nerves, spinal nerve roots, and peripheral nerves, and is myelinated by a different type of glial cell—the Schwann cell. The border between central and peripheral myelin—the so-called Obersteiner-Redlich zone—lies along cranial nerves and spinal nerve roots, within a few mm of nerve root entry into the brainstem or the spinal cord. The part of the axon proximal to the Obersteiner-Redlich zone (nearer the cell body) is myelinated with central myelin made by oligodendrocytes, and the part of the axon distal to this zone (farther from the cell body) is myelinated with peripheral myelin made by Schwann cells.

A single oligodendrocyte myelinates between 40 and 60 different axons but only one segment per axon (Simons and Nave, 2015). Thus, each axon in the CNS is myelinated by multiple oligodendrocytes, and each oligodendrocyte myelinates multiple axons. Oligodendrocytes myelinate different axons to variable extents depending on axon diameter to maintain optimal g-ratio. Thus, the same oligodendrocyte will myelinate the larger axons more extensively, yielding a thicker myelin sheath compared to the smaller axons (Waxman and Sims, 1984). An oligodendrocyte typically needs only about 5 h to generate all its myelin, which includes the synthesis of all the necessary proteins and lipids (Czopka et al., 2013).

Within the PNS, Schwann cell myelinates only a single axon, not multiple axons, as do oligodendrocytes in the CNS. Peripheral axons' often span considerable length, and many Schwann cells are required to myelinate the length of a single axon. The diameter of axons in the PNS ranges from ~0.1 μm to ~20 μm , while in the CNS, the axons tend to be smaller, ranging from <0.1 μm to >10 μm in diameter. (Stassart et al., 2018).

Another important distinction between oligodendrocytes and Schwann cells is that Schwann cells myelinate only axons that are greater than 1 μm in diameter, a process called ‘radial sorting’. The wider-diameter peripheral axons conduct impulses at a higher speed than narrower axons, and myelination of the wider axons allows for a further increase in the speed and distance of conducted signal (Feltri et al., 2016). Another feature of myelin sheath found only in the peripheral nerves is Schmidt-Lanterman incisures (SLI): cytoplasmic channels that pass through myelin and connect to the cytoplasm at the edge of the myelin sheath. SLI are formed where there is no tight interaction of adjacent myelin membranes, i.e., not within compact myelin sheath. SLI has a circular-truncated cone shape and are described as ‘beads in a stretched state’ (Terada et al., 2019).

Although CNS and PNS myelin are formed by different glial cell types, they share similar morphological structures, with some quantitative differences in their lipid composition and more substantial qualitative differences in protein composition. The differences between PNS and CNS myelin may explain why some diseases, such as acute inflammatory demyelinating polyneuropathy, affect only peripheral myelin while others, such as multiple sclerosis—only central myelin. Understanding the differences between the two types of myelin may yield clues into the pathogenesis of these disorders and the processes that underlie myelin degeneration in the nervous system (Quarles, 2005).

Other glial cells—astrocytes and microglia—contribute indirectly to myelinogenesis (Bilimoria and Stevens, 2015; Traiffort et al., 2020). Astrocytes promote the development of myelinating oligodendrocytes and accelerate myelin growth. Microglia remove damaged neurons and promote recovery by eliminating degenerated myelin that accumulates with aging and disease (Prineas et al., 2001; Bsibsi et al., 2014). In early development, myelin with ultrastructural abnormalities is phagocytosed by microglia (Djannatian et al., 2021). Microglia also play a neuroprotective and regenerative role by supporting myelination of axons during development and across the lifespan (Lenz and Nelson, 2018; Santos and Fields, 2021). Interestingly, Schwann cells also participate in myelin clearance after nerve injury (Brosius et al., 2017).

4 Diverse functions of myelin

In addition to creating tightly packed multilayered insulating segments called ‘internodes’ around the axon, myelin also plays a role in the assembly of the unmyelinated nodes of Ranvier (NR) between the internodes. The NRs are located roughly equidistant from each other along the axon and are the only points of contact between a myelinated axon and the extracellular environment. The main function of NR is to recharge neuron impulses, ensuring signal spreads along the entire length of the axon, which may be over a meter long in humans. Since the impulse appears to ‘leap’ from one NR to another, this process is known as “saltatory conduction”, from the Latin ‘saltus’ –a leap. The mechanism underlying saltatory conduction relies on clusters of voltage-gated Na^+ and K^+ channels within NR, which open and close depending on changes in the membrane potential of the NR.

Formation of ion channel cluster in the NR, reviewed in (Rasband and Peles, 2021), involves multiple players: cytoskeletal scaffold proteins actin, ankyrin G, beta IV spectrin (Letierrier C. et al., 2015), adhesion molecule neurofascin (Alpizar et al., 2019) and

others. Myelin proteins are also essential in NR formation as they attach the myelin sheath to the axon on both sides of the node and thereby ‘fix’ the size of NR. An increase in NR length may alter conduction speed by ~20%, similar to the effect produced by altering the number of myelin wraps or the internode length (Arancibia-Cárcamo et al., 2017). Because myelin is necessary for NR assembly and ‘size fixing’, problems with myelination also compromise NR function and thereby further impair saltatory conduction and exacerbate neurologic dysfunction (Arancibia-Carcamo and Attwell, 2014).

By insulating the axon along its length, the myelin sheath also inhibits access to nutrients from the extracellular compartment to the axon. An area of intense interest is whether myelin sheath may also serve for the provision of trophic support to the underlying axon. It has been postulated that oligodendrocytes can switch their own intermediate metabolism so that the end-product of glycolysis is lactate, which is then taken up by an axon and used by axonal mitochondria to generate ATP (Nave et al., 2010). The process of lactate delivery from oligodendrocytes to axon requires the formation of narrow cytosolic channels, such as Schmidt–Lanterman incisures discussed above, that connect the glial cell body with the axon during myelination (Spiegel and Peles, 2002). Such channels may exist in non-compact myelin, which differs from compact myelin in its molecular structure. An oligodendrocyte-specific protein 2',3'-cyclic nucleotide 3'-phosphodiesterase (CNP) is essential for preserving cytoplasmic spaced between inner leaflets of non-compact myelin (Snaidero et al., 2017), as will be discussed below. It is also possible that oligodendrocytes provide energy supplies to axons *via* exosomes (Frühbeis et al., 2020). Failure of the energy-trophic function of oligodendrocytes may contribute to axonal neurodegeneration (Nave et al., 2010; Tepavčević, 2021).

5 An overview of myelin composition

Myelin sheath, like all cell membranes, is constituted of three main components - water, lipids, and protein molecules, but the ratio of these components in myelin differs from the respective ratio of a more typical cell membrane. The dry myelin sheath is characterized by a high proportion of lipids (70%–85%) and a low proportion of proteins (15%–30%), while the typical cell membrane has an approximatively equal ratio of proteins to lipids (50%/50%) (Poitelon et al., 2020). The high proportion of lipids in myelin makes it less permeable to ions and a better electrical insulator. It also affects the membrane's physical properties, such as rigidity and membrane deformation (Harayama and Riezman, 2018). Myelin is highly susceptible to changes in its composition, and even small changes in the ratio of its constituent elements can result in the breakdown of myelin structure (Chrast et al., 2011).

5.1 Myelin water

Quantitative electron microscopy (electron probe X-ray microanalysis) shows that CNS myelin *in situ* is 33%–55% water, the lowest water content of any morphological compartment (LoPachin et al., 1991). Near the polar phospholipid headgroups, water molecules have an electrostatic orienting effect and form bonds with the hydrophilic groups of lipid and myelin proteins. Myelin

prevents water diffusion transversally to the axon and thereby contributes to anisotropy. Therefore, an increase in anisotropy reflects an increase in myelination (Almeida and Lyons, 2017). A change in myelin concentration has a profound impact on the signal strength on magnetic resonance imaging (MRI), and loss of signal on certain sequences may be a biomarker for myelin degeneration (Abel et al., 2020; Edwards et al., 2022). Advanced MRI techniques can differentiate water protons interacting with lipid bilayers (lipid-associated) from intra- and extracellular water protons (Watanabe et al., 2019).

5.2 Myelin lipids

Lipids differ from other major biological macromolecules in that they do not form polymers *via* covalent bonding of monomers but self-assemble due to the hydrophobic effect into macromolecular aggregates, such as lipid bilayer, the basic structure of all cell membranes. Lipids are the main constituents of membranes, but myelin differs from the typical cell membrane in the overall higher proportions of lipids, as well as in the ratio of three major classes of lipid components. In myelin sheath, the proportion of major lipid components is 40% cholesterol, 40% phospholipids, and 20% glycolipids, while in most biological membranes, the ratio is closer to 25%:65%:10%, respectively (Poitelon et al., 2020). Thus, the relative contribution of cholesterol and glycolipids is greater in the formation of a unique multilayer compact myelin structure than in conventional membranes. Slight changes in lipid composition in myelin can alter the intermembrane adhesive properties and lead to the destruction of the myelin structures (Chrast et al., 2011) and serious neurologic illness (Lamari et al., 2013).

Lipids are not directly genetically encoded, but they are synthesized by genetically-encoded enzymes. Thus, myelinogenesis is a strictly regulated process involving the coordinated expression of genes coding for enzymes involved in myelin lipid synthesis and myelin proteins (Campagnoni and Macklin, 1988; Dowhan, 2009). The importance of strictly regulated lipid composition is underscored by a large number of lipid-related genetic diseases. Supplementary Figure 1 of (Harayama and Riezman, 2018) lists 135 genetic defects in lipid metabolism that cause or contribute to human disease.

The process of spontaneous self-organization of lipid molecules into the lipid bilayer in water is largely due to their hydrophobic properties. When lipids are dispersed in water, their hydrophobic tails promote water molecules to form quasi-regular 'clathrate cages' around these hydrophobic parts. Depending on the phospholipid head group, six or more water molecules surround a lipid molecule (Chattopadhyay et al., 2021). When lipid molecules come together, water molecules lose their clathrate cage structure and form more disordered water clusters, thereby increasing the total entropy of the system and making the self-organization of the monolayer of lipid molecules a thermodynamically favorable process (Gao et al., 2022). The free energy is further decreased when two lipid monolayers pack tail-to-tail to form a more favorable arrangement with minimal contact with water—a phospholipid bilayer—the basic structure of biomembranes.

5.2.1 Cholesterol

Cholesterol is amphipathic. It has a polar head with only one hydroxyl group and four rings and a hydrophobic hydrocarbon tail that can readily

insert into the hydrophobic interior of cell membranes. The four fused hydrocarbon rings in cholesterol have an almost flat rigid structure, and their contact with other lipids and proteins within the membrane leads to a higher packing density. Thus, cholesterol helps to reduce the penetration of water, gases (e.g., oxygen), and small neutral molecules (e.g., glucose) through the membrane (Shinoda, 2016; Olżyńska et al., 2020). The importance of cholesterol for myelin structure and function can be inferred from its relatively high proportion in myelin (40%) compared to typical cell membranes (25%). A study of electron paramagnetic resonance signals found that cholesterol content strongly influences the membrane's structural organization and permeability (Subczynski, et al., 2017). High cholesterol content (30%–50%) ensures the high hydrophobicity of the membrane and increases membrane packing. Cholesterol is also a key determinant of membrane fluidity. The critical significance of cholesterol in myelin membrane is further highlighted by a study of mice, which lacked the ability to synthesize cholesterol, and had markedly reduced myelination (Saher et al., 2005). Conversely, the process of myelin repair–remyelination – is more efficient when the rate of cholesterol synthesis is increased (Berghoff et al., 2021).

5.2.2 Phospholipids

Two of the major classes of membrane phospholipids—sphingomyelins and phosphatidylcholines—constitute more than 50% of membrane phospholipids. The long lengths of the hydrophobic tails of these phospholipids—ranging from 14 to 24 carbon atoms—increase the interaction between tails, promote tight packing, decrease the fluidity of lipid association and provide a less permeable barrier for ions allowing for better insulation of axons (Chrast et al., 2011; Montani, 2021).

5.2.3 Glycolipids

Two of the most abundant glycolipids in the myelin membrane are galactocerebroside (GalC) and galactosulfatide (sGalC). Glycolipids' long alkyl chains are closely aligned—they can form up to eight intermolecular hydrogen bonds. Glycolipids also interact with phospholipids and cholesterol to promote the formation of dense packing in the bilayer of the myelin membrane (Stoffel and Bosio, 1997). Phospholipids and glycolipids are asymmetrically arranged on the membrane, with phospholipids predominating on the inner sheet of the lipid bilayer and glycolipids on the outer sheet (Stoffel and Bosio, 1997). The network of hydrogen contacts among lipids is conducive to the formation of micro lipid rafts, a kind of liquid crystal structures. These densely packed regions decrease the overall motion of the membrane and make it more rigid and more resistant to fluid/solid phase transition, resulting in the phase transition temperature of the myelin membrane above the physiological body temperature. The deficiency of glycolipid molecules impairs the packing of the lipid bilayer, increases membrane permeability, and causes the breakdown of the conductance of myelinated axons. The important contribution of glycolipids to myelin explains the twofold increase in the proportion of glycolipids in myelin compared to typical biomembrane.

5.3 Myelin proteins

Myelin in the CNS and the PNS contains a relatively small quantity of proteins, but they constitute a highly diverse group

(Jahn et al., 2020). A search for human myelin proteins in UniProtKB yields 223 results (<https://www.uniprot.org/>, accessed 12/14/2022). These proteins have very diverse sequences, functions, and structures yet share some common characteristics: they are typically small, usually no more than 30 kDa in weight, have long half-lives (Toyama et al., 2013), and are multifunctional. Another feature common to many myelin proteins is that they are either intrinsically disordered proteins (IDP) or have intrinsically disordered regions (IDR) (Dyson and Wright 2005; Raasakka and Kursula, 2020). The absence of a fixed, ordered three-dimensional structure in part or the whole of myelin protein is due to a relatively small proportion of hydrophobic amino acids and a higher proportion of disorder-promoting amino acids - R, K, E, P, and S, which prevent the formation of an ordered structural domain with a stable hydrophobic core (Romero et al., 2001; He et al., 2009). The high conformational flexibility of IDR allows myelin proteins to adopt variable structures depending on their neighboring contacts. Upon binding with other molecules within myelin, IDRs often undergo a disorder-to-order transition known as coupled folding and binding (Wright and Dyson, 2009). IDRs within myelin proteins play an important role in forming multilayer myelin membranes. For example, the disordered region of the myelin protein zero (P0) participates in developing the mature myelin membrane (Raasakka and Kursula, 2020). In the following sections, we will discuss three structurally important and common myelin proteins: proteolipid protein (PLP), myelin basic protein (MBP), and myelin protein zero. These three proteins are representative of the diversity of myelin-associated proteins and are illustrative of some of the key features of this protein group.

5.3.1 Proteolipid protein (PLP)

PLP is the most abundant myelin protein in the CNS, where it constitutes 38% of the total myelin protein mass. In contrast, the

amount of PLP in the PNS is minimal (Jahn et al., 2020). PLP1 gene encodes human PLP and is expressed in oligodendrocytes, but also in oligodendrocytes, astrocytes, and even in some neuronal progenitor cells (Harlow et al., 2014). A high level of PLP in myelin is required to preserve myelin integrity. The key role of PLP in the formation of a compact multilayer membrane structure is to bring myelin membranes closer to each other. A reduction in PLP content by 50% causes altered myelin ultrastructure and axonal pathology (Lüders et al., 2019). Mutations in PLP1 gene may result in hypomyelination and a spectrum of neurogenetic disorders, including Pelizaeus-Merzbacher disease and spastic paraplegia 2 (Inoue, 2019; Wolf et al., 2019).

PLP is a highly conserved hydrophobic protein. It comprises four transmembrane segments spanning residues 10–36, 64–88, 152–177, and 234–260, of which 79 amino acids (76%) have hydrophobic side chains. Both the N- and C-termini of PLP are on the cytoplasmic side. PLP exists as two isoforms (UniProt P60201). The larger isoform weighs 30 kDa and is 277 amino acids long, and the shorter isoform, PLP/DM20, is 26 kDa and is identical in sequence to the longer version, except for a deletion of 35 amino acids in the intracellular loop (Spörkel et al., 2002). A recent publication shows that both full-length human PLP and its shorter DM20 isoform have a dimeric, α -helical conformation and discusses structural differences between the isoforms in terms of their impact on protein function and interaction with lipids (Ruskamo et al., 2022).

Experimental 3D structural information for the full-length PLP or DM20 has not been reported, but there is X-ray data of a small fragment of the PLP chain (UniProt P60201-1: residues 45–53) in the loop between the first and second transmembrane helices (PDB structure 2XPG). This peptide (KLIETVFSK), which covered only 3% of the PLP molecule, forms a complex with HLA class I histocompatibility molecule HLA-A*0301 (McMahon et al., 2011) and may therefore play a role in autoimmunity. It is interesting to note

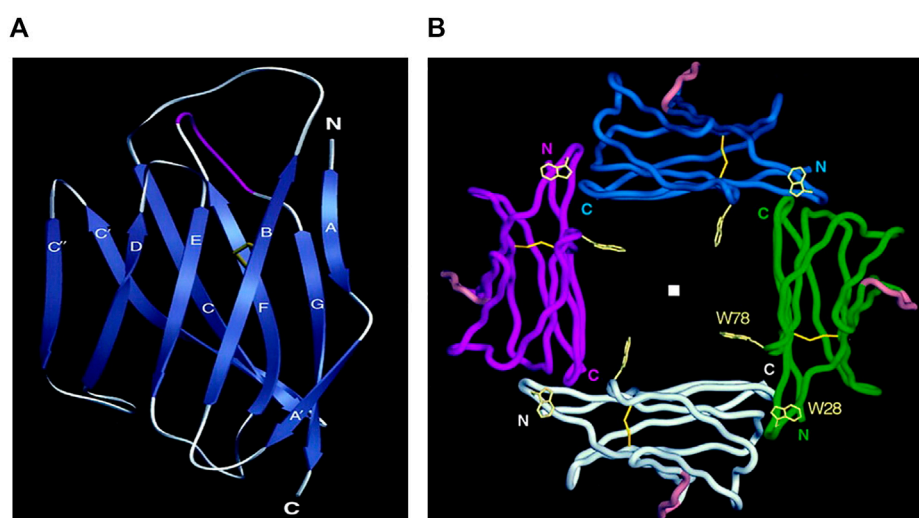


FIGURE 2

Structure of myelin protein zero. (A): Extracellular domain with labeled 10 beta strands in the standard immunoglobulin designation. Strands A (2–4), B (17–24), D (70–73) and E (82–85) make up one beta-sheet, and strands A' (8–11), C (33–40), C' (47–54), C'' (57–60), F (93–101) and G (109–118) make up the other beta-sheet. Five residues make major contributions to the formation of the dimer: Trp 57, Asp 61 (C–C' loop), Lys 84, Gly 85 (loop C'–C''), and Ser 106 (loop C''–D). (B): Four extracellular Ig-like domains form a tetramer. The position of the fourfold axis is indicated by a square. N-termini and C-termini point the beginning and the end of amino acid chains, respectively. Trp-28 makes van der Waals contacts with main chain atoms of the opposing B–C loop. Adapted from Shapiro L et al., *Neuron*. Sep;17(3):435–449.

in this context that patients with multiple sclerosis, a chronic demyelinating disorder of CNS, exhibit elevated T-cell and antibody responses to PLP (Greer et al., 2020).

The three-dimensional structure of the PLP was recently predicted using the highly-accurate AlphaFold method (Jumper et al., 2021). AlphaFold predicted that the largest part of the PLP chain forms helical structures (<https://alphafold.ebi.ac.uk/entry/P60201>). In the predicted model, most residues (with the exception of residues 110–140) have relatively small expected position errors.

5.3.2 Myelin basic protein (MBP)

MBP is the second most abundant myelin protein in CNS: it constitutes about 30% of dry protein mass in CNS myelin. MBP is less abundant in the PNS, where it accounts for only 5%–18% of the total myelin protein (Garbay et al., 2000). MBP has a number of different functions: it interacts with other proteins and participates in the transmission of the extracellular signal to the cytoskeleton and tight junctions (Boggs et al., 2006). MBP was called the ‘executive’ molecule of the myelin membrane in view of its critical role in compact myelin sheath formation (Moscarello et al., 1997).

In mammals, the MBP gene that codes for MBP comprises seven exons. Differential splicing of the primary mRNA leads to different isoforms of the protein. Not all of them are involved in axon myelination: for example, isoform 1 (UniProt P02686-1, 304 amino acids, 33.1 kDa) participates in the early brain development before the onset of myelination (Vassall et al., 2015). The so-called ‘classic myelin isoforms’ are part of the myelin membrane mostly; they vary in their molecular mass from 14 to 21.5 kDa. The 18.5-kDa isoform (UniProt P02686-5; 171 amino acids) is the most abundant isoform of MBP in mature human myelin in the CNS, while the 17.2 kDa isoform (UniProt P02686-6; 160 amino acids) is the major MBP isoform in the PNS.

In addition to isoform variability, MBP isoforms undergo a large number of post-translational modifications, which include phosphorylation, citrullination of arginyl residues, acetylation of lysine, and other reactions (Zhang, 2012). Such post-translational modification gives rise to eight charged isomers (C1–C8) of isoform 18.5 kDa. The mostly unmodified C1 isomer has the highest positive charge (net charge of +19 at pH 7). In contrast, the mostly modified isomer C8 has the smallest net positive charge of all the isomers (net charge of +13 at pH 7) because of deimination (citrullination) of six arginine residues into uncharged non-canonical amino acid citrulline at positions 26, 32, 123, 131, 160, 170 (UniProt P02686-5) (Wood and Moscarello, 1989; Tranquill et al., 2000). The irreversible citrullination reaction reduces the positive surface charge of the MBP, thereby weakening the interactions of the MBP with negatively charged lipids, which leads to a decrease in myelin stability (Martinsen and Kursula, 2022). The process of citrullination may also have clinical implications. In one fulminant case of multiple sclerosis, known as ‘Marburg variant,’ deimination of 18 of 19 arginyl residues to citrulline within acutely demyelinating plaque led to a dramatic decrease in MBP positive charge. Such a decrease of positivity in MBP is incompatible with MBP function in compacting myelin and may have triggered fatal autoimmune demyelination in this patient (Wood et al., 1996). In this context, it is notable that multiple sclerosis patients’ T cells appear to preferentially respond to citrullinated MBP, which suggests that citrullination of MBP may be involved in the induction or perpetuation of multiple sclerosis (Tranquill et al., 2000).

Different charge isomers may have different functions in various stages of myelin development. The most positive charged variants C1, C2, and C3 are part of a stable myelin sheath, while C8 charge variant might be of importance during the sheath’s development (Moscarello et al., 1994). C1 isomer of isoform 18.5-kDa is characterized by low hydrophobic content - about 25% of all its residues are hydrophobic (Haraux and Boggs, 2013). This is consistent with the localization of this MBP isoform to the cytoplasmic part of the myelin membranes (Figure 1B). The role of MBP is to bring closer together two apposing negatively charged cytoplasmic leaflets of the myelin membrane that form the major dense line. Force–distance measurements show that maximum adhesion force and minimum cytoplasmic spacing occur when each negative lipid in the membrane can be bound to a positively charged lysine or arginine group on MBP (Min et al., 2009). Excess of MBP causes the formation of a weak gel between myelin surfaces, while an excess of negative charge causes electrostatic swelling of the water gap (Smith, 1992). Thus, excess or deficiency of MBP causes the myelin bilayers to repel each other and may lead to the destruction of myelin (demyelination).

The lipid composition of the myelin leaflet has a major impact on its interactions with MBP. A cholesterol content of 44% in myelin yields the most thermodynamically favorable MBP interaction and is optimal for membrane compaction and thermodynamic stability (Träger et al., 2020). In addition to its structural importance—*via* interactions with lipids and myelin membrane-associated proteins—MBP also interacts with a large group of proteins related to protein expression and may play a regulatory role in myelinogenesis (Smirnova et al., 2021).

5.3.3 Myelin protein zero

Myelin protein zero molecule (P0) is expressed in higher vertebrates only in the PNS (Yoshida and Colman, 1996), where it makes up more than 50% of all myelin protein. P0 synthesis is regulated by Schwann cell/axon interactions, the so-called ‘axonal signal’. Axons can up- and downregulate the expression of Schwann cell genes *via* a cyclic adenosine monophosphate (cAMP)—dependent pathway (Lemke and Chao, 1988).

The human P0 molecule (P25189 · MYP0_HUMAN) is 248 amino acids long and consists of an N-terminal region (29 residues) and three domains. The structure of two rat and human P0 extracellular domains have been determined with high resolution by X-ray crystallography (rat—PDB ID 1NEU; Shapiro et al., 1996; human—PDB ID 3OAI; Liu et al., 2012). The structure of the extracellular domain (125 residues) is similar to typical variable domains of immunoglobulins with two beta sheets—sandwich-like structure with a set of Ig-conservative residues, including a pair of Cys residues in the B- and F—strands that form a disulfide bond contact between the two sheets, and Trp residue in the C-strand, which is involved in many intradomain contacts (Figure 2A). An important consequence of the homophilic adhesion properties of extracellular domains of P0 molecule is their ability to form dimers and tetramers. Two extracellular P0 domains form antiparallel dimers, and two neighboring dimers create a tetramer between lipid membranes (Figure 2B). The dimer and tetramer formation between extracellular domains is strengthened through the participation of the two other P0 domains (Shapiro et al., 1996; Plotkowski et al., 2007).

The 27 residues-long transmembrane domain of P0 forms a single helix. The role of this domain in the formation of P0 dimers and tetramers was analyzed in detail by Plotkowski et al., 2007. An

important feature of the transmembrane domain is the presence of a conserved glycine zipper motif-GxxxGxxxG (in human 159GAVIGGVLG167), which is conserved across many membranes' protein sequences. Zipper motif is the primary packing interface of the transmembrane helix. The interaction between helices within the membrane determines the correct orientation Ig domains for dimer formation in extracellular space.

The third domain of P0, the 67 residue-long C-terminal cytoplasmic domain, plays a role in tetramer formation. This domain exists in a disordered state, typical for many membrane proteins that interact with lipids, and has a high content of positive charged R, K, and H residues. In the sequence of the human domain shown below, these residues are bolded and marked in red.

RYCWLRRQAALQRRLSAMEKGGKLHKPGKDASKRG****
RQTPVLYAMLDHSRSTKAVSEKKAKGLGESRKDKK

Thus, there are 23 positive charged residues in the third domain that are approximately evenly distributed throughout the sequence and only six negative charged residues. Electrostatic interactions of mostly positive cytoplasmic domain with the negative cytoplasmic phospholipid headgroups are largely responsible for the formation of a stable helical-ordered protein structure (Raasakka and Kursula, 2020). As a result of these interactions, important structural transformations occur within myelin, which brings two neighboring P0 molecules together and 'tighten' the two adjacent membranes. These contacts have a similar function to contacts between MBP within the cytoplasmic part of the myelin membranes, considered above. Four neighboring P0 extracellular domains are assembled as a tetramer with a fourfold symmetry axis Figure 2B. Because this tetrameric association is so stable, it may be considered the main structural unit of the native myelin membrane structure in PNS (Thompson et al., 2002).

6 Myelin: History of discovery and questions for future research

Van Leeuwenhoek was the first to detect myelinated fibers in 1717, and Rudolf Virchow described myelin's chemical nature in 1854 and gave it its name. More than another century passed until it was conclusively established that CNS myelin is formed by oligodendrocytes (Bunge et al., 1962). In 1878, Ranvier established that myelin coverage of axons is not continuous but periodically interrupted by non-myelinated sections, which we now call the 'nodes of Ranvier' (NR). Only very recently, the molecular mechanism of the NR assembly was described in detail (Rasband

and Peles, 2021), yet many unresolved questions remain. For example, it is not known how the distance between NR is regulated during the process of myelination. The distance between the nodes changes in accordance with the growth of the axon, but how this information is conveyed to oligodendrocytes is unknown. The rich and fascinating history of myelin research from the Renaissance to the present was a subject of a recent review (Boullerne, 2016).

Traditionally, the study of myelin has focused on understanding its properties as an axonal insulator. The current trend in the field is to enlarge the focus to encompass the entire complex involving myelin, oligodendrocyte, axon, and other cells involved in myelination. From this perspective, the study of myelin is not so much an investigation into its complex chemical nature but of the interrelationship and interdependence between living cellular elements that contribute to myelination (Bonetto et al., 2021). This perspective allows one to appreciate the system's plasticity-how functional and structural changes occur in response to changes in the living organism. An example of how this shift in focus yields new insights into myelin biology is the newly described concept of 'adaptive myelination' (Bechler et al., 2018; Bloom et al., 2022). It is clear that the investigation will not end at this stage of cellular plasticity but will proceed to the next level of organizational complexity: the neuroplasticity of the organ level-that of the brain and nervous tissue.

Author contributions

These authors contributed equally to this work and share senior authorship. The authors are listed in alphabetical order.

Conflict of interest

The authors declare that the research was conducted in the absence of any commercial or financial relationships that could be construed as a potential conflict of interest.

Publisher's note

All claims expressed in this article are solely those of the authors and do not necessarily represent those of their affiliated organizations, or those of the publisher, the editors and the reviewers. Any product that may be evaluated in this article, or claim that may be made by its manufacturer, is not guaranteed or endorsed by the publisher.

References

- Abel, S., Vavasour, L., Lee, L. E., Johnson, P., Ristow, S., Ackermans, N., et al. (2020). Associations between findings from myelin water imaging and cognitive performance among individuals with multiple sclerosis. *JAMA Netw. Open* 3 (9), e2014220. doi:10.1001/jamanetworkopen.2020.14220
- Almeida, R. G., and Lyons, D. A. (2017). On myelinated axon plasticity and neuronal circuit formation and function. *J. Neurosci.* 37 (42), 10023-10034. doi:10.1523/JNEUROSCI.3185-16.2017
- Alpizar, S. A., Baker, A. L., Gullledge, A. T., and Hoppe, M. B. (2019). Loss of neurofascin-186 disrupts alignment of AnkyrinG relative to its binding partners in the axon initial segment. *Front. Cell Neurosci.* 13, 1. doi:10.3389/fncel.2019.00001
- Arancibia-Carcamo, I. L., and Attwell, D. (2014). The node of Ranvier in CNS pathology. *Acta Neuropathol.* 128 (2), 161-175. doi:10.1007/s00401-014-1305-z
- Arancibia-Carcamo, I. L., Ford, M. C., Cossell, L., Ishida, K., Tohyama, K., and Attwell, D. (2017). Node of Ranvier length as a potential regulator of myelinated axon conduction speed. *Elife* 6, e23329. doi:10.7554/eLife.23329
- Bechler, M. E., Swire, M., and Ffrench-Constant, C. (2018). Intrinsic and adaptive myelination-A sequential mechanism for smart wiring in the brain. *Dev. Neurobiol.* 78 (2), 68-79. doi:10.1002/dneu.22518
- Berg, R. C., Menegaux, A., Amthor, T., Gilbert, G., Mora, M., Schlaeger, S., et al. (2022). Comparing myelin-sensitive magnetic resonance imaging measures and resulting g-ratios in healthy and multiple sclerosis brains. *Neuroimage* 264, 119750. doi:10.1016/j.neuroimage.2022.119750
- Berghoff, S. A., Spieth, L., Sun, T., Hosang, L., Depp, C., Sasmita, A. O., et al. (2021). Neuronal cholesterol synthesis is essential for repair of chronically demyelinated lesions in mice. *Cell Rep.* 37 (4), 109889. doi:10.1016/j.celrep.2021.109889

- Bilimoria, P. M., and Stevens, B. (2015). Microglia function during brain development: New insights from animal models. *Brain Res.* 1617, 7–17. doi:10.1016/j.brainres.2014.11.032
- Bloom, M. S., Orthmann-Murphy, J., and Grinspan, J. B. (2022). Motor learning and physical exercise in adaptive myelination and remyelination. *ASN Neuro* 14, 175909142210975. doi:10.1177/17590914221097510
- Boggs, J. M. (2006). Myelin basic protein: A multifunctional protein. *Cell Mol. Life Sci.* 63 (17), 1945–1961. doi:10.1007/s00018-006-6094-7
- Bonetto, G., Belin, D., and Káradóttir, R. T. (2021). Myelin: A gatekeeper of activity-dependent circuit plasticity? *Science* 374 (6569), eaba6905. doi:10.1126/science.aba6905
- Boullerne, A. I. (2016). The history of myelin. *Exp. Neurol.* 283, 431–445. doi:10.1016/j.expneurol.2016.06.005
- Brosius Lutz, A., Chung, W. S., Sloan, S. A., Carson, G. A., Zhou, L., Lovelett, E., et al. (2017). Schwann cells use TAM receptor-mediated phagocytosis in addition to autophagy to clear myelin in a mouse model of nerve injury. *Proc. Natl. Acad. Sci. U. S. A.* 114 (38), E8072–E8080–E8080. doi:10.1073/pnas.1710566114
- Bsibi, M., Peferoen, L. A., Holtman, I. R., Nacken, P. J., Gerritsen, W. H., Witte, M. E., et al. (2014). Demyelination during multiple sclerosis is associated with combined activation of microglia/macrophages by IFN- γ and alpha B-crystallin. *Acta Neuropathol.* 128 (2), 215–229. doi:10.1007/s00401-014-1317-8
- Bunge, M. B., Bunge, R. P., and Ppas, G. D. (1962). Electron microscopic demonstration of connections between glia and myelin sheaths in the developing mammalian central nervous system. *J. Cell Biol.* 12, 448–453. doi:10.1083/jcb.12.2.448
- Campagnoni, A. T., and Macklin, W. B. (1988). Cellular and molecular aspects of myelin protein gene expression. *Mol. Neurobiol.* 2 (1), 41–89. doi:10.1007/BF02935632
- Chattopadhyay, M., Krok, E., Orlikowska, H., Schwill, P., Franquelim, H. G., and Piatkowski, L. (2021). Hydration layer of only a few molecules controls lipid mobility in biomimetic membranes. *J. Am. Chem. Soc.* 143 (36), 14551–14562. doi:10.1021/jacs.1c04314
- Chomiak, T., and Hu, B. (2009). What is the optimal value of the g-ratio for myelinated fibers in the rat CNS? A theoretical approach. *PLoS One* 4 (11), e7754. doi:10.1371/journal.pone.0007754
- Chrast, R., Saher, G., Nave, K. A., and Verheijen, M. H. (2011). Lipid metabolism in myelinating glial cells: Lessons from human inherited disorders and mouse models. *J. Lipid Res.* 52 (3), 419–434. doi:10.1194/jlr.R009761
- Czopka, T., Ffrench-Constant, C., and Lyons, D. A. (2013). Individual oligodendrocytes have only a few hours in which to generate new myelin sheaths *in vivo*. *Dev. Cell* 25 (6), 599–609. doi:10.1016/j.devcel.2013.05.013
- Djannatian, M., Weikert, U., Safaiyan, S., Wrede, C., Kislinger, G., Ruhwedel, T., et al. (2021) Myelin biogenesis is associated with pathological ultrastructure that is resolved by microglia during development. *BioRxiv* doi:10.1101/2021.02.02.429485
- Dowhan, W. (2009). Molecular genetic approaches to defining lipid function. *J. Lipid Res.* 50, S305–S310. doi:10.1194/jlr.R800041-JLR200
- Dyson, H. J., and Wright, P. E. (2005). Intrinsically unstructured proteins and their functions. *Nat. Rev. Mol. Cell Biol.* 6 (3), 197–208. doi:10.1038/nrm1589
- Edwards, E. M., Wu, W., and Fritz, N. E. (2022). Using myelin water imaging to link underlying pathology to clinical function in multiple sclerosis: A scoping review. *Mult. Scler. Relat. Disord.* 59, 103646. doi:10.1016/j.msard.2022.103646
- Ellerbrock, L., and Mohammadi, S. (2018). Four *in vivo* g-ratio-weighted imaging methods: Comparability and repeatability at the group level. *Hum. Brain Mapp.* 39 (1), 146724–146741. doi:10.1002/hbm.23858
- Feltri, M. L., Poitelson, Y., and Previtali, S. C. (2016). How Schwann cells sort axons: New concepts. *Neuroscientist* 22 (3), 252–265. doi:10.1177/1073858415572361
- Frühbeis, C., Kuo-Elsner, W. P., Müller, C., Barth, K., Peris, L., Tenzer, S., et al. (2020). Oligodendrocytes support axonal transport and maintenance via exosome secretion. *PLoS Biol.* 18 (12), e3000621. doi:10.1371/journal.pbio.3000621
- Gao, Y., Fang, H., Ni, K., and Feng, Y. (2022). Water clusters and density fluctuations in liquid water based on extended hierarchical clustering methods. *Sci. Rep.* 12 (1), 8036. doi:10.1038/s41598-022-11947-6
- Garbay, B., Heape, A. M., Sargueil, F., and Cassagne, C. (2000). Myelin synthesis in the peripheral nervous system. *Prog. Neurobiol.* 61 (3), 267–304. doi:10.1016/s0301-0082(99)00049-0
- Greer, J. M., Trifileff, E., and Pender, M. P. (2020). Correlation between anti-myelin proteolipid protein (PLP) antibodies and disease severity in multiple sclerosis patients with PLP response-permissive HLA types. *Front. Immunol.* 11, 1891. doi:10.3389/fimmu.2020.01891
- Harauz, G., and Boggs, J. M. (2013). Myelin management by the 18.5-kDa and 21.5-kDa classic myelin basic protein isoforms. *J. Neurochem.* 125 (3), 334–361. doi:10.1111/jnc.12195
- Harayama, T., and Riezman, H. (2018). Understanding the diversity of membrane lipid composition. *Nat. Rev. Mol. Cell Biol.* 19 (5), 715281–715296. doi:10.1038/nrm.2017.138
- Harlow, D. E., Saul, K. E., Culp, C. M., Vesely, E. M., and Macklin, W. B. (2014). Expression of proteolipid protein gene in spinal cord stem cells and early oligodendrocyte progenitor cells is dispensable for normal cell migration and myelination. *J. Neurosci.* 34 (4), 1333–1343. doi:10.1523/JNEUROSCI.2477-13.2014
- He, B., Wang, K., Liu, Y., Xue, B., Uversky, V. N., and Dunker, A. K. (2009). Predicting intrinsic disorder in proteins: An overview. *Cell Res.* 19 (8), 929–949. doi:10.1038/cr.2009.87
- Inoue, K. (2019). Pelizaeus-merzbacher disease: Molecular and cellular pathologies and associated phenotypes. *Adv. Exp. Med. Biol.* 1190, 201–216. doi:10.1007/978-981-32-9636-7_13
- Jahn, O., Siems, S. B., Kusch, K., Hesse, D., Jung, R. B., Liepold, T., et al. (2020). The CNS myelin proteome: Deep profile and persistence after post-mortem delay. *Front. Cell Neurosci.* 14, 239. doi:10.3389/fncel.2020.00239
- Jumper, J., Evans, R., Pritzel, A., Green, T., Figurnov, M., Ronneberger, O., et al. (2021). Highly accurate protein structure prediction with AlphaFold. *Nature* 596 (7873), 583–589. doi:10.1038/s41586-021-03819-2
- Kaiser, T., Allen, H. M., Kwon, O., Barak, B., Wang, J., He, Z., et al. (2021). MyelTracer: A semi-automated software for myelin g-ratio quantification. *eNeuro* 8 (4), ENEURO.0558. doi:10.1523/ENEURO.0558-20.2021
- Kamagata, K., Zalesky, A., Yokoyama, K., Andica, C., Hagiwara, A., Shimoji, K., et al. (2019). MR g-ratio-weighted connectome analysis in patients with multiple sclerosis. *Sci. Rep.* 9 (1), 13522. doi:10.1038/s41598-019-50025-2
- Lamari, F., Mochel, F., Sedel, F., and Saudubray, J. M. (2013). Disorders of phospholipids, sphingolipids and fatty acids biosynthesis: Toward a new category of inherited metabolic diseases. *J. Inher. Metab. Dis.* 36 (3), 411–425. doi:10.1007/s10545-012-9509-7
- Lemke, G., and Chao, M. (1988). Axons regulate Schwann cell expression of the major myelin and NGF receptor genes. *Development* 102 (3), 499–504. doi:10.1242/dev.102.3.499
- Lenz, K. M., and Nelson, L. H. (2018). Microglia and beyond: Innate immune cells as regulators of brain development and behavioral function. *Front. Immunol.* 9, 698. doi:10.3389/fimmu.2018.00698
- Letierrier, C., Potier, J., Caillol, G., Debarnot, C., Rueda Boroni, F., and Dargent, B. (2015). Nanoscale architecture of the axon initial segment reveals an organized and robust scaffold. *Cell Rep.* 13 (12), 2781–2793. doi:10.1016/j.celrep.2015.11.051
- Liu, Z., Wang, Y., Yedidi, R. S., Brunzelle, J. S., Kovari, I. A., Sohi, J., et al. (2012). Crystal structure of the extracellular domain of human myelin protein zero. *Proteins* 80 (1), 307–313. doi:10.1002/prot.23164
- LoPachin, R. M., Castiglia, C. M., and Saubermann, A. J. (1991). Elemental composition and water content of myelinated axons and glial cells in rat central nervous system. *Brain Res.* 549 (2), 253–259. doi:10.1016/0006-8993(91)90465-8
- Lüders, K. A., Nessler, S., Kusch, K., Patzig, J., Jung, R. B., Mobius, W., et al. (2019). Maintenance of high proteolipid protein level in adult central nervous system myelin is required to preserve the integrity of myelin and axons. *Glia* 67 (4), 634–649. doi:10.1002/glia.23549
- Mancini, M., Giuletta, G., Dowell, N., Spano, B., Harrison, N., Bozzali, M., et al. (2018). Introducing axonal myelination in connectomics: A preliminary analysis of g-ratio distribution in healthy subjects. *Neuroimage* 182, 351–359. doi:10.1016/j.neuroimage.2017.09.018
- Martinsen, V., and Kursula, P. (2022). Multiple sclerosis and myelin basic protein: Insights into protein disorder and disease. *Amino Acids* 54 (1), 99–109. doi:10.1007/s00726-021-03111-7
- McMahon, R. M., Friis, L., Siebold, C., Friese, M. A., Fugger, L., and Jones, E. Y. (2011). Structure of HLA-A*0301 in complex with a peptide of proteolipid protein: Insights into the role of HLA-A alleles in susceptibility to multiple sclerosis. *Acta Crystallogr. D. Biol. Crystallogr.* 67 (5), 447–454. doi:10.1107/S0907444911007888
- Min, Y., Kristiansen, K., Boggs, J. M., Husted, C., Zasadzinski, J. A., and Israelachvili, J. (2009). Interaction forces and adhesion of supported myelin lipid bilayers modulated by myelin basic protein. *Proc. Natl. Acad. Sci. U. S. A.* 106 (9), 3154–3159. doi:10.1073/pnas.0813110106
- Montani, L. (2021). Lipids in regulating oligodendrocyte structure and function. *Semin. Cell Dev. Biol.* 112, 114–122. doi:10.1016/j.semcdb.2020.07.016
- Moscarello, M. A., Wood, D. D., Ackerley, C., and Boulias, C. (1994). Myelin in multiple sclerosis is developmentally immature. *J. Clin. Invest.* 94 (1), 146–154. doi:10.1172/JCI117300
- Moscarello, M. A. (1997) Myelin basic protein, the 'executive' molecule of the myelin membrane. In: *Cell biology and pathology of myelin: Evolving biological concepts and therapeutic approaches* (B. H. J. Juurlink, R. M. Devon, J. R. Doucette, A. J. Nazarali, D. J. Schreyer, and V. M. K. Verge Eds.), pp. 13–25, Plenum, New York.
- Nave, K. A. (2010). Myelination and the trophic support of long axons. *Nat. Rev. Neurosci.* 11 (4), 275–283. doi:10.1038/nrn2797
- Olżyńska, A., Kulig, W., Mikkolainen, H., Czerniak, T., Jurkiewicz, P., Cwiklik, L., et al. (2020). Tail-oxidized cholesterol enhances membrane permeability for small solutes. *Langmuir* 36 (35), 10438–10447. doi:10.1021/acs.langmuir.0c01590
- Plotkowski, M. L., Kim, S., Phillips, M. L., Partridge, A. W., Deber, C. M., and Ju, Bowie (2007). Transmembrane domain of myelin protein zero can form dimers: Possible implications for myelin construction. *Biochemistry* 46 (43), 12164–12173. doi:10.1021/bi701066h
- Poitelson, Y., Kopec, A. M., and Belin, S. (2020). Myelin fat facts: An overview of lipids and fatty acid metabolism. *Cells* 9 (4), 812. doi:10.3390/cells9040812

- Prineas, J. W., Kwon, E. E., Cho, E. S., Sharer, L. R., Barnett, M. H., Oleszak, E. L., et al. (2001). Immunopathology of secondary-progressive multiple sclerosis. *Ann. Neurol.* 50 (5), 646–657. doi:10.1002/ana.1255
- Quarles, R. H. (2005). Comparison of CNS and PNS myelin proteins in the pathology of myelin disorders. *J. Neurol. Sci.* 228 (2), 187–189. doi:10.1016/j.jns.2004.10.005
- Raasakka, A., and Kursula, P. (2020). How does protein zero assemble compact myelin? *Cells* 9 (8), 1832. doi:10.3390/cells9081832
- Rasband, M. N., and Peles, E. (2021). Mechanisms of node of Ranvier assembly. *Nat. Rev. Neurosci.* 22 (1), 7–20. doi:10.1038/s41583-020-00406-8
- Romero, P., Obradovic, Z., Li, X., Garner, E. C., Brown, C. J., and Dunker, A. K. (2001). Sequence complexity of disordered protein. *Proteins* 42 (1), 38–48. doi:10.1002/1097-0134(20010101)42:1<38::aid-prot50>3.0.co;2-3
- Ruskamo, S., Raasakka, A., Pedersen, J. S., Martel, A., Skubnik, K., Darwish, T., et al. (2022). Human myelin proteolipid protein structure and lipid bilayer stacking. *Cell Mol. Life Sci.* 79 (8), 419. doi:10.1007/s00018-022-04428-6
- Saher, G., Brügger, B., Lappe-Siefke, C., Mobius, W., Tozawa, R. i., Wehr, M. C., et al. (2005). High cholesterol level is essential for myelin membrane growth. *Nat. Neurosci.* 8 (4), 468–475. doi:10.1038/nrn1426
- Santos, E. N., and Fields, R. D. (2021). Regulation of myelination by microglia. *Sci. Adv.* 7 (50), eabk1131. doi:10.1126/sciadv.abk1131
- Shapiro, L., Doyle, J. P., Hensley, P., Colman, D. R., and Hendrickson, W. A. (1996). Crystal structure of the extracellular domain from P0, the major structural protein of peripheral nerve myelin. *Neuron* 17 (3), 435–449. doi:10.1016/s0896-6273(00)80176-2
- Shinoda, W. (2016). Permeability across lipid membranes. *Biochim. Biophys. Acta* 1858 (10), 2254–2265. doi:10.1016/j.bbame.2016.03.032
- Simons, M., and Nave, K. A. (2015). Oligodendrocytes: Myelination and axonal support. *Cold Spring Harb. Perspect. Biol.* 8 (1), a020479. doi:10.1101/cshperspect.a020479
- Smirnova, E. V., Rakitina, T. V., Ziganshin, R. H., Arapidi, G. P., Saratov, G. A., Kudriaeva, A. A., et al. (2021). Comprehensive atlas of the myelin basic protein interaction landscape. *Biomolecules* 11 (11), 1628. doi:10.3390/biom11111628
- Smith, R. (1992). The basic protein of CNS myelin: Its structure and ligand binding. *J. Neurochem.* 59 (5), 1589–1608. doi:10.1111/j.1471-4159.1992.tb10989.x
- Sneider, N., Velte, C., Myllykoski, M., Raasakka, A., Ignatev, A., Werner, H. B., et al. (2017). Antagonistic functions of MBP and CNP establish cytosolic channels in CNS myelin. *Cell Rep.* 18 (2), 314–323. doi:10.1016/j.celrep.2016.12.053
- Spiegel, I., and Peles, E. (2002). Cellular junctions of myelinated nerves (Review). *Mol. Membr. Biol.* 19 (2), 95–101. doi:10.1080/09687680210130009
- Spörkel, O., Uschkureit, T., Büssow, H., and Stoffel, W. (2002). Oligodendrocytes expressing exclusively the DM20 isoform of the proteolipid protein gene: Myelination and development. *Glia* 37 (1), 19–30. doi:10.1002/glia.10014
- Stassart, R. M., Möbius, W., Nave, K. A., and Edgar, J. M. (2018). The axon-myelin unit in development and degenerative disease. *Front. Neurosci.* 12, 467. doi:10.3389/fnins.2018.00467
- Stikov, N., Campbell, J. S., Stroh, T., Lavelee, M., Frey, S., Novek, J., et al. (2015). *In vivo* histology of the myelin g-ratio with magnetic resonance imaging. *Neuroimage* 118, 397–405. doi:10.1016/j.neuroimage.2015.05.023
- Stoffel, W., and Bosio, A. (1997). Myelin glycolipids and their functions. *Curr. Opin. Neurobiol.* 7 (5), 654–661. doi:10.1016/s0959-4388(97)80085-2
- Subczynski, W. K., Pasenkiewicz-Gierula, M., Widomska, J., Mainali, L., and Raguz, M. (2017). High cholesterol/low cholesterol: Effects in biological membranes: A review. *Cell Biochem. Biophys.* 75 (3–4), 369–385. doi:10.1007/s12013-017-0792-7
- Tepavčević, V. (2021). Oligodendroglial energy metabolism and (re)Myelination. *Life (Basel)* 11 (3), 238. doi:10.3390/life11030238
- Terada, N., Saitoh, Y., Kamijo, A., Yamauchi, J., Ohno, N., and Sakamoto, T. (2019). Structures and molecular composition of schmidt-lanterman incisures. *Adv. Exp. Med. Biol.* 1190, 181–198. doi:10.1007/978-981-32-9636-7_12
- Thompson, A. J., Cronin, M. S., and Kirschner, D. A. (2002). Myelin protein zero exists as dimers and tetramers in native membranes of *Xenopus laevis* peripheral nerve. *J. Neurosci. Res.* 67 (6), 766–771. doi:10.1002/jnr.10167
- Toyama, B. H., Savas, J. N., Park, S. K., Harris, M., Ingolia, N., Yates, J., et al. (2013). Identification of long-lived proteins reveals exceptional stability of essential cellular structures. *Cell* 154 (5), 971–982. doi:10.1016/j.cell.2013.07.037
- Träger, J., Widder, K., Kerth, A., Harauz, G., and Hinderberger, D. (2020). Effect of cholesterol and myelin basic protein (MBP) content on lipid monolayers mimicking the cytoplasmic membrane of myelin. *Cells* 9 (3), 529. doi:10.3390/cells9030529
- Traiffort, E., Kassoussi, A., Zahaf, A., and Laouarem, Y. (2020). Astrocytes and microglia as major players of myelin production in normal and pathological conditions. *Front. Cell Neurosci.* 14, 79. doi:10.3389/fncel.2020.00079
- Tranquill, L. R., Cao, L., Ling, N. C., Kalbacher, H., Martin, R. M., and Whitaker, J. N. (2000). Enhanced T cell responsiveness to citrulline-containing myelin basic protein in multiple sclerosis patients. *Mult. Scler.* 6 (4), 220–225. doi:10.1177/135245850000600402
- Vassall, K. A., Bamm, V. V., and Harauz, G. (2015). MyelStones: The executive roles of myelin basic protein in myelin assembly and destabilization in multiple sclerosis. *Biochem. J.* 472 (1), 17–32. doi:10.1042/BJ20150710
- Watanabe, T., Wang, X., Tan, Z., and Frahm, J. (2019). Magnetic resonance imaging of brain cell water. *Sci. Rep.* 9 (1), 5084. doi:10.1038/s41598-019-41587-2
- Waxman, S. G., and Sims, T. J. (1984). Specificity in central myelination: Evidence for local regulation of myelin thickness. *Brain Res.* 292 (1), 179–185. doi:10.1016/0006-8993(84)90905-3
- West, K. L., Kelm, N. D., Carson, R. P., and Does, M. D. (2016). A revised model for estimating g-ratio from MRI. *Neuroimage* 125, 1155–1158. doi:10.1016/j.neuroimage.2015.08.017
- Wolf, N. I., van Spaendonk, R. M. L., Hobson, G. M., and Kamholz, J. (2019). “PLP1 Disorders,” in *GeneReviews*® Editors M. P. Adam, D. B. Everman, and G. M. Mirzaa (Seattle (WA): University of Washington, Seattle).
- Wood, D. D., Bilbao, J. M., O’Connors, P., and Moscarello, M. A. (1996). Acute multiple sclerosis (Marburg type) is associated with developmentally immature myelin basic protein. *Ann. Neurol.* 40 (1), 18–24. doi:10.1002/ana.410400106
- Wood, D. D., and Moscarello, M. A. (1989). The isolation, characterization, and lipid-aggregating properties of a citrulline containing myelin basic protein. *J. Biol. Chem.* 264 (9), 5121–5127. doi:10.1016/s0021-9258(18)83707-3
- Wright, P. E., and Dyson, H. J. (2009). Linking folding and binding. *Curr. Opin. Struct. Biol.* 19 (1), 31–38. doi:10.1016/j.sbi.2008.12.003
- York, E. N., Martin, S. J., Meijboom, R., Thrippleton, M. J., Bastin, M. E., Carter, E., et al. (2021). MRI-derived g-ratio and lesion severity in newly diagnosed multiple sclerosis. *Brain Commun.* 3 (4), fcab249. doi:10.1093/braincomms/fcab249
- Yoshida, M., and Colman, D. R. (1996). Parallel evolution and coexpression of the proteolipid proteins and protein zero in vertebrate myelin. *Neuron* 16 (6), 1115–1126. doi:10.1016/s0896-6273(00)80138-5
- Zalc, B. (2006). The acquisition of myelin: A success story. *Novartis Found. Symp.* 276, 15–21. doi:10.1002/9780470032244.ch3
- Zhang, C., Walker, A. K., Zand, R., Moscarello, M. A., Yan, J. M., and Andrews, P. C. (2012). Myelin basic protein undergoes a broader range of modifications in mammals than in lower vertebrates. *J. Proteome Res.* 11 (10), 4791–4802. doi:10.1021/pr201196e



OPEN ACCESS

EDITED BY

Francisco Solano,
University of Murcia, Spain

REVIEWED BY

Constantinos K. Zacharis,
Aristotle University of Thessaloniki,
Greece
Riku Kubota,
Koken Co., Ltd., Japan

*CORRESPONDENCE

Salvatore Petralia,
✉ salvatore.petralia@unict.it

SPECIALTY SECTION

This article was submitted to
Chemical Biology,
a section of the journal
Frontiers in Chemistry

RECEIVED 13 February 2023

ACCEPTED 20 March 2023

PUBLISHED 10 April 2023

CITATION

Messina MA, Maugeri L, Forte G,
Ruggieri M and Petralia S (2023), A highly
sensitive colorimetric approach based on
tris (bipyridine) Ruthenium (II/III) mediator
for the enzymatic detection
of phenylalanine.
Front. Chem. 11:1164014.
doi: 10.3389/fchem.2023.1164014

COPYRIGHT

© 2023 Messina, Maugeri, Forte, Ruggieri
and Petralia. This is an open-access
article distributed under the terms of the
Creative Commons Attribution License
(CC BY). The use, distribution or
reproduction in other forums is
permitted, provided the original author(s)
and the copyright owner(s) are credited
and that the original publication in this
journal is cited, in accordance with
accepted academic practice. No use,
distribution or reproduction is permitted
which does not comply with these terms.

A highly sensitive colorimetric approach based on tris (bipyridine) Ruthenium (II/III) mediator for the enzymatic detection of phenylalanine

Maria Anna Messina¹, Ludovica Maugeri², Giuseppe Forte²,
Martino Ruggieri^{1,3} and Salvatore Petralia^{2*}

¹Expanded Newborn Screening Laboratory, A.O.U Policlinico "G. Rodolico—San Marco", Catania, Italy, ²Department of Drug and Health Sciences, University of Catania, Catania, Italy, ³Department of Clinical and Experimental Medicine, University of Catania, Catania, Italy

The accurate monitoring of phenylalanine concentration plays a prominent role in the treatment of phenylketonuria (PKU). In this study, we present an enzymatic assay based on Phenylalanine Dehydrogenase/NAD⁺ and tris (bipyridine) Ruthenium (II/III) as a colorimetric mediator for the detection of Phenylalanine concentration. The amount of amino acid was quantitatively recognized by optical absorption measurements at 452 nm through the conversion of Ru (byp)₃³⁺ to Ru (byp)₃²⁺, which is induced by the neoformed NADH. A detection limit of 0.33 μM, a limit of quantification of 1.01 μM, and a sensitivity of 36.6 a.u nM⁻¹ were obtained. The proposed method was successfully tested using biological specimens from patients affected by hyperphenylalaninemia. The proposed enzymatic assay showed a high selectivity, making it a promising alternative for the development of versatile assays for the detection of phenylalanine in diluted serums.

KEYWORDS

phenylalanine, enzymatic-sensing, phenylketonuria, tris (bipyridine) Ruthenium (II/III), colorimetric-assay

1 Introduction

Hyperphenylalaninemia (HPA), including phenylketonuria (PKU), is a class of diseases caused by the impairment of the enzyme Phenylalanine hydroxylase (PAH), both for mutations in the corresponding *PAH* gene encoding the enzyme and for deficiency of the BH₄ cofactor (Shintaku, 2002). The enzyme deficiency results in the accumulation of phenylalanine (Phe) in the blood, causing brain damage, intellectual disability, and neurological problems. There is no cure for HPA, but early treatment can prevent intellectual disabilities and other health issues (PubMed Health, 2011). Patients with PKU require a severe diet that limits the intake of Phe (Poustie and Wildgoose, 2010). To date, Phe is the main biomarker used to monitor the progress of the PKU disease. Therefore, given the importance of frequently monitoring Phe levels' intake with meals, a straightforward growth in the development of new analytic assays (Matulis and Naglis Malys, 2023), sensors (Dinu et al., 2022), and wearable devices (Parrilla et al., 2022) for Phe recognition was observed. The integration of the assay into a miniaturized device is a critical key for the setup of effective and multiplexing point-of-care platforms (Ventimiglia

and Petralia, 2013). In this context, a great effort has been focused on the development of innovative nanostructured materials for effective assay miniaturization. Recently, our team developed novel photothermal nanomaterials based on β -CD/Co₃O₄ for the photothermal activation of Phe conversion into phenylpyruvate mediated by the Phenylalanine Dehydrogenase (PDH) NAD-dependent enzyme (Maugeri et al., 2022). Similarly, non-enzymatic and mediator-free approaches for the detection of Phe have been developed. They include methods based on Surface Plasmon Resonance imprinted polymers (Cimen et al., 2021) and on the recognition of Phe by interacting with specific DNA-aptamers sequences (Cheung et al., 2019). Despite great efforts in the development of enzyme-mimics nanosystems, the excellent specificity of the enzymatic reactions together with the good performance of the redox/colorimetric mediators makes enzymatic-based-assay the most used approach for the detection of Phe. Phenylalanine ammonia lyase (PAL) was the first investigated enzyme. It converts Phe to *trans*-cinnamic acid, producing a quantitative amount of ammonia, which can be detected by direct optical measurements (Sari et al., 2022) through an easy color change of the pH indicator (Villalonga et al., 2008) or by capacitive measurements using zirconia oxide nanostructures (Ando et al., 2022). The PDH is the most investigated NAD-dependent enzyme used for the development of enzymatic-analytical assays for Phe recognition. It converts, specifically, Phe, in the presence of NAD⁺, to Phenylpyruvate and NADH (nicotinamide adenine dinucleotide hydrogen). The direct optical spectroscopic measurement of neo-formed NADH at 340 nm is limited by its low absorption coefficient value. To overcome this drawback, a great effort has been made to develop novel transduction processes based on specific reactions with mediators, producing optical or electrical signals. Various electrochemical and colorimetric mediators, including the cationic dye MTT⁺, which is converted, in the presence of NADH and diaphorase enzyme, to the colored formazan have been reported in previous works of literature (Jafari et al., 2021). Similarly, methoxy phenazine-methosulfate and nitroblue tetrazolium are converted by NADH to colored formazan derivatives (Robinson et al., 2016). Although good results in terms of Lod and sensitivity were obtained, the not-quantitative colorimetric reaction requires additional enzymatic steps, making the protocol more cumbersome. Recently, our team has developed an enzymatic assay based on the PAL enzyme for the measurement of Phe levels. The Phe amount was easily recognized through pH-indicator color changes induced by the ammonia formation. The system permits the monitoring of Phe in a dynamic range concentration of 10–3,000 μ M with a limit of detection of approximately 19 μ M. The assay was successfully integrated into a miniaturized paper-based lab-on-chip device (Messina et al., 2017). In this study, we reported an innovative colorimetric-enzymatic assay based on tris (bipyridine) Ruthenium (II/III) complex (Ru (byp)₃^{2+/3+}) as a colorimetric-redox mediator through the PDH/NAD⁺ enzyme. The amount of NADH formed is revealed by the reaction with the colorimetric Ru (byp)₃³⁺ mediator through the formation of an intense absorption band centered at 452 nm. The method was successfully tested using human blood from patients affected with HPA.

2 Experimental sections

2.1 Materials and methods

All reagents including L-Phenylalanine (Phe) 98% (M.W. = 165.19 gr mol⁻¹), Phenylalanine Dehydrogenase (PDH) from *Sporosarcina* sp (6.0 U/mg), NAD⁺ (M.W. = 663.43 gr mol⁻¹), and Tris (2,2'-bipyridyl) dichlororuthenium (II) were purchased from Sigma-Aldrich in their highest purity and used without further purification. MilliQ-water was used in all experiments. The L-amino acid spectrophotometric commercial quantitation kit (cod. ACMAK002KT) was used. UV-Vis-NIR spectroscopic analyses in transmission mode were carried out on the Perkin-Elmer 365 using a standard quartz cuvette with an optical length of 1 cm. The plasma separation process was performed on the Vivid Plasma Separation Membranes (PALL, thickness, 300 \pm 20 μ m, and Grade GR). They were handled as received, and no pre-treatment was performed.

2.2 Colorimetric mediator solution preparation

The mediator Ru (byp)₃³⁺ solution was prepared by oxidation reaction of the commercial Ru (byp)₃Cl₂ product with Cerium (IV) ammonium nitrate (CAN), which is a strong one-electron oxidant ($E_{1/2}$ = 1.6 V vs. NHE) (Pérez-Ruiz, et al., 2003). It follows the reaction. $\text{Ru(byp)}_3^{2+} + \text{Ce(NO}_3)_6^{2-} \rightarrow \text{Ru(byp)}_3^{3+} + \text{Ce(NO}_3)_6^{3-}$

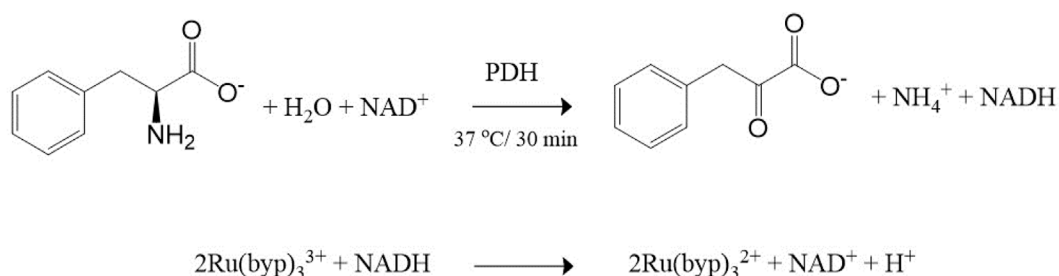
In detail, to a volume of 2 mL of Tris (2,2'-bipyridyl) dichlororuthenium (II) (Ru (byp)₃Cl₂) (7 mg/mL) was added a portion of 2 mL of cerium (IV) ammonium nitrate (CAN) with continuous stirring at room temperature. After 30 min, the solution was filtered (0.2 μ m filter pore size) and used. The CAN stock solution was prepared by dissolving an amount of 25 mg of product into 4 mL of hydrochloride acid (10 mM).

2.3 Enzymatic-assay procedure

To a volume of 1.0 mL of phosphate buffer saline (PBS) at a pH value of 8.3 were added 150 μ L NAD⁺ (75 mM) and 0.2 U of the PDH enzyme. Various amounts of Phe were added to obtain a final concentration ranging from 1 μ M to 12.7 μ M. The mixture was incubated at 37°C for 30 min then Ru (byp)₃⁽³⁺⁾ colorimetric mediator solution (30 μ M) was added with continuous stirring, and the UV-Vis optical spectra were recorded after 10 min of incubation at 24°C. The same procedure was used for the testing of filtered human plasma samples. Each analysis was replicated three times.

2.4 Plasma separation procedure

The plasma separation was conducted using the polysulfone membrane Grade GR. An amount of 20 μ L of fresh human blood was deposited on the membrane disk (diameter of approximately 8 mm), and after 3 min of filtration, a volume of approximately 7–10 μ L of plasma sample was collected and tested. Each analysis was replicated three times.



SCHEME 1

Phe sensing mechanism: (1) Enzymatic reaction catalyzed by PDH/NAD⁺ and (2) colorimetric transduction process based on Ru(byp)₃^{2+/3+} mediator.

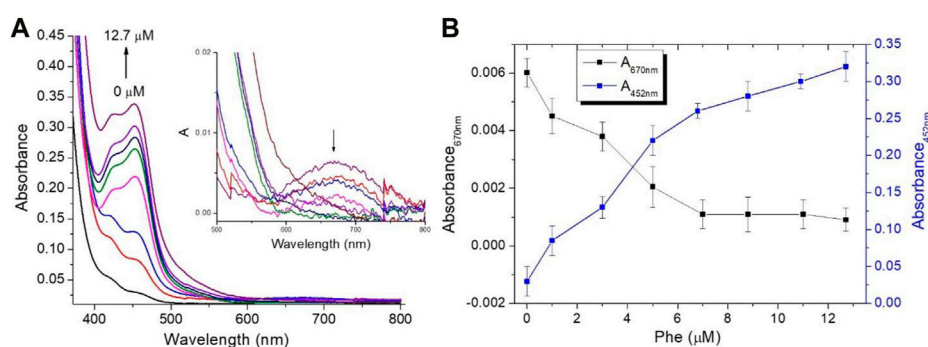


FIGURE 1

Spectroscopic measurements for the mixture assay at different Phe concentrations (0, 1.0, 3.0, 5.0, 6.8, 8.8, 10.9, and 12.7 μM) (A) Optical absorption changes in PBS, and the presence of a Ru-complex mediator concentration of 30 μM insets the optical absorption spectra change in the region from 500 to 800 nm and (B) Absorbance values at 452 nm and 670 nm at different Phe amounts.

3 Results and discussion

3.1 Enzymatic-assay mechanism

Based on the experimental observations and literature data, the working mechanism for the sensing of Phe using Ru(III/II) complexes mediator is proposed in Scheme 1. Firstly, the enzymatic reaction converts Phe into phenylpyruvate through PDH/NAD⁺ with NADH formation (Reaction 1). The neoformed NADH was spectroscopically confirmed through the appearance of the absorption band centered at 340 nm (Supplementary Figure S1). The second step involves one-electron transfer from NADH to the Ru(byp)₃³⁺ in an outer sphere manner to yield the Ru(byp)₃²⁺ and the NADH^{•+} radical. The reduction of another molecule of the Ru(III) complex by NADH^{•+} radical occurred in a subsequent rapid and kinetically inconsequential step (Reaction 2) (Chrzanowska et al., 2022). The conversion of Ru(byp)₃³⁺ to Ru(byp)₃²⁺ is revealed by the formation of the metal-ligand charge transfer (MLCT) absorption band centered at approximately 452 nm (Figure 1A).

The proposed mechanism in the reduction of a similar Ru³⁺ complex system induced by NADH was supported by recent literature data (Reyes and Tanaka, 2017). Moreover, to confirm the role of NAD⁺ on the mechanism, additional experiments were carried out in the absence of NAD⁺ species. In this case, no Ru^{III}/Ru^{II} complexes conversion was observed;

whereas, in the presence of NAD⁺ (10 μM), the reduction in conversion arose as confirmed by the formation of the optical absorption band centered at 452 nm (Supplementary Figure S2). The optical properties, in terms of optical absorption and emission spectra for the Ru(byp)₃^{3+/2+} mediator, are reported in Supplementary Figure S3.

To assess the potential of the proposed colorimetric mediator, various Phe amounts (0, 1.0, 3.0, 5.0, 6.8, 8.8, 10.9, and 12.7 μM) were investigated. Figure 1A illustrates the optical absorption changes of the assay at different Phe amounts in the presence of Ru(byp)₃³⁺ mediator concentration of approximately 30 μM. It is evident that there is a conversion of Ru(byp)₃³⁺ to Ru(byp)₃²⁺ as Phe amounts increase, as confirmed by the formation of the absorption band centered at 452 nm and by the disappearance of the absorption band centered at 670 nm for the Ru(byp)₃³⁺ (Figure 1A-inset). Figure 1B illustrates the change in the absorbance values recorded at 452 nm and 670 nm at different Phe levels.

3.2 Analytical parameters assessment

In order to evaluate the analytical performance of the proposed assay, linear response range, sensitivity, the limit of detection (LoD), the limit of quantification (LoQ), and selectivity were investigated. Figure 2A illustrated the linear relationship between the absorbance

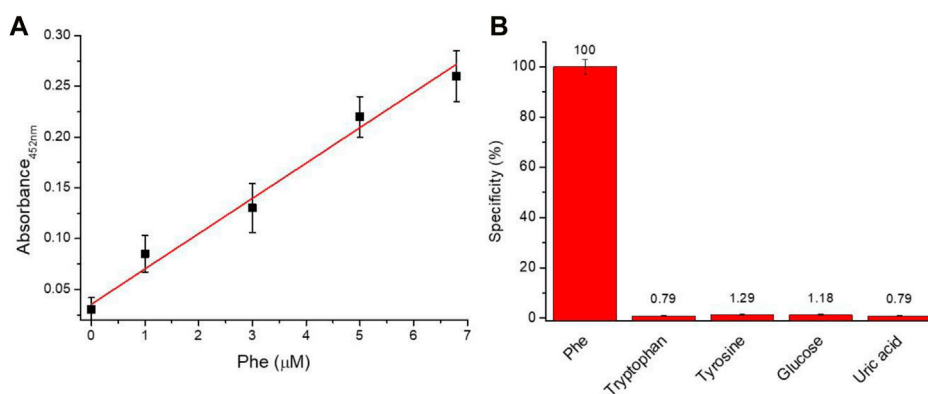


FIGURE 2

Analytical performance (A) Linearity response of the assay ($Y = 0.0356 + 0.04821X$; $R^2 = 0.9958$) and (B) Selectivity (%) of Phe assay versus different biomolecules.

TABLE 1 A comparison of different methods for Phe detection.

Detection method	LoD	References
Enzymatic (PAL)/colorimetric pH indicator	~19 μM	Messina et al. (2017)
Enzymatic (PDH/NAD ⁺)/MTT-AuNPs colorimetric mediator	34.5 μM	Jafari et al. (2021)
Enzymatic (PDH/NAD ⁺)/NBT colorimetric mediator	66.5 μM	Jafari et al. (2021)
Enzymatic (PDH/NAD ⁺)/Ru ^{II} colorimetric mediator	330 nM	This work
DNA aptamers coupled with Nansized-In ₂ O ₃ /electric detection	Range ~ fM	(Cheung et al., 2019)
DNA aptamer immobilized gold nanostructure/electrochemical detection	0.23 μM	Hasanzadeh et al. (2018)
Enzymatic PDH/NAD/1-Methoxy-PMS colorimetric mediator	5.0 μM	Nakamura et al. (2002)
Enzymatic PDH/NAD/1-Methoxy-PMS colorimetric mediator in the dry film	50 μM	DeSilva et al. (2006)
Aptamer/organometallic receptor-based methodology for label-free and amplified electrochemical determination of phenylalanine	1.03 μM	Yang et al. (2023)

value at 452 nm and the amount of Phe. A dynamic linear range of 0–7 μM was observed with a sensitivity of approximately 36.6 a.u. nM⁻¹. Moreover, an LoD of 0.33 μM and LoQ of 1.01 μM were obtained using the following formulas: $LoD = 3\sigma/slope$ and $LoQ = 10\sigma/slope$ (where the background standard deviation σ is 0.00372). The capability of the assay to selectively discriminate between Phe versus other molecules was investigated. In detail, the assay was tested in the presence of tryptophan, tyrosine, glucose, and uric acid at a concentration of 12.7 μM. The data reported in Figure 2B confirm the high specificity (~98.5%) of the proposed assay for the recognition of Phe.

3.3 Phe detection in human blood

To assess the capability of the proposed assay to measure Phe concentrations in human specimens, an aliquot of fresh whole blood (20 μl) was deposited on the membrane filters (diameter of approximately 8 mm) (Supplementary Figure S4). After 3 min, a volume of approximately 7–10 μl of plasma samples was collected

and the amount of Phe was measured in a final volume of 200 μl as reported in the experimental section. Phe concentration value of approximately $3.6 \pm 0.2 \mu\text{M}$ was obtained by calibration line interpolation (Figure 2A). Phe concentration, corrected by the dilution and filtration factors, corresponds to a final Phe concentration of $51.6 \pm 2.0 \mu\text{M}$ on the whole blood sample. The proposed method was successful, compared with the commercial quantification amino acid kit which discloses a final Phe concentration of $53.5 \pm 3.0 \mu\text{M}$. The analysis was replicated three times.

3.4 Comparison of Phe detection methods

Various enzymatic and non-enzymatic approaches for the detection of Phe have been recently developed and reported in previous works of literature. These are mainly based on colorimetric and electric detections and some of these were successfully integrated into miniaturized devices for the development of portable systems. Table 1 reports a comparison between the different approaches recently reported in previous works of literature for the recognition of Phe. Non-

enzymatic approaches based on the electric recognition of Phe by DNA-aptamers have been independently reported by Cheung et al. (2019) and Hasanzadeh et al. (2018). Both works report excellent sensitivity and good specificity, but the assays' preparation requires laborious procedures and is hard to integrate into a miniaturized and disposable device. Among the enzymatic approaches, PAL and PDH are the most investigated enzymes. Recently, a colorimetric paper-based biosensor based on the PDH enzyme was proposed by Jafari et al. (2021) for the highly sensitive and selective determination of Phe, using MTT^{xy} and NBT^{xy} as mediators, reaching an LoD of 66.5 μM and 34.5 μM , respectively. In addition, different patents for Phe recognition were recently granted. Nakamura and co-inventors report a PDH/NAD enzymatic approach using 1-Methoxy-PMS as an electrochemical mediator (Nakamura et al., 2002). This method was successfully integrated into a disposable device reaching an LoD of 5.0 μM . An innovative enzymatic-sensing method using a carbon-based colorimetric mediator for Phe recognition in the dry film was invented by DeSilva et al. (2006). Despite the good sensitivity and the easy testing procedure, the dynamic range of 1–15 mM obtained with real samples would limit its diffusion. Recently, an alternative approach based on the aptamer/organometallic receptor was reported by Yang and colleagues for the electrochemical determination of phenylalanine. A linear range of 10–260 μM and an LoD of 1.03 μM were declared by the authors Yang et al. (2023).

Compared with previously published approaches, our proposed method shows excellent sensitivity and good LoD together with high specificity (> 98.5%). These parameters are crucial to allow effective integration of the assay on the microfluidics system.

4 Conclusion

In summary, a highly sensitive enzymatic approach based on PDH/NAD⁺ and Ru-complexes colorimetric mediator was demonstrated for the sensitive and convenient quantification of Phe. This approach can measure Phe concentrations in diluted filtered plasma by optical absorption measurements at 452 nm through the enzymatic conversion of Phe in phenylpyruvate. The neoformed NADH induces the quantitative conversion of Ru (byp)₃³⁺ in Ru (byp)₃²⁺ species with the formation of the MLCT absorption band centered at 452 nm. The determination of Phe with a limit of detection of 0.33 μM , a limit of quantification of 1.01 μM , and a sensitivity of 36.6 a.u. nM⁻¹ was demonstrated. Compared with traditional methods, the employment of colorimetric mediators improves detection sensitivity and selectivity. Considering these advantages, this approach should be integrated into a miniaturized biosensor for the self-testing of Phe concentrations, paving the way for the future development of PoC platforms. The system should be an excellent improvement to the quality of life of patients with HPA through the monitoring of diet therapy for HPA disorders in real-time.

4.1 Notes

^{xy} MTT= (3-(4,5-dimethylthiazol-2-yl)-2,5-diPhenyltetrazolium bromide).

^{xy} NBT = nitro blue tetrazolium.

Data availability statement

The original contributions presented in the study are included in the article/Supplementary Material. Further inquiries can be directed to the corresponding author.

Ethics statement

The studies involving human participants were reviewed and approved by Institutional review board of University Hospital of Catania. The patients/participants provided their written informed consent to participate in this study.

Author contributions

MM performed the statistical analysis; LM performed the experiments; GF and MR contributed to the revision; SP contributed to the conception, supervision, and design of the study. All authors contributed to manuscript revision, read, and approved the submitted version.

Funding

This research was supported by “PKU Smart Sensor” project and funded under Action 1.1.5 POR FESR 2014-2020, CUP G89J18000710007.

Conflict of interest

The authors declare that the research was conducted in the absence of any commercial or financial relationships that could be construed as a potential conflict of interest.

Publisher's note

All claims expressed in this article are solely those of the authors and do not necessarily represent those of their affiliated organizations, or those of the publisher, the editors and the reviewers. Any product that may be evaluated in this article, or claim that may be made by its manufacturer, is not guaranteed or endorsed by the publisher.

Supplementary material

The Supplementary Material for this article can be found online at: <https://www.frontiersin.org/articles/10.3389/fchem.2023.1164014/full#supplementary-material>

References

- Ando, B., Baglio, S., Castorina, S., Graziani, S., Tondepu, S. V. G., Petralia, S., et al. (2022). A capacitive sensor, exploiting a YSZ functional layer, for ammonia detection. *IEEE Trans. Instrum. Meas.* 71, 9505811–11. doi:10.1109/tim.2022.3167766
- Cheung, M. K., Yang, K. A., Nakatsuka, N., Zhao, C., Ye, M., Jung, M. E., et al. (2019). Phenylalanine monitoring via aptamer-field-effect transistor sensors. *ACS Sensors* 4 (12), 3308–3317. doi:10.1021/acssensors.9b01963
- Chrzanowska, M., Katafias, A., van Eldik, R., and Chatterje, D. (2022). Oxidoreductase mimicking activity of Ru(edta) complexes in conversion of NAD coenzymes. *Polyhedron* 221, 115872. doi:10.1016/j.poly.2022.115872
- Cimen, D., Bereli, N., and Denizli, A. (2021). Surface Plasmon resonance based on molecularly imprinted polymeric film for L-phenylalanine detection. *Biosensors* 11 (1), 21. doi:10.3390/bios11010021
- DeSilva, V., Oldham, C. D., May, S. W., and Shunnnarah, R. D. (2006). *Medical device for monitoring blood phenylalanine levels*. EP 1618207.
- Dinu, A., and Apetrei, C. (2022). A review of sensors and biosensors modified with conducting polymers and molecularly imprinted polymers used in electrochemical detection of amino acids: Phenylalanine, tyrosine, and tryptophan. *Int. J. Mol. Sci.* 23, 1218.
- Hasanzadeh, M., Zargami, A., Baghban, H. N., Mokhtarzadeh, A., Shadjou, N., and Mahboob, S. (2018). Aptamer-based assay for monitoring genetic disorder phenylketonuria (PKU). *Int. J. Biol. Macromol.* 116, 735–743. doi:10.1016/j.ijbiomac.2018.05.028
- Jafari, P., Beigi, S. M., Yousefi, F., Aghabalazadeh, S., Mousavizadegan, M., Hosseini, M., et al. (2021). Colorimetric biosensor for phenylalanine detection based on a paper using gold nanoparticles for phenylketonuria diagnosis. *Microchem. J.* 163, 105909. doi:10.1016/j.microc.2020.105909
- Matulis, P., and Naglis Malys, N. (2023). Nanomolar biosensor for detection of phenylacetic acid and L-phenylalanine. *Biochem. Eng. J.* 191, 108765. doi:10.1016/j.bej.2022.108765
- Maugeri, L., Forte, G., Messina, M. A., Camarda, M., Ventimiglia, G., Letizia Consoli, G. M., et al. (2022). Photochemical synthesis of β -cyclodextrin/cobalt oxide nanoparticles as photothermal agents for photothermal-induced enzymatic reaction. *ACS Appl. Nano Mat.* 5, 10167–10173. doi:10.1021/acsanm.2c01240
- Messina, M. A., Meli, C., Conoci, S., and Petralia, S. (2017). A facile method for urinary phenylalanine measurement on paper-based lab-on-chip for PKU therapy monitoring. *Analyst* 142, 4629–4632. doi:10.1039/c7an01115f
- Nakamura, K., Yokoyama, T., and Shinozuka, N. (2002). Method for assaying L-phenylalanine and sensor. *U. S. Pat. N. 6* (468), 416.
- Parrilla, M., Vanhooydonck, A., Watts, R., and De Wael, K. (2022). Wearable wristband-based electrochemical sensor for the detection of phenylalanine in biofluids. *Biosens. Bioelectron.* 197, 113764. doi:10.1016/j.bios.2021.113764
- Pérez-Ruiz, T., Martínez-Lozano, C., Tomás, V., and Fenoll, J. (2003). Chemiluminescence determination of citrate and pyruvate and their mixtures by the stopped-flow mixing technique. *Anal. Chim. Acta* 485 (1), 63–72. doi:10.1016/s0003-2670(03)00402-1
- Poustie, V. J., and Wildgoose, J. (2010). Dietary interventions for phenylketonuria. *Cochrane Database Syst. Rev.* 1, CD001304. doi:10.1002/14651858.cd001304.pub2
- PubMed Health (2011). *Phenylketonuria*. Bethesda, MD (US): National Library of Medicine, Medlineplus.
- Reyes, R. L., and Tanaka, K. (2017). The NAD⁺/NADH redox couple—insights from the perspective of electrochemical energy transformation and biomimetic Chemistry. *Kimika* 28 (1), 32–43. doi:10.26534/kimika.v28i1.32-43
- Robinson, R., Wong, L., and Monnat, R. J. Fu E. (2016). Development of a whole blood paper-based device for phenylalanine detection in the context of PKU therapy monitoring. *Micromachines* 7 (2), 28. doi:10.3390/mi7020028
- Sari, T., Dede, S., Yusufoglu, B., and Karakuş, E. (2022). Determination of L-phenylalanine in human plasma samples with new fluorometric method. *Appl. Biochem. Biotechnol.* 194, 1259–1270. doi:10.1007/s12010-021-03694-7
- Shintaku, H. (2002). Disorders of tetrahydrobiopterin metabolism and their treatment. *Curr. Drug Metab.* 3, 123–131. doi:10.2174/1389200024605145
- Ventimiglia, G., and Petralia, S. (2013). Recent advances in DNA microarray technology: An overview on production strategies and detection methods. *Bionanoscience* 3, 428–450. doi:10.1007/s12668-013-0111-8
- Villalonga, R., Fujii, S. A., Tachibana, S., and Asano, Y. (2008). Covalent immobilization of phenylalanine dehydrogenase on cellulose membrane for biosensor construction. *Sensors Actuators B Chem.* 129, 195–199. doi:10.1016/j.snb.2007.07.097
- Yang, J., Bi, Q., Song, X., Yuan, R., and Xiang, Y. (2023). Aptamer/organometallic receptor-based and label-free sensitive electrochemical detection of amino acid via multi-pedal DNA walker/DNAzyme amplifications. *Sensors Actuators B Chem.* 375, 132876. doi:10.1016/j.snb.2022.132876



OPEN ACCESS

EDITED BY

Mahmoud Moradi,
University of Arkansas, United States

REVIEWED BY

Mrinal Shekhar,
Broad Institute, United States
Sándor Volkán-Kacsó,
California Institute of Technology,
United States

*CORRESPONDENCE

Sunil Nath,
✉ sunil_nath_iit@yahoo.com,
✉ sunath@iitd.ac.in

RECEIVED 04 October 2022

ACCEPTED 10 May 2023

PUBLISHED 30 May 2023

CITATION

Nath S (2023), Beyond binding change: the molecular mechanism of ATP hydrolysis by F_1 -ATPase and its biochemical consequences.
Front. Chem. 11:1058500.
doi: 10.3389/fchem.2023.1058500

COPYRIGHT

© 2023 Nath. This is an open-access article distributed under the terms of the [Creative Commons Attribution License \(CC BY\)](#). The use, distribution or reproduction in other forums is permitted, provided the original author(s) and the copyright owner(s) are credited and that the original publication in this journal is cited, in accordance with accepted academic practice. No use, distribution or reproduction is permitted which does not comply with these terms.

Beyond binding change: the molecular mechanism of ATP hydrolysis by F_1 -ATPase and its biochemical consequences

Sunil Nath*

Department of Biochemical Engineering and Biotechnology, Indian Institute of Technology Delhi, Hauz Khas, New Delhi, India

F_1 -ATPase is a universal multisubunit enzyme and the smallest-known motor that, fueled by the process of ATP hydrolysis, rotates in 120° steps. A central question is how the elementary chemical steps occurring in the three catalytic sites are coupled to the mechanical rotation. Here, we performed cold chase promotion experiments and measured the rates and extents of hydrolysis of preloaded bound ATP and promoter ATP bound in the catalytic sites. We found that rotation was caused by the electrostatic free energy change associated with the ATP cleavage reaction followed by P_i release. The combination of these two processes occurs sequentially in two different catalytic sites on the enzyme, thereby driving the two rotational sub-steps of the 120° rotation. The mechanistic implications of this finding are discussed based on the overall energy balance of the system. General principles of free energy transduction are formulated, and their important physical and biochemical consequences are analyzed. In particular, how exactly ATP performs useful external work in biomolecular systems is discussed. A molecular mechanism of steady-state, trisite ATP hydrolysis by F_1 -ATPase, consistent with physical laws and principles and the consolidated body of available biochemical information, is developed. Taken together with previous results, this mechanism essentially completes the coupling scheme. Discrete snapshots seen in high-resolution X-ray structures are assigned to specific intermediate stages in the 120° hydrolysis cycle, and reasons for the necessity of these conformations are readily understood. The major roles played by the “minor” subunits of ATP synthase in enabling physiological energy coupling and catalysis, first predicted by Nath’s torsional mechanism of energy transduction and ATP synthesis 25 years ago, are now revealed with great clarity. The working of nine-stepped (bMF_1 , hMF_1), six-stepped (TF_1 , EF_1), and three-stepped (PdF_1) F_1 motors and of the $\alpha_3\beta_3\gamma$ subcomplex of F_1 is explained by the same unified mechanism without invoking additional assumptions or postulating different mechanochemical coupling schemes. Some novel predictions of the unified theory on the mode of action of F_1 inhibitors, such as sodium azide, of great pharmaceutical importance, and on more exotic artificial or hybrid/chimera F_1 motors have been made and analyzed mathematically. The detailed ATP hydrolysis cycle for the enzyme as a whole is shown to provide a biochemical basis for a theory of “unisite” and steady-state multisite catalysis by F_1 -ATPase that had remained elusive for a very long time. The theory is supported by a probability-based calculation of enzyme species distributions and analysis of catalytic site occupancies by Mg-nucleotides and the activity of F_1 -ATPase. A new concept of energy coupling in ATP synthesis/hydrolysis based on fundamental ligand substitution chemistry has been advanced, which offers a deeper

understanding, elucidates enzyme activation and catalysis in a better way, and provides a unified molecular explanation of elementary chemical events occurring at enzyme catalytic sites. As such, these developments take us beyond binding change mechanisms of ATP synthesis/hydrolysis proposed for oxidative phosphorylation and photophosphorylation in bioenergetics.

KEYWORDS

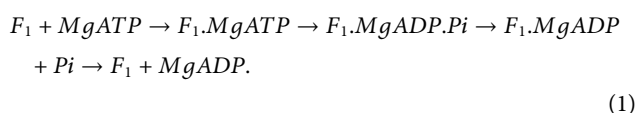
bioenergetics, ATP theory and mechanism, consistency with physical laws, Boyer's binding change mechanism of ATP synthesis/hydrolysis, Nath's torsional mechanism of energy transduction and ATP synthesis/hydrolysis and two-ion theory of energy coupling, molecular motors, mode of action of F₁-ATPase inhibitors, ligand displacement/substitution, ADP-ATP exchange

1 Introduction

The F₀F₁-ATP synthase catalyzes the ATP synthesis/hydrolysis reaction, vital to life in all living organisms (Penefsky, 1985; Boyer, 1993; Abrahams et al., 1994; Weber and Senior, 1997; Allison, 1998; Nath, 2002; Nath, 2003; Adachi et al., 2007; Nath, 2008; Nath and Nath, 2009; Nakano et al., 2022). It contains a hydrophilic F₁ moiety that lies ~4.5 nm above the surface of the membrane containing a hydrophobic F₀ sector connected by two ~1-nm-thick central and peripheral stalks (Abrahams et al., 1994; Aggeler et al., 1997; Nath, 2002; Nakano et al., 2022). The headpiece of F₁ houses three β-catalytic sites, whereas the membrane-bound F₀ contains access pathways that couple ion translocation to conformational changes of catalytic sites in F₁ (Abrahams et al., 1994; Aggeler et al., 1997; Noji et al., 1997; Nath, 2002; Nath, 2003; Adachi et al., 2007; Nath, 2008; Martin et al., 2015).

The *Escherichia coli* enzyme, containing eight different subunits, is considered a prototype for ATP synthases from different organisms. The isolated F₁ sector is an ATPase consisting of five subunits (α, β, γ, δ, and ε) with a conserved subunit stoichiometry α₃β₃γδε in all organisms. In *E. coli* F₁, the molecular masses of α, β, γ, δ, and ε measure 55.3, 50.3, 31.6, 19.3, and 14.9 kDa, respectively (Weber and Senior, 1997).

The reaction mechanism of the hydrolysis of ATP in a catalytic site of the soluble F₁ (Weber and Senior, 1997; Allison, 1998; Nath, 2003; Adachi et al., 2007; Nath, 2008; Nath and Nath, 2009) or membrane-bound F₀F₁ (Penefsky, 1985; Boyer, 1993; Nath, 2008; Nath and Nath, 2009; Nakano et al., 2022) of the ATP synthase can be described by the following elementary kinetic steps:



The first step represents the formation of the enzyme–substrate complex, the second step is the catalytic step, and steps 3 and 4 describe the sequential release of products. The ATP hydrolysis rate can be readily monitored by stopped/quench flow kinetic techniques.

The enzyme complex contains three catalytic sites located primarily on the β-subunits of the F₁ portion at the α–β interface (Abrahams et al., 1994; Weber and Senior, 1997; Nath, 2002; Nakano et al., 2022), which work together during multisite hydrolysis (Adachi et al., 2007; Nath, 2008). It has now been conclusively established that a domain consisting of the “minor” γ- and ε-

subunits rotates relative to the α₃β₃ hexamer during ATP hydrolysis and synthesis. The rotation, inferred first from biochemical crosslinking studies (Aggeler et al., 1997), has been visualized directly using epifluorescence microscopy during ATP hydrolysis by the F₁-ATPase (Noji et al., 1997) and during ATP synthesis (Martin et al., 2015).

Although the direct link between catalytic site events and rotation has been confirmed, no unequivocal correlation has been established between the rate of rotation of the γ–ε domain and the kinetics of the individual steps in the ATP hydrolysis (Eq. 1) and ATP synthesis reactions. The analysis is greatly complicated by the fact that ATP can bind in three β-catalytic sites that are characterized by high (site 1), intermediate (site 2), and low (site 3) affinity for nucleotides. Thus, *a priori*, the driving force for rotation during steady-state V_{max} ATP hydrolysis could be the binding energy of ATP and/or the free energy change associated with the ATP cleavage reaction and product release in any of these three catalytic sites. Boyer's binding change mechanism (Boyer et al., 1973; Boyer, 1993) and Nath's torsional mechanism of ATP synthesis/hydrolysis (Nath, 2002; Nath, 2008; Mehta et al., 2020) are two important and detailed theories that have been proposed to explain the functioning of the enzyme during steady-state ATP synthesis/hydrolysis. Other physical models of F₁-ATPase have been developed by various theory groups (Wang and Oster, 1998; Bai et al., 2020; Gerritsma and Gaspard, 2010; Lenz et al., 2003; Mukherjee and Warshel, 2011; Volkán-Kacsó and Marcus, 2017; Nam and Karplus, 2019; Volkán-Kacsó and Marcus, 2022). These latter works, though important in their own right, do not address the biochemical issues of “unisite” catalysis, cold chase, and rate enhancement in multisite catalysis when the substrate binds to additional catalytic sites. However, we agree with the reviewer that greater attention should be given to theory and that the right theory has the power to catalyze rapid progress in bioenergetics and several interdisciplinary fields of biology.

Functioning in these β-catalytic sites can be biochemically differentiated because ATP hydrolysis in the high-affinity catalytic site 1 can be monitored by so-called “unisite” catalysis measurements with sub-stoichiometric amounts of [γ-³²P]ATP relative to F₁ (Penefsky, 1985). These conditions lead to preferential binding of the substrate in a single site (i.e., in the high-affinity site 1), resulting in the formation of the enzyme–substrate complex in the site (Step 1 in Eq. 1). Therefore, it can be distinguished from nucleotide binding into lower affinity catalytic sites (preferentially site 2, and with a far lower probability of filling the least affinity site 3), which causes product

release from the high-affinity site 1 in cold chase experiments (Penefsky, 1985; García and Capaldi, 1998). Such equilibrium and kinetic experiments can help elucidate the mechanism of ATP hydrolysis by F_1 -ATPase.

The chemical reactions of “unisite” catalysis shown in Eq. 1 characterize a single turnover event. However, whether all the elementary steps of the reaction scheme take place in a single catalytic site [site 1, or T, as hypothesized by Penefsky (1985)], in site 2 (i.e., in L), or in both has not been conclusively established. Furthermore, does the catalytic conformation of site 1 (T) need to be altered to site 2 (L), as proposed previously (Nath, 2003; Nath, 2008), to enable ATP hydrolysis occurrence in the “unisite” mode described previously (Penefsky, 1985) or in its transition to multisite catalysis (Nath, 2008)? There has been no report on “unisite” ATP synthesis to date. Therefore, what exactly is “unisite” ATP hydrolysis? Under what special conditions does it occur? What is the biochemical basis underlying “unisite” catalysis? Can its relationship to steady state (multisite) ATP hydrolysis be characterized and can the rate enhancement in the progress from “unisite” to multisite hydrolysis be understood mechanistically? These problems have been considered “elusive” in recent work (Nakano et al., 2022).

A major reason for the difficulty and elusiveness of the problems stated above in ATP hydrolysis by F_1 -ATPase arises from their concatenated nature. A detailed solution of the molecular mechanism of steady-state ATP hydrolysis by F_1 -ATPase is required to fully understand turnover events underlying “unisite” catalysis (Penefsky, 1985; Nakano et al., 2022), cold chase (García and Capaldi, 1998), and progression to multisite hydrolysis (Weber and Senior, 1997; Adachi et al., 2007; Nath, 2008). Such a unified mechanism of ATP synthesis/hydrolysis has already been formulated (Nath, 2008). Can it help solve the problem? Looking at the problem from another angle, experiments in unisite and cold chase ATP hydrolysis can offer novel insights into steady-state multisite ATP hydrolysis by F_1 -ATPase. How do models and mechanisms of ATP hydrolysis perform with respect to these experiments? Can the models be refined in light of these experimental results?

A definitive solution to the aforementioned longstanding “elusive” problems is attempted in this work. The refined molecular mechanism of ATP hydrolysis by F_1 -ATPase helps interpret X-ray structural snapshots, especially those close to the ATP-waiting state at 0° (or 120°) in the catalytic cycle, and assign them to specific conformations of the enzyme during catalysis.

This article is organized as follows. Section 2 describes the experimental methods used. Section 3.1 reports data on the rates and extents of hydrolysis of preloaded bound ATP and promoter ATP in cold chase promotion experiments. Mechanistic implications arising from steady-state ATP hydrolysis by F_1 -ATPase are deduced in Section 3.2. This enables the formulation of general principles for biological free energy transduction with its manifold physical and biochemical consequences, which are analyzed in Section 3.3. A molecular mechanism of steady-state, trisite ATP hydrolysis by F_1 -ATPase consistent with physical laws and principles and the body of available biochemical information that goes beyond previous theories (Boyer et al., 1973; Boyer, 1993) is formulated in Section 3.4. The structural and biochemical consequences of the new molecular vistas are presented in Section 4. In particular, the central role of the γ -subunit and

especially of the ϵ -subunit as conduits in energy coupling, that enable fine-tuned conformational changes of the β -catalytic sites essential to catalysis in ATP synthesis/hydrolysis by F_0F_1 -ATP synthase/ F_1 -ATPase, are discussed. The working of nine-stepped (bMF_1 , hMF_1), six-stepped (TF_1 , EF_1), and three-stepped (PdF_1) F_1 motors and of the $\alpha_3\beta_3\gamma$ subcomplex of F_1 is explained by a unified mechanism. The theory is supported by a probability-based calculation of enzyme species distributions and analysis of catalytic site occupancies by Mg-nucleotides and the activity of F_1 -ATPase. Some novel predictions of the unified theory that are of pharmacological importance are also made in Section 4. A new concept of energy coupling in ATP synthesis/hydrolysis based on fundamental *ligand substitution chemistry* is proposed, which takes us beyond the binding change mechanism of ATP synthesis/hydrolysis.

A mathematical model for estimating economics and opportunity cost in choosing between competing theories is developed in the Supplementary Section.

2 Methods

MF_1 was prepared from bovine heart mitochondria using standard procedures, as described previously (Penefsky, 1979). The specific activity of the enzyme was 95 units/mg. The Mg buffer contained 40 mM Tris-MES, 0.25 M sucrose, and 0.5 mM $MgSO_4$, with a pH of 8.0 at $23^\circ C$. The P_i concentration was kept constant at 2 mM in the reaction mixture. Aliquots of an ammonium sulfate suspension of MF_1 were centrifuged, and the pellets were separated from the $(NH_4)_2SO_4$ supernatant. The pellets were dissolved in 100 μL Mg buffer, and the enzyme solution was passed through a centrifuge column equilibrated with the same buffer. The enzyme was incubated with Mg buffer for 1 h at $23^\circ C$. $[\gamma\text{-}^{32}P]ATP$ was prepared as described previously (Glynn and Chappell, 1964). The specific activity of the $[\gamma\text{-}^{32}P]ATP$ used was $10^6\text{--}10^7$ counts min^{-1} nmol^{-1} . Equilibrium chase promotion experiments were performed in 1 ml reaction mixtures with magnetic stirring, and kinetic rate promotion experiments were performed in a quenched flow apparatus (Penefsky, 1985). The error bars arise in part from a small percentage in $[\gamma\text{-}^{32}P]ATP$ solutions that are unreactive with hexokinase ($\sim 2\text{--}3\%$).

A measure of 100 μL of a solution containing 1 nmol MF_1 in Mg buffer was added to a glass reaction vessel containing Mg buffer to determine the maximum equilibrium hydrolysis of preloaded and promoter ATP in cold chase experiments. The solution was stirred at high speed with a magnetic stirrer and stirrer bar. A volume of 20 μL of 15 μM $[\gamma\text{-}^{32}P]ATP$ or ATP was pipetted and incubated for 3 s. Chase solutions were pipetted from 0.5 mM stock solutions of ATP or $[\gamma\text{-}^{32}P]ATP$, respectively. The final volume measured 1.0 ml in Mg buffer. After the addition of the chase, the solutions were incubated for 10 s, and the reaction was thereafter terminated by adding 0.2 ml of 70% perchloric acid. For the control without adding promoter ATP, the reaction was allowed to continue for 10 s and quenched by adding perchloric acid before the chase. $^{32}P_i$ was separated from $[\gamma\text{-}^{32}P]ATP$ and counted as described (Penefsky, 1985), and results are expressed as percent hydrolysis of added $[\gamma\text{-}^{32}P]ATP$.

TABLE 1 Maximum extent of hydrolysis of preloaded, bound [γ - 32 P]ATP and promoter [γ - 32 P]ATP during a cold chase experiment (mean \pm SD).

Concentration of promoter ATP (μ M)	Hydrolysis of loaded [γ - 32 P]ATP (%)	Hydrolysis of promoter [γ - 32 P]ATP (%)
0	30 \pm 2	0
5	92 \pm 2	92 \pm 3
10	92 \pm 2	93 \pm 3
15	95 \pm 2	94 \pm 3
20	96 \pm 2	94 \pm 3

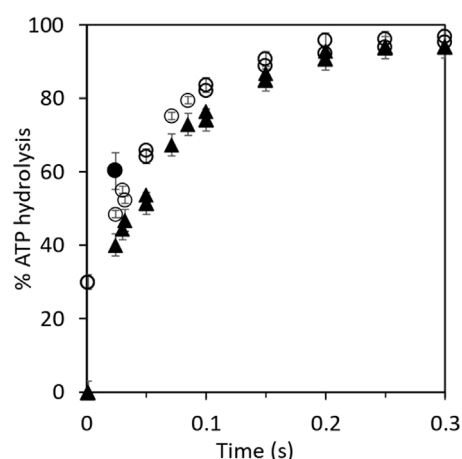
For determining the kinetic rate of hydrolysis of preloaded, bound [γ - 32 P]ATP, and promoter [γ - 32 P]ATP in the cold chase experiments, equal volumes of 3 μ M MF₁ in Mg buffer and 1 μ M [γ - 32 P]ATP or ATP were first mixed for 2 s to allow the formation of the enzyme–substrate complex. Then, the contents were mixed with 15 μ M chase ATP or [γ - 32 P]ATP, and the chased reaction mixtures passed into a vessel containing 0.8 ml Mg buffer, 0.2 ml of 70% perchloric acid, and 0.1 ml of 100 mM ATP. The residence time is the time between mixing of the MF₁- 32 P enzyme–substrate complex with the chase ATP and quenching in acid. The reference point of zero time was obtained by directly collecting the solution containing the enzyme–substrate complex into the perchloric acid quench without the chase. 32 Pi formed was isolated and counted as described (Penefsky, 1985), and the data were plotted as percent hydrolysis of added [γ - 32 P]ATP.

F₁ and [γ - 32 P]ATP were mixed at 1) 0.5 μ M each and 2) 1 μ M each in Mg buffer at 23°C. In other experiments, 10% excess F₁ was employed with respect to the substrate to obtain the distribution of bound substrate and product at F₁-ATPase catalytic sites. A complex between the two species was allowed to form, and unbound 32 P was removed on centrifuge columns. Column effluents were collected at 1, 5, 10, and 15 min in perchloric acid quench, the bound 32 Pi was determined, and the fraction *f* of total bound 32 P present as 32 Pi was quantitated at various times.

3 Results

3.1 Rates and extents of hydrolysis of bound [γ - 32 P]ATP and chase [γ - 32 P]ATP in promotion experiments

As shown in step 1 of the reaction scheme (Eq. 1), incubation of 1 μ M MF₁ with 0.3 μ M [γ - 32 P]ATP, i.e., under sub-stoichiometric conditions that predominantly favor substrate binding to a single catalytic site of the F₁-ATPase [site 1, the tight (T) site with the highest affinity for ATP], results in the formation of an enzyme–substrate complex. This is followed by the hydrolysis of ATP to ADP.Pi on the enzyme, limited by the slow rate of dissociation of the products (Eq. 1). The first line of Table 1 shows that the percentage of hydrolysis of added [γ - 32 P]ATP after 10 s incubation time is only 30%. Addition as a cold chase of 5–20 μ M of promoter ATP (that binds predominantly to a second catalytic site of the enzyme, i.e., site 2, the loose (L) site with intermediate affinity for ATP) results in hydrolysis of 92%–96% of [γ - 32 P]ATP bound in the highest affinity catalytic site 1. Similar

**FIGURE 1**

Kinetics of hydrolysis of bound [γ - 32 P]ATP and of promoter [γ - 32 P]ATP in cold chase experiments. Equal volumes of 3 μ M MF₁ in Mg buffer and 1 μ M [γ - 32 P]ATP or ATP were first mixed for 2 s before the addition of the chase. (O) Rates of hydrolysis of 3 μ M MF₁ in Mg buffer and 1 μ M preloaded, bound [γ - 32 P]ATP with 15 μ M chase ATP. The final concentrations in the chased reaction mixtures measured 1 μ M MF₁, 0.3 μ M [γ - 32 P]ATP, and 5 μ M cold chase ATP. (▲) Rates of hydrolysis of 15 μ M chase (promoter) [γ - 32 P]ATP with 3 μ M MF₁ in Mg buffer and 1 μ M preloaded ATP. The final concentrations in the chased reaction mixtures measured 1 μ M MF₁, 0.3 μ M ATP, and 5 μ M cold chase [γ - 32 P]ATP. The bold circle (●) shows the observation when the promoter ATP concentration was increased from 5 μ M to 3 mM. The unisite MF₁- 32 P complex was mixed with a large excess of nonradioactive MgATP (final concentration of 3 mM in the chase), and the reaction was allowed to proceed for 20 ms before injection into perchloric acid quench. By the next temporal assay point of 50 ms, almost complete hydrolysis (>95%) of [γ - 32 P]ATP had already occurred at 3 mM promoter ATP concentration. This data point is not plotted on the graph because complete hydrolysis could, in principle, have occurred at any time between 20 and 50 ms at 3 mM promoter [ATP].

results were obtained when 3 mM ATP is used as the chase when all the three catalytic sites of F₁ are expected to be occupied by bound nucleotide. Note that a super-stoichiometric concentration of promoter ATP is essential to ensure that the F₁-ATPase undergoes multiple cycles of rotation during the 10 s incubation time, given that a major objective of the work is to detect the rate enhancement (over unisite rates) that increases turnover to *V*_{max} when ATP is allowed to bind at multiple catalytic sites. However, complete (i.e., 100%) hydrolysis of the added ATP was not observed even with mM concentrations of the cold chase. Table 1 shows that when normal ATP is bound in the highest affinity site 1 (T) and

5–20 μM radioactive $[\gamma\text{-}^{32}\text{P}]\text{ATP}$ is used as the chase, 92%–94% of the promoter ATP is hydrolyzed in site 2 (L) in the same 10 s time period.

The aforementioned results were examined further by kinetic analysis, and the results are plotted in **Figure 1**. The 30% residual hydrolysis of preloaded $[\gamma\text{-}^{32}\text{P}]\text{ATP}$ at the end of the 2 s incubation period is plotted as the zero time value on the y-axis for the upper curve before the addition of chase ATP. The final concentrations in the chased reaction mixtures were 1 μM F_1 , 0.3 μM $[\gamma\text{-}^{32}\text{P}]\text{ATP}$, and 5 μM cold chase ATP (**Figure 1**). In the case of the lower curve, normal ATP was loaded in the highest affinity catalytic site, and $[\gamma\text{-}^{32}\text{P}]\text{ATP}$ was used as the chase (**Figure 1**). This enabled measurement of the rate and extent of the hydrolysis of chase ATP under the same conditions as for the upper curve. The features of the progress curve of hydrolysis of the chase ATP bound in site 2 (lower curve) are kinetically similar to those of the hydrolysis of ATP bound in the highest affinity catalytic site 1 (upper curve), as long as well-mixed conditions were ensured in the experiments. This observation requires separate interpretation and discussion (**Sections 3.2, 3.4**). Under the chosen experimental conditions and in the presence of rapid and efficient mixing of the solutions, both progress curves in **Figure 1** are well characterized by a first-order rate constant measuring 12–15 s^{-1} , given the experimental errors. Data on the rapid hydrolysis of $[\gamma\text{-}^{32}\text{P}]\text{ATP}$ in site 1 when promoter ATP concentration was increased from 5 μM to 3 mM are also shown in **Figure 1**.

3.2 Mechanistic implications

The results described in **Section 3.1** have several mechanistic implications for ATP hydrolysis by $\text{F}_1\text{-ATPase}$. **Bullough et al. (1987)** had previously performed experiments in which ATP bound in the highest affinity catalytic site of $\text{F}_1\text{-ATPase}$ appeared to hydrolyze severalfold slower than ATP added as a promoter. Based on these observations, the authors suggested that the highest affinity site 1 is not a normal catalytic site on F_1 (**Bullough et al., 1987**). However, we did not observe such a rate discrepancy between the two promotion experiments. The experimental results in **Table 1** and **Figure 1** show that the enzyme molecules undergoing single turnover events of slow “unsite” catalysis (on the order of 0.1 s^{-1}) are recruited into the “normal” catalytic pathway of $\text{F}_1\text{-ATPase}$ during rapid multisite V_{max} hydrolysis of at least 100 s^{-1} by the addition of excess ATP, and as a result, the unisite characteristics of F_1 are amalgamated. Furthermore, the bound ATP in site 1 is hydrolyzed during the chase at approximately the same rate as the chase ATP bound at a catalytic site with intermediate affinity and not at substantially lower rates as reported (**Bullough et al., 1987**). We estimate that ATP bound in the catalytic sites is hydrolyzed at V_{max} rates of $>100 \text{ s}^{-1}$ at promoter concentrations of 5 μM since the shortest residence time in our experiments is 20 ms. Under these conditions, 20% hydrolysis represents at least one enzyme turnover. Similar results were obtained when 3 mM ATP was used in the cold chase, except that the V_{max} rates were higher (**Figure 1**). In this experiment, the unisite $\text{MF}_1\text{-}^{32}\text{P}$ complex formed previously was mixed with a large excess of normal MgATP at a final concentration of 3 mM. The reaction was allowed to proceed

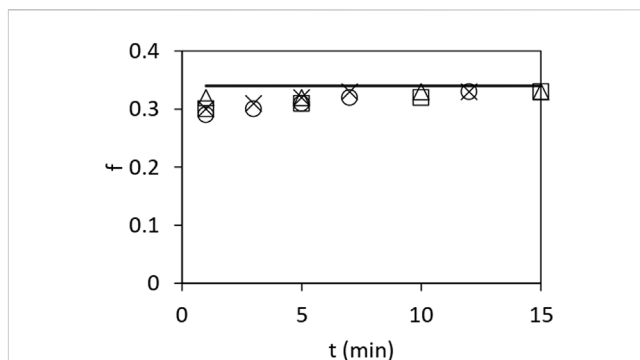


FIGURE 2

Fraction f of bound ^{32}Pi to total bound ^{32}P as a function of time after mixing mitochondrial F_1 and $[\gamma\text{-}^{32}\text{P}]\text{ATP}$. Enzyme and substrate concentrations of 0.5 μM each (□), 1 μM each (Δ), with 10% excess enzyme concentration over 0.5 μM substrate (○), and with 10% excess enzyme concentration over 1 μM substrate (×). The data are bounded from above by the bold horizontal line given by $f = 0.333$.

for 20 ms before quenching into perchloric acid. The promoted hydrolysis occurred very rapidly within this chase time period, as shown by the bold circle, and hydrolysis of $[\gamma\text{-}^{32}\text{P}]\text{ATP}$ was essentially complete by the next temporal measurement point of 50 ms. The results shown in **Table 1** and **Figure 1** raise a question: how do two different catalytic sites on the multisubunit F_1 enzyme that are spatially distant away from each other (and purportedly possess different affinities for binding ATP) hydrolyze ATP at approximately the same rates and with similar kinetics (the following paragraph and **Section 3.4**)?

The cold chase experimental results have an even more important biological implication: they show that two catalytic sites on F_1 (at different times) can hydrolyze ATP at the so-called highest affinity site 1 (T) (**Penefsky, 1985; García and Capaldi, 1998**) and at the intermediate affinity site 2 (L). This important conclusion arises from the analysis given the two progress curves/rows in **Figure 1** and **Table 1** of the hydrolysis of $[\gamma\text{-}^{32}\text{P}]\text{ATP}$ when preloaded in site 1 or when bound as a promoter in site 2. If the conformational change ($\sim 80^\circ$ rotation of the central γ -subunit of the enzyme) due to binding and subsequent hydrolysis of ATP at site 2 causes site 1 (T) to be converted to (a new) site 2 (L), then similar rates and extents of ATP hydrolysis in the two cases are also logically explained. In other words, the two sites are the same: both are L-sites (site 2). In other words, only site 2 can hydrolyze ATP and release products.

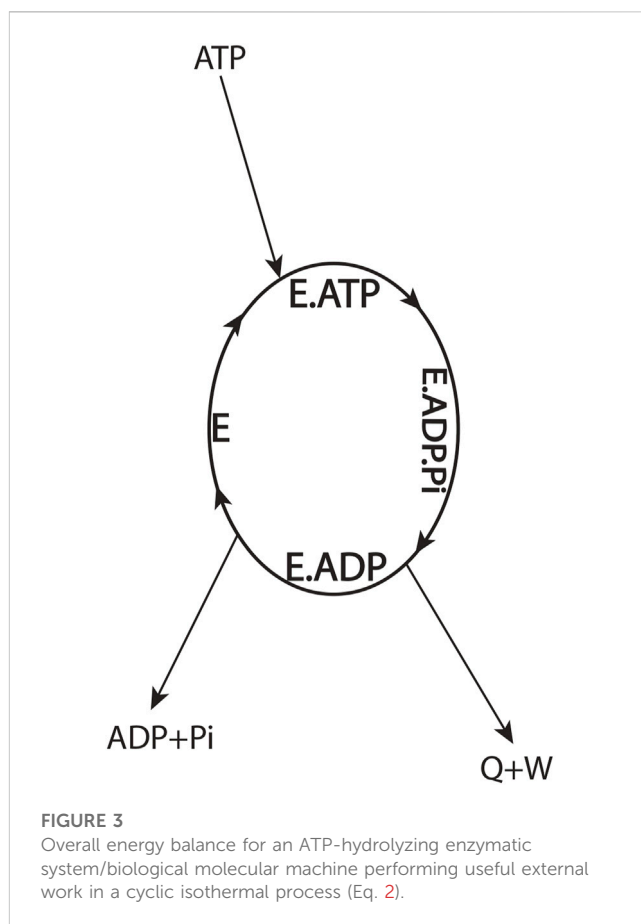
Figure 2 shows the ratio f of bound ^{32}Pi to total bound ^{32}P at two different concentrations of F_1 and $[\gamma\text{-}^{32}\text{P}]\text{ATP}$ and various incubation times from 1 to 15 min. This ratio was approximately constant at one-third under all conditions tested; i.e., the data shown in **Figure 2** are bounded from above by the line $f = 0.333$. Similar results were obtained when 10% excess F_1 over substrate was used. It should be clearly understood that the total bound ^{32}P includes both bound ^{32}Pi and bound $[\gamma\text{-}^{32}\text{P}]\text{ATP}$ species. The results can be either interpreted in terms of an equilibrium constant for reversible hydrolysis or explained equally well by a quasi-steady state constant for irreversible hydrolysis in which $f = 0.333$ remains constant for any mode of catalysis (e.g., trisite catalysis); i.e., f defines a characteristic kinetic property of the system.

In summary, it is not sufficient that the F_1 -ATPase simply binds ATP in site 2 (L); the enzyme needs to additionally hydrolyze the bound ATP (that had exchanged with ADP in site 2 (L)) (Nath, 2008) to ADP.Pi in site 2, after which Pi needs to leave site 2 (L) to induce rotation by the chase ATP. Thus, after bond cleavage due to ATP hydrolysis on the enzyme and the reduction in binding of Pi, it is the progressive moving away of the Pi from bound MgADP (Nath and Nath, 2009) in site 2 (L) and the firing of Pi into the solution to infinity that donates energy and is responsible for the rotation of γ , whereupon the L site changes to a closed (C) site. This primary clockwise rotation of the top of γ (viewed from the F_1 side) also changes the conformation of site 1 (T) to a new site 2 (L), after which the bound ATP hydrolyzes in the new site 2 (L) to ADP.Pi, and Pi subsequently leaves and donates energy for a further $\sim 40^\circ$ rotation, as described in great detail previously (Nath, 2008), and mathematically modeled using basic electrostatic principles (Nath and Nath, 2009) (Section 3.4). The new aspect is contained in the key insight that ATP hydrolysis and Pi release [not ATP binding as in previous theories of free energy transduction (Boyer et al., 1973; Boyer, 1993)] in site 2 are required to explain the chase promotion experiments because otherwise, no ^{32}P i counts should have been registered. This has major biological implications and permits us to formulate general physical principles for free energy transduction.

3.3 General physical principles of energy transduction and biochemical consequences: how does ATP perform useful external work?

According to the basic tenets of the binding change mechanism (Boyer et al., 1973; Boyer, 1993), the principal energy-releasing step in F_1 -ATPase, muscle contraction, and other processes utilizing ATP is the one accompanying ATP binding, with hydrolysis merely serving for release of ADP and Pi. The mechanism proposed that ATP binds very tightly in site 1 (T), with a very low dissociation constant K_d —vis-à-vis site 2 (L) such that ATP is differentially stabilized on the enzyme surface relative to ADP + Pi by ≥ 60 kJ/mol. Hence, the mechanism proposed that a catalytic site shows reversible ATP synthesis/hydrolysis with an equilibrium constant K_{eq} close to 1. Historically, these concepts have greatly influenced the interpretation of experimental measurements and catalytic mechanism in F_1 -ATPase and muscle myosin. However, are these concepts correct?

As discussed previously, a highly sequestered catalytic site was required as ATP synthesis is believed to occur with free reversal of ATP hydrolysis on the enzyme (Boyer, 1993). Earlier measurements of a K_d of 1 pM for catalytic site 1 (Penefsky, 1985) seemed apparently consistent with the aforementioned suggestion because, with a typical K_d value of $0.5 \mu\text{M}$ for site 2, this corresponded to a difference in the binding energy of $RT \ln \left(\frac{0.5 \times 10^{-6}}{1 \times 10^{-12}} \right) = 33.8$ kJ/mol, slightly less than the standard free energy change of ATP hydrolysis of ~ 36 kJ/mol under physiological conditions (Phillips et al., 1969; Rosing and Slater, 1972; Nath and Nath, 2009), though still greatly short of the complete thermodynamic ΔG of ~ 60 kJ/mol. However, the initial expectation of a sequestered site 1 was never met. Subsequent measurements using radioactive ATP and a hexokinase/glucose



trap gave a binding affinity value of K_d for catalytic site 1 of only 0.2 nM (Senior et al., 1992) for the *E. coli* F_1 , leading to a relative stability of enzyme-bound intermediates of $RT \ln \left(\frac{0.5 \times 10^{-6}}{0.2 \times 10^{-9}} \right) = 20.2$ kJ/mol only. This is a serious shortcoming of the theory (Boyer, 1993) because expected values of the differential stabilization are not validated by experimental measurements of the binding constants, and binding energy changes are insufficient in magnitude to perform the catalysis.

New technologically advanced experiments with various nucleotides also led to similar results (Weber and Senior, 2001). We have previously hailed these advancements in the direct measurement of catalytic site binding affinities and dissociation constants in F_1 -ATPase as an experimental breakthrough [p. 73 of Nath (2002)]. These measurements were made possible by developing a genetically engineered tryptophan probe β -Trp-331 inserted into the adenine-binding subdomain of the β -catalytic sites of *E. coli* F_1 -ATPase and optically monitoring its fluorescence during steady-state catalysis. For *E. coli* F_1 -ATPase for the physiologically important conditions of Mg^{2+} in excess over ATP, these new experiments yielded values of the dissociation constants for site 1 (T), site 2 (L), and site 3 (O) of 0.02 , 1.4 , and $23 \mu\text{M}$, respectively (Weber and Senior, 2001). This leads to a differential stabilization of MgATP in site 1 with respect to site 2 of $RT \ln \left(\frac{1.4 \times 10^{-6}}{0.02 \times 10^{-6}} \right) = 10.9$ kJ/mol only, which is in great shortfall of the expected stabilization. Experiments with MgITP using the optical probes gave similar values for the differential stabilization of the Mg-nucleotide between sites 1 and 2. However, ATP is readily synthesized at

V_{\max} rates using MgITP (Weber and Senior, 2001). We consider these the best measurements of binding affinities in F_1 catalytic sites to date. We conclude that binding energy changes are energetically not competent to carry out ATP synthesis/hydrolysis in F_1 as per the tenets of the binding change mechanism (Boyer et al., 1973; Boyer, 1993).

To better understand the thermodynamic aspects of the aforementioned conundrum, let us define the F_1 -ATPase or the molecular motor as the system by drawing a system boundary about the ellipse (Figure 3) and carry out an overall energy balance. For the cyclic, isothermal process mediated by the enzyme depicted by the ellipse, all thermodynamic property changes are necessarily zero. From inspection of such a diagram, we notice that binding energy changes, such as those that occur during the $E + ATP \rightarrow E \cdot ATP$ elementary binding step, are internal to the system boundary. A general statement of the first law of thermodynamics for steady-state open systems (Figure 3) is given by the following equation, written in terms of enthalpy H as follows:

$$H_{ATP} - H_{ADP} - H_{Pi} = Q + W, \quad (2)$$

where the enthalpies of the species H_i can be replaced by their internal energies U_i if the PV work is negligible. The equation can also be written in terms of Gibbs energies G_i instead of the enthalpies, with due consideration for the nonequilibrium nature of the process or in terms of the chemical potentials μ_i (Section 3.5 of Nath (2003)). As free ATP enters the system boundary in Figure 3 and free ADP and P_i leave it, Eq. 2 shows that the difference between the enthalpies or internal/electrostatic free energies of ATP and (ADP + P_i) must equal the heat released from the system Q plus work performed by the system W or equal W if heat losses are neglected.

One can argue that the first law of thermodynamics can be saved by redistribution of the overall enthalpy change from the $ATP \rightarrow ADP + P_i$ couple (Eq. 2) among the binding steps internal to the system boundary (Figure 3) to obtain $Q + W$. Unfortunately, the magnitude of the stabilization obtained upon redistribution of the binding state energies (only ~ 10 kJ/mol) falls well short of the expected values, as shown previously. Hence, the binding energy released upon ATP binding to a catalytic site in F_1 -ATPase is insufficient for performance of the proposed magnitude of useful external work. Nath's torsional mechanism of energy transduction and ATP synthesis/hydrolysis (Nath, 2008; Nath and Nath, 2009; Mehta et al., 2020) offers a resolution of the aforementioned conundrum.

According to a basic tenet of the torsional mechanism, the energy employed for the performance of useful external work in a cyclic isothermal process must have been locked in the ATP molecule (as electrostatic potential) relative to (ADP + P_i) (Nath and Nath, 2009). The enzyme/motor serves as a key to unlocking this stored energy by the elementary step of ATP hydrolysis, and two negatively charged cleavage products (ADP and P_i) are generated. However, the electrostatic energy of these charges remains stored as potential energy, and, only after the binding of one of them (typically P_i) to the enzyme is reduced, thereby allowing the P_i to move away from bound ADP, is this potential energy made available for the performance of useful external work. Hence, only upon product P_i release can the Coulombic repulsion energy or stored potential energy of the

two charges be harnessed for performing useful work. Typically, this electrostatic potential energy needs to be stored (e.g., as torsional energy or twist or as elastic strain in general) (Nath, 2008; Nath and Nath, 2009) in a region of the protein molecule by conformational changes. The protein then does useful work as it returns to its original conformation, rebinds ATP, and undergoes repeated cycles of free energy transduction.

The aforementioned general principle of energy transduction also explains why non-hydrolyzable analogs of ATP cannot perform useful external work. This primarily arises because the free energy available by reversal of the conformational change due to the binding of the ATP analog is used for the release of the bound analog. Hence, it cannot perform useful mechanical work. However, in the case of ATP hydrolysis, the products ADP and P_i are more stable in solution (relative to free ATP in solution; see Figure 3) and do not recombine. Therefore, such a reversal of the change in protein conformation is not required to release bound nucleotide. Hence, the protein conformational change can do useful work using the $ATP \rightarrow ADP + P_i$ couple.

In summary, the general physical principle emerges that the electrostatic free energy is released when ATP's terminal P_{β} -O- P_{γ} bond (γ -phosphorus-oxygen anhydride bond) is cleaved, the binding of P_i to the catalytic site is reduced, and the P_i allowed to move away to infinity from bound ADP; this energy can be used for the performance of useful work by F_1 and by biological systems in general (Eq. 2; Figure 3).

Other differences between the binding change mechanism and the torsional mechanism have been discussed previously (Nath, 2008; Nath, 2003, and Table 1 therein). General physical principles in the membrane-bound F_0 portion of the ATP synthase of biochemically clean reconstituted enzyme systems and during physiological steady-state ATP synthesis, such as the inviolability of electroneutrality and differences with the chemiosmotic theory (Mitchell, 1966; Mitchell, 1969; Mitchell, 1981), have been covered in earlier publications (Nath, 2010b; Nath, 2017; Nath, 2018a; Nath, 2021a; Nath, 2022a; Jain et al., 2004; Agarwal, 2011; Channakeshava, 2011; Villadsen et al., 2011; Wray, 2015; Levy and Calvert, 2021; Juretić, 2022).

3.4 Detailed molecular mechanism of ATP hydrolysis by F_1 -ATPase consistent with the biochemical observations and the physical laws

The detailed molecular mechanism of V_{\max} ATP hydrolysis by F_1 -ATPase (Nath, 2008) can now be refined to make it consistent with our experimental observations in Section 3.1 and the mechanistic implications and physical principles of biological energy transduction determined in Sections 3.2 and 3.3. Such a mechanism is illustrated in Figure 4.

The molecular mechanism of ATP hydrolysis by F_1 -ATPase (Figure 4) incorporates a key result arising from this experimental study that it is not sufficient to exchange bound ADP in the catalytic site 2 (L) with medium ATP to activate the enzyme and cause an $\sim 80^\circ$ primary rotation of the central γ -subunit (in a clockwise sense when viewed from the F_1 side) in F_1 . The enzyme also needs to hydrolyze the bound ATP in site 2 (L) (exchanged with ADP in the catalytic site) to

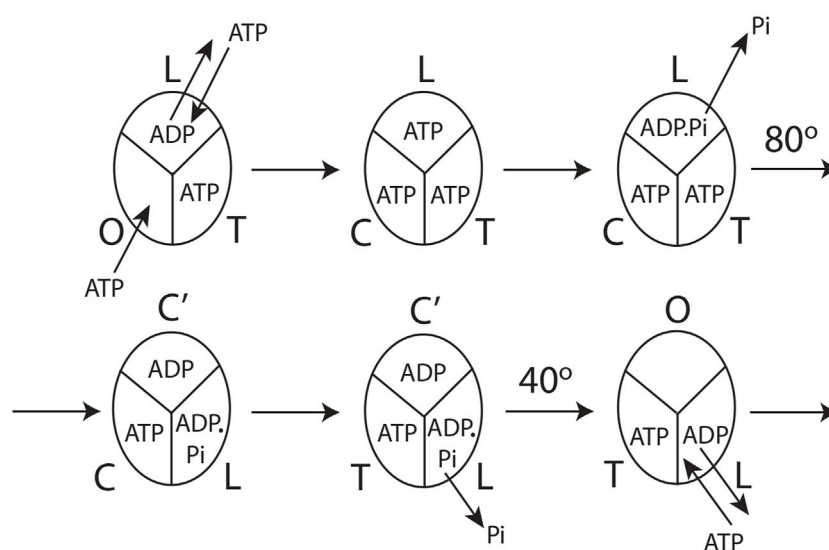


FIGURE 4

Model for steady-state multisite hydrolysis of ATP by F_1 -ATPase based on experimental data and Nath's torsional mechanism of ATP synthesis/hydrolysis and the unified theory (Nath, 2002; Nath, 2008; Nath and Nath, 2009; Wray, 2015; Mehta et al., 2020). The three β -catalytic sites of the *Escherichia coli* enzyme or the enzyme from thermophilic bacterium are depicted. The system is viewed from the F_1 side. T represents the catalytic site of highest affinity for MgATP (site 1); L represents the catalytic site of intermediate affinity (site 2); O represents the site of lowest affinity (site 3); C' stands for the conformation adopted by a closed catalytic site (which could even be half-closed, i.e., C) relative to the open (O) site. The diagram is drawn to represent steady-state V_{max} hydrolysis at high (\sim mM) concentrations of ATP, i.e., when there is sufficient ATP to fill all three catalytic sites before the rotation of the top of the γ -subunit. The diagram can be easily adapted to a possible scenario at intermediate (micromolar) concentrations of ATP when site 3 is filled after the 80° rotation of γ_{top} , already described cogently (Nath, 2008), or, for that matter, at any instant of time during or after activation of the 80° rotary step of γ_{top} by elementary chemical events occurring in site 2. However, site 3 can only adopt a completely closed conformation or tight (T) conformation after the occurrence of the ATP cleavage reaction step in (the new) site 2 upon undergoing a site 1 to site 2 (T \rightarrow L) transition due to 80° rotation of γ_{top} , and after the ϵ -subunit has rotated clockwise and its interactions with site 3 (O) have been broken, as explained by Nath (2008). The model is described in detail in Section 3.4.

ADP.Pi. Subsequently, Pi needs to move away and be released from L, as explained in detail in Section 3.3. Hence, a revision of our previous mechanism (Nath, 2008) to include the aforementioned fact is necessary. The exchange of bound MgATP for MgADP in site 2 releases an excess binding energy of 9 kJ/mol in the *E. coli* F_1 -ATPase, i.e., the difference between the binding energy of MgATP in L (36 kJ/mol) and the binding energy of MgADP in L (27 kJ/mol). This 9 kJ/mol energy released weakens the binding of bound Pi formed upon ATP hydrolysis in site 2 to approximately zero (i.e., cleavage of the terminal bond of ATP originally at a bond distance of 0.3 nm (Nath and Nath, 2009)). The effect of ejecting ADP with a certain velocity helps break the \sim 9 kJ/mol γ - β_{TP} interactions between γ and site 2. Now, the γ -subunit is free to rotate, and Pi is free to move away from bound MgADP (Section 3.3). As Pi moves stepwise from 0.3 to 0.4 and then to 0.6 nm (Nath and Nath, 2009), it releases a Coulombic repulsion energy of $9 + 9 = 18$ kJ/mol. Another 18 kJ/mol is made available as Pi is fired out from 0.6 nm to ∞ and released into the solution. This 36 kJ/mol electrostatic potential energy rotates the top of the γ -subunit by $\sim 80^\circ$ relative to the stationary β -subunits with an average torque measuring ~ 40 pN nm generated at the β - γ interface at a radial distance of approximately 1 nm from the central axis of the $\alpha_3\beta_3$ hexamer (Figure 4).

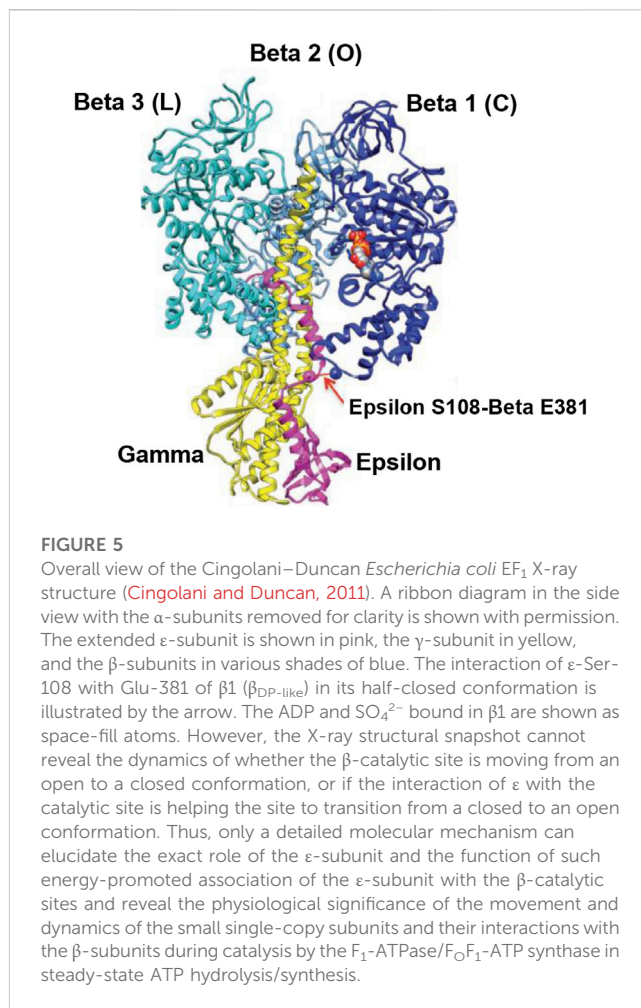
After initiation of the 80° rotation of the top of γ , site 2 (L) changes to a closed conformation C'. Upon the above 80° rotation, the top of γ interacts with the β -catalytic site 1 [T or β_{DP} -like in Nath (2008)] and alters its conformation to loose [i.e., site 2, L or

β_{TP} in Nath (2008)]. In other words, the rotation of γ_{top} causes a T \rightarrow L transition of the β -catalytic site, due to which a ~ 9 kJ/mol destabilization (reduction in the binding energy of intermediate bound in the site) occurs. Concomitantly, ATP hydrolyzes to ADP.Pi upon the T \rightarrow L transition of the catalytic site. Pi, which is bound to L with ~ 9 kJ/mol binding energy, is now bound in L with \sim zero binding energy and is, therefore, free to move away. The 0.3 \rightarrow 0.4 \rightarrow 0.6 nm movement of Pi away from bound ADP releases ~ 18 kJ/mol, which is transmitted from site 2 to site 3 (O or β_E) along the ϵ -helix and helps break the ϵ - β_E interaction (e.g., between ϵ -Ser-108 and β_E -Glu-381 in the DELSEED loop) (Nath, 2002) along with the ~ 27 kJ/mol binding energy of MgATP in site 3 (O or β_E), as already described in detail by Nath (2008). The open site O or β_E closes due to these interactions and relieves the steric hindrance that the open site offered to further rotation of the γ -subunit (beyond 80°). If MgATP does not bind to site 3 or only free ATP is present in the external/crystallization medium, then the ATP only binds weakly to site 3, which, therefore, retains its open conformation. The torsional strain in the γ -subunit helps break the ϵ -Ser-108- β_E and ϵ -Met-138- β_{TP} interactions and hence the bottom of the γ -subunit and the ϵ -subunit rotate 80° clockwise about the central axis of $\alpha_3\beta_3$, as viewed from the F_1 side (Figure 4). Concomitantly, O \rightarrow T. The two coiled-coil α -helices of the γ -subunit are unwound, thereby relieving the torsional strain. After the 80° rotation of γ - ϵ is complete, Pi release from the new L (β_{TP}) and its movement

from 0.6 nm away from ADP to infinity provides the energy for the remaining 40° rotation of the γ - and ϵ -subunits. Upon this rotation, the interaction of ϵ with C' changes its conformation to an O-site (open, site 3, the site with lowest affinity for Mg-nucleotide) from which bound MgADP is released. During steady-state V_{\max} hydrolysis, the order of conformations that a single catalytic site of F_1 -ATPase passes through is O \rightarrow T, T \rightarrow L, L \rightarrow C', and C' \rightarrow O. Looking at the enzyme as a whole, the order of the conformational changes of the catalytic sites during multi-site hydrolysis by F_1 -ATPase is L \rightarrow C', followed by T \rightarrow L, followed by O \rightarrow T, and lastly, C' \rightarrow O, which is in accordance with our previous predictions and shown to be the microscopic reversal of the ATP synthesis cycle (Nath, 2008). The cycle (Figure 4) then repeats; other details are given by Nath (2008).

The catalytic cycle for the steady-state V_{\max} hydrolysis depicted in Figure 4 is in accordance with biochemical crosslinking studies. These studies inferred from the data that the rotation of the γ - and ϵ -subunits in *E. coli* F_1 -ATPase is not linked to unisite hydrolysis of ATP at the highest affinity catalytic site 1 (T) but to ATP binding and/or ATP hydrolysis and product release at the second or third catalytic site on the enzyme (i.e., site 2 or 3) (García and Capaldi, 1998). The studies also showed that the effect of covalently crosslinking β -Cys-381 to γ -Cys-87 (i.e., forming the β - γ crosslink) increased the rate of unisite catalysis to that obtained by the cold chase of ATP of the non-crosslinked enzyme (Section 3.1). As β - γ in the biochemical crosslinking studies corresponds to β_{TP} in the X-ray structure of the enzyme in the Mg-inhibited state (Abrahams et al., 1994), we infer that β_{TP} (site 2 or L) is the catalytic site to which ATP binds (in which it subsequently hydrolyzes; see Section 3.2) in the native non-crosslinked enzyme. These events are responsible for rotating γ by 80°, changing the conformation of site 1 to site 2, and causing hydrolysis of the bound ATP in the (new) site 2, as shown in Figure 4.

The molecular mechanism shown in Figure 4 also satisfies the fact that V_{\max} ATP hydrolysis follows trisite catalysis (Weber and Senior, 2001; Nath, 2002; Nath, 2003), a fact experimentally proven today. This by itself takes it beyond the binding change mechanism, which was necessarily a bisite model (Boyer, 1993). However, over the past 2 decades (Weber and Senior, 1997; Wang and Oster, 1998) and up to the present day (Nakano et al., 2022), ATP binding to site 3 (O) has been repeatedly postulated to cause rotation in F_1 -ATPase. We have pointed out previously that the O-site (site 3) is open and distorted, and the binding energy of MgATP is only 27 kJ/mol (Nath, 2008), which is grossly insufficient energetically to change the conformation of the catalytic site from O to closed (C) and also cause a primary rotation of the γ - and ϵ -subunits by 80° (Nath, 2008). Above all, as proved in Section 3.3, the ATP binding step is not fully competent to perform the useful work of rotation in the enzyme/molecular machine (Figure 3). It should also be stressed that the detailed mechanism of steady-state multisite ATP hydrolysis by F_1 -ATPase presented here (Section 3.4, Figure 4) is the microscopic reverse of the molecular mechanism of steady-state ATP synthesis by F_0F_1 -ATP synthase formulated by us in previous publications (Nath, 2002; Nath, 2008; Mehta et al., 2020). The difficult constraint of microscopic reversibility has not been shown to be satisfied by other mechanisms. For these compelling reasons, we consider the mechanism shown in Figure 4 superior to extant mechanisms in the field.



4 Discussion

The detailed molecular mechanism shown in Figure 4 and discussed in Section 3.4 was not the result of the application of standard structural or biochemical techniques. It was realized based on a sound knowledge of molecular mechanics (Nath, 2003), protein science and bioinformatics (Nath, 2008), and a unique molecular systems approach (Nath, 2002; Nath, 2006a) developed by creative integration of concepts from physics (Nath, 2017; Nath, 2018c; Nath, 2019a; Nath, 2019b; Nath, 2019c; Nath, 2021a), chemistry (Nath and Nath, 2009; Nath, 2018a; Nath, 2018b; Mehta et al., 2020), biochemistry (Nath, 2010a; Nath, 2010b; Nath and Elangovan, 2011; Nath and Villadsen, 2015; Nath, 2016; Nath, 2020a), biology (Nath, 2020b; Nath, 2022b), physiology (Nath, 2022a), biophysics (Nath, 2021b; Nath, 2021c), pharmacology (Nath, 2022c), pure mathematics (Nath, 2022d), economics (Nath, 2019d), engineering (Nath et al., 1999; Nath, 2002; Nath, 2003), and medicine (Nath, 2019e) spanning 3 decades of research by the author. For perspectives on this approach by other researchers, see Channakeshava (2011), Villadsen et al. (2011), Wray (2015), and Juretić (2022). For a summary of the author's innovative approach to discovery, see Nath (2006b). However, it is possible to embellish Figure 4 with molecular snapshots from high-resolution X-ray structures (Cingolani and Duncan, 2011; Shirakihara et al., 2015) that were solved several years after the aforementioned molecular interactions of ϵ -Ser-108 with β_E -Glu-381 (Nath, 2002; Nath,

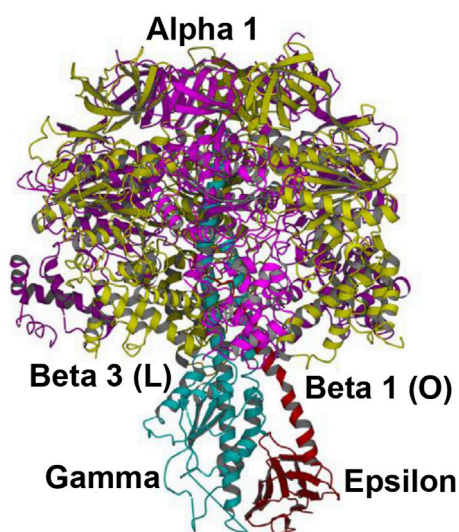


FIGURE 6

Overall view of the Shirakihara TF₁ X-ray structure from a thermophilic bacterium (Shirakihara et al., 2015) in side view, drawn with permission. The ϵ -subunit in its extended conformation is shown in red, the γ -subunit in blue, and the β -subunits β_1 and β_3 in gold. An intervening α -subunit is shown in magenta. The penetrating C-terminal helix of the ϵ -subunit into the $\alpha_3\beta_3$ cavity and its interactions with the β -catalytic sites are shown.

2008) and ϵ -Met-138 with β_{TP} (Nath, 2008), along with their functional roles during catalysis, were postulated.

4.1 Structural interpretations and relationship to the F₁-ATPase catalytic cycle

The overall high-resolution X-ray structures of *E. coli* F₁ (Cingolani–Duncan EF₁ structure, 3OAA) (Cingolani and Duncan, 2011) and of F₁ from a thermophilic bacterium (Shirakihara TF₁ structure, 4XD7) (Shirakihara et al., 2015) are shown in side view as ribbon diagrams in Figure 5 and Figure 6, respectively. The overview of the structures (Cingolani and Duncan, 2011; Shirakihara et al., 2015) in Figures 5 and 6 clearly reveals the interactions of ϵ -Ser-108 with β_E -Glu-381 and of the tip of epsilon ϵ -Met-138 with β_{TP} (Nath, 2008) postulated by Nath's torsional mechanism of ATP synthesis/hydrolysis as previously (Nath, 2002; Nath, 2008), diagrammed in Figure 4, and described in Section 3.4. The following features of the X-ray crystal structures can be related to the detailed mechanism of ATP hydrolysis by F₁-ATPase.

4.1.1 Cingolani–Duncan EF₁ structure (Cingolani and Duncan, 2011)

The overall EF₁ structure shows a highly extended conformation of the ϵ -subunit (pink) that inserts into the central cavity and interacts with two of the three β -catalytic sites, designated as β_1 , β_2 , and β_3 (various shades of blue) (Figure 5). The β_2 catalytic site is open and contains no bound nucleotide. It does not interact with the C-terminal of the ϵ -subunit and corresponds to O (β_E) in panel 1 of Figure 4. The site has not closed or changed its conformation to T (panels 5, 6 in Figure 4),

although ϵ has moved away clockwise (looking from the F₁-side) because the nucleotide has not bound to the catalytic site.

The catalytic site β_1 adopts a half-closed conformation and contains bound ADP (and SO₄²⁻). ϵ -Ser-108 interacts with β_1 -Glu-381, as shown in Figure 5 and visualized by the X-ray structure in the close-up view of Figure 7A. The β_1 -site is akin to β_{DP} (Nath, 2008) or C' (closed) in Figure 4, also labeled as C in Figure 5 [half-closed with reference to the open site O; note that half-closed, three-fourths closed, etc. mean closed with respect to O in a continuum of conformations (Nath, 2002), of which a frozen snapshot has been captured by the structure]. The N-terminal of the ϵ -subunit has rotated clockwise from β_2 , and its C-terminal has started to interact with β_1 ; however, β_1 has not yet fully opened due to these interactions. Thus, the site has not yet been converted to O (site 3).

Figure 5 visualizes the interactions of the ϵ -hook with β_3 , and Figure 7B depicts these interactions in detail, as seen in the Cingolani–Duncan EF₁ structure (Cingolani and Duncan, 2011), including the interactions of the helix tip ending in ϵ -Met-138 with β_{TP} (L) postulated previously (Nath, 2008) and discussed in Section 3.4. β_3 adopts a closed conformation but contains no bound nucleotide (ADP). The catalytic site β_3 is akin to β_{TP} or L in panel 6 of Figure 4 after hydrolysis and release of Pi. The X-ray structure (Cingolani and Duncan, 2011) is a snapshot before ϵ -hook has broken its interactions with β_3 (L or site 2) and rotated clockwise (looking from F₁) toward β_2 (Section 3.4). In that sense, it has not “rotated farthest in the direction of ATP hydrolysis,” as previously postulated (Cingolani and Duncan, 2011). This conclusion is also validated by the fact that β_1 has not yet adopted an open conformation in the structure as noted previously, and as expected in our interpretation, if the structure had rotated farthest in the ATP hydrolysis direction and had therefore corresponded exactly to the 0°/120° ATP-waiting state.

Finally, single-molecule rotational studies on various F₁ species (Kato et al., 1997; Konno et al., 2006; Watanabe et al., 2015) have revealed that the presence of the ϵ -subunit arrests the ATPase cycle at the catalytic dwell angle of ~80°, which contradicts the assignment of the structure (Cingolani and Duncan, 2011) as depicting an ATP-waiting dwell state of 0°/120°. A possible reason for this discrepancy could be that the assignment was primarily based on structural alignment by a γ -core method that employed 99 Ca atoms (Shah et al., 2013). However, such assignment is dependent on the choice of the number and distribution of amino acid residues in the γ -subunit. In particular, residues at the bottom of the γ -subunit in structures of F₁ display considerable angular play. One must be careful before making a unique superposition, as also pointed out by the group that solved the X-ray structures (Rees et al., 2012).

Thus, the crystal structure captures a state of the F₁-ATPase closer to (but not exactly at) the 0° (or rather 120°) ATP-binding dwell than the three-nucleotide filled Leslie–Walker structure, 1H8E (Menz et al., 2001) that traps a post-hydrolysis, pre-product release conformation at $\theta \sim 80^\circ$ (Nath, 2008).

4.1.2 Shirakihara TF₁ Bacillus PS3 structure (Shirakihara et al., 2015)

This high-resolution thermophilic TF₁ Bacillus PS3 X-ray crystal structure (Shirakihara et al., 2015) (Figure 6) is even closer to the 0° (or 120°) ATP-binding dwell state compared to the Cingolani–Duncan

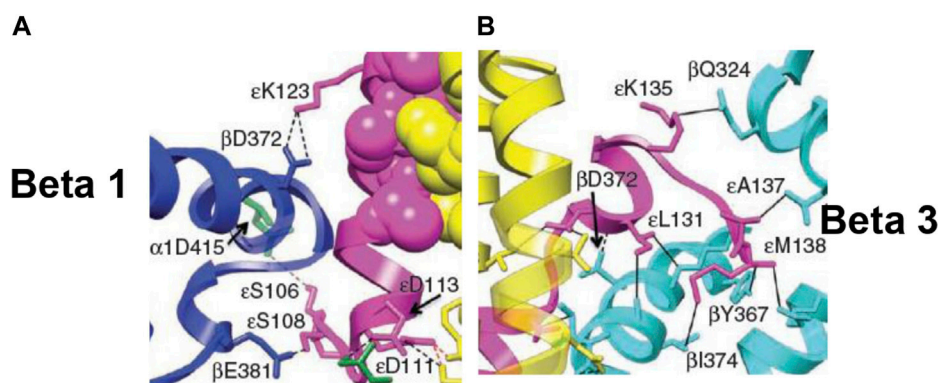


FIGURE 7

Snapshots from the X-ray structure of EF₁ (Cingolani and Duncan, 2011), revealing, close-up, the interactions of the ϵ -subunit with the β -catalytic sites inside the $\alpha_3\beta_3$ cavity, shown with permission. (A) The interactions of the C-terminal domain of the ϵ -subunit with β_1 ($\beta_{DP-like}$), especially of ϵ -Ser-108 with β_1 -Glu-381 [predicted previously by Nath (2002)], are highlighted. (B) The interactions of the helix 1-loop-helix 2 motif of the C-terminal domain of the ϵ -subunit with β_3 (β_{TP}), especially of the tip of the hook region ending in ϵ -Met-138 with the nucleotide-binding pocket in β_3 [predicted previously by Nath (2008)], are highlighted. Similar interactions of the ϵ -subunit with β_1 ($\beta_{DP-like}$) and β_3 (β_{TP}) are seen in the X-ray structure of TF₁ (Shirakihara et al., 2015).

structure. The site β_2 is as described in Section 4.1.1. As to β_1 , unlike in the Cingolani–Duncan EF₁ structure (Cingolani and Duncan, 2011), β_1 adopts an open conformation (O) with no bound nucleotide. The N-terminal of the ϵ -subunit has rotated clockwise from β_2 (viewed from F₁) and lies close to the β_1 -catalytic site. The ϵ -Ser-108 interacts strongly with DELSEED of β_1 . Thus, the closed site here has been converted to O by the interaction of the C-terminal of ϵ with β_1 (Nath, 2002; Nath, 2008). The remaining aspects are described in Section 4.1.1. The TF₁ β_3 contains bound ADP, adopts a closed conformation, as after Pi release, and is analogous to L or β_{TP} (Figure 4, Section 3.4). The ϵ -C-terminal residues 125–130 interact strongly with β_3 (Shirakihara et al., 2015).

The overall state of the enzyme is like panel 6 in Figure 4, except that T is open as the nucleotide has not bound to it. Thus, this structure is the closest among the solved high-resolution X-ray structures to the true resting/ground state of the enzyme (Section 3.4).

4.1.3 The Leslie–Walker MF₁ structure (Menz et al., 2001)

As explained previously (Nath, 2008), the 1H8E Leslie–Walker structure (Menz et al., 2001) with nucleotide bound in all three catalytic sites captures a metastable post-hydrolysis, pre-product release state of the mitochondrial MF₁, trapped at an angular position of $\sim 80^\circ$. It should be noted that the half-closed site (i.e., closed with respect to the open β_E (O) site in the 1BMF MF₁ structure (Abrahams et al., 1994)) had been anticipated several years earlier by Nath et al. (2000) and Nath and Jain (2000) before the Leslie–Walker structure (Menz et al., 2001) revealed the existence of such a closed conformation, reviewed by Nath (2002) and Wray (2015) and communicated personally to this effect by Dr. Andrew Leslie to the author (Leslie, 2006).

4.1.4 The Sobti et al. Cryo-EM structures (Sobti et al., 2016; Sobti et al., 2019)

The aforementioned views are corroborated by the recent moderate-resolution cryo-EM structures of Sobti et al. (2016) and Sobti et al.

(2019). Their structure of detergent-solubilized *E. coli* ATP synthase at the $0^\circ/120^\circ$ ATP-waiting dwell in the absence of added nucleotides or Pi (Sobti et al., 2016) revealed a conformation of the β -catalytic sites, very similar to that observed in the Shirakihara *Bacillus* PS3 structure (Shirakihara et al., 2015). In particular, the structure showed a highly extended conformation of ϵ and an open conformation of β_1 without bound MgADP or Pi, as in Shirakihara et al. (2015) and unlike Cingolani and Duncan (2011). The important point is that the mechanism proposed in Figure 4 after a C'-site has converted to an O-site (panel 6) is consistent with the observation of an open β_1 site in the cryo-EM structure of Sobti et al. (2016) at the $0^\circ/120^\circ$ ATP-waiting dwell.

The addition of mM MgATP to the *E. coli* F₀F₁ ATP synthase enzyme led to major changes in the site conformations at the $0^\circ/120^\circ$ ATP-waiting dwell visualized in a subsequent cryo-EM structure (Sobti et al., 2019). Now, all three β -catalytic sites contained bound nucleotide, the second helix of the ϵ -subunit at its C-terminal showed an intermediate half-up state, and above all, the site β_1 adopted a closed conformation. The mechanism in Figure 4 and Section 3.4 is consistent with these observations; see panels 1–2/3 containing the O to C transition of a catalytic site before the 80° rotational sub-step of γ .

4.1.5 Difficulties with previous mechanistic interpretations and consistency of the interpretations of Nath's torsional mechanism of ATP synthesis/hydrolysis with structural and biochemical observations

A major difficulty with the mechanistic interpretations of Cingolani and Duncan (2011) and Shirakihara et al. (2015) lies in the fact that they consider the ϵ - β interactions as inhibiting or preventing the conformational changes of the catalytic sites β_1 and β_3 . This view can be justified if rotation is blocked from occurring in F₀F₁. However, in our interpretation, for function with its driving force (i.e., in the presence of ion gradients during ATP synthesis or ATP during hydrolysis by F₀F₁-ATPase/F₁-ATPase), the dynamic movement of the ϵ -subunit and its interactions with β_1 and

$\beta 3$ enable the finely tuned β -conformational changes in the process of ATP hydrolysis. The energy transmission required for continued rotation and the progression of the catalytic cycle is funneled to the β -catalytic sites *via* the minor single copy γ - and ϵ -subunit interactions (Figure 4). Hence, we considered them minor subunits with major roles in catalysis by F_1 -ATPase.

In summary, the large-scale movements of the γ - and ϵ -subunits described previously are of physiological relevance to ATP hydrolysis/synthesis. These conformational changes of the single copy γ - and ϵ -subunits and their interactions with the β -catalytic sites reflect functionally distinct intermediate states that are absolutely essential for catalysis by F_1 -ATPase.

Other difficulties exist. The Cingolani–Duncan mechanism requires the dissociation of MgADP and Pi and postulates a rotation of γ by $\sim 40^\circ$ before the C-terminal helix 2 of the ϵ -subunit can switch from its highly extended state and escape from its inserted position in the central cavity (Cingolani and Duncan, 2011). However, an open conformation of $\beta 1$ without bound nucleotides is observed at this position in the structures of Shirakihara et al. (2015) and Sobti et al. (2016), and the aforementioned interpretation and mechanism are belied by the observation of a closed $\beta 1$ with bound ADP and sulfate (Cingolani and Duncan, 2011). The molecular mechanism of Figure 4 and the proposals within Nath's torsional mechanism of energy transduction and ATP synthesis/hydrolysis satisfy the requirement of a rotational sub-step—different from the $\sim 40^\circ$ sub-step—for the transition of ϵ from its fully extended to its half-up/down state.

The torsional mechanism is also consistent with the rotational data obtained from single-molecule recordings (Kato et al., 1997; Konno et al., 2006; Watanabe et al., 2015) that the presence of the ϵ -subunit pauses the F_1 -ATPase at the 80° catalytic dwell angle. This fact is difficult to reconcile with previous mechanistic interpretations (Cingolani and Duncan, 2011).

The known non-competitive behavior of ATP *vis-à-vis* ϵ in *E. coli* F_1 -ATPase (Sternweis and Smith, 1980; Weber et al., 1999) imposes another difficult constraint, which is not addressed/supported by previous proposals (Cingolani and Duncan, 2011). Since the extended-up state of the ϵ -subunit is only observed in the absence of ATP, the implication suggests that nucleotide binding to an alternate catalytic site is required to release the extreme C-terminal domain of the ϵ -subunit. However, MgATP binding to the site/s *per se* cannot relieve the so-called inhibition by the ϵ -subunit and release the subunit to its half-up/down conformation, in which rotation is permitted, to account for the non-competitive nature of the process. The molecular mechanism shown in Figure 4 and Section 3.4 that incorporates key elements of the proposals of the torsional mechanism (Nath, 2008; Nath and Nath, 2009) is miraculously able to satisfy these very difficult enzymological constraints.

The interpretation of Shirakihara et al.'s (2015) structure, i.e., that functional rotation can be achieved with the C-terminal domain of ϵ remaining in its extended-up state, is contradicted by the observation of the half-up mobile state of the ϵ -subunit in the cryo-EM structure of Sobti et al. (2019) in the presence of excess MgATP. The presence of the mobile, almost horizontal helix 2 in an intermediate half-up state of the ϵ -subunit in which rotation is possible in the enzyme—without the necessity for the ϵ -subunit to

adopt a completely down compact state in which helix 2 is neatly packed between helix 1 and the N-terminal domain of ϵ —is also consistent with trypsin cleavage studies (Mendel-Hartvig and Capaldi, 1991; Wilkens and Capaldi, 1998), as explained previously (Cingolani and Duncan, 2011). This half-up conformation of ϵ would allow cleavage by trypsin of the exposed ϵ -helix 2 while keeping its helix 1 anchored to the γ -subunit and permits ϵ -Ser-108 in the intervening loop between the two ϵ -helices to interact with the DELSEED of $\beta 1$ during functional rotation. The C-terminal helix 2 of ϵ can re-insert itself into the central cavity and interact with site 1 (T) in a subsequent step before it changes its conformation to site 2 (L), as explained by the torsional mechanism (Section 3.4).

This is not to say that the cryo-EM structures have led to the correct or definitive molecular mechanism of ATP hydrolysis or have always provided meaningful mechanistic insights. In their most recent cryo-EM study, Sobti et al. (2021) performed a snapshot analysis on a slowly hydrolyzing $\beta E190D$ mutant from the thermophilic bacterium *Bacillus* PS3 ATP synthase under different experimental conditions. However, the authors proposed a considerably different model of rotation in which ATP binding drives the initial 80° rotation and ATP hydrolysis drives the subsequent 40° rotation in F_1 -ATPase. Based on the present biochemical results and our previous work on the torsional mechanism (Nath et al., 1999; Nath et al., 2000; Nath and Jain, 2000; Nath, 2002; Nath, 2003; Nath, 2008; Nath and Nath, 2009; Mehta et al., 2020; Nath, 2021a), we consider the molecular mechanism depicted in Figure 4 and discussed in Section 3.4 to be the right mechanism of steady-state ATP hydrolysis by F_1 -ATPase.

4.2 Biochemical consequences

4.2.1 Angular positions of ATP binding, ATP cleavage, Pi release, and ADP release in F_1 -ATPase

The molecular mechanism of ATP hydrolysis by F_1 -ATPase formulated here has several important biochemical consequences. Looking at a single catalytic site, MgATP binds to O (site 3 or β_E) at 0° , which becomes T (site 1 or $\beta_{DP-like}$) (Nath, 2008) after the ϵ -subunit moves away during the $0 \rightarrow 120^\circ$ rotation of γ - ϵ . The bound MgATP is hydrolyzed at 200° due to the conformational change from $\beta_{DP-like}$ to β_{TP} (site 2), owing to a T \rightarrow L transition of the site. Pi is then released from L at 200° , leading to a 40° rotary sub-step (Figure 4, Section 3.4). The ADP unbinds from L at 240° and is fired out because the ADP is displaced by medium ATP, which now binds in L (ligand substitution). However, the L-site is meant for ADP.Pi. Therefore, ATP immediately hydrolyzes in site 2 (L), following which Pi is released (“unisite” catalysis in site 2), which gives energy for the 80° rotation sub-step. The L-site now changes to a closed site. The interaction of the C-terminal of the rotated ϵ -subunit with the closed site induces a conformational change of the catalytic site to its open (O) conformation from which the bound MgADP is unbound and released. A new MgATP binds to O, and the cycle repeats.

In summary, the elementary chemical processes and the angular position at which they occur during ATP hydrolysis by F_1 -ATPase

that are consistent with our cold chase experiments with promoter ATP and its analysis are as follows: ATP binding, 0°; ATP bond cleavage, 200°; Pi release, 200°; and ADP release, 240°.

The aforementioned correlation of the timing of elementary chemical processes in F_1 -ATPase with rotary angle agrees with the latest biochemical study (2023) in which Nishizaka and coworkers generated a hybrid F_1 consisting of one mutant β and two wild-type β s in thermophilic *Bacillus* PS3. The enzyme carried a β (E190D/F414E/F420E) mutation, which caused extremely slow rates of both ATP cleavage and ATP binding that enabled unequivocal determination of the angular position of the ATP cleavage reaction (200°) after ATP binding at 0° (Hasimoto et al., 2023). However, these authors were not able to decipher the entire mechanism from such experiments, and above all, they could not explain in detail the how and why of the mechanism in F_1 -ATPase.

Our proposed mechanism of ATP hydrolysis is also consistent with our other biochemical findings on mitochondrial F_1 , for instance, those shown in Figure 2, that the ratio of bound ^{32}P i to that of bound ^{32}P i and bound $[\gamma\text{-}^{32}\text{P}]\text{ATP}$ remains constant at approximately 0.333 under various conditions. This result implies that Pi is not bound to more than one of the three catalytic sites on the enzyme at any time. This observed distribution between the bound product and bound substrate is difficult to accommodate using other models.

4.2.2 Mechanism of ATP hydrolysis by the $\alpha_3\beta_3\gamma$ subcomplex of F_1

The model of Figure 4 can be readily adapted to explain ATP hydrolysis by the simpler $\alpha_3\beta_3\gamma$ subcomplex of F_1 (Adachi et al., 2007). Note that the reverse extrapolation from the mechanism of the $\alpha_3\beta_3\gamma$ subcomplex to that in the complete F_1 is non-trivial (i.e., from greater symmetry to greater asymmetry) and cannot be termed scientific as per systems theory (Nath, 2008). In the absence of the ϵ -subunit, “the identity of the catalytic sites is altered compared to intact F_1 or $F_1\text{F}_0$ ” and the “O-site exhibits properties, especially of nucleotide binding affinity, akin to that of the C-site,” as explained earlier (Nath, 2008). In terms of the discussion in this article, we can say that the asymmetry conferred by the ϵ -subunit to site 3 (O) in the intact/normal F_1 or $F_1\text{F}_0$ is lost in the absence of the ϵ -subunit. Hence, the O-site behaves like a closed site (C), and we can start the catalytic cycle for the $\alpha_3\beta_3\gamma$ subcomplex from the state sketched in panel 3 of Figure 4.

Starting from panel 3 in Figure 4, we can follow the catalytic cycle of the $\alpha_3\beta_3\gamma$ subcomplex seen as a whole as it progresses from panel 3 to panel 6 in Figure 4, as $\text{L} \rightarrow \text{C}'$, $\text{T} \rightarrow \text{L}$, $\text{C} \rightarrow \text{T}$, and $\text{C}' \rightarrow \text{C}$ (instead of $\text{C}' \rightarrow \text{O}$ in the presence of the ϵ -subunit). The ADP-ATP exchange readily occurs in C' . Hence, the C' -site containing bound ADP (as in panel 5 of Figure 4) is displaced by medium ATP so that the new closed site (C) now contains bound ATP, which cannot hydrolyze in C. In terms of nucleotide exchangeability properties of the catalytic sites in $\alpha_3\beta_3\gamma$, T contains tightly-bound non-exchangeable ATP, L can exchange bound ADP for bound ATP whose terminal $\text{P}_{\beta}\text{-O-P}_{\gamma}$ phosphoanhydride bond can be cleaved in the L-site by ATP hydrolysis in L, while C' engages in ADP-ATP exchange but the closed site containing bound MgATP (C) cannot be hydrolyzed in C. However, in addition to the L-site, the C-site needs to engage in the ADP-ATP exchange with the medium as otherwise inhibitory MgADP will remain bound in it, and the enzyme shall display its

characteristic MgADP inhibition. Therefore, the catalytic cycle of the subcomplex will be arrested at an intermediate angular position of $\sim 80^\circ$, as the site does not contain bound MgATP that can hydrolyze, release Pi, and carry out the 40° rotation sub-step to complete the 120° cycle when the site's conformation changes from C' to C to T to L.

Looking at the subcomplex as a whole, the catalytic cycle of ATP hydrolysis by $\alpha_3\beta_3\gamma$ can display considerable variability and differences from the coupling scheme of Section 3.4 for ATP hydrolysis by the complete F_0F_1 or F_1 -ATPase, for reasons that we shall discuss in the following section. It also explains the difficulty in establishing by single-molecule recordings the relative timing of the various catalytic events, particularly the timing of ADP release. It was impossible to simply add ADP in the medium, as in the experiments on $\alpha_3\beta_3\gamma$ with phosphate, because of the generic insidious phenomenon of MgADP inhibition (Hirono-Hara et al., 2001). Resolving the angle of ADP release during rapid stepping rotation of $\alpha_3\beta_3\gamma$ was technically beyond the resolution of even ultra-fast video recording rates. However, various groups in Japan developed innovative imaging approaches to address the aforementioned problem and to resolve the sub-steps during rotation. For instance, Shimabukuro et al. (2003) used the ATP analog ATP- γS whose cleavage on the enzyme was slow, as a result of which the catalytic dwell at 80° was extended to ~ 70 ms. The use of fluorescent Cy3-ATP in conjunction with the slowly hydrolyzing ATP- γS at nanomolar concentrations (~ 60 nM) allowed the 120° step to be clearly resolved into 80° and 40° sub-steps (Adachi et al., 2007).

Based on the aforementioned single-molecule imaging approaches, Nishizaka et al. (2004) showed that the $\alpha_3\beta_3\gamma$ subcomplex releases ADP in a 120° step between 240° and 360° . Adachi et al. (2007) further narrowed this range and showed that ADP release occurs between 240° and 320° . The angle between the binding of Cy3-ATP and its release as Cy3-ADP was $245^\circ \pm 57^\circ$ (mean \pm SD), independent of rotary speed, which was interpreted as $\sim 240^\circ$ (Adachi et al., 2007). Careful inspection of the raw data reveals a wide angular spread between ADP binding and ADP release spanning a range from $\sim 120^\circ$ to $\sim 360^\circ$. What were the reasons for such a wide angular spread for what are presumed to be discrete elementary chemical events?

We can glean the following interesting details from a statistical analysis of the 297 recorded pairs of ATP binding-ADP release counts versus angle histogram during single-molecule rotation of $\alpha_3\beta_3\gamma$ (Adachi et al., 2007). (i) In 69% of the pairs, Cy3-ATP binding occurred at the ATP-waiting dwell at 0° immediately before or after, and almost coincident with an 80° rotational sub-step of the γ -subunit (and occasionally with an unresolved 120° step). On the other hand, release as Cy3-ADP occurred within the angular play of an 80° sub-step (or within the time-frame of an unresolved 120° step) starting from 240° . (ii) In 9% of the cases (i.e., 26 pairs), ADP release occurred after 360° rotation or more. (iii) In the remaining 22% (i.e., 66 pairs of binding-release events), angles between ATP binding and ADP release were separated by $< 240^\circ$, or ADP release occurred at 240° without rotation. In most cases in (iii), either binding or release was not synchronous with rotation. These apparently “irregular behaviors” (Adachi et al., 2007) posed a difficult conundrum to explain.

Explanations of the irregular statistics summarized previously based on rare blinking events where fluorescence disappears

temporarily or resorts to photobleaching and irreversible destruction of Cy3 fluorescence (Adachi et al., 2007) are highly unsatisfactory. The average time for photobleaching in the aforementioned single-molecule experiments was 56 s, an order of magnitude longer than the time for a rotational step of < 1 s. Behavior (ii) cannot be explained away by the successive binding of two (or more) Cy3-ATP molecules. Justifying the irregular behaviors (ii) and (iii) as arising from “non-major reaction pathways” (Adachi et al., 2007) is not acceptable to a theoretician.

Therefore, what is a satisfactory resolution of the aforementioned mechanistic conundrum in terms of the coupling scheme discussed previously and in Section 3.4? The answer depends on how and when one defines the ATP binding step as occurring with respect to the primary 80° rotation of γ after ADP-ATP exchange and P_i release from site 2. Based on this conception, we can take ATP binding as occurring at $0^\circ/80^\circ$ or between these two angles, giving us an 80° angular distribution for the binding step. Furthermore, which ATP molecule is one considering in that definition? These complexities were not considered previously (Nishizaka et al., 2004; Adachi et al., 2007) but can now be analyzed with the help of Figure 4. If the ATP molecule that binds to C is considered a substrate, then as ATP is expected to bind immediately above a critical concentration (i.e., at high medium ATP concentrations) into that site, which is the case shown in Figure 4 (i.e., before the 80° primary rotation of γ sets the stage for subsequent catalytic events), we can consider ATP binding to C as occurring at 0° . However, especially at low ATP concentrations in the medium, the C-site can be filled after the 80° primary rotation of γ , in which case we can say that ATP binding occurred at an angular position of 80° . Similarly, ADP release can occur at 240° , after the $C \rightarrow T$ and $T \rightarrow L$ transitions (and ATP bond cleavage and subsequent P_i release at 200°), or since ADP release is recorded to occur between 240° and 320° in the forced rotation experiments and also during stepping motion (Adachi et al., 2007), we can take ADP release as occurring between 240° and 320° , consistent with the aforementioned results from single-molecule studies. This gives us an angle between ATP binding and ADP release that varies between 160° and 320° or even more if unresolved steps of 120° , seen in a minority of the single-molecule traces, are also considered. At mM ATP concentrations, we shall observe a mean angle between ATP binding to C and release from L of 240° , as found in prior histograms (Adachi et al., 2007).

The aforementioned scheme was applicable to the case of ATP binding to C for hydrolysis by the $\alpha_3\beta_3\gamma$ subcomplex. However, if we consider the ATP that binds to L/C' after ADP-ATP exchange in L-site (Figure 4), then the angle between ATP binding and ADP release events will increase accordingly, as the ATP bound to C' shall only be released after $C' \rightarrow C$, $C \rightarrow T$, and $T \rightarrow L$ transitions of the catalytic site. The elementary chemical processes and the angular position at which they occur during ATP hydrolysis by the $\alpha_3\beta_3\gamma$ subcomplex in that case are as follows: ATP binding, $0^\circ/80^\circ$ (depending on how and when one defines the ATP binding step as occurring with respect to the primary 80° rotation of γ after P_i release from L, and which ATP molecule one is considering in that definition); ATP bond cleavage, 320° ; P_i release, 320° ; and ADP release, 360° . Given the angular play and uncertainties in the assignment of the ATP binding and ADP release positions discussed previously, both normal and “aberrant” statistics in

(i)–(iii) described previously for the $\alpha_3\beta_3\gamma$ subcomplex are satisfactorily explained by our coupling scheme. Thus, the conundrum posed in this section is resolved without requiring unnecessary, arbitrary assumptions that are difficult to rationalize.

It is of some consequence to reflect on the reasons why 25 years of technologically advanced, superb state-of-the-art single-molecule studies (Kato et al., 1997; Noji et al., 1997; Hirono-Hara et al., 2001; Shimabukuro et al., 2003; Nishizaka et al., 2004; Sakaki et al., 2005; Konno et al., 2006; Shimabukuro et al., 2006; Adachi et al., 2007; Suzuki et al., 2014; Martin et al., 2015; Watanabe et al., 2015; Kobayashi et al., 2020; Zarco-Zavala et al., 2020; Hasimoto et al., 2023) by peerless experimental groups (see Acknowledgments section) are unable to resolve the mechanistic issues in the field of bioenergetics with finality. The first reason concerns the inherent limitation of available experimental techniques in probing complex biological systems. For example, single-molecule imaging can only record the movement of the central γ -subunit on which the fluorescence/optical probe is bound; it cannot observe and dissect the critical accompanying events occurring in (multiple) catalytic sites of the enzyme. The second aspect (no less important) is the lack of attention to theoretical developments in the field. Nath's torsional mechanism of energy transduction and ATP synthesis/hydrolysis has been available for the past 25 years (Rohatgi et al., 1998; Jain and Nath, 2000; Nath, 2002; Nath and Jain, 2002; Nath, 2003; Nath, 2004; Nath, 2008; Nath and Nath, 2009; Nath, 2010a; Nath, 2010b; Nath, 2017; Nath, 2018a; Mehta et al., 2020; Nath, 2021a; Nath, 2022a), i.e., for the same length of time as single-molecule imaging studies on F_1 -ATPase. If we take the help of such a theory for the interpretation of data and use it as a guide for the design of new experiments, which in turn shall provide a fillip to further theoretical refinement, then a productive synergy shall result, which will greatly accelerate progress in these interdisciplinary fields of research.

To sum up, it is clear that the mechanism of ATP hydrolysis by the $\alpha_3\beta_3\gamma$ subcomplex of F_1 is not identical to the mechanism of ATP hydrolysis by the complete F_1 -ATPase enzyme. To a large extent, this occurs because of the lack of the ϵ -subunit in the single-molecule experiments on the subcomplex. Therefore, inordinate care must be taken not to extrapolate results obtained by single-molecule studies on the $\alpha_3\beta_3\gamma$ subcomplex—or on the enzyme lacking the full ϵ -subunit, especially its C-terminus (Keis et al., 2006)—to the complete F_1 , as cautioned by us 15 years ago (Nath, 2008).

4.2.3 Relationship of the proposed mechanism to the single-molecule experiments on bovine mitochondrial F_1 -ATPase by Noji and coworkers (Kobayashi et al., 2020)

Our proposed mechanism of ATP hydrolysis, if interpreted correctly, is consistent with a recent single-molecule study on F_1 -ATPase from bovine mitochondria (bMF₁) that contains the $\alpha_3\beta_3$ ring and the $\gamma\delta\epsilon$ complex (compare with Section 4.2.2 on the $\alpha_3\beta_3\gamma$ subcomplex). In our proposed mechanism [Nath (2008), Section 3.4, Section 4.2.1, Figure 4], as in the experiments on bMF₁ (Kobayashi et al., 2020), the ATP binding dwell is identified as occurring at 0° , and the long dwell at $\sim 80^\circ$ – 90° . The long dwell is also the angular position of the catalytic pause/dwell and represents the angular position of the ATP cleavage event in both views. These are also broadly consistent with findings on F_1 molecules from other species (e.g., EF₁ and TF₁).

The differences arise from the postulated identity/cause of the short pause/dwell and its chemical state at $\sim 20^\circ$ in bMF_1 , the proposed driving force for the $80^\circ/90^\circ$ – 120° rotational sub-step, and the order of product release steps as per the two views. In fact, in both views, the short pause/dwell is a Pi dwell, except that in Nath's torsional mechanism of ATP hydrolysis and the unified theory, the short pause originates due to the enzyme activation process in the L catalytic site upon ATP hydrolysis (described at great length already) and the primary rotation of γ that arises from the step-wise Pi movement in the catalytic site away from MgADP (Nath and Nath, 2009) before its release into the surrounding medium. Since this movement of Pi through its exit tunnel after unbinding from its binding site is *quantized* in sub-steps, as formulated quantitatively from first principles in Nath and Nath (2009), a slowing down of any one of the sub-steps during the passage of Pi and before its release into the external medium will be reflected as a pause at an intervening angle between the ATP binding dwell and the catalytic dwell in fast recordings at substrate-saturated high ATP ($\sim \text{mM}$), as previously observed (Kobayashi et al., 2020). This pause can be relatively short or long (or remain undetected) compared to the catalytic pause/dwell at $80^\circ/90^\circ$, depending on the passage time of Pi, the resolution of the single-molecule recordings, and the intrinsically stochastic nature of the sub-steps, and can occur at a variable angular position depending on the nature and kinetics of F_1S from different species. Whatever the variable nature of the angle of the intermediate sub-step, the duration of the pause and its kinetics, or the number of sub-steps, the same mechanism operates in Nath, and the process after activation will cause rotation from the angular position of the binding dwell at $\theta = 0^\circ$ to the catalytic dwell position at $\theta = 80^\circ$ – 90° as per Nath's theory. Subsequently, Pi release from the (new) site 2 of F_1 after hydrolysis of substrate ATP during the catalytic dwell causes rotation of γ - ϵ from $\theta = 80^\circ$ – 90° to $\theta = 120^\circ$ (Nath, 2008).

However, in contrast, Noji and coworkers cannot propose the same driving force for the sub-step rotation from $\theta = 80^\circ$ – 90° to $\theta = 120^\circ$ as in Nath's model mentioned previously because the authors have already released Pi at 10° – 20° in bMF_1 and driven the sub-step from $\theta = 10^\circ/20^\circ$ – $80^\circ/90^\circ$ before the catalytic dwell (in which ATP hydrolysis takes place) has occurred. The authors are, therefore, forced to postulate ATP hydrolysis as the driving force for the $\theta = 80^\circ$ – 90° to $\theta = 120^\circ$ sub-step in Kobayashi et al. (2020) and Sobti et al. (2021). Furthermore, their postulated order of product release (ADP followed by Pi) is opposite to that in Nath's model, which proposes an ordered and sequential release process with Pi release followed by ADP release. It should be stressed that the order of product release proposed previously (Kobayashi et al., 2020) contradicts the order determined by X-ray crystallographic studies (Rees et al., 2012).

As a result, the driving force for the first (primary/activation) sub-step is also different between the two models. We note at the outset that the proposal of ATP binding alone (or ATP binding plus ADP release from different catalytic sites) as driving the first rotation step of $\sim 80^\circ$ is not supported by the results of cold chase experiments reported in this work (Figures 1 and 2). Moreover, a further difficulty posed by the results of Kobayashi et al. (2020) is that the first rotation step is composed of two sub-steps, first from 0° to $\sim 10^\circ$ – 20° and then (after Pi release) from $\sim 10^\circ$ – 20° to $\sim 80^\circ$ – 90° . Therefore, it is problematic to assign one or the other sub-step as

arising from ATP binding alone (or to be powered by ADP release in addition to ATP binding) and another as being due to Pi release. The angular distance between the Pi dwell ($\sim 10^\circ$ – 20°) and the catalytic dwell ($\sim 80^\circ$ – 90°), measuring $\sim 60^\circ$ – 80° , is far too large to be powered by Pi release in bMF_1 . If ATP binding and/or ADP release are postulated to cause the entire step of rotation of $\sim 80^\circ$ – 90° , then the function of the Pi release step remains unassigned and unknown, and it appears to have no role in driving the rotation. All these acute mechanistic difficulties are overcome by the alternative model.

Models proposed for ATP hydrolysis by F_1 -ATPase based on single-molecule studies contradict experimental data based on direct, real-time monitoring of catalytic site nucleotide occupancies recorded by Senior's group (Weber and Senior, 2001; Weber et al., 1993; Weber et al., 1996; Löbau et al., 1998). In these models based on single-molecule experiments, rotation occurs with only two sites occupied by Mg-nucleotide. For example, in the models of Yasuda et al. (2001) and Adachi et al. (2007), postulated for the $\alpha_3\beta_3\gamma$ subcomplex of TF_1 from thermophilic *Bacillus* PS3, both the 80° and 40° sub-steps of the rotation of the γ -subunit occur in the bisite mode. In the model proposed for human mitochondrial F_1 -ATPase, all three sub-steps for rotation of γ - ϵ of 0° – 65° , 65° – 90° , and 90° – 120° , postulated to be driven by ATP binding, Pi release, and ATP bond cleavage, respectively (Suzuki et al., 2014), occur with two sites containing bound Mg-nucleotide. For bovine MF_1 , a bisite mode of catalysis is suggested for rotation of γ - ϵ for the sub-step from 10° – 20° to 80° and for the 80° – 120° sub-step (Kobayashi et al., 2020). Models that propose concerted ATP binding to a site and ADP release from a different site (Adachi et al., 2007; Suzuki et al., 2014; Kobayashi et al., 2020) as driving rotation cannot be trisite. These models are incorrect, given that the operative mode of catalysis during steady-state ATP hydrolysis by F_1 -ATPase is trisite. Similarly, physical models (Mukherjee and Warshel, 2011; Nam and Karplus, 2019; Volkán-Kacsó and Marcus, 2022) proposed for the working of the F_1 motor are not true trisite models and hence are incorrect. Designating an ATPase mechanism as trisite simply because it alternates between having two and three catalytic sites filled with nucleotide at any time is insufficient and constitutes an imperfect criterion. For a mechanism to be truly trisite, catalysis must occur, and rotation must take place during steady-state V_{\max} hydrolysis only when all three catalytic sites are occupied by bound Mg-nucleotide. This condition is satisfied by the model proposed within the torsional mechanism (Figure 4).

Studies that directly monitored nucleotide occupancies of β -subunits proposed true trisite models of ATP hydrolysis by F_1 -ATPase (Weber and Senior, 2001; Weber et al., 1993; Weber et al., 1996; Löbau et al., 1998). However, these models contradict longstanding results from single-molecule recordings (Yasuda et al., 2001; Nishizaka et al., 2004; Adachi et al., 2007; Suzuki et al., 2014; Kobayashi et al., 2020; Hasimoto et al., 2023). For instance, the former studies realized that in a trisite mechanism, ATP binding to site 3 with a K_{d3} value of only $\sim 100 \mu\text{M}$ is too weak to provide sufficient energy to drive the 80° rotational sub-step. Hence, the authors proposed that ATP binding to site 3, followed by ATP hydrolysis in site 1 acting in sequence, provides energy for the 80° sub-step of the γ rotation (Weber and Senior, 2001; Senior et al., 2002). The problem for these models is that single-molecule experiments on F_1 have conclusively shown that ATP hydrolysis takes place in site 1 during the catalytic dwell that occurs after the

80° sub-step of the γ rotation (Yasuda et al., 2001; Nishizaka et al., 2004; Adachi et al., 2007; Suzuki et al., 2014; Kobayashi et al., 2020; Hasimoto et al., 2023). Hence, the bond cleavage step in site 1 cannot be invoked to drive the 80° sub-step of rotation.

Models that invoke ATP binding to site 3 as solely or primarily responsible for driving rotation (Wang and Oster, 1998; Oster and Wang, 2000; Yasuda et al., 2001; Nishizaka et al., 2004; Mukherjee and Warshel, 2011; Nakano et al., 2022) are also problematic for the reasons spelled out above and in the last paragraph of Section 3.4. Several other difficulties with proposed models of ATP synthesis and hydrolysis have been discussed previously (Weber and Senior, 2001; Nath, 2002; Senior et al., 2002; Nath, 2008). These inconsistencies and mechanistic problems are eliminated by the model shown in Figure 4.

Enzymological studies designed to test the dependence of steady-state rates of ATP hydrolysis on substrate [ATP] concentrations from sub-micromolar to millimolar, along with the simultaneous assessment of nucleotide occupancies in the catalytic sites of F_1 -ATPase in this concentration range, would greatly help provide further mechanistic insights.

4.2.4 Proposed mechanism and single-molecule studies on human mitochondrial F_1 -ATPase by Yoshida and coworkers (Suzuki et al., 2014) and in other mutants and organisms (Shimabukuro et al., 2006; Zarco-Zavala et al., 2020)

Section 4.2.3 shows how the same mechanism is operative irrespective of whether the F_1 motor is a six- or nine-stepper. Hence, no new assumptions are required to explain the function of F_1 motors with an intermediate pause before $\sim 80^\circ$, such as human mitochondrial F_1 (hMF₁), a nine-stepped motor that has been shown to exhibit a Pi dwell/pause at an intermediate angle of $\sim 65^\circ$ (Suzuki et al., 2014). Furthermore, the equal distribution of the Gibbs energies among certain sub-steps of Pi movement selected by Nath and Nath (2009) for a general molecular motor documented an ideal case, which anyhow seems to work quite perfectly for the six-stepped TF₁ and EF₁ motors, and for nine-stepped motors with a catalytic pause at $\sim 80^\circ$, such as bMF₁ (Section 4.2.3). A slightly uneven distribution between step 3 and steps (1 + 2) in Table 1 of Nath and Nath (2009) can readily replicate larger angular catalytic dwell positions, for example, in hMF₁, which has been shown to exhibit the catalytic dwell at 90° (Suzuki et al., 2014). This slightly larger angle ($> 80^\circ$) at which the catalytic dwell occurs in hMF₁ could have to do with the different binding affinities of the catalytic sites and the values of the interaction energies of the single copy subunits with the β -catalytic sites in hMF₁.

The unified mechanism also readily explains the working of three-stepped F_1 motors without making additional assumptions. Yoshida and coworkers previously identified a mutant TF₁ that rotates without sub-steps at low MgATP concentration when the ATP binding dwell is several seconds long (Shimabukuro et al., 2006). In this mutant, ATP binding, hydrolysis, and product (Pi) release occur within the same 0° dwell. Such a wild-type motor (PdF₁) has recently been identified in *Paracoccus denitrificans* (Zarco-Zavala et al., 2020). The behavior of such motors is readily explained because the distance between the $\alpha_3\beta_3$ surface and the surface of γ (i.e., the interface thickness) determines the

magnitude of the average torque produced, τ , and energy conservation determines the rotation angle θ as follows:

$$\Delta G_{ATP}^0 = \text{constant} = \tau\theta. \quad (3)$$

If the magnitude of τ generated at the interface lies below or in the vicinity of a threshold value (approximately ~ 30 pN nm), then θ can readily reach 120° in a single step, and a three-stepped $3 \times 120^\circ$ rotary motor results. Since nucleotide exchange, ATP binding, followed by ATP bond cleavage and Pi release occur in the ATP-waiting dwell at 0° , the primary rotation of γ_{top} occurs as detailed in Section 3.4, except that rotation does not stop at $\sim 80^\circ$ but now continues all the way until 120° and generates high torsional strain in γ (Nath et al., 1999; Nath et al., 2000; Nath and Jain, 2000). Relief of this torsional strain in the γ -subunit enables the bottom of the central stalk to rotate in steps in the complete F_0F_1 or in a single step in F_1 to $\theta = 120^\circ$. The relay continues the hydrolysis and Pi release in the next catalytic site as described by the torsional mechanism, and the three-stepped cycle continues.

The aforementioned torsional mechanism naturally explains rotation in three-step F_1 motors because the same process (after ATP binding and hydrolytic cleavage) of Pi unbinding, its movement away from bound MgADP, and Pi release into the medium contributes energy for driving rotation or performing useful work in molecular motors, irrespective of the angular position of the dwell at which this fundamental process occurs (Nath, 2008; Nath and Nath, 2009).

The three-stepped rotation in PdF₁ (Zarco-Zavala et al., 2020) and in thermophilic *Bacillus* PS3 mutants (Shimabukuro et al., 2006) is very difficult to explain by other models of ATP hydrolysis, at least in their current form.

4.2.5 Novel predictions

Several novel predictions can be made based on the proposed mechanism and the unified theory of ATP synthesis/hydrolysis. They explain the mechanism of action of various inhibitors of hMF₁ that have major pharmacological applications. For example, Yoshida and coworkers clearly showed that inhibition by sodium azide blocks rotation of hMF₁ at $\theta = \sim 65^\circ$ (Suzuki et al., 2014). This corresponds to the arrest of the primary rotation step of the torsional mechanism and unified theory at $\sim 65^\circ$, i.e., before the γ -subunit can reach the catalytic dwell state at 90° in which the second hydrolytic cleavage event can occur. Hence, the conformational relay for multisite hydrolysis (signal transmission) will be irreversibly blocked at $\theta = 65^\circ$ by azide, and the enzyme shall exhibit a unique state and nucleotide occupancy of the catalytic sites corresponding to panel 2 in Figure 4, according to Nath's torsional mechanism and the unified theory. Thus, azide inhibition is distinct from the MgADP inhibition that takes place at a different angular position ($\theta = 90^\circ$ for hMF₁) and occurs by a different mechanism.

The pharmaceutically important case of azide inhibition has been discussed previously. More exotic examples include artificial or fused/hybrid F_1 motors that combine α , β , and γ subunits of F_1 s from various species for which the generated average torque τ lies above a critical value τ_c (Eq. 3). As a rough estimate, $\tau_c \cong 50$ pN nm. In such constructs, γ shall rotate only to $\theta < 80^\circ$; therefore, rotation shall cease because the γ -subunit is unable to reach the $\sim 80^\circ$ position of

the catalytic dwell in which subsequent elementary chemical events in another β -subunit can continue the rotation. Hence, the prediction can be made that it should be possible to reconstitute/assemble and find at least a few chimera motors for which continuous rotation will not be detected by the single-molecule rotation assay under the experimental conditions usually employed in such studies.

4.2.6 “Unisite” catalysis by F_1 -ATPase

The present work shows that site 1 (T) contains bound ATP that does not hydrolyze by itself in T. In other words, site 1 contains tightly bound, non-exchangeable MgATP. Hence, “unisite” hydrolysis cannot take place in site 1, contrary to the original view of Cross et al. (1982) and Penefsky (1985). However, the second site contains tightly bound (but exchangeable) nucleotide and “unisite” ATP hydrolysis and Pi release readily occurs in site 2 (L). This is the conclusion we have drawn from our radioactive promoter [γ - 32 P]ATP cold chase experiments (Figure 1; Table 1).

Berden et al. had indeed reached the correct conclusion by biochemical site occupancy experiments that site 1 of the normal F_1 enzyme does not hydrolyze ATP (Hartog and Berden, 1999; Berden and Hartog, 2000). However, the authors overextended their results to conclude that site 1 does not participate in multisite catalysis. Unfortunately, this logic (in the spirit of Nath (2022a) is correct only if site 1 remains unchanged in conformation during multisite catalysis. If site 1 changes to site 2 owing to rotation of the γ -subunit during the catalytic cycle, as we propose (Figure 4, Section 4.2.1), then (the new) site 2 can hydrolyze ATP, release Pi, and participate in multisite catalysis. In any case, the biochemical experiments of Berden showed that site 2 (L) performs “unisite” ATP cleavage and product release (Hartog and Berden, 1999; Berden and Hartog, 2000). The authors also went on the wrong track by focusing on the non-existence of rotation in F_1 -ATPase (Hartog and Berden, 1999; Berden and Hartog, 2000), which is a proven fact (Kato et al., 1997; Noji et al., 1997; Hirono-Hara et al., 2001; Shimabukuro et al., 2003; Nishizaka et al., 2004; Sakaki et al., 2005; Konno et al., 2006; Shimabukuro et al., 2006; Adachi et al., 2007; Suzuki et al., 2014; Watanabe et al., 2015; Kobayashi et al., 2020; Zarco-Zavala et al., 2020; Hasimoto et al., 2023).

Our conclusion that “unisite” hydrolysis occurs in site 2 (β_{TP}) is also in full agreement with the finding of an important recent cryo-EM structural study performed under various reaction conditions (Nakano et al., 2022). However, their proposed mechanism for multisite hydrolysis by F_1 -ATPase in which ATP binding to β_E causes 120° rotation of γ -subunit is incorrect and suffers from several deficiencies (Nakano et al., 2022), some of which have been outlined in the last paragraph of Section 3.4.

4.2.7 Cold chase and multisite catalysis by F_1 -ATPase

Section 4.2.6 summarizes the important fact that, contrary to the current dogma, bound ATP does not hydrolyze in site 1. Thus, one has to change the conformation of site 1 to cause hydrolysis of the ATP bound in site 1 (T) (Nath, 2003). However, this change cannot occur without rotation of the γ -subunit, and rotation cannot occur unless site 2 (L) binds and hydrolyzes promoter ATP and releases Pi (cold chase). Moreover, since site 2 contains bound ADP, medium ATP needs to kick ADP off in the catalytic site and bind instead

[ADP-ATP exchange (Nath, 2008), i.e., *ligand displacement/substitution*] for activation of the system and initiation of rotation. Hence, one is compelled to postulate the coupling scheme shown in Figure 4 for multisite catalysis in F_1 -ATPase, where sequential participation of catalytic sites in a trisite mode leads to steady-state V_{max} activity.

The filling of multiple F_1 sites by ligand (MgATP) can be modeled by a simple probabilistic approach. If c is the ligand concentration and K_d the dissociation constant of the site for the ligand, then the probability p that the site is occupied by the ligand is given as follows:

$$p = \frac{c}{c + K_d}. \quad (4)$$

The probability that the site is not occupied by bound ligand is given by

$$p = 1 - \frac{c}{c + K_d}. \quad (5)$$

In principle, the aforementioned equations apply to the multisite catalysis case where any of the three catalytic sites are occupied by bound ligands (represented by 1) or remain empty (represented by 0). The fractions of the enzyme species f that contain or do not contain bound ligands are then determined by the product of the relevant expressions written for each site with its characteristic thermodynamic dissociation constant. The fraction of each species then represents the fractional specific activity of the enzyme $\frac{v}{V_{max}}$. Hence, the contribution of each enzyme species to V_{max} can be quantified in terms of percentages.

If K_{d1} , K_{d2} , and K_{d3} represent the dissociation constants for sites 1, 2, and 3 of F_1 -ATPase, respectively, then the fraction of the enzyme species with all three sites occupied (i.e., in state [111]) is given as follows:

$$f_{111} = \left(\frac{c}{c + K_{d1}} \right) \left(\frac{c}{c + K_{d2}} \right) \left(\frac{c}{c + K_{d3}} \right). \quad (6)$$

The fraction of species with sites 1 and 2 occupied by MgATP (but with site 3 unoccupied) is given by

$$f_{110} = \left(\frac{c}{c + K_{d1}} \right) \left(\frac{c}{c + K_{d2}} \right) \left(1 - \frac{c}{c + K_{d3}} \right). \quad (7)$$

Dissociation constant values for MF_1 for the three sites have not been reliably measured. However, we can simulate the system with the K_d values for EF_1 . It is known from previous studies that EF_1 is very similar to MF_1 in terms of nucleotide exchangeability and other biochemical properties, except that the binding at the lowest-affinity catalytic sites is less tight (Cross et al., 1982; Berden and Hartog, 2000; Hartog and Berden, 1999; Cross and Nalin, 1982). Using conditions of Mg^{2+} in excess of ATP, K_{d1} , K_{d2} , and K_{d3} for sites 1, 2, and 3 measure 0.02, 1.4, and 23 μ M, respectively (Weber and Senior, 2001). Use of a lower value of the binding affinity of site 3 for MF_1 ($K_{d3} \sim 100$ – 150 mM) does not alter the results presented in the next paragraph to any appreciable extent.

Using the above K_d values at 0.3 μ M ATP, we find from Eq. 6 that $f_{111} \approx 2 \times 10^{-3}$, while at 10 μ M ATP, $f_{111} \approx 0.25$. If trisite species are responsible for multisite hydrolysis, this corresponds to a rate enhancement by a factor of ~ 125 . At 1 mM ATP, $f_{111} \rightarrow 1.0$, implying that the rate enhancement from unisite to multisite conditions is about $1/(2 \times 10^{-3})$ or 500-fold. A calculation that is

more accurate and considers [110] and [100] enzyme species in addition to [111] species is given in [Supplementary Section S1](#). These calculations based on a simple stochastic population model explain all our experimental observations in this context in outline and remarkably model several details of the hydrolysis process ([Figure 1](#); [Table 1](#)). We have previously shown that a stochastic kinetic theory based on a master differential equation approach successfully captures the details of oxygen exchange processes occurring at a single catalytic site in the ATP synthesis mode during catalysis by the F_0F_1 -ATP synthase ([Mehta et al., 2020](#)). Hence, our approach is remarkably robust and useful in modeling various related biological energy transduction and catalysis processes.

The aforementioned calculations show that, based on the aforementioned K_d values of the three β -catalytic sites, there exists a small fraction of enzyme population with [110] and [111] nucleotide occupancies ([TLO] designates the nucleotide occupancies of tight, loose, and open sites respectively, with 1 standing for a filled site and 0 for an unoccupied site), even at sub-stoichiometric conditions of $0.3\ \mu\text{M}$ ATP and $1\ \mu\text{M}$ F_1 ([Cross and Nalin, 1982](#)). Enzyme molecules in state [110] lead to cold chase and radioactive P_i release from site 1, a single turnover event, recorded by the isotope trap. The small fraction of enzyme molecules in state [110] and [111] yields a slow ($\sim 0.1\ \text{s}^{-1}$) rate of ATP hydrolysis. At higher ATP concentrations (super-stoichiometric conditions), events due to cold chase by [110] species are integrated into multisite catalysis ([Figure 4](#)). Several turnovers due to [111] populated enzyme species (multisite hydrolysis) by the cycle of [Figure 4](#) provide the $\sim 10^3$ -fold rate enhancement to $\sim 100\ \text{s}^{-1}$ over “unisite” rates—the so-called positive catalytic cooperativity. In [Supplementary Section S1](#), we start from the 1:3 sub-stoichiometric ATP: F_1 loading initial condition and simulate F_1 -ATPase enzyme activity for the experimental conditions of [Figure 1](#) and [Table 1](#).

Previously, we explained that the differential affinity of nucleotide binding to the three catalytic sites in ATP synthase does not fundamentally arise from “negative cooperativity of binding,” as proposed by the binding change mechanism ([Boyer, 1993](#)), but as per the torsional mechanism is “due to asymmetric interactions of the catalytic sites with the γ and ϵ subunits” ([Nath and Jain, 2000](#)). We explained the above so-called positive catalytic cooperativity to be due to the “mode of functioning of the enzyme itself” ([Nath and Jain, 2000](#)) and further owing to “an increase in the fraction of the F_1 enzyme population containing bound nucleotide in all three catalytic sites with increase in substrate concentration” ([Nath, 2003](#)). A 2022 structural work stated that “Assuming that F_0F_1 adopts an asymmetric architecture during ATP hydrolysis, the alternating participation of β subunits does not require positive catalytic cooperativity,” ([Nakano et al., 2022](#)) which is in line with our previous proposals ([Nath et al., 2000](#); [Nath and Jain, 2000](#); [Nath, 2002](#); [Nath, 2003](#)) made more than 20 years ago. Here, we calculated enzyme activity based on a probability-based occupancy model of enzyme catalytic sites, which offers further strong support to the aforementioned conclusion ([Supplementary Section S1](#) of Supporting Material).

The aforementioned results also agree with single-molecule recordings that showed that a single (trisite) rotary mechanism operates for F_1 -ATPase over the entire range of ATP concentration from nanomolar to millimolar ([Sakaki et al., 2005](#)).

We have thus shown in [Sections 4.1.1–4.1.5](#) and [Sections 4.2.1–4.2.7](#) that various structural and biochemical observations made in the context of ATP hydrolysis by F_1 -ATPase are logically explained.

4.2.8 Differences between competing mechanisms

We have already discussed the lack of competence of binding energy changes in promoting catalysis by F_1 -ATPase ([Section 3.3](#)). Furthermore, Boyer’s binding change mechanism was necessarily bisite ([Boyer, 1993](#)). However, excellent data obtained using tryptophan fluorescence quenching by Senior and colleagues ([Weber and Senior, 2001](#); [Weber et al., 1993](#); [Weber et al., 1996](#); [Löbau et al., 1998](#)) showed that the ATP hydrolysis activity of *E. coli* F_1 is fully in accordance with the occupation of all three catalytic sites by the substrate (trisite catalysis) ([Nath, 2003](#)), in clear conflict with bisite catalysis proposed by the Boyer model. Another fundamental reason for the inadequacy of the binding change mechanism stemmed from the fact that Boyer mainly considered β – β interactions in developing his model. However, during the formulation of Nath’s torsional mechanism of energy transduction and ATP synthesis, which was a trisite mechanism ([Nath et al., 1999](#)), we considered the *asymmetric* interactions of the β -catalytic sites with γ and ϵ of fundamental importance ([Table 1](#) of [Nath \(2003\)](#) ([Nath et al., 2000](#); [Nath, 2002](#)), and we developed these aspects further in this work. Finally, the important chemical concept of *ligand displacement* is highlighted by our model. However, this concept was missed or ignored during the formulation of Boyer’s binding change mechanism, and a complex double hypothesis of negative binding cooperativity and positive catalytic cooperativity was proposed by it ([Boyer, 1993](#)). However, there is no chemical necessity for invoking site–site cooperativity or additional allosteric interactions since ligand substitution (e.g., ADP–ATP exchange at a β -catalytic site ([Nath, 2008](#))) can readily cause activation of the asymmetric enzymatic system. Hence, we do not require these additional assumptions. Therefore, we believe that Nath’s torsional mechanism of energy transduction and ATP synthesis/hydrolysis and the unified theory offers a simpler solution to the problem and a more elegant and aesthetically appealing picture of energy coupling, transduction, and catalysis by the F_0F_1 -ATP synthase ([Nath, 2002](#); [Nath, 2008](#)).

5 Conclusion

The molecular mechanism of ATP synthesis/hydrolysis has inspired a vast amount of research ever since the discovery of ATP almost a hundred years ago. However, the detailed mechanism of the order of the elementary steps in the multiple catalytic sites of an enzyme and how the chemical and mechanical steps are coupled in biological molecular machines has eluded resolution. The current theory considers the binding energy of ATP as the energy source of mechanical rotation in F_1 -ATPase. This view has been shown to be incomplete and incorrect. Fresh insights into the mechanism are obtained by measuring the maximum extents and kinetic rates of hydrolysis of preloaded bound $[\gamma\text{-}^{32}\text{P}]\text{ATP}$ and promoter $[\gamma\text{-}^{32}\text{P}]\text{ATP}$ in cold chase experiments. Mechanistic implications arising from the experiments and the first law of thermodynamics have been spelled out, and general physical principles for biological free

energy transduction have been formulated. The question of how ATP acts as an energy source and performs useful external work has been asked and answered. A molecular mechanism of steady-state trisite ATP hydrolysis by F_1 -ATPase, which is consistent with the formulated physical principles and the body of available biochemical information, has been constructed. Only such a detailed mechanism can truly explain the function of F_1 -ATPase as a molecular energy machine. The detailed mechanism of the 120° catalytic cycle (Figure 4) helps us understand the state of the enzyme captured by the unique X-ray structures of *E. coli* EF_1 (Cingolani and Duncan, 2011), thermophilic TF_1 (Shirakihara et al., 2015), and the cryo-EM structures of Sobti et al. (2016) and Sobti et al. (2019) that are close to the 0° (or 120°) ATP-binding dwell compared to the Leslie–Walker structures (Abrahams et al., 1994; Menz et al., 2001) that trap a metastable post-hydrolysis pre-product release conformation of the mitochondrial MF_1 at an intermediate angle of ~80°–90° (Nath, 2008). The key and essential involvement of the ϵ -subunit in sequential energy transfer to/from the β -catalytic sites in F_1 and the energy-promoted association and asymmetry-causing interactions of the single copy γ - and ϵ -subunits with the β -catalytic sites (Nath et al., 1999; Nath et al., 2000; Nath and Jain, 2000; Nath, 2002; Nath, 2003; Nath, 2008), leading to critical functionally important changes in the conformation of the catalytic sites, were highlighted in our detailed mechanism. A mathematical model for the estimation of economics and opportunity cost in choosing between competing theories has also been developed (Supplementary Section S2).

A major achievement of the work has been to provide a biochemical basis for interpreting “unisite” catalysis, cold chase, and their relationship to steady-state multisite V_{\max} hydrolysis by F_1 -ATPase. These problems have proved frustratingly difficult to solve since the first discovery of “unisite” catalysis more than 40 years ago (Section 4.2). Probability-based calculations of enzyme species distributions and activity have been performed (Supplementary Section S1) to verify the biochemical theory of “unisite” catalysis, cold chase, and multisite catalysis by F_1 -ATPase that offer further support to the results in Table 1 and Figures 1 and 2.

The formulated general physical principles of free energy transduction [(Nath and Nath, 2009) and Section 3.3] and the proposed detailed molecular mechanism of ATP hydrolysis by F_1 -ATPase (Figure 4 and Section 3.4) have important biochemical consequences (Sections 4.1, 4.2). Several novel predictions of pharmacological importance on the mechanism of action of F_1 inhibitors have been made. The proposed new concept of energy coupling in ATP synthesis/hydrolysis based on ligand substitution chemistry takes us beyond the binding change mechanism of ATP synthesis/hydrolysis. The working mechanism of nine-stepped (b MF_1 , h MF_1), six-stepped (TF_1 , EF_1), and three-stepped (Pd F_1) F_1 motors and of the $\alpha_3\beta_3\gamma$ subcomplex of F_1 is explained by the unified theory without invoking additional assumptions or postulating different coupling schemes. The aforementioned developments have wide ramifications (Sections 4.1, 4.2) for a whole gamut of ATP-hydrolyzing molecular motors in biology.

Data availability statement

The raw data supporting the conclusions of this article will be made available by the authors, without undue reservation.

Author contributions

SN conceptualized the research program, performed research, analyzed the results, developed the model, and wrote and edited the manuscript. The author confirms being the sole contributor of this work and has approved it for publication.

Acknowledgments

The author is very grateful to Professors S. Ishiwata and K. Kinoshita for the luxurious financing of his sabbatical leave stay at the Physics Department, Waseda University, Tokyo, during 2006–2007, and for allowing him to participate in and be privy to their state-of-the-art single-molecule works in progress. The author thanks the Villum Foundation, Copenhagen, for generous financial support through a VELUX Visiting Professorship at the Technical University of Denmark for the academic year 2013–2014 and to the Niels Bohr Institute, Copenhagen, in 2022, when this work was finally completed. This article is dedicated to Professor Kazuhiko Kinoshita Jr. in memory of his pioneering single-molecule experimental studies on the F_1 -ATPase.

Conflict of interest

The author declares that the research was conducted in the absence of any commercial or financial relationships that could be construed as a potential conflict of interest.

Publisher's note

All claims expressed in this article are solely those of the authors and do not necessarily represent those of their affiliated organizations or those of the publisher, the editors, and the reviewers. Any product that may be evaluated in this article, or claim that may be made by its manufacturer, is not guaranteed or endorsed by the publisher.

Supplementary material

The Supplementary Material for this article can be found online at: <https://www.frontiersin.org/articles/10.3389/fchem.2023.1058500/full#supplementary-material>

References

- Abrahams, J. P., Leslie, A. G. W., Lutter, R., and Walker, J. E. (1994). Structure at 2.8 Å resolution of F₁-ATPase from bovine heart mitochondria. *Nature* 370, 621–628. doi:10.1038/370621a0
- Adachi, K., Oiwa, K., Nishizaka, T., Furuike, S., Noji, H., Ito, H., et al. (2007). Coupling of rotation and catalysis in F₁-ATPase revealed by single-molecule imaging and manipulation. *Cell* 130, 309–321. doi:10.1016/j.cell.2007.05.020
- Agarwal, B. (2011). A role for anions in ATP synthesis and its molecular mechanistic interpretation. *J. Bioenerg. Biomembr.* 43, 299–310. doi:10.1007/s10863-011-9358-3
- Aggeler, R., Ogilvie, I., and Capaldi, R. A. (1997). Rotation of a γ-ε subunit domain in the *Escherichia coli* F₁F₀-ATP synthase complex. *J. Biol. Chem.* 272, 19621–19624. doi:10.1074/jbc.272.31.19621
- Allison, W. S. (1998). F₁-ATPase: A molecular motor that hydrolyzes ATP with sequential opening and closing of catalytic sites coupled to rotation of its γ-subunit. *Accounts Chem. Res.* 31, 819–826. doi:10.1021/ar960257v
- Bai, C., Asadi, M., and Warshel, A. (2020). The catalytic dwell in ATPases is not crucial for movement against applied torque. *Nat. Chem.* 12, 1187–1192. doi:10.1038/s41557-020-0549-6
- Berden, J. A., and Hartog, A. F. (2000). Analysis of the nucleotide binding sites of mitochondrial ATP synthase provides evidence for a two-site catalytic mechanism. *Biochim. Biophys. Acta* 1458, 234–251. doi:10.1016/s0005-2728(00)00076-1
- Boyer, P. D., Cross, R. L., and Momsen, W. (1973). A new concept for energy coupling in oxidative phosphorylation based on a molecular explanation of the oxygen exchange reactions. *Proc. Natl. Acad. Sci. U. S. A.* 70, 2837–2839. doi:10.1073/pnas.70.10.2837
- Boyer, P. D. (1993). The binding change mechanism for ATP synthase – some probabilities and possibilities. *Biochim. Biophys. Acta* 1140, 215–250. doi:10.1016/0005-2728(93)90063-1
- Bullough, D. A., Verburg, J. G., Yoshida, M., and Allison, W. S. (1987). Evidence for functional heterogeneity among the catalytic sites of the bovine heart mitochondrial F₁-ATPase. *J. Biol. Chem.* 262, 11675–11683. doi:10.1016/s0021-9258(18)60863-4
- Channakeshava, C. (2011). New paradigm for ATP synthesis and consumption. *J. Biosci.* 36, 3–4. doi:10.1007/s12038-011-9015-3
- Cingolani, G., and Duncan, T. M. (2011). Structure of the ATP synthase catalytic conformation (F₁) from *Escherichia coli* in an autoinhibited conformation. *Nat. Struct. Mol. Biol.* 18, 701–707. doi:10.1038/nsmb.2058
- Cross, R. L., Grubmeyer, C., and Penefsky, H. S. (1982). Mechanism of ATP hydrolysis by beef heart mitochondrial ATPase. Rate enhancements resulting from cooperative interactions between multiple catalytic sites. *J. Biol. Chem.* 257, 12101–12105. doi:10.1016/s0021-9258(18)33684-6
- Cross, R. L., and Nalin, C. M. (1982). Adenine nucleotide binding sites on beef heart F₁-ATPase: Evidence for three exchangeable sites that are distinct from three noncatalytic sites. *J. Biol. Chem.* 257, 2874–2881. doi:10.1016/s0021-9258(19)81045-1
- García, J. J., and Capaldi, R. A. (1998). Unisite catalysis without rotation of the γ-ε domain in the *Escherichia coli* F₁-ATPase. *J. Biol. Chem.* 273, 15940–15945. doi:10.1074/jbc.273.26.15940
- Gerritsma, E., and Gaspard, P. (2010). Chemomechanical coupling and stochastic thermodynamics of the F₁-ATPase molecular motor with an applied external torque. *Biophys. Rev. Lett.* 5, 163–208. doi:10.1142/s1793048010001214
- Glynn, I. M., and Chappell, J. B. (1964). A simple method for the preparation of ³²P-labelled adenosine triphosphate of high specific activity. *Biochem. J.* 9, 147–149. doi:10.1042/bj0900147
- Hartog, A. F., and Berden, J. A. (1999). One of the non-exchangeable nucleotides of the mitochondrial F₁-ATPase is bound at a β-subunit: Evidence for a non-rotatory two-site catalytic mechanism. *Biochim. Biophys. Acta* 1412, 79–93. doi:10.1016/s0005-2728(99)00054-7
- Hasimoto, Y., Sugawa, M., Nishiguchi, Y., Aeba, F., Tagawa, A., Suga, K., et al. (2023). Direct identification of the rotary angle of ATP cleavage in F₁-ATPase from *Bacillus* PS3. *Biophys. J.* 122, 554–564. doi:10.1016/j.bpj.2022.12.027
- Hirono-Hara, Y., Noji, H., Nishiura, M., Muneyuki, E., Hara, K. Y., Yasuda, R., et al. (2001). Pause and rotation of F₁-ATPase during catalysis. *Proc. Natl. Acad. Sci. U. S. A.* 98, 13649–13654. doi:10.1073/pnas.241365698
- Jain, S., Murugavel, R., and Hansen, L. D. (2004). ATP synthase and the torsional mechanism: Resolving a 50-year-old mystery. *Curr. Sci.* 87, 16–19.
- Jain, S., and Nath, S. (2000). Kinetic model of ATP synthase: pH dependence of the rate of ATP synthesis. *FEBS Lett.* 476, 113–117. doi:10.1016/s0014-5793(00)01716-6
- Juretić, D. (2022). *Bioenergetics: A bridge across life and universe*. Boca Raton, FL, USA: CRC Press.
- Kato, Y., Matsui, T., Tanaka, N., Muneyuki, E., Hisabori, T., and Yoshida, M. (1997). Thermophilic F₁-ATPase is activated without dissociation of an endogenous inhibitor, epsilon subunit. *J. Biol. Chem.* 272, 24906–24912. doi:10.1074/jbc.272.40.24906
- Keis, S., Stocker, A., Dimroth, P., and Cook, G. M. (2006). Inhibition of ATP hydrolysis by thermoalkaliphilic F₁F₀-ATP synthase is controlled by the C terminus of the ε subunit. *J. Bacteriol.* 188, 3796–3804. doi:10.1128/jb.00040-06
- Kobayashi, R., Ueno, H., Chun-Biu, L., and Noji, H. (2020). Rotary catalysis of bovine mitochondrial F₁-ATPase studied by single-molecule experiments. *Proc. Natl. Acad. Sci. U. S. A.* 117, 1447–1456. doi:10.1073/pnas.1909407117
- Konno, H., Murakami-Fuse, T., Fujii, F., Koyama, F., Ueoka-Nakanishi, H., Pack, C. G., et al. (2006). The regulator of the F₁ motor: Inhibition of rotation of cyanobacterial F₁-ATPase by the epsilon subunit. *EMBO J.* 25, 4596–4604. doi:10.1038/sj.emboj.7601348
- Lenz, P., Joanny, J.-F., Jülicher, F., and Prost, J. (2003). Membranes with rotating motors. *Phys. Rev. Lett.* 91, 108104. doi:10.1103/physrevlett.91.108104
- Leslie, A. G. W. (2006). *Personal communication by A.G.W. Leslie to S. Nath*. Cambridge, U.K.: Medical Research Council Laboratory of Molecular Biology.
- Levy, W. B., and Calvert, V. G. (2021). Communication consumes 35 times more energy than computation in the human cortex, but both costs are needed to predict synapse number. *Proc. Natl. Acad. Sci. U. S. A.* 118, e2008173118. doi:10.1073/pnas.2008173118
- Löbba, S., Weber, J., and Senior, A. E. (1998). Catalytic site nucleotide binding and hydrolysis in F₁F₀-ATP synthase. *Biochemistry* 37, 10846–10853. doi:10.1021/bi9807153
- Martin, J., Hudson, J., Hornung, T., and Frasch, W. D. (2015). F₀-driven rotation in the ATP synthase direction against the force of F₁ ATPase in the F₀F₁ ATP synthase. *J. Biol. Chem.* 290, 10717–10728. doi:10.1074/jbc.m115.646430
- Mehta, R., Singh, J., and Nath, S. (2020). Time-resolved oxygen exchange measurements offer novel mechanistic insights into enzyme-catalyzed ATP synthesis during photophosphorylation. *J. Phys. Chem. B* 124, 5139–5148. doi:10.1021/acs.jpcc.0c03505
- Mendel-Hartwig, J., and Capaldi, R. A. (1991). Nucleotide-dependent and dicyclohexylcarbodiimide-sensitive conformational changes in the ε subunit of *Escherichia coli* ATP synthase. *Biochemistry* 30, 10987–10991. doi:10.1021/bi00109a025
- Menz, R. I., Walker, J. E., and Leslie, A. G. W. (2001). Structure of bovine mitochondrial F₁-ATPase with nucleotide bound to all three catalytic sites: Implication for the mechanism of rotary catalysis. *Cell* 106, 331–341. doi:10.1016/s0092-8674(01)00452-4
- Mitchell, P. (1981). “Bioenergetic aspects of unity in biochemistry: Evolution of the concept of ligand conduction in chemical, osmotic and chemiosmotic reaction mechanisms,” in *Of oxygen, fuels and living matter, Part 1*. Editor G. Semenza (New York: John Wiley), 30–56.
- Mitchell, P. (1969). “Chemiosmotic coupling and energy transduction,” in *Theoretical and experimental biophysics: A series of advances*. Editor A. Cole (New York: Marcel Dekker), 159–216.
- Mitchell, P. (1966). Chemiosmotic coupling in oxidative and photosynthetic phosphorylation. *Biol. Rev.* 41, 445–501. doi:10.1111/j.1469-185x.1966.tb01501.x
- Mukherjee, S., and Warshel, A. (2011). Electrostatic origin of the mechanochemical rotary mechanism and the catalytic dwell of F₁-ATPase. *Proc. Natl. Acad. Sci. U. S. A.* 108, 20550–20555. doi:10.1073/pnas.1117024108
- Nakano, A., Kishikawa, J., Nakanishi, A., Mitsuoka, K., and Yokoyama, K. (2022). Structural basis of unisite catalysis of bacterial F₀F₁-ATPase. *PNAS Nexus* 1, pgac116–8. doi:10.1093/pnasnexus/pgac116
- Nam, K., and Karplus, M. (2019). Insights into the origin of the high energy-conversion efficiency of F₁-ATPase. *Proc. Natl. Acad. Sci. U. S. A.* 116, 15924–15929. doi:10.1073/pnas.1906816116
- Nath, S. (2020b). A novel conceptual model for the dual role of F₀F₁-ATP synthase in cell life and cell death. *Biomol. Concepts* 11, 143–152. doi:10.1515/bmc-2020-0014
- Nath, S. (2006a). A novel systems biology/engineering approach solves fundamental molecular mechanistic problems in bioenergetics and motility. *Process Biochem.* 41, 2218–2235. doi:10.1016/j.procbio.2006.07.003
- Nath, S. (2017). Analysis of molecular mechanisms of ATP synthesis from the standpoint of the principle of electrical neutrality. *Biophys. Chem.* 224, 49–58. doi:10.1016/j.bpc.2017.03.002
- Nath, S. (2010a). Beyond the chemiosmotic theory: Analysis of key fundamental aspects of energy coupling in oxidative phosphorylation in the light of a torsional mechanism of energy transduction and ATP synthesis – Invited review part 1. *J. Bioenerg. Biomembr.* 42, 293–300. doi:10.1007/s10863-010-9296-5
- Nath, S. (2010b). Beyond the chemiosmotic theory: Analysis of key fundamental aspects of energy coupling in oxidative phosphorylation in the light of a torsional mechanism of energy transduction and ATP synthesis – Invited review part 2. *J. Bioenerg. Biomembr.* 42, 301–309. doi:10.1007/s10863-010-9295-6
- Nath, S. (2021b). Charge transfer across biomembranes: A solution to the conundrum of high desolvation free energy penalty in ion transport. *Biophys. Chem.* 275, 106604. doi:10.1016/j.bpc.2021.106604
- Nath, S. (2020a). Consolidation of Nath's torsional mechanism of ATP synthesis and two-ion theory of energy coupling in oxidative phosphorylation and photophosphorylation. *Biophys. Chem.* 257, 106279. doi:10.1016/j.bpc.2019.106279

- Nath, S. (2019a). Coupling in ATP synthesis: Test of thermodynamic consistency and formulation in terms of the principle of least action. *Chem. Phys. Lett.* 723, 118–122. doi:10.1016/j.cplett.2019.03.029
- Nath, S. (2021c). Coupling mechanisms in ATP synthesis: Rejoinder to “Response to molecular-level understanding of biological energy coupling and transduction”. *Biophys. Chem.* 272, 106579. doi:10.1016/j.bpc.2021.106579
- Nath, S., and Elangovan, R. (2011). New perspectives on photosynthetic phosphorylation in the light of a torsional mechanism of energy transduction and ATP synthesis. *J. Bioenerg. Biomembr.* 43, 601–610. doi:10.1007/s10863-011-9396-x
- Nath, S. (2021a). Energy landscapes and dynamics of ion translocation through membrane transporters: A meeting ground for physics, chemistry, and biology. *J. Biol. Phys.* 47, 401–433. doi:10.1007/s10867-021-09591-8
- Nath, S. (2006b). *Energy, life, and a systems approach to biology*, Vikram Sarabhai research award lecture. Ahmedabad, India: Physical Research Laboratory. <https://web.iitd.ac.in/~sunath>.
- Nath, S. (2019c). Entropy production and its application to the coupled nonequilibrium processes of ATP synthesis. *Entropy* 21:746, 1–22. doi:10.3390/e21080746
- Nath, S. (2019d). Integration of demand and supply sides in the ATP energy economics of cells. *Biophys. Chem.* 252, 106208. doi:10.1016/j.bpc.2019.106208
- Nath, S. (2019e). Interpretation of the mechanism of action of antituberculosis drug bedaquiline based on a novel two-ion theory of energy coupling in ATP synthesis. *Bioeng. Transl. Med.* 4, 164–170. doi:10.1002/btm2.10106
- Nath, S., and Jain, S. (2002). The detailed molecular mechanism of ATP synthesis in the F_0 portion of ATP synthase reveals a non-chemiosmotic mode of energy coupling. *Thermochim. Acta* 394, 89–98. doi:10.1016/s0040-6031(02)00242-3
- Nath, S., and Jain, S. (2000). Kinetic modeling of ATP synthesis by ATP synthase and its mechanistic implications. *Biochem. Biophys. Res. Commun.* 272, 629–633. doi:10.1006/bbrc.2000.2774
- Nath, S. (2019b). Modern theory of energy coupling and ATP synthesis. Violation of Gauss's law by the chemiosmotic theory and validation of the two-ion theory. *Biophys. Chem.* 255, 106271. doi:10.1016/j.bpc.2019.106271
- Nath, S. (2003). Molecular mechanisms of energy transduction in cells: Engineering applications and biological implications. *Adv. Biochem. Eng. Biotechnol.* 85, 125–180. doi:10.1007/3-540-36466-8_5
- Nath, S. (2018a). Molecular mechanistic insights into coupling of ion transport to ATP synthesis. *Biophys. Chem.* 241, 20–26. doi:10.1016/j.bpc.2018.07.006
- Nath, S. (2018b). Molecular mechanistic insights into uncoupling of ion transport from ATP synthesis. *Biophys. Chem.* 242, 15–21. doi:10.1016/j.bpc.2018.08.006
- Nath, S. (2022d). Network representation and analysis of energy coupling mechanisms in cellular metabolism by a graph-theoretical approach. *Theory Biosci.* 141, 249–260. doi:10.1007/s12064-022-00370-0
- Nath, S. (2022b). Novel molecular insights into ATP synthesis in oxidative phosphorylation based on the principle of least action. *Chem. Phys. Lett.* 796, 139561. doi:10.1016/j.cplett.2022.139561
- Nath, S. (2018c). Optimality principle for the coupled chemical reactions of ATP synthesis and its molecular interpretation. *Chem. Phys. Lett.* 699, 212–217. doi:10.1016/j.cplett.2018.03.068
- Nath, S., Rohatgi, H., and Saha, A. (1999). The torsional mechanism of energy transfer in ATP synthase. *Curr. Sci.* 77, 167–169.
- Nath, S. (2022c). Supercomplex supercomplexes: Raison d'être and functional significance of supramolecular organization in oxidative phosphorylation. *Biomol. Concepts* 13, 272–288. doi:10.1515/bmc-2022-0021
- Nath, S. (2002). The molecular mechanism of ATP synthesis by F_1F_0 -ATP synthase: A scrutiny of the major possibilities. *Adv. Biochem. Eng. Biotechnol.* 74, 65–98. doi:10.1007/3-540-45736-4_4
- Nath, S. (2022a). The need for consistency with physical laws and logic in choosing between competing molecular mechanisms in biological processes: A case study in modeling ATP synthesis. *Function* 3 (6), zqac054. doi:10.1093/function/zqac054
- Nath, S. (2008). The new unified theory of ATP synthesis/hydrolysis and muscle contraction, its manifold fundamental consequences and mechanistic implications and its applications in health and disease. *Int. J. Mol. Sci.* 9, 1784–1840. doi:10.3390/ijms9091784
- Nath, S. (2016). The thermodynamic efficiency of ATP synthesis in oxidative phosphorylation. *Biophys. Chem.* 219, 69–74. doi:10.1016/j.bpc.2016.10.002
- Nath, S. (2004). The torsional mechanism of energy transduction and ATP synthesis as a breakthrough in our understanding of the mechanistic, kinetic and thermodynamic details. *Thermochim. Acta* 422, 5–17. doi:10.1016/j.tca.2004.08.004
- Nath, S., and Villadsen, J. (2015). Oxidative phosphorylation revisited. *Biotechnol. Bioeng.* 112, 429–437. doi:10.1002/bit.25492
- Nath, S., Rohatgi, H., and Saha, A. (2000). The catalytic cycle of ATP synthesis by means of a torsional mechanism. *Curr. Sci.* 78, 23–27.
- Nath, S. S., and Nath, S. (2009). Energy transfer from adenosine triphosphate: Quantitative analysis and mechanistic insights. *J. Phys. Chem. B* 113, 1533–1537. doi:10.1021/jp809678n
- Nishizaka, T., Oiwa, K., Noji, H., Kimura, S., Muneyuki, E., Kinoshita, K., et al. (2004). Chemomechanical coupling in F_1 -ATPase revealed by simultaneous observation of nucleotide kinetics and rotation. *Nat. Struct. Mol. Biol.* 11, 142–148. doi:10.1038/nsmb721
- Noji, H., Yasuda, R., Yoshida, M., and Kinoshita, K. (1997). Direct observation of the rotation of F_1 -ATPase. *Nature* 386, 299–302. doi:10.1038/386299a0
- Oster, G., and Wang, H. (2000). Reverse engineering a protein: The mechanochemistry of ATP synthase. *Biochim. Biophys. Acta* 1458, 482–510. doi:10.1016/s0005-2728(00)00096-7
- Penefsky, H. S. (1979). Preparation of beef heart mitochondrial ATPase. *Methods Enzymol.* 55, 304–308. doi:10.1016/0076-6879(79)55035-6
- Penefsky, H. S. (1985). Reaction mechanism of the membrane-bound ATPase of submitochondrial particles from beef heart. *J. Biol. Chem.* 260, 13728–13734. doi:10.1016/s0021-9258(17)38786-0
- Phillips, R. C., George, P., and Rutman, R. J. (1969). Thermodynamic data for the hydrolysis of adenosine triphosphate as a function of pH, Mg^{2+} ion concentration, and ionic strength. *J. Biol. Chem.* 244, 3330–3342. doi:10.1016/s0021-9258(18)93131-5
- Rees, D. M., Montgomery, M. G., Leslie, A. G., and Walker, J. E. (2012). Structural evidence of a new catalytic intermediate in the pathway of ATP hydrolysis by F_1 -ATPase from bovine heart mitochondria. *Proc. Natl. Acad. Sci. U. S. A.* 109, 11139–11143. doi:10.1073/pnas.1207587109
- Rohatgi, H., Saha, A., and Nath, S. (1998). Mechanism of ATP synthesis by protonmotive force. *Curr. Sci.* 75, 716–718.
- Rosing, J., and Slater, E. C. (1972). The value of ΔG° for the hydrolysis of ATP. *Biochim. Biophys. Acta* 267, 275–290. doi:10.1016/0005-2728(72)90116-8
- Sakaki, N., Shimo-Kon, R., Adachi, K., Itoh, H., Furuie, S., Muneyuki, E., et al. (2005). One rotary mechanism for F_1 -ATPase over ATP concentrations from millimolar down to nanomolar. *Biophys. J.* 88, 2047–2056. doi:10.1529/biophysj.104.054668
- Senior, A. E., Lee, R. S. F., Al-Shawi, M. K., and Weber, J. (1992). Catalytic properties of *Escherichia coli* F_1 -ATPase depleted of endogenous nucleotides. *Arch. Biochem. Biophys.* 297, 340–344. doi:10.1016/0003-9861(92)90682-m
- Senior, A. E., Nadanaciva, S., and Weber, J. (2002). The molecular mechanism of ATP synthesis by F_1F_0 -ATP synthase. *Biochim. Biophys. Acta* 1553, 188–211. doi:10.1016/s0005-2728(02)00185-8
- Shah, N. B., Hutcheon, M. L., Haarer, B. K., and Duncan, T. M. (2013). F_1 -ATPase of *Escherichia coli*: The epsilon-inhibited state forms after ATP hydrolysis, is distinct from the ADP-inhibited state, and responds dynamically to catalytic site ligands. *J. Biol. Chem.* 288, 9383–9395. doi:10.1074/jbc.m113.451583
- Shimabukuro, K., Muneyuki, E., and Yoshida, M. (2006). An alternative reaction pathway of F_1 -ATPase suggested by rotation without 80°/40° substeps of a sluggish mutant at low ATP. *Biophys. J.* 90, 1028–1032. doi:10.1529/biophysj.105.067298
- Shimabukuro, K., Yasuda, R., Muneyuki, E., Hara, K. Y., Kinoshita, K., and Yoshida, M. (2003). Catalysis and rotation of F_1 motor: Cleavage of ATP at the catalytic site occurs in 1 ms before 40° substep rotation. *Proc. Natl. Acad. Sci. U. S. A.* 100, 14731–14736. doi:10.1073/pnas.2434983100
- Shirakihara, Y., Shiratori, A., Tanikawa, H., Nakasako, M., Yoshida, M., and Suzuki, T. (2015). Structure of a thermophilic F_1 -ATPase inhibited by an ϵ -subunit: Deeper insight into the ϵ -inhibition mechanism. *FEBS J.* 282, 2895–2913. doi:10.1111/febs.13329
- Sobti, M., Ishmukhametov, R., Bouwer, J. C., Ayer, A., Suarna, C., Smith, N. J., et al. (2019). Cryo-EM reveals distinct conformations of *E. coli* ATP synthase on exposure to ATP. *eLife* 8, e43864. doi:10.7554/eLife.43864
- Sobti, M., Smits, C., Wong, A. S. W., Ishmukhametov, R., Stock, D., Sandin, S., et al. (2016). Cryo-EM structures of the autoinhibited *E. coli* ATP synthase in three rotational states. *eLife* 5, e21598. doi:10.7554/eLife.21598
- Sobti, M., Ueno, H., Noji, H., and Stewart, A. G. (2021). The six steps of the complete F_1 -ATPase rotary catalytic cycle. *Nat. Commun.* 12, 4690. doi:10.1038/s41467-021-25029-0
- Sternweis, P. C., and Smith, J. B. (1980). Characterization of the inhibitory (ϵ -subunit) subunit of the proton-translocating adenosine triphosphatase from *Escherichia coli*. *Biochem. J.* 19, 526–531. doi:10.1021/bi00544a021
- Suzuki, T., Tanaka, K., Wakabayashi, C., Saita, E., and Yoshida, M. (2014). Chemomechanical coupling of human mitochondrial F_1 -ATPase motor. *Nat. Chem. Biol.* 10, 930–936. doi:10.1038/nchembio.1635
- Villadsen, J., Nielsen, J., and Lidén, G. (2011). *Bioreaction engineering principles*. 3rd ed. New York: Springer. Chapter 4.
- Volkán-Kacsó, S., and Marcus, R. A. (2022). F_1 -ATPase rotary mechanism: Interpreting results of diverse experimental modes with an elastic coupling theory. *Front. Microbiol.* 13, 861855. doi:10.3389/fmicb.2022.861855
- Volkán-Kacsó, S., and Marcus, R. A. (2017). Theory of long binding events in single-molecule-controlled rotation experiments on F_1 -ATPase. *Proc. Natl. Acad. Sci. U. S. A.* 114, 7272–7277. doi:10.1073/pnas.1705960114
- Wang, H., and Oster, G. (1998). Energy transduction in the F_1 -motor of ATP synthase. *Nature* 396, 279–282. doi:10.1038/24409
- Watanabe, R., Koyasu, K., You, H., Tanigawara, M., and Noji, H. (2015). Torque transmission mechanism via DELSEED loop of F_1 -ATPase. *Biophys. J.* 108, 1144–1152. doi:10.1016/j.bpj.2015.01.017
- Weber, J., Bowman, C., and Senior, A. E. (1996). Specific tryptophan substitution in catalytic sites of *Escherichia coli* F_1 -ATPase allows differentiation between bound

substrate ATP and product ADP in steady-state catalysis. *J. Biol. Chem.* 271, 18711–18718. doi:10.1074/jbc.271.31.18711

Weber, J., Dunn, S. D., and Senior, A. E. (1999). Effect of the ϵ -subunit on nucleotide binding to *Escherichia coli* F₁-ATPase catalytic sites. *J. Biol. Chem.* 274, 19124–19128. doi:10.1074/jbc.274.27.19124

Weber, J., and Senior, A. E. (2001). Bi-site catalysis in F₁-ATPase: Does it exist? *J. Biol. Chem.* 276, 35422–35428. doi:10.1074/jbc.m104946200

Weber, J., and Senior, A. E. (1997). Catalytic mechanism of F₁-ATPase. *Biochim. Biophys. Acta* 1319, 19–58. doi:10.1016/s0005-2728(96)00121-1

Weber, J., Wilke-Mounts, S., Lee, R. S.-F., Grell, E., and Senior, A. E. (1993). Specific placement of tryptophan in the catalytic sites of *Escherichia coli* F₁-ATPase provides a direct probe of nucleotide binding: Maximal ATP hydrolysis occurs with three sites occupied. *J. Biol. Chem.* 268, 20126–20133. doi:10.1016/s0021-9258(20)80703-0

Wilkens, S., and Capaldi, R. A. (1998). Solution structure of the ϵ subunit of the F₁-ATPase from *Escherichia coli* and interactions of this subunit with β subunits in the complex. *J. Biol. Chem.* 273, 26645–26651. doi:10.1074/jbc.273.41.26645

Wray, V. (2015). Commentary on Nath and Villadsen review entitled “Oxidative phosphorylation revisited” *Biotechnol. Bioeng.* 112, 1984–1985.

Yasuda, R., Noji, H., Yoshida, M., Kinosita, K., and Itoh, H. (2001). Resolution of distinct rotational substeps by submillisecond kinetic analysis of F₁-ATPase. *Nature* 410, 898–904. doi:10.1038/35073513

Zarco-Zavala, M., Watanabe, R., McMillan, D. G. G., Suzuki, T., Ueno, H., Mendoza-Hoffmann, F., et al. (2020). The $3 \times 120^\circ$ rotary mechanism of *Paracoccus denitrificans* F₁-ATPase is different from that of the bacterial and mitochondrial F₁-ATPases. *Proc. Natl. Acad. Sci. U. S. A.* 117, 29647–29657. doi:10.1073/pnas.2003163117



OPEN ACCESS

EDITED BY

Marta De Zotti,
University of Padua, Italy

REVIEWED BY

Kalavathy Rajan,
The University of Tennessee, Knoxville,
United States
Ajaya Bhattarai,
Tribhuvan University, Nepal

*CORRESPONDENCE

Wooseog Jeong,
✉ wjeong@korea.kr

RECEIVED 12 April 2023

ACCEPTED 07 June 2023

PUBLISHED 16 June 2023

CITATION

Rhee CH, Lee H-s, Yun H-j, Lee G-H,
Kim S-J, Song S, Lee M-H, Her M and
Jeong W (2023), Chemical stability of
active ingredients in diluted veterinary
disinfectant solutions under simulated
storage conditions.
Front. Chem. 11:1204477.
doi: 10.3389/fchem.2023.1204477

COPYRIGHT

© 2023 Rhee, Lee, Yun, Lee, Kim, Song,
Lee, Her and Jeong. This is an open-
access article distributed under the terms
of the [Creative Commons Attribution
License \(CC BY\)](#). The use, distribution or
reproduction in other forums is
permitted, provided the original author(s)
and the copyright owner(s) are credited
and that the original publication in this
journal is cited, in accordance with
accepted academic practice. No use,
distribution or reproduction is permitted
which does not comply with these terms.

Chemical stability of active ingredients in diluted veterinary disinfectant solutions under simulated storage conditions

Chae Hong Rhee^{1,2}, Hye-sook Lee³, Hyeong-jun Yun³,
Ga-Hee Lee³, Su-Jeong Kim¹, Sok Song¹, Myoung-Heon Lee¹,
Moon Her¹ and Wooseog Jeong^{1*}

¹Veterinary Drugs and Biologics Division, Animal and Plant Quarantine Agency, Gimcheon-si, Gyeongsangbuk-do, Republic of Korea, ²Laboratory of Veterinary Pharmacokinetics and Pharmacodynamics, College of Veterinary Medicine, Kyungpook National University, Daegu, Republic of Korea, ³Korea Animal Health Products Association, Seongnam-si, Gyeonggi-do, Republic of Korea

Introduction: The product labels of veterinary disinfectants specify their expiration dates to prevent the use of outdated products, as these may result in disinfection and biosecurity failures during outbreak situations. However, a clear standard for the storage conditions of diluted disinfectant solutions has not yet been established, and the effects of storage conditions have scarcely been investigated. To fill this research gap, our study examined the stability of the active ingredients of diluted veterinary disinfectants based on their change in concentrations when stored at various temperatures for various time periods.

Methods: Twenty veterinary disinfectants effective against either foot-and-mouth disease or avian influenza viruses were selected. The disinfectants were diluted to effective concentrations following the manufacturer's instructions. Using selective analytical techniques, the concentrations of the active ingredients of the samples that had been stored for varying intervals at different temperatures (4, 20, 30, and 45°C) were determined. These samples included soaps and detergents, acids, oxidizing agents, aldehydes, and copper compounds. The active ingredient concentrations of two of the samples were determined following freezing/thawing cycle, to establish their stability when exposed to simulated winter conditions.

Results: Our results showed that most of the active ingredients had concentrations of 90% or greater of their initial concentrations, indicating ≥90% stability over a 21-day period under the experimental storage conditions. However, there were some exceptions. Glutaraldehyde, formaldehyde, and malic acid are over 90% stable at ≤ 30°C for 21 days, but their concentrations decreased to below 90% of their initial concentrations at 45°C, indicating a decline in stability when stored at 45°C for 21 days. The concentrations of potassium peroxydisulfate and peracetic acid rapidly declined with increasing time and temperature to less than 90% of their initial concentrations.

Discussion: Based on our findings, we propose that diluted disinfectant solutions should preferably be prepared daily. However, if the daily preparation of a diluted disinfectant solution is not feasible, then our results can be used as a reference, providing basic scientific data on the chemical stability of diluted disinfectant

solutions commonly used in the veterinary field, thus indicating suitable storage conditions.

KEYWORDS

content analysis, disinfectant, chemical stability, HPLC, active ingredient, titration, icp-oes

1 Introduction

The active ingredients in a disinfectant are the chemicals responsible for inhibiting the growth of microorganisms. The contents of these ingredients are listed as percentages or concentrations on the product label, along with their respective expiration dates. The expiry period is based on the stability of the active ingredients, known to decline over time owing to several chemical processes triggered by various conditions.

In South Korea, the Animal and Plant Quarantine Agency (APQA) performs quality control of commercial veterinary disinfectants, both through an official approval step and an annual post-market surveillance study, evaluating their efficacy against the targeted microorganisms and the contents of the active ingredients in the final product (Rhee et al., 2022). Currently, the efficacy against the targeted microorganism is assessed by the dilution concentration indicated on the label; however, the content of the active ingredient in the final product is used to determine whether it conforms to the stability specification of 90%–120% of the label claim (Rhee et al., 2022).

Disinfectants are classically grouped into soaps and detergents, alkalis, acids, chlorine and chlorine compounds, oxidizing agents, aldehydes, phenol compounds, quaternary ammonium compounds (QACs), and alcohols (Maris, 1995; Geering et al., 2001; De Benedictis et al., 2007). The World Organization for Animal Health (OIE) has grouped viruses into three categories, denoted as A, B, and C, in terms of resistance to chemical agents, and has presented the best type of disinfectant to use on a range of commonly contaminated items for each disease or group of diseases (Geering et al., 2001). The choice of disinfectant for a specific application is critical in achieving maximum effectiveness. In addition, an appropriate concentration of a disinfectant is important to achieve optimal results in an outbreak situation, whereas the stability of its active ingredient is crucial to ensure the efficacy of the disinfectant throughout its shelf life (Farrag et al., 2023). Stability of the active ingredient is one of many factors that influence the overall stability of a disinfectant product (Singh and Bakshi, 2000; Bajaj et al., 2012; Farrag et al., 2023).

Numerous studies have investigated the efficacy of active ingredients or disinfectants against microorganisms; at specific concentrations, for given time intervals and/or various temperatures (Muhammad et al., 2001; Yilmaz et al., 2004; De Benedictis et al., 2007; Jang et al., 2014; Singh et al., 2017; Lin et al., 2020; Pironti et al., 2021; Kobayashi et al., 2022; Xiao et al., 2022). Phenol compounds have been tested for their ability to inactivate the highly pathogenic avian influenza virus (HPAIV) at different concentrations (0.1%, 0.2% and 0.4%) and for different contact times (6, 12, 18 and 24 h) (Muhammad et al., 2001). The efficacies of chlorhexidine gluconate and ethanol, the active ingredients of hand sanitizers, have been investigated by a time-kill test against bacteria and fungi (Kobayashi et al., 2022), whereas

the efficacy of a commercial organic acid containing disinfectant against a low pathogenic avian influenza virus (LPAIV) has been investigated at different concentrations (0.1%, 0.5%, 1% and 2%) and temperatures (4, 10 and 20°C), and for different contact times (5, 10, 15, 30, 60 and 120 min) (Yilmaz et al., 2004). Singh et al. (2017) have evaluated the virucidal efficacy of commercial disinfectants belonging to chlorine, phenol, and a combination of QACs and aldehydes, against the Senecavirus A at 4°C–25°C with contact intervals of 1–15 min. Jang et al. (2014) have evaluated the changes in the efficacies of disinfectants belonging to acids, oxidizing agents, and aldehydes at different temperatures (25, 4, 0 and –10°C) and different contact times (1 and 5 min) to establish the optimal conditions for disinfection against H9N2 LPAIV. Pironti et al. (2021) have assessed the antimicrobial properties of permaleic acid (PMA) and peracetic acid (PAA) against *Escherichia coli* and *Staphylococcus aureus* at concentrations ranging from 10 to 0.002 g/L and at contact times of 30, 60 and 90 min. Other authors have summarized the studies on the common chemical disinfectants and their virucidal efficacies under various application conditions. Lin et al. (2020) have reviewed the effectiveness of disinfectants against viruses under various conditions, such as concentration, exposure time duration, and temperature, whereas Xiao et al. (2022) have reviewed the virucidal efficacy of disinfectants against SARS-CoV-2. Xiao et al. have included the types and concentrations of the chemical disinfectants, the formulations, and the exposure times in their review.

However, research on the stability of active ingredients, based on concentration changes in diluted veterinary disinfectant solutions under certain storage conditions, is scarce and there is a lack of scientific evidence regarding the relationship between the actual concentration of active ingredients in diluted disinfectant solutions and their efficacies. Moreover, as no clear standard has yet been established for the storage conditions of diluted disinfectant solutions, daily replacement and preparation of fresh dilutions are recommended in most disinfection protocols to ensure optimal efficacy (Dvorak, 2008; Rutala and Weber, 2008). In infectious animal disease outbreaks, disinfectants are used in large quantities outdoors. The required amounts depend on various factors, such as the target organisms, degree of traffic flow, area size, and organic matter. In such situations, the daily preparation of a diluted disinfectant solution may not be feasible.

In this study we attempted to elucidate how the concentrations of the active ingredients of diluted disinfectant solutions and therefore their stabilities change under various storage conditions. The study included the assessment of the stability of diluted disinfectant solutions when exposed to a freezing/thawing cycle, to investigate the stability of diluted disinfectant solutions during January, known as the coldest month in South Korea with average temperatures reaching –6.9°C to 3.6°C (KMA, 2023). In the winter season, heat wires, thermostats, indoor storage, and other means are used to prevent freezing of the diluted disinfectant solutions as their

TABLE 1 Description and contents of active ingredients in the twenty disinfectants used in this study.

Classification	Disinfectant	Active ingredient		Content on label*	Active concentration** (%)	Analytical application
Soaps and detergents	A	Quaternary ammonium chloride	Didecyl dimethyl ammonium chloride	5% (w/v)	0.100	Titration
Combinations (Soaps and detergents + Acids)	B	Quaternary ammonium chloride	Alkyl dimethyl benzyl ammonium chloride	10% (w/v)	0.063	Titration
		Citric acid		20% (w/v)	0.125	HPLC
Combinations (Soaps and detergents + Aldehydes)	C	Quaternary ammonium chloride	Alkyl dimethyl benzyl ammonium chloride	6% (w/v)	0.040	Titration
		Glutaraldehyde		5% (w/v)	0.033	HPLC
		Formaldehyde		8% (w/v)	0.053	HPLC
Combinations (Soaps and detergents + Aldehydes)	D	Quaternary ammonium chloride	Alkyl dimethyl benzyl ammonium chloride	10% (w/v)	0.042	Titration
		Citric acid		30% (w/v)	0.125	HPLC
Combinations (Soaps and detergents + Acids)	E	Quaternary ammonium chloride	Alkyl dimethyl benzyl ammonium chloride	10% (w/v)	0.063	Titration
		Citric acid		20% (w/v)	0.125	HPLC
		Phosphoric acid		10% (w/v)	0.063	ICP-OES
Combinations (Soaps and detergents + Aldehydes)	F	Quaternary ammonium chloride	Coco dimethyl benzyl ammonium chloride	10% (w/v)	0.156	Titration
		Glutaraldehyde		15% (w/v)	0.234	Titration
Acids	G	Citric acid		50% (w/v)	0.333	HPLC
Acids	H	Citric acid		50% (w/v)	0.313	HPLC
Acids	I	Citric acid		40% (w/v)	0.267	HPLC
Acids	J	Citric acid		20% (w/v)	0.080	HPLC
		Acetic acid		10% (w/v)	0.040	HPLC
		Phosphoric acid		10% (w/v)	0.040	ICP-OES
Oxidizing agents	K	Potassium peroxymonosulfate		50% (w/w)	0.250	Titration
Oxidizing agents	L	Potassium peroxymonosulfate		50% (w/w)	0.250	Titration
Oxidizing agents	M	Potassium peroxymonosulfate		50% (w/w)	0.250	Titration
		Sodium dichloroisocyanurate		5% (w/w)	0.025	
Oxidizing agents	N	Potassium peroxymonosulfate		50% (w/w)	0.500	Titration
		Malic acid		10% (w/w)	0.100	HPLC
Oxidizing agents	O	Hydrogen peroxide		25% (w/w)	0.031	Titration
		Peracetic acid		5% (w/w)	0.006	Chronoamperometry
Oxidizing agents	P	Hydrogen peroxide		27.5% (w/v)	0.034	Titration
		Peracetic acid		5.8% (w/v)	0.007	Chronoamperometry

(Continued on following page)

TABLE 1 (Continued) Description and contents of active ingredients in the twenty disinfectants used in this study.

Classification	Disinfectant	Active ingredient	Content on label*	Active concentration** (%)	Analytical application
Oxidizing agents	Q	Hydrogen peroxide	27.5% (w/v)	0.046	Titration
		Peracetic acid	5.8% (w/v)	0.010	Chronoamperometry
Aldehydes	R	Glutaraldehyde	10% (w/v)	0.200	Titration
Oxidizing agents	S	Sodium hypochlorite (4%–6%)	99% (w/v)	0.079–0.119	Titration
Copper compound	T	Copper sulfate pentahydrate	20% (w/w)	0.318	Titration

* Concentration of active ingredient.

** Concentration of active ingredient in the diluted disinfectant solution used in the experiments.

stability when frozen has not been confirmed scientifically. We evaluated diluted disinfectant solutions of various chemical compositions in our study, including soaps and detergents, acids, oxidizing agents, aldehydes, and copper compounds, under various storage conditions (Table 1). These conditions were chosen to assess how specific storage conditions such as temperatures and storage times affect the efficacy of disinfectants. Concentration-based assays were performed to determine the changes in the contents of the active ingredients, thereby generating basic scientific data to establish the stabilities of the active ingredients, and to suggest suitable storage conditions for the diluted disinfectant solutions.

2 Materials and methods

2.1 Disinfectants

Twenty veterinary disinfectants, approved by the APQA as effective against either foot-and-mouth disease virus (FMDV) or avian influenza virus (AIV), were selected and classified according to their major active ingredients. The categories of active ingredients in disinfectants are detergents, acids, oxidizing agents, aldehydes, and copper compounds. A summary of the disinfectants and the classification of chemical disinfectants is presented in Table 1. All disinfectants were diluted with tap water to obtain the authorized effective concentrations against the targeted pathogens, and defined as diluted disinfectant solutions.

2.2 Stability testing conditions

The stability of the active ingredients in the 20 diluted disinfectant solutions was studied at four temperatures (4, 20, 30 and 45°C) and at different time intervals (0, 1, 2, 3, 5, 7, 10, 14 and 21 days). The active ingredient of each sample was assessed immediately after preparation (Day 0), prior to storage at the set temperature, and again after removal from storage at the set time intervals, using selective analytical techniques. Additionally, two diluted disinfectant solutions were assayed for changes in the content of active ingredients during a freezing/thawing cycle, i.e., the solutions were frozen after testing on the day of dilution (Day 0), thawed on the next day (Day 1), tested, and frozen again. The active ingredient of a sample was considered stable if it was within 90%–120% of its initial concentration.

2.3 Content analysis applications

2.3.1 Chemical reagents

U.S. Pharmacopeia (USP) reference standards for citric acid (CA, ≥99% purity), malic acid (MA, ≥99% purity), acetic acid (AA, ≥99% purity), glutaraldehyde (GLT, Grade I, 25% in H₂O), and formaldehyde (FAL, 37% stabilized with methanol) were used for high-performance liquid chromatography (HPLC) analysis. A phosphorus standard solution (1,000 mg/L) was purchased from Sigma–Aldrich (St. Louis, MO, United States) for inductively coupled plasma optical emission spectroscopy (ICP-OES). HPLC-grade water was obtained from Honeywell Burdick and Jackson (Morristown, NJ, United States). For the titration method validation, potassium peroxydisulfate (PPMS, 99% purity), hydrogen peroxide (H₂O₂, 35% in H₂O), and GLT (Grade I, 25% in H₂O) were purchased from Sigma–Aldrich, and other active ingredients were obtained from the manufacturers. The standard solutions of quaternary ammonium compounds (QACs), sodium hypochlorite (NaOCl, 5.50% available chlorine), and copper sulfate pentahydrate (CuSO₄·5H₂O, 99.6% purity) were provided by the manufacturers. The QACs of didecyl dimethyl ammonium chloride (DDAC), alkyl dimethyl benzyl ammonium chloride (ADBAC), and coco dimethyl benzyl ammonium chloride (CDBAC) were of 81%, 50.58%, and 50.12% purity, respectively. All other reagents were of analytical grade.

2.3.2 Titration

Determination of the QACs, GLT, PPMS, sodium dichloroisocyanurate (NaDCC), H₂O₂, NaOCl, and CuSO₄·5H₂O were directly performed via titration using an automated titrator (888 Titrand, Metrohm, Herisau, Switzerland), according to the previously validated and/or slightly modified APQA procedures (APQA, 2015; APQA, 2017; Rhee et al., 2022). Supplementary Figures S1, S2 illustrate the analytical procedure for the titration methods. The QACs were quantified using three different manual titration procedures: DDAC was determined using a titrant of silver nitrate (Supplementary Figure S1); ADBAC was determined using a titrant of sodium tetraphenylborate solution (Supplementary Figure S1); and CDBAC was determined using a titrant of sodium lauryl sulfate (Supplementary Figure S1). The concentrations of GLT and H₂O₂, as the single active ingredient in the disinfectant, were determined using a titration method (Supplementary Figure S2).

Available oxygen was determined for the content analysis of PPMS and/or a combination of PPMS and NaDCC (Supplementary Figure S2), and available chloride was determined for NaOCl content analysis (Supplementary Figure S2). The concentration of copper sulfate (CuSO_4) was determined for $\text{CuSO}_4 \cdot 5\text{H}_2\text{O}$ content analysis (Supplementary Figure S2). Each experiment was performed in triplicate, and the average values were used for analysis. The results were expressed as a percentage of the results obtained on Day 0 (baseline).

2.3.3 HPLC-DAD analysis

All samples taken from the diluted disinfectant solutions were filtered through a $0.45\ \mu\text{m}$ membrane filter (Millipore, Bedford, MA, United States) before injection. An HPLC system (Agilent 1,260 Infinity II series, United States) equipped with a pump (Model G7111 A), autosampler (Model G7129 A), sample thermostat (Model G4761 A), column oven (Model G7116 A), and a diode array detector (DAD; Model G7117C) was used to analyze CA, MA, AA, GLT, and FAL. Chemstation Software (Version Rev C.01.10 (236)) was used for data processing and evaluation. The analytical chromatographic separations of CA, MA, and AA were performed on a Zorbax SB-Aq column ($4.6 \times 150\ \text{mm}$, $5\ \mu\text{m}$), with the following conditions. A mobile phase composed of a 50 mM potassium phosphate buffer (KH_2PO_4) adjusted to pH 2.0 with phosphoric acid; flow rate of 1.0 mL/min; column compartment temperature of 35°C ; injection volume of $10\ \mu\text{L}$; and ultraviolet (UV) detection at 210 nm. The analytical chromatographic separations of GLT and FAL were performed after derivatization with 2,4-dinitrophenylhydrazine (DNPH), on a Zorbax SB-Aq column ($4.6 \times 150\ \text{mm}$, $5\ \mu\text{m}$) with a mobile phase composed of acetonitrile and water (72:28 v/v); flow rate of 1.0 mL/min; column compartment temperature of 40°C ; injection volume of $5\ \mu\text{L}$; and UV detection at 360 nm. The concentrations of the active ingredients were obtained using a calibration curve. Each experiment was performed in triplicate, and the average values were used for analysis. The results were expressed as a percentage of the results obtained on Day 0 (baseline).

2.3.4 ICP-OES analysis

The phosphoric acid (PA) content was determined by quantifying the phosphorus in the samples, using an ICP-OES (Perkin Elmer, United States, Model Optima 2100 DV). Phosphorus was determined in the axial configuration, and argon (99.99 v/v%) was used for plasma generation at a flow rate of 1.0 mL/min. The spectral wavelength selected for phosphorus analysis was 213.617 nm. The phosphorus concentration was obtained using a calibration curve. Each experiment was performed in triplicate, and the average values were used for analysis. The results were expressed as a percentage of the results obtained on Day 0 (baseline).

2.3.5 Chronoamperometry measurement

To measure the concentration of peracetic acid (PAA), the chronoamperometry test Kemio™ (Palintest, Gateshead, United Kingdom) with corresponding sensors for PAA was used. Each experiment was performed in triplicate, and the average values were used for analysis. The results were expressed as a percentage of the results obtained on Day 0 (baseline).

2.4 Data analysis

Data analyses were performed using Microsoft Excel 2019. All data were expressed as the mean, and significant differences were calculated using an ANOVA. Linear regression analyses were performed on Excel, and the 95% confidence intervals (CIs) were calculated using a reported formula (Hossain et al., 2013). The active ingredient contents obtained on each day of analysis were converted to a percentage of that measured on Day 0 (baseline). For each active ingredient, the time dependence of the mean percentage of the Day 0 concentration was determined, and the active ingredient was considered stable if the sample was within 90%–120% of its initial concentration. Content stability was reported as the number of days in which the lower level of the 95% CI for each ingredient at each temperature remained at or above 90% of the initial baseline concentration, indicating $\geq 90\%$ stability.

3 Results

A total of 14 active ingredients in 20 diluted disinfectant solutions were analyzed for content stability in this study: QACs including DDAC, ADBAC, and CDBAC; acids including CA, MA, PA, AA, and PAA; oxidizing agents including PPMS, H_2O_2 , and NaOCl; aldehydes including GLT and FAL; and $\text{CuSO}_4 \cdot 5\text{H}_2\text{O}$.

3.1 Analytical method validation

The analytical methods were validated to demonstrate their suitability for the intended purposes.

3.1.1 Titration methods

For the titration method, the titrant volume at the end-point increased linearly with increasing concentrations for each active ingredient. Five tests were conducted for each titration assay, over a standard concentration range covering the concentrations of the compounds in the samples; the regression coefficients (R^2) were ≥ 0.9998 in all cases. The standard concentration ranges were 10–100 mg for DDAC, 1–10 mg for ADBAC, 5–50 mg for CDBAC, 10–80 mg for GLT, 2–30 mg for PPMS, 5–75 mg for H_2O_2 , 5.5–60 mg for NaOCl, and 5–40 mg for $\text{CuSO}_4 \cdot 5\text{H}_2\text{O}$. Precision was expressed as a percentage relative standard deviation (RSD%), and the obtained RSD% values were: $\leq 1\%$ for DDAC, $\leq 0.5\%$ for ADBAC, $\leq 1.56\%$ for CDBAC, $\leq 0.5\%$ for GLT, $< 1\%$ for PPMS, $\leq 1.5\%$ for H_2O_2 , $\leq 1.2\%$ for NaOCl, and $\leq 0.8\%$ for $\text{CuSO}_4 \cdot 5\text{H}_2\text{O}$. These results represent both intra-day and inter-day performances, indicating an acceptable degree of precision for all the titration methods.

3.1.2 HPLC methodology

Table 2 presents the analytical parameters, including linearity, limit of detection (LOD), limit of quantification (LOQ), precision, and accuracy, obtained for the validation of the HPLC method used for AA, CA, MA, GLT, and FAL determinations. Calibration graphs were prepared over a 5-point standard concentration range. All compounds exhibited linear relationships between concentrations and instrument responses, with regression coefficients of ≥ 0.9999 , and the methods showed adequate precision. The RSD values were within 0.90% and 0.58%, the mean recoveries of the standard solutions were within

TABLE 2 Analytical features of the method used for the determination of acids and aldehydes using HPLC.

Active ingredient	Linearity			LOD (µg/mL)	LOQ (µg/mL)	Accuracy			Precision		
	Concentration (µg/mL)	Regression equation	R^{2*}			Added concentration (µg/mL)	Recovery mean (%) ± SD	RSD (%)	Amount (g)	Measured mean (%) ± SD	RSD (%)
Acetic acid	2–20	$y = 0.6785x + 0.1136$	0.9999	0.55	1.68	30	101.58 ± 0.42	0.35	1.0	97.73 ± 0.22	0.22
(AA)						50	102.76 ± 0.48	0.34	2.0	96.99 ± 0.23	0.23
						100	100.19 ± 0.35	0.19	3.0	97.08 ± 0.20	0.21
Citric acid	2–20	$y = 1.2856x + 0.198$	1.0000	0.54	1.65	30	103.40 ± 0.71	0.44	0.1	101.69 ± 0.81	0.81
(CA)						50	99.28 ± 1.28	0.72	0.2	101.13 ± 0.90	0.90
						100	99.75 ± 1.60	0.70	0.3	101.45 ± 0.26	0.26
Malic acid	2–20	$y = 1.046x + 0.101$	1.0000	0.32	0.97	30	98.10 ± 0.09	0.07	10.0	100.63 ± 0.27	0.27
(MA)						50	100.74 ± 0.39	0.26	20.0	99.41 ± 0.32	0.32
						100	100.69 ± 0.17	0.08	30.0	98.40 ± 0.20	0.20
Glutaraldehyde	1–10	$y = 183.55x - 9.4153$	1.0000	0.17	0.51	1.05	100.00 ± 0.0131	0.43	1.0	100.00 ± 0.1660	0.17
(GLT)						2.11	101.40 ± 0.0134	0.33	1.5	101.36 ± 0.5828	0.58
						4.22	102.80 ± 0.0121	0.19	2.0	100.27 ± 0.0958	0.10
Formaldehyde	1–10	$y = 342.30x + 14.264$	1.0000	0.14	0.42	1.02	98.04 ± 0.0051	0.13	1.0	100.00 ± 0.1080	0.11
(FAL)						2.04	99.02 ± 0.0054	0.11	1.5	101.46 ± 0.1080	0.11
						4.09	100.49 ± 0.0033	0.05	2.0	100.18 ± 0.0624	0.06

Abbreviations: LOD, limit of detection; LOQ, limit of quantification; SD, standard deviation; RSD, relative standard deviation.

*Regression coefficient.

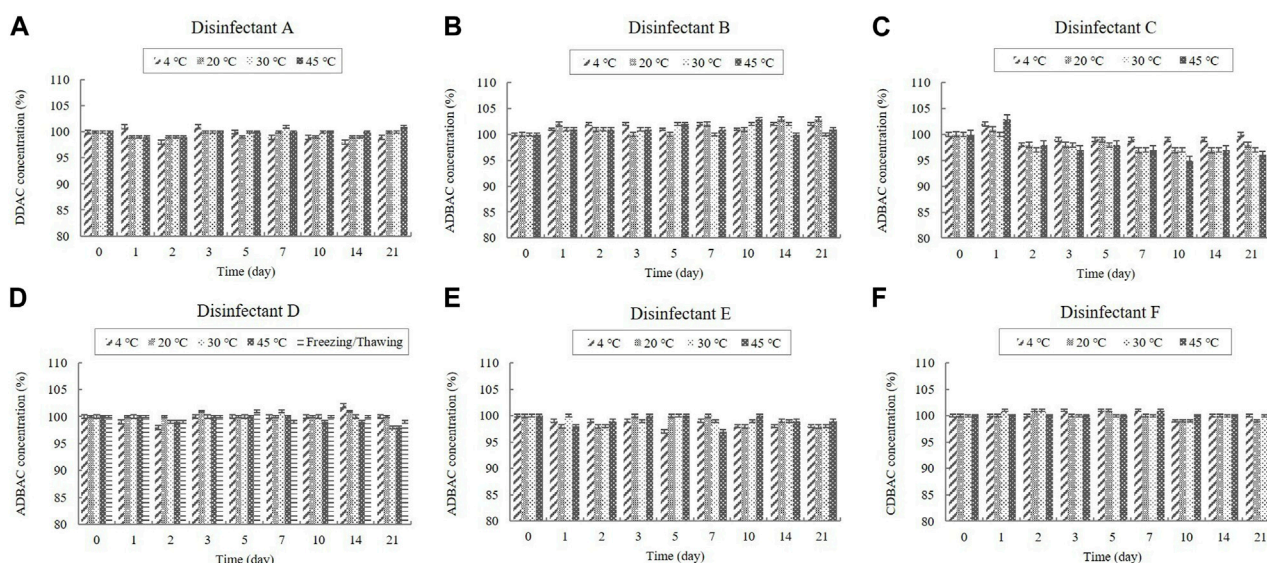


FIGURE 1

Stability of quaternary ammonium compounds (QACs) at various temperatures over time. QAC concentration in the diluted (A) disinfectant A solution, (B) disinfectant B solution, (C) disinfectant C solution, (D) disinfectant D solution, (E) disinfectant E solution, and (F) disinfectant F solution. Concentration is expressed as a percentage of the concentration measured at study initiation. Here, the abbreviations represent: DDAC, didecyl dimethyl ammonium chloride; ADBAC, alkyl dimethyl benzyl ammonium chloride; CDBAC, coco dimethyl benzyl ammonium chloride.

99.28%–103.40% and 98.04%–101.40%, and the LODs ranged from 0.32 to 0.55 $\mu\text{g/mL}$ and 0.14 to 0.17 $\mu\text{g/mL}$, for the acids and aldehydes, respectively.

3.1.3 ICP-OES methodology

The ICP-OES method, employed for determining the phosphorus content in the PA of the samples, was validated for linearity, LOD, LOQ, precision, and accuracy using standard PA solutions. A linear relationship was obtained over the five-point standard concentration range (0.1–10 $\mu\text{g/mL}$) with a regression equation of $y = 38534x + 387.7$ and, a regression coefficient of 0.9998. Intra-assay repeatability was assessed in one laboratory by a single operator, by testing identical samples ($n = 10$) of 0.02 $\mu\text{g/mL}$; the RSD% was 4.72%. The mean recoveries ($\pm\text{SD}$) and RSD% of the standard solutions were: 94.80% \pm 10.31% and 10.87% for 0.1 $\mu\text{g/mL}$, 106.70% \pm 3.56% and 3.33% for 1 $\mu\text{g/mL}$, and 104.29% \pm 0.71% and 0.68% for 5 $\mu\text{g/mL}$. The LOD and LOQ of the phosphorus content were 0.0037 and 0.0110 $\mu\text{g/mL}$, respectively.

3.2 Contents of active ingredients

3.2.1 Stable active ingredients

3.2.1.1 QAC content

Disinfectants A, B, C, D, E, and F are QAC-based disinfectants that either contain a single active ingredient or a combination of acids and aldehydes. QACs are present in diluted disinfectant solutions at concentrations of 0.03%–0.16% (Table 1). The QAC concentrations in the samples of the diluted disinfectant D solution exhibited no significant change at any temperature during the experimental storage period, nor when subjected to a freezing/thawing cycle (Figure 1).

3.2.1.2 CA, AA, and PA contents

The contents of the organic acids (CA and AA) were determined using HPLC, whereas the content of the inorganic acid (PA) was determined using ICP-OES. CA was present in the diluted disinfectant solutions of disinfectants B, D, E, G, H, I, and J at concentrations of 0.08%–0.33%. The diluted disinfectant solution of disinfectant J also contained AA at a concentration of 0.040% (Table 1). PA was present in the diluted disinfectant solutions of disinfectants E and J at concentrations of 0.06% and 0.04%, respectively (Table 1). The CA, AA, and PA concentrations in the samples did not change significantly at any of the temperatures during the experimental storage period. Moreover, the CA concentration in the samples of the diluted disinfectant D solution did not change significantly when exposed to a freezing/thawing cycle (Figure 2; Figure 3).

3.2.1.3 H_2O_2 content

H_2O_2 was present in the diluted disinfectant solutions of disinfectants O, P, and Q at concentrations of 0.03%–0.05% (Table 1). The H_2O_2 concentration in the samples did not change significantly at 4, 20, and 30°C during the experimental storage period (Figure 4). However, the concentrations decreased significantly ($p < 0.05$) at 45°C from Day 10 onwards in the samples of disinfectants O and P. Nevertheless, the concentrations were above 90% of the initial concentrations at the end of the experimental storage period (Figure 4).

3.2.1.4 NaOCl and CuSO_4 contents

NaOCl was present in the diluted disinfectant solution of disinfectant S at a concentration of 0.1%, whereas CuSO_4 was present in the diluted disinfectant solution of disinfectant T at a concentration of 0.318% (Table 1). The concentrations in the

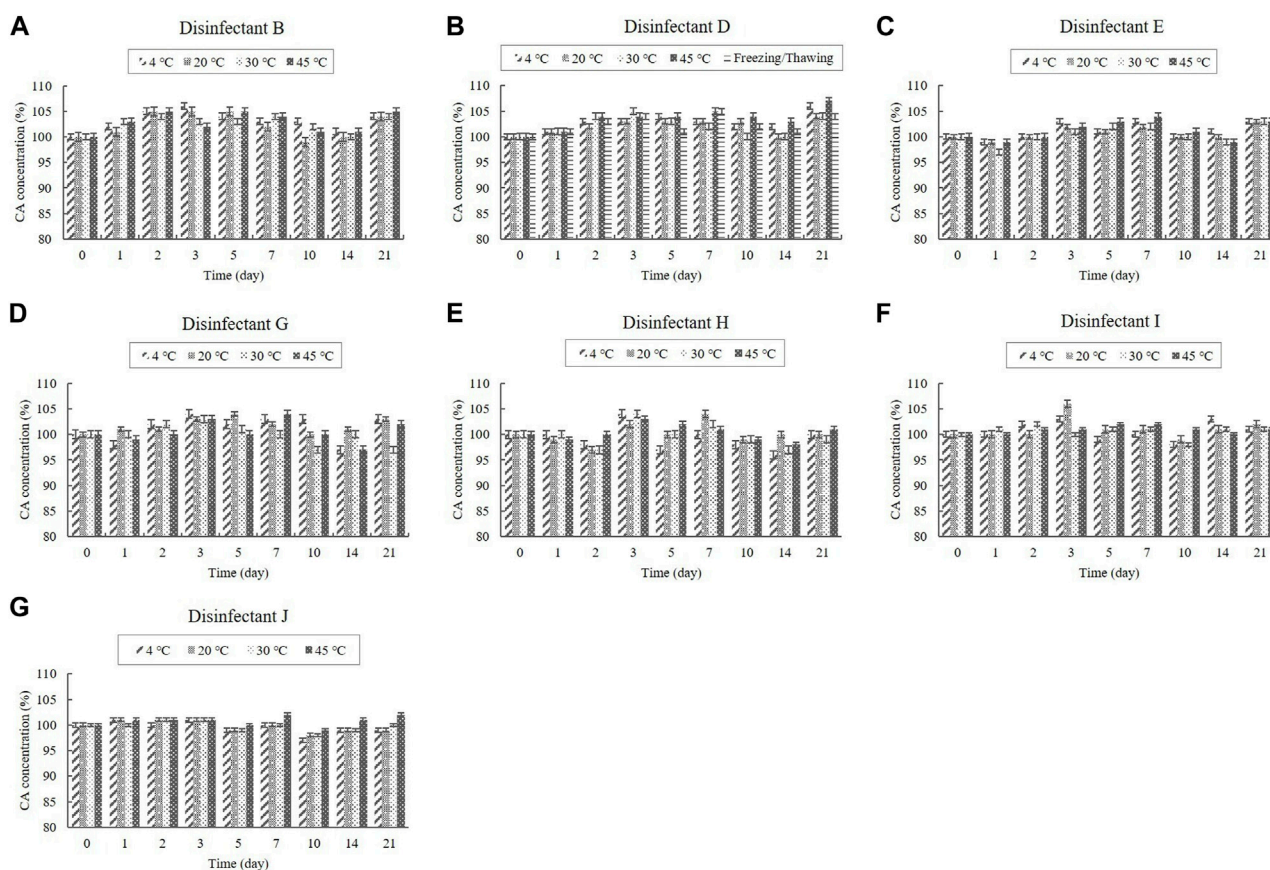


FIGURE 2

Stability of citric acid (CA) at various temperatures over time. CA concentration in the diluted (A) disinfectant B solution, (B) disinfectant D solution, (C) disinfectant E solution, (D) disinfectant G solution, (E) disinfectant H solution, (F) disinfectant I solution, and (G) disinfectant J solution. Concentration is expressed as a percentage of the concentration measured at study initiation.

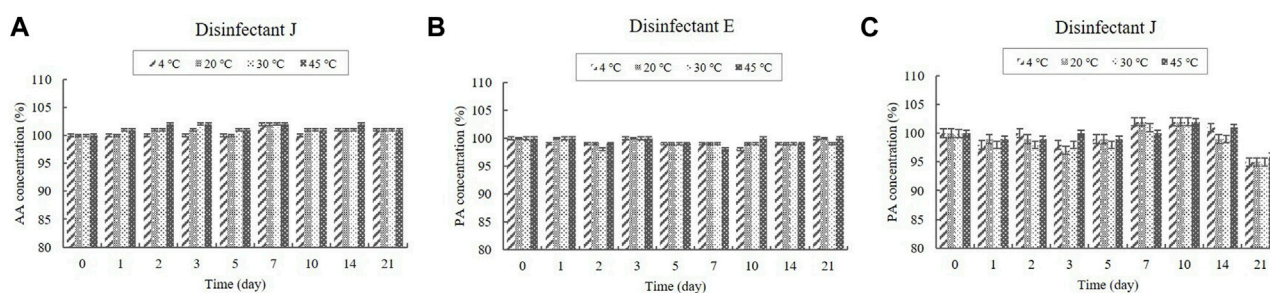


FIGURE 3

Stability of acetic acid (AA) and phosphoric acid (PA) at various temperatures over time. (A) AA concentration in the diluted disinfectant J solution. PA concentration in the diluted (B) disinfectant E solution and (C) disinfectant J solution. Concentration is expressed as a percentage of the concentration measured at study initiation.

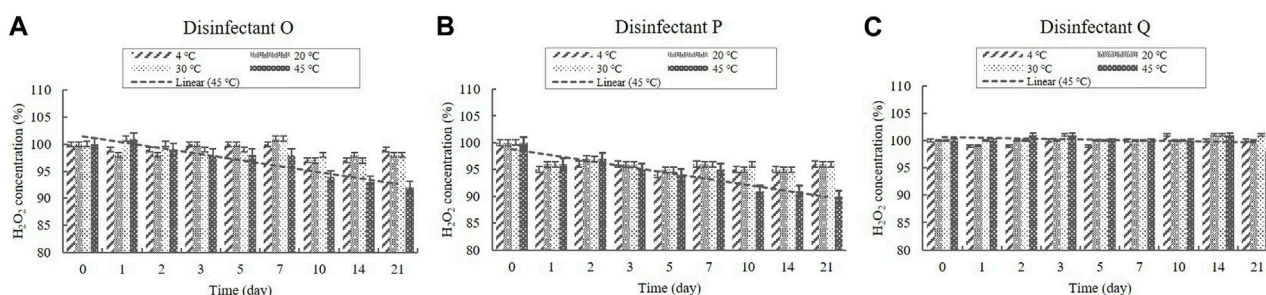


FIGURE 4

Stability of H₂O₂ at various temperatures over time. H₂O₂ concentration in the diluted (A) disinfectant O solution, (B) disinfectant P solution, and (C) disinfectant Q solution. Concentration is expressed as a percentage of the concentration measured at study initiation. A linear trend line fit (dotted line) of the 45°C data is displayed.

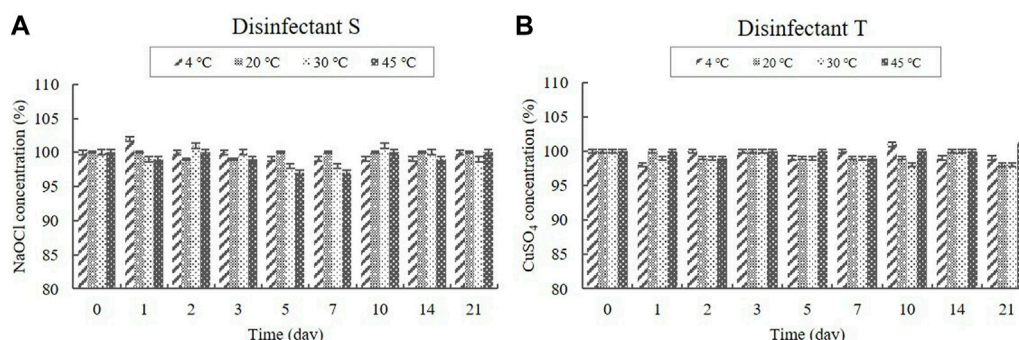


FIGURE 5

Stability of NaOCl and CuSO₄ at various temperatures over time. (A) NaOCl concentration in the diluted disinfectant S solution, (B) CuSO₄ concentration in the diluted disinfectant T solution. Concentration is expressed as a percentage of the concentration measured at study initiation.

samples did not change significantly at any of the temperatures during the experimental storage period (Figure 5).

3.2.2 Content changes of active ingredients on conditional change

3.2.2.1 GLT and FAL contents

Disinfectants C and F are QAC-based disinfectants combined with the aldehydes GLT and FAL. GLT and FAL were present in the diluted disinfectant solutions of disinfectant C at concentrations of 0.033% and 0.053%, respectively. GLT was present in the diluted disinfectant solutions of disinfectant F at a concentration of 0.234% (Table 1). Disinfectant R contained GLT as the single active ingredient, which had a concentration of 0.200% in the diluted disinfectant R solution (Table 1). The concentrations in the samples did not change significantly at 4, 20, and 30°C during the experimental storage period. However, the contents of both GLT and FAL decreased significantly ($p < 0.05$) at 45°C during the experimental storage period. GLT exhibited a 51, 10, and 17% content reduction in the diluted disinfectants C, F, and R solutions after 21 days (Figure 6), whereas FAL exhibited a 14% content reduction in the diluted disinfectant C solution (Figure 6). Furthermore, the lower level of the 95% CI was below 90% of the

initial concentrations on Days 3 and 8 for GLT and FAL at 45°C, respectively (Figure 7).

3.2.2.2 PPMS content

Disinfectants K, L, M, and N are PPMS-based disinfectants with an active ingredient either alone or combined with an acid. PPMS was present in the diluted disinfectant solutions at concentrations of 0.250%–0.500% (Table 1). Samples taken from the diluted disinfectant solutions exhibited a drastic decrease in the PPMS concentration in a time-temperature-dependent manner, i.e., the concentration decreased over time as the temperature increased. After 21 days, the PPMS concentration measured, on average, 90.25% of its initial concentration at 4°C; however, at 20, 30, and 45°C, the concentration measured, on average, lower than 90% of its initial concentration on Days 7, 5, and 1, respectively. When exposed to a freezing/thawing cycle, the PPMS concentration in the diluted disinfectant N solution measured lower than 90% of its initial concentration on Day 5 (Figure 8). The lower 95% CI displayed below 90% of the initial concentrations on Day 5 at 20°C, on Day 2 at 30°C, and on Day 1 under a freezing/thawing cycle. The degradation of PPMS at 45°C occurred too quickly to enable an accurate stability assessment (Figure 9).

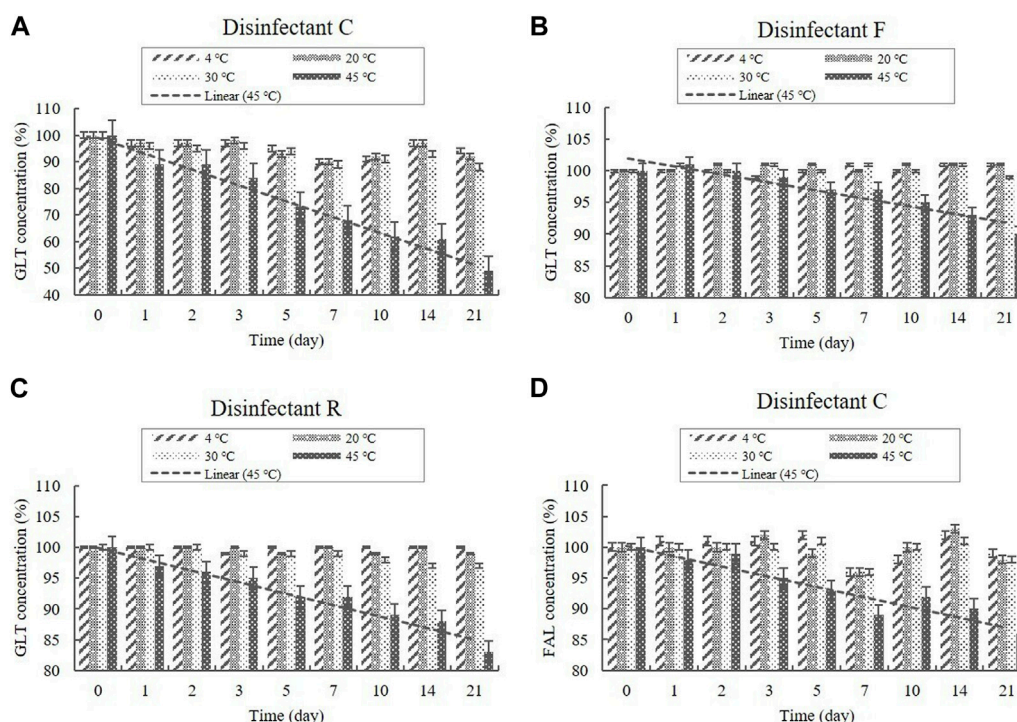


FIGURE 6 Stability of GLT and FAL at various temperatures over time. GLT concentration in the diluted (A) disinfectant C solution, (B) disinfectant F solution, and (C) disinfectant R solution. (D) FAL concentration in the diluted disinfectant C solution. Concentration is expressed as a percentage of the concentration measured at study initiation. Linear trend line fit (dotted line) of the 45°C data is displayed.

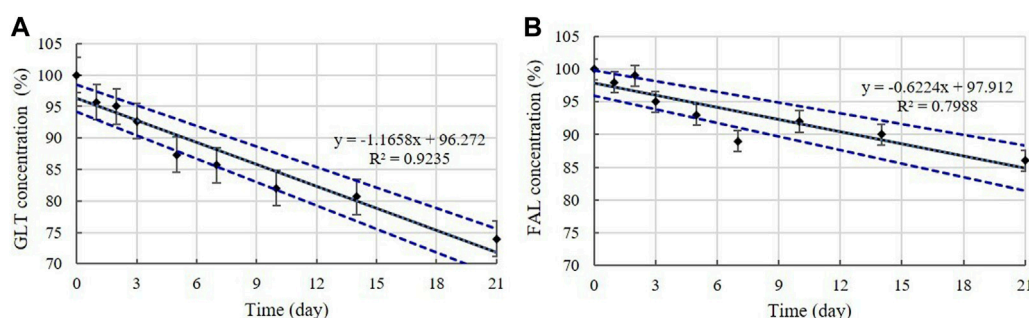


FIGURE 7 Linear regression with 95% confidence intervals for GLT and FAL at 45°C. (A) GLT concentration. (B) FAL concentration. Concentration is expressed as a percentage of the concentration measured at study initiation. Linear trend line fit (solid line), and the lower and upper 95% CI (dotted line) of the data are displayed.

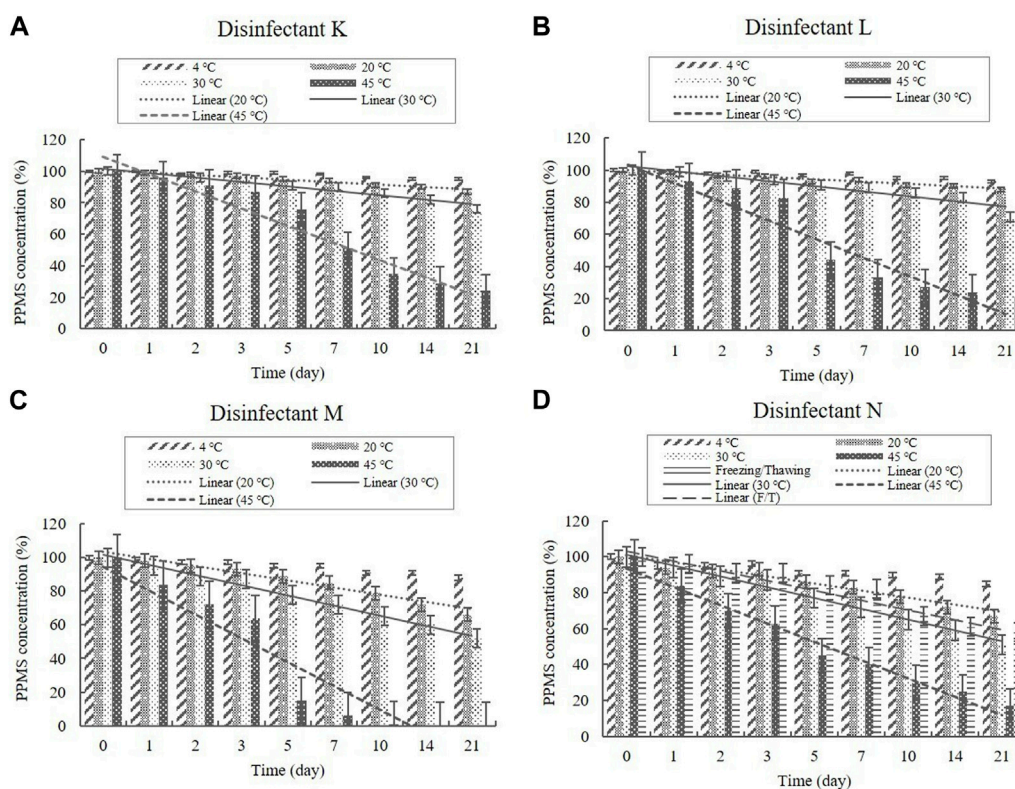
3.2.2.3 MA content

The MA content in the diluted disinfectant N solution was measured using HPLC at a concentration of 0.100% (Table 1). The changes in the MA concentration of the samples did not significantly differ at 4, 20, and 30°C during the experimental storage period, nor under the freezing/thawing cycle (Figure 10). However, the concentration decreased significantly ($p < 0.05$) at 45°C during the experimental storage period, showing a 12% reduction in MA

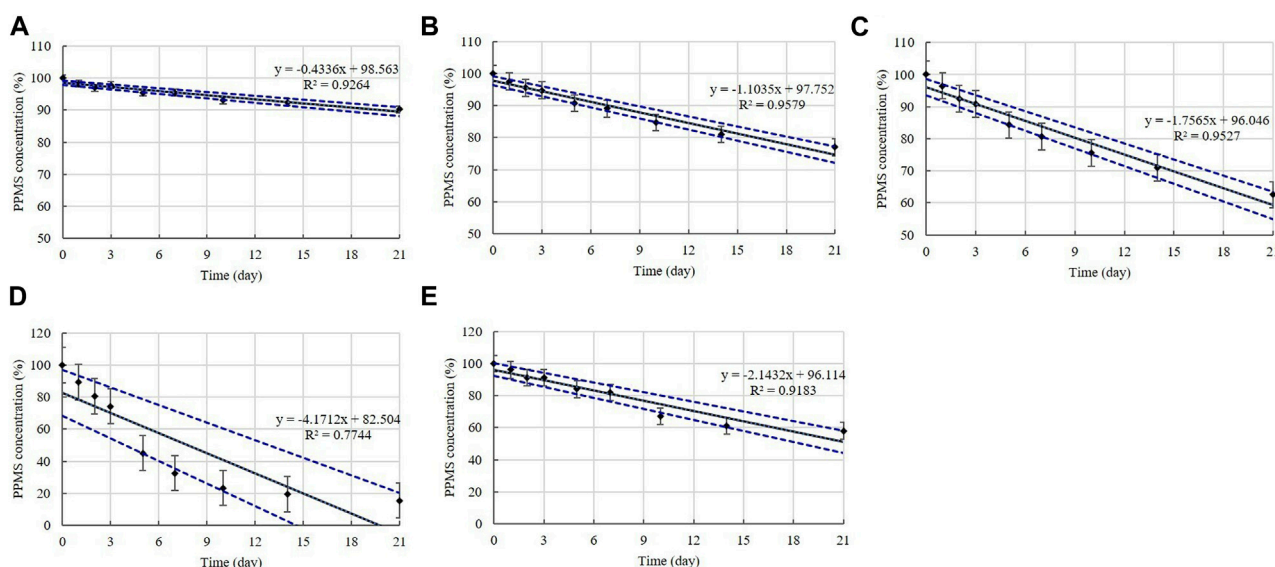
concentration. The lower 95% CI displayed below 90% of the initial concentration on Day 7 at 45°C (Figure 10).

3.2.2.4 PAA content

PAA is present in the diluted solutions of disinfectants O, P, and Q at concentrations of 0.006%–0.010% (Table 1). The concentrations in the samples were >90% of the initial concentrations at 4°C during the experimental storage period (Figure 11). However, samples taken from the diluted

**FIGURE 8**

Stability of potassium peroxymonosulfate (PPMS) at various temperatures over time. PPMS concentration in the diluted (A) disinfectant K solution, (B) disinfectant L solution, (C) disinfectant M solution, and (D) disinfectant N solution. Concentration is expressed as a percentage of the concentration measured at study initiation. Linear trendline fit of each temperature data is displayed.

**FIGURE 9**

Linear regression with 95% confidence intervals for PPMS. PPMS concentration at: (A) 4°C, (B) 20°C, (C) 30°C, (D) 45°C, and (E) under freezing/thawing cycle. Concentration is expressed as a percentage of the concentration measured at study initiation. Linear trendline fit (solid line), and the lower and upper 95% CI (dotted line) of the data are displayed.

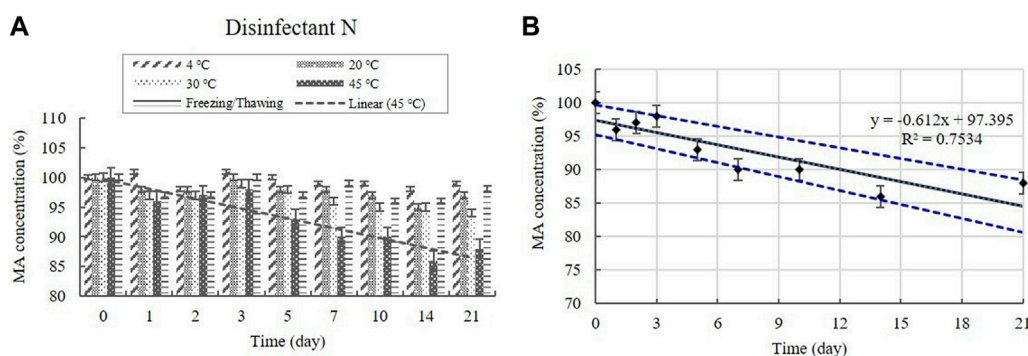


FIGURE 10

(A) Stability of malic acid (MA) at various temperatures over time. MA concentration in the diluted disinfectant N solution. Linear trendline fit of each temperature data are displayed. (B) Linear regression with 95% confidence intervals for MA at 45°C. Concentration is expressed as a percentage of the concentration measured at study initiation. Linear trendline fit (solid line), and the lower and upper 95% CI (dotted line) of the data are displayed.

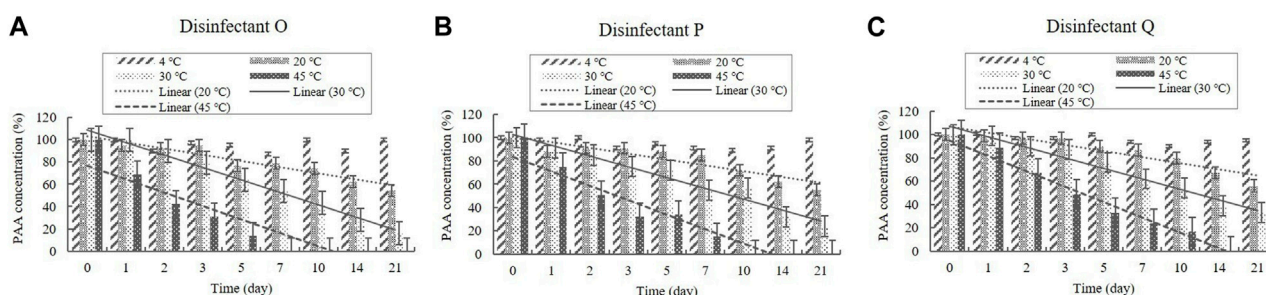


FIGURE 11

Stability of peracetic acid (PAA) at various temperatures over time. PAA concentration in the diluted (A) disinfectant O solution, (B) disinfectant p solution, and (C) disinfectant Q solution. Concentration is expressed as a percentage of the concentration measured at study initiation. Linear trendline fit of each temperature data is displayed.

disinfectant solutions exhibited a drastic decrease in PAA concentrations over time as the temperature increased. After 21 days, the PAA concentration measured, on average, 55% of its initial concentration at 20°C, whereas at 30°C and 45°C it measured, on average, below 90% of its initial concentration on Days 2 and 1, respectively (Figure 11). The lower 95% CI indicates that the degradation of PAA at 20, 30, and 45°C occurred too quickly enable an accurate stability assessment (Figure 12).

5 Discussion

Effective disinfection is dependent on the correct disinfectant concentration. Using a concentration lower than the recommended level may affect the efficacy of the disinfectant. Conversely, over-concentrations result in disinfectant waste, which can cause serious harm to people, livestock, and the environment. Disinfectants are typically dispersed in the environment after dilution, and temperature is critical in determining the duration of their effectiveness. Typically, the effectiveness of the disinfectant decreases at temperatures below 15°C and above 20°C (Kim et al., 2013). The chemical potency of disinfectants decreases at low

temperatures (Lin et al., 2020), making disinfection in cold climates a huge challenge. To compensate for any loss of efficacy under colder conditions, the disinfectant dosage is usually increased. Kim et al. (2020) conducted an on-site assessment of livestock disinfection facilities from winter to early spring (February to May 2017) in South Korea, and reported that 93.9% of all samples of the diluted disinfectant solutions, used over several days, had either inadequate concentrations or over-concentrations of active ingredients. In some cases, no active ingredients were detected in the solutions.

The stability of reactive species is critical in determining the inactivation effectiveness and shelf life of diluted disinfectant solutions. The chemical stability and disinfection potential of disinfectants are affected by storage conditions; however, the influence of such storage conditions on active ingredients is unclear and little information has been published on the stability of diluted disinfectant solutions under simulated storage conditions.

The stability of a chemical product is affected by the physical changes it undergoes due to temperature fluctuations, such as freezing and thawing (Bajaj et al., 2012). The potential adverse effects of the instability of chemical products, based on content changes of the active ingredients, are: 1) degradation of the active

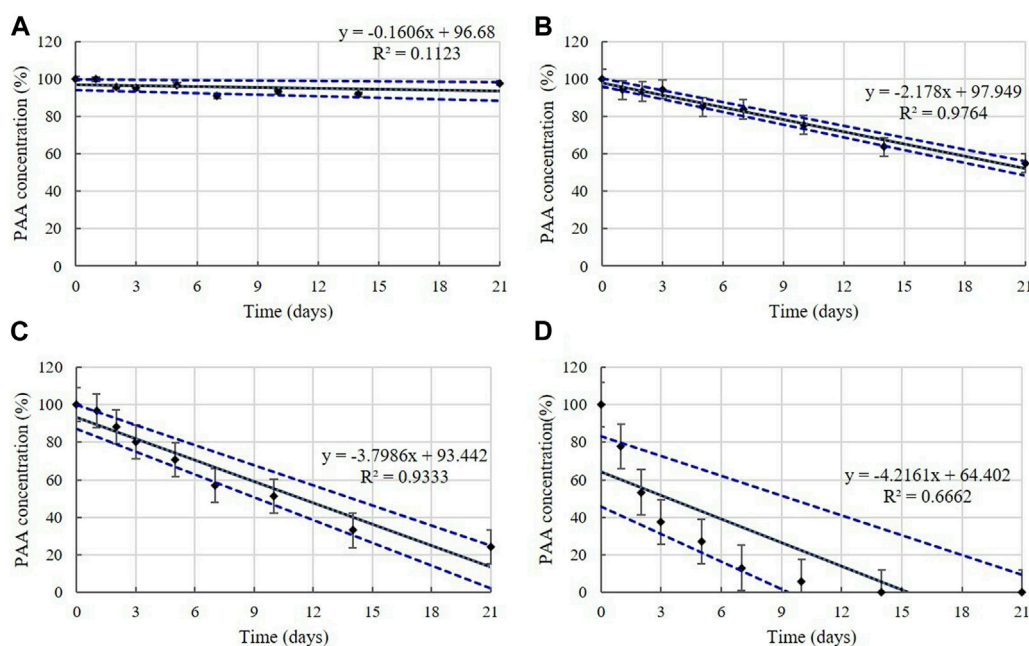


FIGURE 12

Linear regression with 95% confidence intervals for PAA. PAA concentration at: (A) 4°C, (B) 20°C, (C) 30°C, and (D) 45°C. Concentration is expressed as a percentage of the concentration measured at study initiation. Linear trendline fit (solid line), and the lower and upper 95% CI (dotted line) of the data are displayed.

ingredient to less than 90% of the label claim (unacceptable quality), 2) increase in concentration of the active ingredient due to solvent escape or evaporation, caused by insufficiently sealed packaging (container), and 3) loss of content uniformity due to loss of content as a function of time (Bajaj et al., 2012). Some disinfectants lose stability quickly upon preparation for use, whereas others are unstable over long storage periods, particularly in the presence of heat (Dvorak, 2008).

Stability testing is used to determine how the quality of chemical ingredients fluctuates over time when exposed to a range of environmental conditions, so that storage conditions can be prescribed and the shelf life of chemicals can be established (Farrag et al., 2023). In this study, we performed concentration-based assays to test the stability of the active ingredients in diluted disinfectant solutions under varying storage conditions. The data indicated that the active ingredients, such as QACs, CA, AA, PA, H_2O_2 , NaOCl, and $CuSO_4 \cdot 5H_2O$, retained 90% of their initial concentration for the 21-day study period at storage temperatures of 4, 20, 30, and 45°C. In addition, QACs and CA were stable during freezing/thawing cycles. QACs consist of only stable chemical bonds, such as C–N, C–C, and C–H, which make their natural degradation rather difficult (Zhang et al., 2021). A recently published study presented the thermal stability of an aqueous solution of QACs up to 200°C (Zhuravlev et al., 2022). Tembo et al. (2017) reported that the CA content in juice samples was generally not strongly influenced by storage temperatures (freezing, 4, 6, 15, and 30°C) for 60 days, and that the decrease in CA content was significantly lower ($p \leq 0.05$) under refrigeration storage (6°C) than at elevated temperatures (15°C and 30°C). The effects of temperature on the decomposition of disinfectant solutions vary; however, the concentration of active species in AA and PA solutions typically

decreases, and their critical temperatures are 230°C and 450°C, respectively (Li et al., 2017; Joseph and White, 2021; Xu et al., 2021). H_2O_2 , one of the most accessible disinfectants in various applications, has a limited stability, which markedly decreases the expiration period of a disinfectant (Madanská et al., 2004). Storage under decreased temperature proved to be more suitable in terms of content stability of H_2O_2 (Madanská et al., 2004), which is consistent with our result that showed that a storage temperature of $\leq 30^\circ\text{C}$ is favorable for a 21-day stability. Gélinas et al. (1984) reported that GLT is much more affected by temperature than NaOCl, thus confirming our results, and that NaOCl is a better disinfectant at low temperatures. Chlorine compounds lose potency over time and are not active at temperatures above 110°F (43.3°C) (Dvorak, 2008). In our study, only one sample was investigated, and no fluctuation in concentrations was observed at $\leq 45^\circ\text{C}$ storage temperatures for the study period. However, chlorine compounds are rapidly inactivated by light and certain metals; thus, fresh solutions should always be used (Dvorak, 2008). According to Cheng et al. (2019), the thermal decomposition reaction of $CuSO_4 \cdot 5H_2O$ is initiated from 50°C, which is consistent with our results of stable conditions at $\leq 45^\circ\text{C}$ storage temperatures.

The aldehydes, GLT and FAL, and MA retained 90% of their initial concentrations at 4, 20, and 30°C for 21 days; however, degradation patterns were observed when stored at 45°C, thus suggesting that they are unstable at high temperatures. In particular, MA was affected more by high-temperature changes than by freezing/thawing cycles. A previous study reported that MA content in juice samples was generally not strongly influenced by storage temperature (freezing, 4, 6, 15, and 30°C) for 60 days (Tembo et al., 2017) and that the decrease in MA was significantly lower ($p \leq 0.05$) under refrigerated storage (6°C) than at elevated temperatures (15°C and 30°C). GLT is an active

ingredient affected by temperature (Gélinas et al., 1984; Russell, 2008). Previous data suggest that the concentration of GLT in hospital biocides appeared to be reduced to 50% after incubation for 2 w at 40°C, whereas smaller variations were observed in the sample incubated at room temperature (Matei et al., 2020). Kim et al. (2013) also reported that the effect of the GLT agents is reduced at temperatures above 20°C. The volatile organic compound FAL is used directly in aqueous solutions as an active ingredient in disinfectants. Increases in temperature and humidity accelerate the release of FAL into the atmosphere because the temperature increases the kinetic energy and accelerates the emission rate of FAL molecules (Liu et al., 2017; Zhang et al., 2022). FAL decomposes into methanol and carbon monoxide at temperatures above 150°C, and the ideal temperature for storage of FAL solutions is between 15°C and 25°C (WHO, 1991). Liu et al. (2017) found that the FAL ventilation increased 10%–30% when the temperature was increased by 5°C. Zhang et al. (2022) found that the FAL ventilation at 60°C was more than ten times of that at 20°C. The FAL content of our sample stored at high temperatures indicated that the FAL in the sample was released into the air as a gas upon heating the solution. Considering the results obtained in this and other studies, diluted disinfectant solution that contain GLT, FAL, and MA as active ingredients should be stored at ≤ 30°C for chemical stability.

PPMS and PAA, are used as oxidizing agents. In this study, the concentration of PAA and PPMS decreased over time with increasing temperature. A stability of 90% was shown at 4°C but not under other conditions. Kim et al. (2013) reported that, at 15°C–20°C, oxidizing agents are active but chemically unstable in an aqueous solution. To maintain stability, PAA should preferably be stored at low temperatures in its original containers (Block, 2001). Diluted PAA solutions (1%) lose 50% of their sanitation power within 6 days (Kunigk et al., 2001). Increasing the temperature causes a more rapid decomposition. For example, the concentration decreased by 50% in 72 h at 45°C, whereas the loss was only 33% in 240 h at 25°C (Kunigk et al., 2001), indicating that temperature plays an important role in the shelf life of PAA solutions. Li et al. (2021) reported that the composition temperature of PPMS is low, and its activity is not stable over long periods in aqueous solutions. PPMS is relatively stable as a salt at ambient temperatures (Suresh et al., 2019); however, Sykes and Weese (2014) demonstrated that a solution prepared from powder remained active for only 7 days. The decomposition of PPMS is exothermic and can accelerate if conditions allow the product temperature to rise; therefore, packaging temperature should not exceed 30°C (Gant and Barr, 2006). The results of this study and those of previous studies demonstrate that disinfectants containing a combination of H₂O₂ and PAA as well as PPMS disinfectants should be used within a short period after dilution. In addition, heating as a means to prevent freezing of the disinfectants in winter should be avoided, as heat reduces the PAA and PPMS contents.

The reactive species have to remain stable during storage to maintain their disinfection properties (Tsoukou et al., 2020). If the concentration of the active ingredient in the disinfectant decreases, the contact time may be increased to achieve effective disinfection. However, this may not always hold true. Thus, when selecting the best disinfectant and optimal conditions for maximum efficacy, the temperature of use and storage conditions should be considered, as well as the active ingredient concentration in the solution. Herein, the results presented provide a basis for the storage of diluted veterinary disinfectant solutions and practical applications for

disinfection in the veterinary field. Despite the current lack of data and relative complexity of this subject, striving towards a better understanding of the effects of temperatures and storage periods on diluted disinfectant solutions will ultimately lead to an improved field guidance for the selection and use of a seasonally appropriate veterinary disinfectants and their storage conditions. To the best of our knowledge, our study is the first to have investigated the chemical stability of active ingredients in diluted veterinary disinfectants under simulated storage conditions.

Data availability statement

The original contributions presented in the study are included in the article/Supplementary Material, further inquiries can be directed to the corresponding author.

Author contributions

Conceptualization, H-SL and WJ; data curation, H-SL, H-JY, and G-HL; formal analysis, H-SL and CR; funding acquisition, M-HL, MH, and WJ; investigation, H-SL, H-JY, and G-HL; methodology, H-SL, H-JY, and G-HL; project administration, H-SL, MH, and WJ; resources, S-JK and SS; validation, H-SL; visualization, CR; writing—original draft, CR; writing—review and editing, CR and WJ. All authors contributed to the article and approved the submitted version.

Funding

This research was funded by the Animal and Plant Quarantine Agency (grant numbers: Z-1543073-2021-22-03 and B-1543073-2023-26-01) of the Republic of Korea.

Conflict of interest

The authors declare that the research was conducted in the absence of any commercial or financial relationships that could be construed as a potential conflict of interest.

Publisher's note

All claims expressed in this article are solely those of the authors and do not necessarily represent those of their affiliated organizations, or those of the publisher, the editors and the reviewers. Any product that may be evaluated in this article, or claim that may be made by its manufacturer, is not guaranteed or endorsed by the publisher.

Supplementary material

The Supplementary Material for this article can be found online at: <https://www.frontiersin.org/articles/10.3389/fchem.2023.1204477/full#supplementary-material>

References

- APQA (Animal and Plant Quarantine Agency) (2015). APQA handbook of analytical methods for veterinary drugs. (Publication No. 11-1543061-000154-01). Available at: https://www.qia.go.kr/viewwebQiaCom.do?id=39863&type=2_14dwyp (in Korean).
- APQA (Animal and Plant Quarantine Agency) (2017). APQA research report. Improvement and monitoring of an analytic method in chemicals for veterinary medicine (Project code No. N-1542058-2013-17-01). APQA. 2017. Available at: <https://scienceon.kisti.re.kr/srch/selectPORSrchReport.do?cn=TRKO201800042117> (in Korean).
- Bajaj, S., Singla, D., and Sakhuja, N. (2012). Stability testing of pharmaceutical products. *J. Appl. Pharm. Sci.* 2012, 129–138.
- Block, S. S. (2001). *Disinfection, sterilization, and preservation*. Pennsylvania, United States: Lippincott Williams and Wilkins.
- Cheng, L., Li, W., Li, Y., Yang, Y., Li, Y., Cheng, Y., et al. (2019). Thermal analysis and decomposition kinetics of the dehydration of copper sulfate pentahydrate. *J. Therm. Anal. Calorim.* 135, 2697–2703. doi:10.1007/s10973-018-7595-y
- De Benedictis, P., Beato, M. S., and Capua, I. (2007). Inactivation of avian influenza viruses by chemical agents and physical conditions: A review. *Zoonoses Public Health* 54, 51–68. doi:10.1111/j.1863-2378.2007.01029.x
- Dvorak, G. (2008). Disinfection 101. *Cent. Food Sec. Public Health* 2008, 1–20.
- Farrag, S. A., Rageh, A. H., Askal, H. F., and Saleh, G. A. (2023). HPTLC/MS and HPTLC/UV for monitoring of degradation behavior of some β -lactam antibiotics mixtures under ambient storage conditions. *Microchem. J.* 185, 108241. doi:10.1016/j.microm.2022.108241
- Gant, R. G., and Barr, T. L. (2006). *Cleaning compound for a medical or dental office*. Washington, DC: US Patent and Trademark Office. U.S. Patent application publication No, US2006/0205626 A1.
- Geering, W. A., Penrith, M., and Nyakahuma, D. (2001). *FAO animal Health manual: Manual on procedures for disease eradication by stamping out*. Rome: Food and Agriculture Organization of the United Nations.
- Gélinas, P., Goulet, J., Tastayre, G. M., and Picard, G. A. (1984). Effect of temperature and contact time on the activity of eight disinfectants: a classification. *J. Food Prot.* 47, 841–848. doi:10.4315/0362-028X-47.11.841
- Hossain, M. D., Ngo, H., and Guo, W. (2013). Introductory of Microsoft Excel SOLVER function-Spreadsheet method for isotherm and kinetics modelling of metals biosorption in water and wastewater. *J. Water Sustain.* 3, 223–237.
- Jang, Y., Lee, J., So, B., Lee, K., Yun, S., Lee, M., et al. (2014). Evaluation of changes induced by temperature, contact time, and surface in the efficacies of disinfectants against avian influenza virus. *Poult. Sci.* 93, 70–76. doi:10.3382/ps.2013-03452
- Joseph, T., and White, D. (2021). Understanding the role of concentrated phosphoric acid solutions as high-temperature silicon nitride etchants. *ECS J. Solid State Sci. Technol.* 10, 024006. doi:10.1149/2162-8777/abe422
- Kim, H. M., Shim, I. S., Baek, Y. W., Han, H. J., Kim, P. J., and Choi, K. (2013). Investigation of disinfectants for foot-and-mouth disease in the Republic of Korea. *J. Infect. Public Health* 6, 331–338. doi:10.1016/j.jiph.2013.04.002
- Kim, S., Chung, H., Lee, H., Myung, D., Choi, K., Kim, S., et al. (2020). Evaluation of the disinfectant concentration used on livestock facilities in Korea during dual outbreak of foot and mouth disease and high pathogenic avian influenza. *J. Vet. Sci.* 21, e34. doi:10.4142/jvs.2020.21.e34
- KMA (Korea Meteorological Administration) (2023). Korea meteorological administration. Available at: <https://www.weather.go.kr/w/obs-climate/climate/statistics/korea-char.do> (Accessed May 30, 2023).
- Kobayashi, R., Murai, R., Sato, Y., Nakae, M., Nirasawa, S., Asanuma, K., et al. (2022). Study of post-opening stability of active ingredients in hand sanitizers. *J. Infect. Chemother.* 28, 1605–1609. doi:10.1016/j.jiac.2022.08.012
- Kunig, L., Gomes, D. R., Forte, F., Vidal, K. P., Gomes, L. F., and Sousa, P. F. (2001). The influence of temperature on the decomposition kinetics of peracetic acid in solutions. *Braz. J. Chem. Eng.* 18, 217–220. doi:10.1590/S0104-66322001000200009
- Li, Q., Yan, X., Chen, J., Shu, X., Jia, P., and Liang, X. (2021). Preparation and characterization of potassium Monopersulfate/Ethyl cellulose microcapsules and their sustained release performance. *J. Renew. Mater.* 9, 1673–1684. doi:10.32604/jrm.2021.014695
- Li, Y., Zhou, S., Li, J., Ma, Y., Chen, K., Wu, Y., et al. (2017). Experimental study of the decomposition of acetic acid under conditions relevant to deep reservoirs. *Appl. Geochem.* 84, 306–313. doi:10.1016/j.apgeochem.2017.07.013
- Lin, Q., Lim, J. Y. C., Xue, K., Yew, P. Y. M., Owh, C., Chee, P. L., et al. (2020). Sanitizing agents for virus inactivation and disinfection. *VIEW (Beijing)* 1, e16. doi:10.1002/viw2.16
- Liu, L., Yu, X., Dong, X., Wang, Q., Wang, Y., and Huang, J. (2017). The Research on formaldehyde concentration distribution in new decorated residential buildings. *Procedia Eng.* 205, 1535–1541. doi:10.1016/j.proeng.2017.10.238
- Madanská, J., Vitková, Z., and Capková, Z. (2004). Examination of the stability of hydrogen peroxide solutions. *Ceska Slov. Farm.* 53, 261–263.
- Maris, P. (1995). Modes of action of disinfectants: -EN- -fr- -es-. *Rev. Sci. Tech.* 14, 47–55. doi:10.20506/rst.14.1.829
- Matei, A., Puscas, C., Patrascu, I., Lehen, M., Ziebro, J., Scurtu, F., et al. (2020). Stability of glutaraldehyde in biocide compositions. *Int. J. Mol. Sci.* 21, 3372. doi:10.3390/ijms21093372
- Muhammad, K., Das, P., Yaqoob, T., Riaz, A., and Manzoor, R. (2001). Effect of physico-chemical factors on survival of avian influenza virus (H7N3 type). *Int. J. Agric. Biol.* 4, 416–418.
- Pironti, C., Dell'Annunziata, F., Giugliano, R., Folliero, V., Galdiero, M., Ricciardi, M., et al. (2021). Comparative analysis of peracetic acid (PAA) and permaleic acid (PMA) in disinfection processes. *Sci. Total Environ.* 797, 149206. doi:10.1016/j.scitotenv.2021.149206
- Rhee, C. H., Her, M., and Jeong, W. (2022). Post-market surveillance monitoring of active ingredient contents in commercial veterinary disinfectants in Korea. *J. Prev. Vet. Med.* 46, 42–47. doi:10.13041/jpvm.2022.46.1.42
- Russell, A. D. (2008). *Factors influencing the efficacy of antimicrobial agents. Principles and practice of disinfection, preservation and sterilization*. London: Blackwell Publishing, 98–127.
- Rutala, W. A., and Weber, D. J. (2008). *Guideline for disinfection and sterilization in healthcare facilities*. Georgia, United States: Centers for Disease Control and Prevention.
- Singh, A., Mor, S. K., Aboubakar, H., Vannucci, F., Patnayak, D. P., and Goyal, S. M. (2017). Polymorphism in XRCC1 gene modulates survival and clinical outcomes of advanced North Indian lung cancer patients treated with platinum-based doublet chemotherapy. *J. Swine Health Prod.* 25, 64–68. doi:10.1007/s12032-017-0923-4
- Singh, S., and Bakshi, M. (2000). Guidance on conduct of stress tests to determine inherent stability of drugs. *Pharm. Technol.* 4, 1–14.
- Suresh, M., Rajanna, K. C., Sriram, Y. H., and Rao, Y. R. (2019). Kinetics and mechanism of peroxysulfate/NaNO₂ mediated nitration of phenols in aqueous bisulfate medium. *SN Appl. Sci.* 1, 485. doi:10.1007/s42452-019-0493-5
- Sykes, J. E., and Weese, J. S. (2014). Infection control programs for dogs and cats. *Canine Feline Infect. Dis.* 2014, 105–118. doi:10.1016/B978-1-4377-0795-3.00011-9
- Tembo, D. T., Holmes, M. J., and Marshall, L. J. (2017). Effect of thermal treatment and storage on bioactive compounds, organic acids and antioxidant activity of baobab fruit (*Adansonia digitata*) pulp from Malawi. *J. Food Compos. Anal.* 58, 40–51. doi:10.1016/j.jfca.2017.01.002
- Tsoukou, E., Bourke, P., and Boehm, D. (2020). Temperature stability and effectiveness of plasma-activated liquids over an 18 months period. *Water* 12, 3021. doi:10.3390/w12113021
- WHO (World Health Organization) (1991). *Formaldehyde: Health and safety guide. Health and safety guide (WHO)*. Geneva, Switzerland: World Health Organization.
- Xiao, S., Yuan, Z., and Huang, Y. (2022). Disinfectants against SARS-CoV-2: A review. *Viruses* 14, 1721. doi:10.3390/v14081721
- Xu, W., Liu, J., Sun, K., Liu, Y., Chen, C., Wang, A., et al. (2021). Effect of activation temperature on properties of H₃PO₄-activated carbon. *BioResources* 16, 4007–4020. doi:10.15376/biores.16.2.4007-4020
- Yilmaz, A., Heffels-Redmann, U., and Redmann, T. (2004). Evaluation of the virucidal efficacy of two chemical disinfectants against avian influenza virus A at different temperatures. *Arch. Geflügelk.* 68, 50–55.
- Zhang, J., Gui, Z., Chen, Y., Xue, L., Song, F., and Zhang, Z. (2022). Faster measurement for formaldehyde emissions from veneered particleboard based on the standardized desiccator method. *Forests* 13, 1566. doi:10.3390/f13101566
- Zhang, X., Kong, H., Zhang, X., Jia, H., Mama, X., Miao, H., et al. (2021). Design and production of environmentally degradable quaternary ammonium salts. *Green Chem.* 23, 6548–6554. doi:10.1039/D1GC01525G
- Zhuravlev, O. E., Voronchikhina, L. I., and Gorbunova, D. V. (2022). Comparative characteristics of thermal stability of quaternary ammonium and pyridinium Tetrachloroferrates. *Russ. J. Gen. Chem.* 92, 348–354. doi:10.1134/S1070363222030021



OPEN ACCESS

EDITED BY

Liang Zhang,
Jiangnan University, China

REVIEWED BY

Lígia O. Martins,
Universidade Nova de Lisboa, Portugal
Carlos Marcuello,
Instituto de Nanociencia y Materiales de
Aragón (INMA), Spain

*CORRESPONDENCE

Faisal H. M. Koua,
✉ faisal.koua@xfel.eu

RECEIVED 12 May 2023

ACCEPTED 20 July 2023

PUBLISHED 01 August 2023

CITATION

Kalkan Ö, Kantamneni S, Brings L, Han H,
Bean R, Mancuso AP and Koua FHM
(2023), Heterologous expression,
purification and structural features of
native *Dictyostelium discoideum* dye-
decolorizing peroxidase bound to a
natively incorporated heme.
Front. Chem. 11:1220543.
doi: 10.3389/fchem.2023.1220543

COPYRIGHT

© 2023 Kalkan, Kantamneni, Brings, Han,
Bean, Mancuso and Koua. This is an
open-access article distributed under the
terms of the [Creative Commons
Attribution License \(CC BY\)](#). The use,
distribution or reproduction in other
forums is permitted, provided the original
author(s) and the copyright owner(s) are
credited and that the original publication
in this journal is cited, in accordance with
accepted academic practice. No use,
distribution or reproduction is permitted
which does not comply with these terms.

Heterologous expression, purification and structural features of native *Dictyostelium discoideum* dye-decolorizing peroxidase bound to a natively incorporated heme

Özlem Kalkan^{1,2}, Sravya Kantamneni¹, Lea Brings¹, Huijong Han¹,
Richard Bean¹, Adrian P. Mancuso^{1,3,4} and Faisal H. M. Koua^{1*}

¹European XFEL GmbH, Schenefeld, Schleswig-Holstein, Germany, ²Department of Molecular Biology
and Genetics, Faculty of Science, Istanbul University, Istanbul, Türkiye, ³La Trobe Institute for Molecular
Science, La Trobe University, Melbourne, VIC, Australia, ⁴Diamond Light Source Ltd., Harwell Science and
Innovation Campus, Didcot, United Kingdom

The *Dictyostelium discoideum* dye-decolorizing peroxidase (DdDyP) is a newly discovered peroxidase, which belongs to a unique class of heme peroxidase family that lacks homology to the known members of plant peroxidase superfamily. DdDyP catalyzes the H₂O₂-dependent oxidation of a wide-spectrum of substrates ranging from polycyclic dyes to lignin biomass, holding promise for potential industrial and biotechnological applications. To study the molecular mechanism of DdDyP, highly pure and functional protein with a natively incorporated heme is required, however, obtaining a functional DyP-type peroxidase with a natively bound heme is challenging and often requires addition of expensive biosynthesis precursors. Alternatively, a heme *in vitro* reconstitution approach followed by a chromatographic purification step to remove the excess heme is often used. Here, we show that expressing the DdDyP peroxidase in x2 YT enriched medium at low temperature (20°C), without adding heme supplement or biosynthetic precursors, allows for a correct native incorporation of heme into the apo-protein, giving rise to a stable protein with a strong Soret peak at 402 nm. Further, we crystallized and determined the native structure of DdDyP at a resolution of 1.95 Å, which verifies the correct heme binding and its geometry. The structural analysis also reveals a binding of two water molecules at the distal site of heme plane bridging the catalytic residues (Arg239 and Asp149) of the GXXDG motif to the heme-Fe(III) via hydrogen bonds. Our results provide new insights into the geometry of native DdDyP active site and its implication on DyP catalysis.

KEYWORDS

biocatalysis, dye-decolorizing peroxidases, heme incorporation, lignin degradation, polycyclic dyes, structural enzymology, redox catalysis

1 Introduction

The *Dictyostelium discoideum* dye-decolorizing peroxidase (DdDyP) is a newly discovered heme peroxidase (Rai et al., 2014; Rai et al., 2021). DdDyP belongs to a new class of DyP-type peroxidases (EC 1.11.1.19), which is different from any other known peroxidases (Kim and Shoda, 1999; Sugano et al., 1999; Sugano et al., 2007; Shrestha et al., 2016). This unique peroxidase family has been shown to perform both H₂O₂-dependent oxidation and hydrolytic functions against a wide-spectrum of substrates, ranging from polycyclic dyes, phenolic compounds, sulfides, carotenoids and interestingly lignin biomass, making it a potential candidate for industrial and biotechnological applications including its possible application as bioenergy catalysts as well as biosurfactants in the biodegradation and biotransformation of emerging environmental contaminants (Salvachua et al., 2013; Rai et al., 2021; Sugano and Yoshida, 2021; Xu et al., 2021; Gan et al., 2022). This broad substrate specificity is attributed to their unique sequence identity and structural properties (Kim and Shoda, 1999; de Gonzalo et al., 2016; Yoshida and Sugano, 2023). DdDyP, as other peroxidases, has been found to function in a wide range of pH milieu displaying higher activity at acidic pH with optimal turnover at pH 4.0 and temperatures ranging from 20°C to 40°C (Colpa et al., 2014; Rai et al., 2021; Xu et al., 2021). It shows optimal activity at pH 3.0 against the known DyP-type peroxidase substrate—the anthraquinone-based dye RB4 (Rai et al., 2021).

DyP-type peroxidases share a typical catalytic mechanism with other peroxidases, in which they depend on the H₂O₂ in their oxidative catalytic function as illustrated in Figure 1 (Scocozza et al., 2021; Sugano and Yoshida, 2021). The resting state of the enzyme proceeds into compound I intermediate state upon interaction of the heme-Fe(III) with hydrogen peroxide (H₂O₂), an oxidizing substrate, forming an oxoferryl porphyrin π -cationic

radical complex [Fe(IV)=O Por[•]]⁺—a porphyrinoid based radical (Colpa et al., 2014; Scocozza et al., 2023). The release of an electron from compound I leads to the formation of compound II [Fe(IV)=O]⁺ intermediate upon reaction with a reducing substrate giving rise to a radical product, in turn compound II relaxes into the resting state when it reacts with more substrates (Chen et al., 2015; Shrestha et al., 2016; Sugano and Yoshida, 2021). The radical product can then be transformed into various sub-products through a non-enzymatic radical coupling. The redox potential of the DyP-type peroxidases, ranging from −50 mV to +250 mV, and that of the substrate determines the feasibility of enzyme catalysis. Generally, a typical DyP-peroxidase catalysis involves several redox couplings, namely, Fe³⁺/Fe²⁺, compound I/Fe³⁺, compound II/compound I and compound II/Fe³⁺ (Shrestha et al., 2016). DyP peroxidases also mediate the hydrolysis of substrates such as anthraquinone dyes, implying that the DyP-type peroxidases are bifunctional enzymes (Colpa et al., 2014). However, the exact mechanism for DyP-type peroxidases and how they perform oxidation and hydrolysis for such a wide range of substrates of different chemical properties remain unclear (Rajhans et al., 2020; Sugano and Yoshida, 2021; Xu et al., 2021).

Despite the importance of the DyP-type peroxidases as mentioned above, their heterologous expression in *Escherichia coli* (*E. coli*) and other expression systems remain challenging as is the case for other heme proteins (Ramzi et al., 2015; Ge et al., 2023). It hampers, for instance, the large-scale mechanistic investigation owing to the difficulties associated with the biosynthesis and availability of heme *b*, thereby limiting its native incorporation into the apo-proteins (Fiege et al., 2018; Park and Kim, 2021; Ge et al., 2023). It was previously shown that *in vitro* reconstitution is needed for obtaining functional DdDyP with the correct heme stoichiometry (Rai et al., 2021). This is an inherently time-consuming process and may result in excess heme and unspecific binding or altering the protein function, making it limited to robust proteins only (Vogel et al., 1999; Denninger et al., 2000; Lemon and Marletta, 2021). Alternatively, heme and iron supplements or heme biosynthetic precursors such as δ -aminolevulinic acid (δ -ALA) can be used during expression, however this is a highly expensive approach as large amounts of such supplements are needed (Fiege et al., 2018).

Here, we report on the use of *E. coli* OverExpress C43(DE3) strain for the expression and production of the DdDyP peroxidase without heme supplement nor its precursor δ -ALA, yielding a stable monomeric enzyme with a natively incorporated heme that displays a Rheinheitszahl (R_Z , A_{Soret}/A_{280}) of ~ 1.0 similar to that of the peroxidase-cyclooxygenase superfamily 6 of the *D. discoideum*, the secreted heme peroxidase DdPoxA, which was prepared by adding hemin supplement during expression (Nicolussi et al., 2018). Furthermore, using X-ray structural analyses, we describe the crystal structure of native DdDyP peroxidase bound to a natively incorporated heme and demonstrate that the geometry of the heme binding pocket resembles in much detail that of a previously reported cyanide native DdDyP structure (Rai et al., 2021), which was prepared following *in vitro* heme reconstitution approach. Our native DdDyP also displays an interesting similarity to the recently identified secreted heme peroxidase A (DdPoxA), which shares only $\sim 21\%$ sequence identity to that of the DdDyP (Nicolussi et al., 2018).

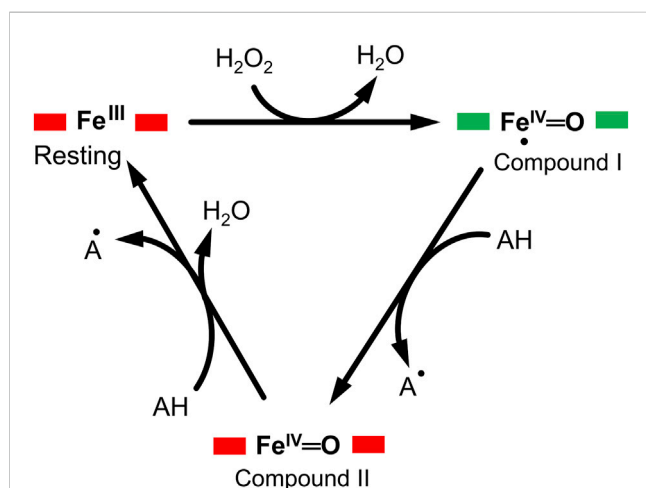


FIGURE 1

A typical enzymatic cycle of DyP-type peroxidases showing the interconversion between the resting state (ferric porphyrin), compound I heme oxoferryl species (porphyrin cationic radical) [Fe(IV)=O Por[•]]⁺; and compound II intermediate state, [Fe(IV)=O]⁺. The AH is the reducing substrate which is oxidized into an intermediate radical product (A[•]) during catalysis.

In both structures the sixth coordination of the heme molecule is provided by a water molecule with ~ 3.0 Å and 2.79 Å for the *DdPoxA* and the *DdDyP*, respectively. The native *DdDyP* also reveals some UV-visible spectral similarities to that of the *DdPoxA* in the Q-band and electron transfer region, whereas the maximum Soret peak of the native *DdDyP* is blue-shifted by $\Delta\lambda = 14$ nm displaying a peak absorbance at 402 nm in comparison with the *DdPoxA*.

2 Materials and methods

2.1 Overexpression and purification of *DdDyP* with natively incorporated heme

The gene sequence encoding dye-decolorizing peroxidase from the slime mold *D. discoideum* AX4 (GenBank: EAL70759.1) was codon optimized for *Escherichia coli*, synthesized and subcloned into the *Bam*HI/*Xho*I cloning site in a pGEX-6P1 vector harboring a Human Rhinovirus 3C excision site and a glutathione transferase (GST) tag at the N-terminal region (BioCat GmbH, Germany). The pGEX-6P1-*DdDyP* construct was transformed into an OverExpress *E. coli* C43(DE3), a chemically competent strain (Sigma-Aldrich, Germany). For purification, a single colony from a freshly streaked plate was inoculated into a Luria-Bertani (LB) or $\times 2$ yeast extract-tryptone ($\times 2$ YT) enriched media containing $100 \mu\text{g mL}^{-1}$ final concentration of ampicillin and incubated at $37^\circ\text{C} \pm 1.0^\circ\text{C}$ for overnight (15–16 h). A starter culture was used to inoculate 6×1 L of LB or $\times 2$ YT containing $100 \mu\text{g mL}^{-1}$ ampicillin and incubated at $37^\circ\text{C} \pm 1.0^\circ\text{C}$ or lower temperatures until the optical density (OD_{600}) reaches 1.0–1.25 before inducing the expression of *DdDyP* with 1.0 mM of isopropyl β -D-1-thiogalactopyranoside. The culture was then incubated for additional 7 or 20 h for expression at 37 ± 1.0 and $20^\circ\text{C} \pm 1.0^\circ\text{C}$, respectively. The cells were harvested by centrifugation with $\times 13,881$ g for 30 min on an F9-6- $\times 1000$ LEX rotor (Thermo Fischer Scientific, Germany) at 4°C and pellets were stored at -80°C until used.

For protein purification, frozen cells were thawed using warm tap water ($\sim 40^\circ\text{C}$) and diluted with $\times 3$ – $\times 5$ of lysis buffer containing 0.05 M Tris-HCl, pH 8.0 and 0.15 M NaCl supplemented with 1.0 mM final concentration of phenylmethylsulfonyl fluoride protease inhibitor or a tablet of EDTA-free protease inhibitor cocktail (Sigma-Aldrich, Germany). The cells were lysed with 35 cycles of sonication at 4°C on ice using 50% amplitude and 25 s sonication pulse with 1.5 min interval. Lysate was clarified with centrifugation at $\times 52,400$ g at 4°C for 45 min and the supernatant was filtered with a $0.45 \mu\text{m}$ syringe filter and mixed with 5–10 mL glutathione sepharose high-performance resin pre-equilibrated with lysis buffer, followed by incubation at 4°C with gentle rotation for 3 h. The mixture was loaded into an empty gravity column and the GST-tagged *DdDyP* was eluted with $\times 5$ column volume of an elution buffer containing 0.05 M Tris-HCl, pH 8.0, 0.15 M NaCl and 15–20 mM L-Glutathione (reduced form). The GST tag was then removed using HRV 3C protease with 1:20 enzyme to protein ratio at 4°C for overnight followed by passing the mixture through a glutathione sepharose column pre-equilibrated with lysis buffer. Purified protein was characterized with SDS-PAGE and UV-visible spectrophotometry. For crystallization the protein was

further purified with gel-filtration using Superdex 75 10/300 Increase column (Cytiva, Sweden). Purified protein was concentrated to 20 – 30 mg mL^{-1} in lysis buffer and stored at -80°C until further use. Overexpression, purification and crystallization were carried out at the XBI BioLab of the European XFEL facility (Han et al., 2021).

2.2 Heme reconstitution

A control heme reconstitution experiment was conducted as described previously (Chen et al., 2015). In brief, purified apo-*DdDyP* from LB expression was mixed with hemin chloride with ~ 1 :2 M ratio in a buffer containing 50 mM Tris-HCl, pH 7.0 and 150 mM NaCl, followed by incubation on ice for 30 min. The heme reconstituted holo-*DdDyP* protein was then passed through a PD-10 desalting column (Cytiva, Sweden) to remove the excess hemin chloride.

2.3 UV-visible spectrophotometry

All spectra were recorded on a Shimadzu UV-2700 PC spectrophotometer (Shimadzu Co., Japan) using a cuvette with 1.0 cm pathlength in a range of 200–700 nm at room temperature ($20^\circ\text{C} \pm 2.0^\circ\text{C}$). For measurements purified *DdDyP* was diluted with lysis buffer to a concentration of 0.4 mg mL^{-1} and the lysis buffer was used as a reference. All spectra were processed using the Origin software 2022b (OriginLab Co., United States).

2.4 Crystallization screening and crystal optimization of *DdDyP*

Crystallization screening was performed using a NT8 Formulatrix robot (Formulatrix, United States). Hit was obtained from the C12 condition (20% PEG 6000, 0.1 M HEPES, pH 7.0, 0.01 M ZnCl_2) of the PACT++ crystallization screen (Jena Bioscience, Germany) with 10 mg mL^{-1} of purified *DdDyP*. This condition was further optimized to 15% PEG 6000, 0.1 M HEPES-NaOH, pH 7.0, and 0.01 M ZnCl_2 crystallized with 15 mg mL^{-1} final concentration of purified *DdDyP*, which gave rise to a maximum crystal size of $200 \mu\text{m} \times 100 \mu\text{m} \times 25 \mu\text{m}$ at $20^\circ\text{C} \pm 1.0^\circ\text{C}$ in 4–6 weeks. Crystals were harvested directly from the drops using nylon loops and flash-cooled in liquid nitrogen.

2.5 X-ray diffraction data collection, processing and structure determination

X-ray diffraction datasets were collected at the P11/PETRA III beamline at DESY (Hamburg, Germany) using a flat focus with $20 \times 20 \mu\text{m}^2$ ($v \times h$) beam area at the sample position, 12.0 keV photon energy, and a photon flux of $\sim 2 \times 10^{10}$ photon sec^{-1} and an exposure time of 100 ms for a total wedge of 360° with 0.1° oscillation recording step on EIGER 16M detector (Burkhardt et al., 2016). Data collection was performed at cryogenic temperature, 100 K. Diffraction datasets were processed using the program XDS, and

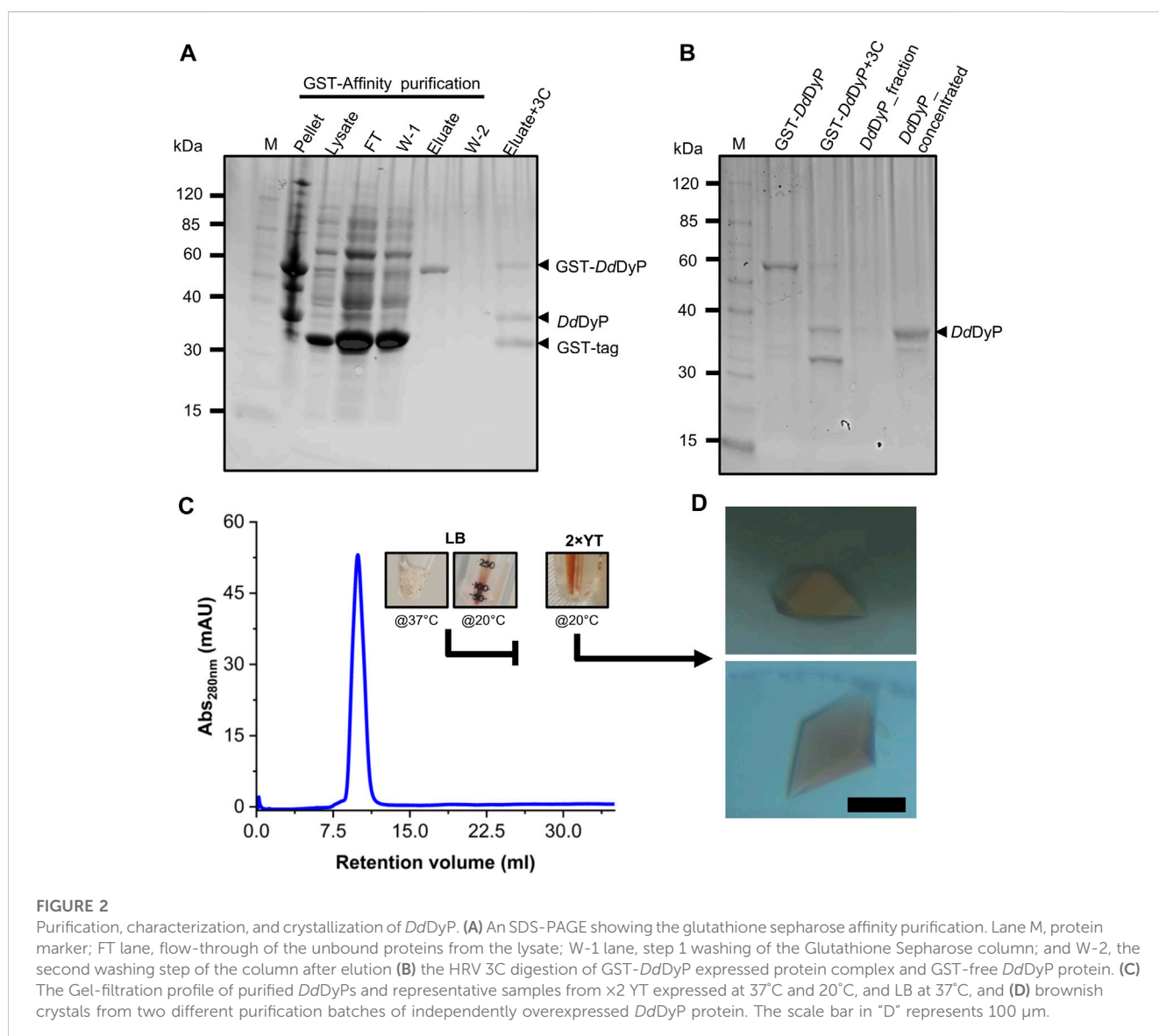
TABLE 1 Characterization of the native heme incorporation into *DdDyP* expressed in *E. coli* C43(DE3) at different conditions, the protein yield and crystallization trials.

Overexpression	Soret peak (nm)	R_z value (A_{soret}/A_{280})	Heme content (%) ^a	Protein yield (mg) ^b	Crystallization hits
LB at 37°C ± 1.0°C	406	0.27	26.5	1.2	No
LB at 20°C ± 1.0°C	405	0.502	49.3	2.96	No
2 × YT at 20°C ± 1.0°C	402	0.93	90	14.1	Yes
Reference ^c	406	1.02	100	1.2	Not tested

^aHeme content relevant to the reference value in this study, which was set to 100%.

^bThe yield is normalized to 25.0 g of wet weight of overexpressed cells used for purification.

^cThe reference is the *DdDyP* with a reconstituted heme; from LB, expression.



scaled with XSCALE in the XDS graphic user interface (Kabsch, 2010). The initial phase was obtained by molecular replacement using the *DdDyP* peroxidase active structure (PDB ID: 7ODZ) as a reference model with the program Phaser in the phenix software (Afonine et al., 2012). The model was then refined in phenix and

manually corrected in coot (Emsley et al., 2010). Radiation dose was estimated using the program RADDOSE-3D as described previously using the abovementioned parameters (Bury et al., 2018). For channel and cavity calculations MOLEontile tool (<https://mole.uplo.cz/method>) was used with the coordinate obtained from the

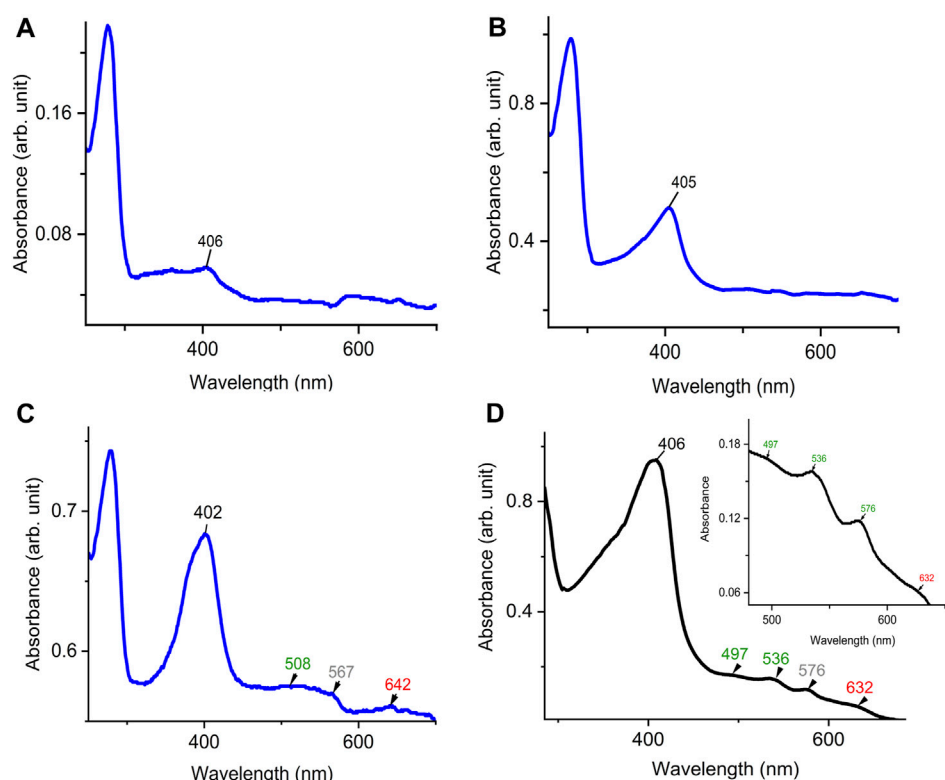


FIGURE 3

UV-visible electronic absorbance of *DdDyP* of different overexpression conditions. (A) a typical spectrum of a purified *DdDyP* when expressed in LB medium at 37°C, (B,C) *DdDyP* electronic spectra when expressed at 20°C in LB and x2 YT medium, respectively. The ET Q-band and charge transfer band in the region from 500 to 700 nm of the x2 YT condition are described in (C). (D) The reference UV-visible spectra of LB *DdDyP* after reconstitution with hemin chloride, and the small box in (D) represents a magnified view of the Q-band and charge transfer regions from 500 to 685 nm.

final cycle of refinement (PDB ID: 8OHY) as a template (Sehna et al., 2013). The interfaces of heme *b* and the oligomeric states analysis of *DdDyP* were calculated using PISA (Protein Interfaces, Surfaces, and Assemblies) server (Krissinel and Henrick, 2007).

3 Results and discussion

3.1 Heterologous expression and characterization of *DdDyP*

For heterologous expression, a *DdDyP* peroxidase gene was cloned into a pGEX-6P1 vector which has an HVR 3C excision site and a GST-tag in its N-terminal region as reported previously (Rai et al., 2021), however, we used the OverExpress *E. coli* C43(DE3) strain instead of BL21-derived Rosetta (DE3) strain for overexpression and purification of *DdDyP*. Note that both strains were derived from BL21(DE3). *DdDyP* was expressed at high and low temperature (37 ± 1.0 and $20^\circ\text{C} \pm 1.0^\circ\text{C}$) in LB and x2 YT medium with different yields, ranging from 2.1 to 14.1 mg of protein in average per 25 g of cells, respectively (Table 1). Figures 2A, B shows the SDS-PAGE analyses of the typical expression and purification of *DdDyP* in *E. coli* C43(DE3) strain. Protein expressed at $37^\circ\text{C} \pm 1.0^\circ\text{C}$, however, has transparent to pale brownish colour, whereas those of $20^\circ\text{C} \pm 1.0^\circ\text{C}$ exhibited a

darker brownish colour (Figure 2C). The proteins purified from high and low temperature have a reasonable purity with less aggregation (Figure 2) with ~35 kDa molecular weight as confirmed by the SDS-PAGE analysis. However, no crystallization hit was obtained from these conditions despite several attempts with various crystallization screens (Table 1). Since that our purified *DdDyP* has sufficient purity for crystallization, yet we did not successfully crystallize it, we concluded that the instability of the protein during expression at $37^\circ\text{C} \pm 1.0^\circ\text{C}$ may be the cause for the unsuccessful crystallization. This is likely due to the improper protein folding, and thus lowering the temperature of the expression may be one method for achieving a stable and correctly folded protein (Francis and Page, 2010; Huang et al., 2021). Indeed, when we expressed *DdDyP* at $20^\circ\text{C} \pm 1.0^\circ\text{C}$, it gave rise to a darker brownish protein (Figure 2C), a typical heme peroxidase colour of a native protein, especially when expressed in a x2 YT enriched medium, which is richer than LB. Intriguingly, *DdDyP* expressed in x2 YT at lower temperature was the only condition that resulted in a successful crystallization yielding dark brownish crystals, an indication that heme *b* is preserved during purification and crystallization (Figure 2D). The x2 YT also yielded several times higher amount of protein than that obtained in LB (Table 1).

To examine the quality of the electronic absorbance of purified *DdDyP* we used a UV-visible spectrophotometer. Figures 3A–D

shows the spectral analysis of the purified *DdDyP* protein from different conditions. *DdDyP* shows weak absorbance Soret peak at $\lambda = 405$ nm and a Reinheitszahl (R_Z) (A_{soret}/A_{280}) value of ~ 0.27 when expressed in LB at $37^\circ\text{C} \pm 1.0^\circ\text{C}$ (Table 1). This R_Z value is about 2 times higher than that obtained previously on peroxidases that were expressed using BL21(DE3) strain (Rai et al., 2014; Fiege et al., 2018). As shown in Table 1, we observed that the R_Z value increases $\times 2$ – 3 times to reach ~ 0.93 with $\lambda = 402$ nm of the Soret peak when expressing *DdDyP* in enriched $\times 2$ YT medium at low temperature ($20^\circ\text{C} \pm 1.0^\circ\text{C}$), indicating a heme occupancy of 90%–95% which is comparable to that of the secreted heme peroxidase (*DdPoxA*) (Nicolussi et al., 2018). This value is comparable to our heme reconstitution reference (Figure 3D) and significantly higher (about 7 times) than those previously reported, when DyP-peroxidases were expressed without adding heme supplements or δ -ALA during expression (Krainer et al., 2015; Fiege et al., 2018). Heme biosynthesis in *E. coli* relies on an L-glutamate, glycine, succinyl-CoA and other nitrogenous biochemicals which are abundant in both tryptone and yeast extracts—major components in $\times 2$ YT and LB medium (Layer et al., 2010; Krainer et al., 2015). The $\times 2$ YT medium has a double amount of tryptone and yeast extracts comparing to LB medium. The L-glutamate, which is a key substrate in the heme biosynthesis substrate δ -ALA in *E. coli*, is ~ 3.5 times higher than in LB (Lessard, 2013). Importantly, the $\times 2$ YT medium has higher concentrations of accessible Fe^{2+} and Mg^{2+} which are required for the ferrochelatase and δ -aminolevulinic dehydratase (the porphobilinogen (hemB) synthase), respectively (Sudhamsu et al., 2010; Zhang et al., 2015). Both enzymes are key to the biosynthesis of heme from L-glutamate in *E. coli* (Woodard and Dailey, 1995; Pranawidjaja et al., 2015; Zhang et al., 2015; Feige et al., 2018; Ge et al., 2023). This might indicate a higher level of heme biosynthesis, and thus its native incorporation into *DdDyP*, in $\times 2$ YT than that in LB (Table 1). The heme reconstituted *DdDyP* from LB expression shows a Soret absorbance at 406 nm and an electron transfer (ET) (Q-band) at $\lambda = 497$ nm plus two additional ET bands at 536 nm and 576 nm as well as a charge transfer (CT) component at 636 nm, preserving some bacterial peroxidase features (Chen and Li, 2016). This region differs significantly from that previously reported in *DdDyP*, which showed an ET and CT band at 506 nm and 636 nm, respectively (Rai et al., 2021). Interestingly, our purified *DdDyP* displays similar features in the Q-band and ET regions to those of the secreted *DdPoxA* heme peroxidase (Nicolussi et al., 2018). We also observed that the *DdDyP* with a natively incorporated heme has a broad ET peak with $\lambda_{\text{max}} = 508$ nm, which is slightly red shifted with $\Delta\lambda = 9$ nm and $\Delta\lambda = 2$ nm, comparing to that of the ET bands of the reference (Figures 3C, D) and a previous work, respectively (Rai et al., 2021). The Q-band region also reveals a unique shoulder at the ET band with 567 nm absorbance (Figure 3C).

3.2 Native structure of *DdDyP* peroxidase and its comparison with the cyanide native structure

Several *DdDyP* structures have been resolved so far including a single native structure that is in complex with cyanide (PDB: 7O9L) (Rai et al., 2021), however there is no available structure that describes

the native resting state. Here, to get insight into the heme binding pocket in its native form, we crystallized the native *DdDyP* peroxidase bound to a natively incorporated heme and compared it with that resolved in complex with cyanide. A single crystal with a size of $150 \times 80 \times 30 \mu\text{m}^3$ size was used for diffraction data collection (Figure 2D). The crystal data collection and refinement statistics are shown in Table 2. Native *DdDyP* peroxidase is crystallized in a tetragonal space group $P4_1 2_1 2$ similar to previously reported structures (Rai et al., 2014), with exception that the X-ray data of the current crystal condition can be equally processed and resolved in an additional space group ($P4_3 2_1 2$) (Table 2). Moreover, the crystal unit cell exhibited significantly shorter axes, giving rise to about 35% smaller cell volume with 52.8% solvent content and $2.62 \text{ \AA}^3 \text{ Da}^{-1}$ of Matthew's coefficient (V_m), indicating the presence of a single molecule per asymmetric unit. The solvent content is decreased by $\sim 20\%$ comparing to that previously reported (Rai et al., 2021). This is more likely due to a relatively high concentration of the dehydrating precipitant ($\sim 30\%$ PEG 6000), as previously reported in other systems (Umena et al., 2011; Koua et al., 2013). Such high PEG concentration causes a shrinking in the protein crystals by mechanism of dehydration which shortens the axes and leads to a tightly packed unit cell (Supplementary Figure S1). The average radiation dose on a single crystal was estimated with RADDOSE-3D (Bury et al., 2018) to be $\sim 0.58 \text{ MGy}$ ($\text{Gy} = \text{J} \cdot \text{kg}^{-1}$) (Table 2) which lies well below the 20 MGy dose limit suggested by Henderson (Henderson, 1990) or the 30 MGy suggested by Owen and Garman (Owen et al., 2006), indicating that the structure is less affected by radiation damage.

The overall architecture of *DdDyP* is similar to that of the typical DyP-type peroxidase superfamily (Figures 4A–D) (Sugano et al., 2007; Chen et al., 2015; Rai et al., 2021). *DdDyP* contains a duplicated ferredoxin-like fold domain arranged as a β -barrel at the N- and C-terminals of the protein (Figures 4A, B). It contains 12 β -sheets and 13 α -helices formed by 185 residues of the full chain (306 residues), and the remaining 121 residues involved in the formation of loop structures that link these secondary structures. Similar to all other known DyP-type peroxidases, *DdDyP* contains α -helices with a unique β -sheet structure at the distal region of the heme plane (Sugano et al., 2007; Strittmatter et al., 2013). We determined the root mean square deviation (r.m.s.d.) between the Ca (1–306 residues) of the present structure with that resolved in complex with cyanide (PDB ID: 7O9L) to be 0.18 \AA , indicating the striking similarity between the two structures (Figure 4C). Our PISA analysis predicted a stable dimer of *DdDyP* in solution with 33 residues contributing to the dimer interface, similar to previously reported *DdDyP* structures (Rai et al., 2021). These interfacial residues are distributed along the dimer interface from the N- to the C-terminal region. The dimeric structure reveals a solvent accessible area of $24,290 \text{ \AA}^2$ and buried surface areas (BSA) of $5,330 \text{ \AA}^2$, corresponding to about 22% of the total surface area of the protein. On the other hand, the BSA of the monomeric structure is $1,341 \text{ \AA}^2$, corresponding to 9.6% of the total surface area of monomeric *DdDyP*. It should be noted that our PISA analysis favoured a tetramer oligomeric state for the native cyanide *DdDyP* (PDB ID: 7O9L) structure, displaying higher binding energy than that of the dimeric state. This indicates that *DdDyP* protein may exist physiologically in various oligomeric states. Indeed, several DyP-type peroxidases have been reported to exist in different functional oligomeric states ranging from

TABLE 2 X-ray diffraction data collection and crystallography refinement statistics.

	Native <i>DdDyP</i> structure
PDB ID	8OHY
Data collection	
Beamline	P11/PETRA III at DESY
Photon energy (keV)	12.0
Photon flux (ph. s ⁻¹)	~2 × 10 ¹⁰
Radiation dose (MGy)	~0.58
Space group	<i>P</i> 4 ₁ 2 ₁ 2
Cell dimensions	
a, b, c (Å)	99.88 99.88 73.12
α, β, γ (°)	90.00 90.00 90.00
Resolution (Å)	44.67–1.95 (2.02–1.95) ^a
<i>R</i> _{merge} ^b	0.2715 (4.643) ^a
<i>I</i> /σ <i>I</i>	12.02 (0.6) ^a
Completeness (%)	98.54 (91.55) ^a
Multiplicity	26.7 (26.0) ^a
<i>CC</i> _{1/2}	0.999 (0.411) ^a
<i>CC</i> ^c	1.0 (0.764) ^a
Wilson <i>B</i> -factor (Å ²)	36.8
Refinement	
Resolution range (Å)	44.67–1.95
No. of reflections (unique)	27,129 (2,471) ^a
Reflections used for <i>R</i> _{free}	1,114 (102)
<i>R</i> _{work} / <i>R</i> _{free} ^c	0.206 (0.400) ^a /0.247 (0.445) ^a
No. of atoms	2,662
Protein	2,459
Ligands	74
Solvent	163
No. of residues	306
Average <i>B</i> -factor (Å ²)	41.29
Protein	41.23
Ligands	39.63
Solvents	42.76
r.m.s. deviations	
Bonds (Å)	0.005
Angles (°)	0.71
Ramachandran (%)	
Favored	98.03
Allowed	1.97
Outliers	0.00

(Continued on following page)

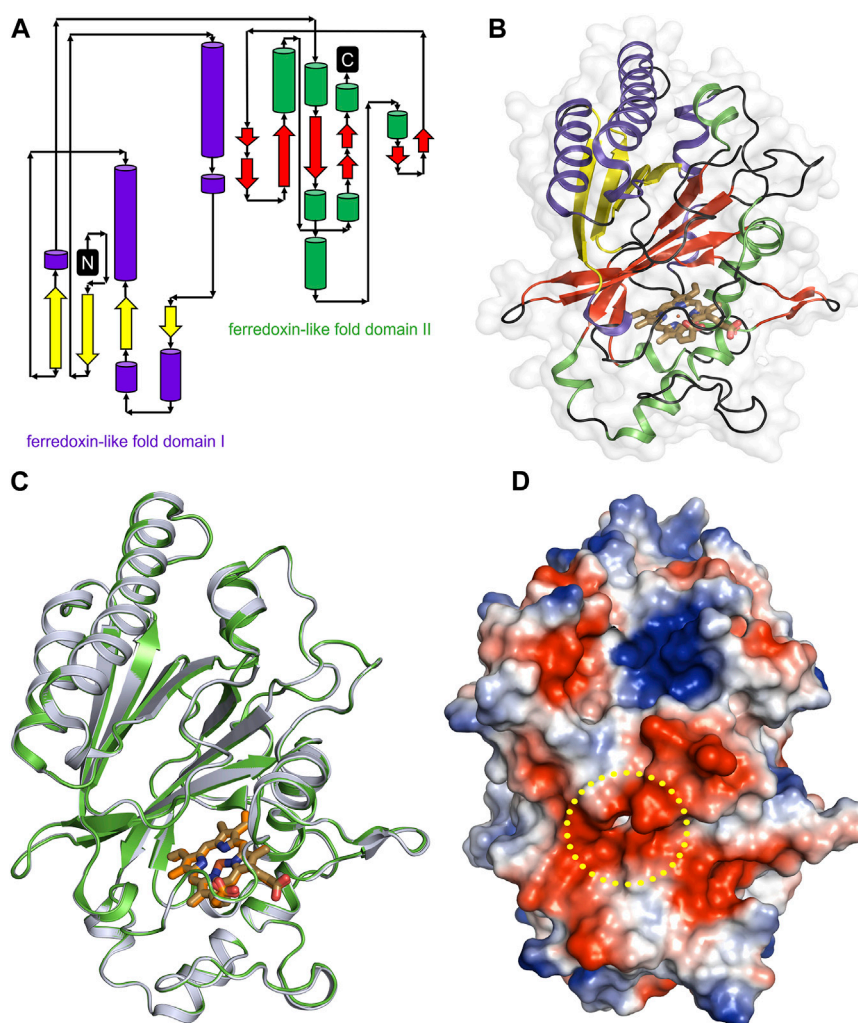
TABLE 2 (Continued) X-ray diffraction data collection and crystallography refinement statistics.

	Native <i>DdDyP</i> structure
Rotamer outliers (%)	0.00
Clashscore	1.00
Number of TLS groups	1

^aValues in parenthesis are of the highest resolution shell.

^b $R_{merge} = \sum_h \sum_i |I_i(h) - \langle I(h) \rangle| / \sum_h \sum_i I_i(h)$, where $I_i(h)$ is the intensity measurement for a reflection h and $\langle I(h) \rangle$ is the mean intensity for this reflection.

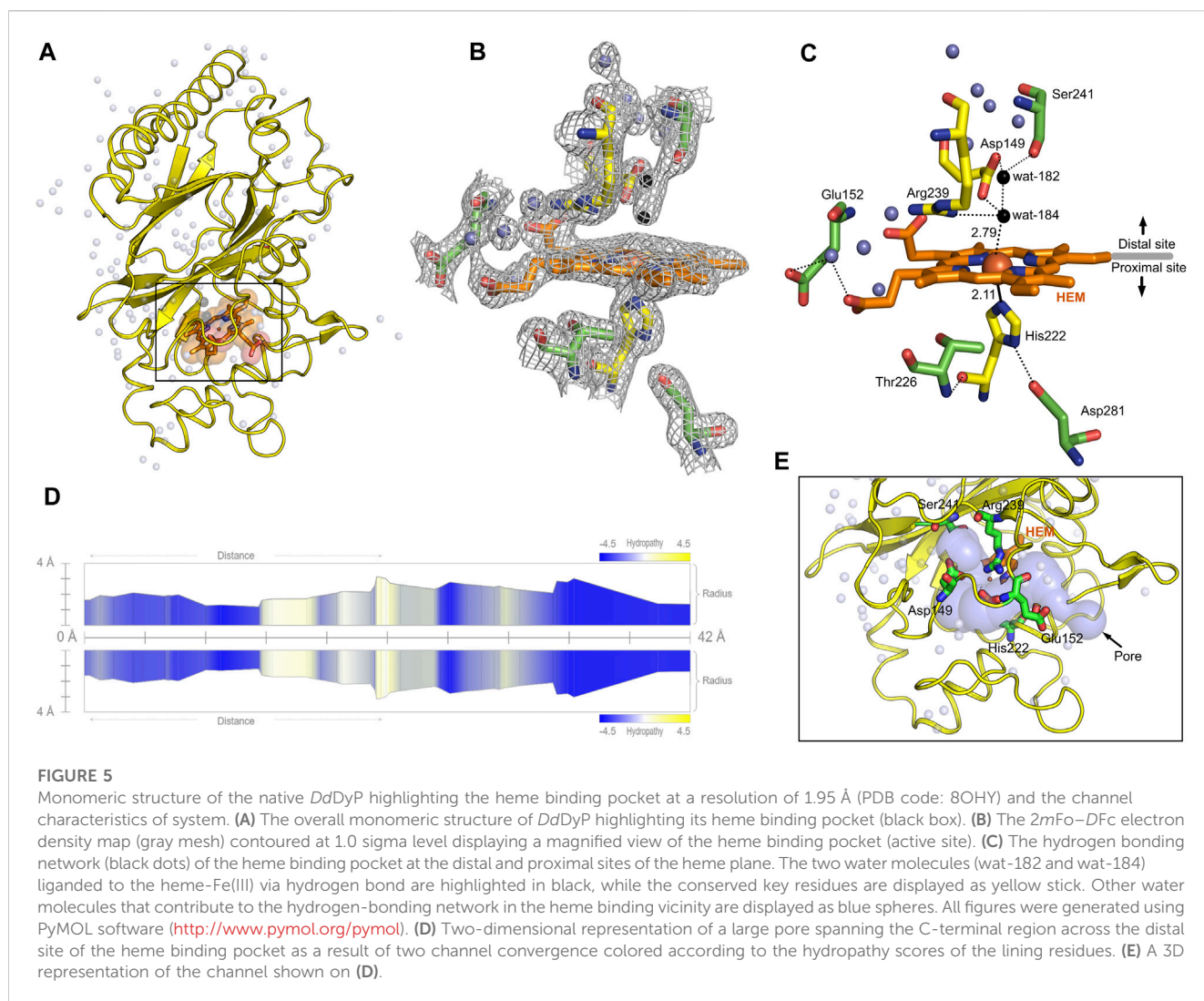
^c $R_{work} = \sum_h \|F_{obs} - F_{calc}\| / \sum_h F_{obs}$ and R_{free} was calculated using a randomly (5.0%) selected reflections.

**FIGURE 4**

Overall structure of native *DdDyP* and its superposition with native cyanide *DdDyP* structure (PDB code: 7O9L). (A) Topology representation of the *DdDyP*-type peroxidase. (B) Overall structure of monomeric *DdDyP* showing the ferredoxin-like folds at the N- and C-terminals colored according to (A). (C) Superimposition of native *DdDyP* structure (green) into a cyanide native structure (gray). (D) Electrostatic potentials surface of native *DdDyP* colored from -5.7 kT (red) to $+5.7$ kT (blue) calculated using the program PyMOL (<http://www.pymol.org/pymol>). The yellow dashed circle highlights the heme binding pocket and possible pathway for H_2O_2 and/or substrate entry.

monomeric to tetrameric state (Zubieta et al., 2007; Liu et al., 2011; Yoshida et al., 2016; Pfanzagl et al., 2020). The catalytic arginine residue, Arg239 in *DdDyP*, has been suggested to play a role in the protein oligomerization owing to its location and hydrogen bonding

network with surface residues (Singh et al., 2012; Chen et al., 2015). In *DdDyP*, Arg239 is buried in the hydrophobic cavity of the heme binding pocket, excluding its contribution in *DdDyP* oligomerization. Moreover, our molecular replacement attempts aiming for a dimeric



solution was not successful, thus we can reasonably conclude that our purified *DdDyP* favours a monomeric state in crystal. It has been previously reported, based on sedimentation velocity analysis with analytical ultracentrifugation, that dimeric *DdDyP* predominates in solution, which yielded a dimeric crystal structure (Rai et al., 2021). The crystal packing behaviour of the present structure (PDB ID: 8OHY) is significantly different from that described previously (Rai et al., 2021), likely due to a significantly low unit cell volume which exerts tight interactions between molecules in the unit cell (Supplementary Figure S1). Note that the molecular contact within the unit cell is contributed by similar regions in both forms that is primarily the loop and β -sheet of the ferredoxin-fold like domain II at the C-terminal region (Supplementary Figure S1).

3.3 Geometry of a natively incorporated heme, its binding pocket and the implication in catalysis.

Heme *b* in the DyP-type peroxidases, a protoheme IX, is either penta- or hexacoordinated (Sugano et al., 2007; Singh et al., 2012;

Rodrigues et al., 2021). The native structure of *DdDyP* accommodates heme *b* in a hydrophobic binding pocket flanked by the unique β -sheet at the distal side of the heme plane, the α -helices of the ferredoxin-like fold domain II (Figures 5A–C, E) and a distinct long loop at its proximal side similar to previously reported DyP structures (Sugano et al., 2007; Zubieta et al., 2007; Liu et al., 2011). Our structural analysis shows that the native *DdDyP* heme is hexacoordinated, of which the pyrrole rings of porphyrin contributed to tetradentate chelation via their nitrogen atoms and via the conserved His222 at the proximal side with a distance of 2.11 Å. The sixth coordination is provided by a water molecule (wat-184) with a distance of 2.79 Å, which is shorter by ~ 0.1 Å than that of the reported Fe(III)–CN distance, indicating a stronger coordination to Fe(III) (Figure 5C). This distance is typical for Fe(III) of the resting state, implying that the model is unaltered by radiation damage (Chen et al., 2015). Wat-184 forms a strong hydrogen bond (~ 2.2 Å) with wat-182 and a weaker hydrogen bond with the catalytic residue Arg239 (Figure 5C). Intriguingly, the environment of our native *DdDyP* heme binding pocket is similar to that of the bacterial DypB and DtpAa peroxidases and that of the peroxidase-cyclooxygenase *DdPoxA* (Chen et al., 2015;

Nicolussi et al., 2018; Ebrahim et al., 2019). The room-temperature serial femtosecond crystallography structure of the DtpAa revealed two water molecules (w1 and w2) in the catalytic vicinity with w1 ligated to the heme-Fe(III) with a distance of 2.32 Å (Ebrahim et al., 2019). We observed that wat-184 has slightly higher *B*-factor than wat-182, which may indicate its mobility and higher reactivity. On the other hand, wat-182 interacts via strong hydrogen bonds with the second catalytic residue Asp149 as well as Ser241, suggesting that these residues may act as proton acceptors to the H₂O₂ during the formation of compound I oxyferryl thereby contributing to its stabilization along with Arg239 (Figure 5C) as revealed in other A-type DyP peroxidases (Pfanzagl et al., 2019). The binding pocket is extensively occupied with water molecules which are in hydrogen bonding interaction with nearby residues that contribute to the heme stability (Figure 5C). Note that two of the water molecules (wat-150 and wat-159), which are in hydrogen bonding interaction with Asp149 and Arg137 near the heme access channel, substituted the 1,2-ethanediol molecule in the cyanide native structure that shifted Asp149 carboxylate group towards the cyanide, giving rise to increased *B*-factor of Asp149 comparing to its surrounding (Rai et al., 2021). This may indicate that this position is natively occupied by water molecules as demonstrated by our native structure.

The heme ligand is well resolved at a resolution of 1.95 Å as revealed by its 2mFo-DFc electron density map (Figure 5B; Supplementary Figure S2), indicating unambiguous incorporation and binding of the heme in the apo-protein. This is an important finding as crystallization with purified DdDyP proteins that have lower *R*_Z values were not successful, which might indicate that the heme on these purified proteins is not well accommodated in the binding pocket, affecting possibly their stability and hence the crystallization (see Table 1). The heme occupies 798 Å² surface area, corresponding to 5.7% of the total surface area of the native structure, similar to that of the cyanide native DdDyP structure and other DdDyP structures (Rai et al., 2021). PISA analysis indicates that the solvation free energy gain (Δ^1G) of the natively incorporated heme is -22.5 kcal mol⁻¹ with 622 Å² interface area comparing to an average of -22.3 kcal mol⁻¹ for the reconstituted heme of the cyanide native structure (PDB ID: 7O9L) which has an interface interaction area of 609 Å², indicating similar heme binding affinity with slightly better properties for the natively incorporated heme. The van der Waals interactions as well as the hydrogen-bonding network provided by nearby residues and water molecules may contribute to the stabilization of heme binding (Figure 5C) (Sacquin-Mora and Lavery, 2006; Mogharrab et al., 2007). Our analysis shows that the heme is stabilized, along the plane, via its carboxylate oxygens by hydrogen bonding with several water molecules (wat-120, wat-79 and wat-166), and three residues, Glu152, Arg204 and Arg239. The Arg239 interacts weakly with the heme carboxylate oxygens via two hydrogen bonds with a distance of 3.3–3.4 Å, whereas Glu152 and Arg204 form hydrogen bonding with the heme via wat-120 and wat-166, respectively. These interactions indicate that the heme is well stabilized in our model (PDB ID: 8OHY), which confirms the correct geometry of its native incorporation, yielding comparable binding pocket geometry to that prepared with *in vitro* reconstitution (Chen et al., 2015; Rai et al., 2021). Furthermore, the superimposition with the cyanide native structure indicates a striking similarity (r.m.s.d. = ~0.18 Å) around the heme binding

pocket including the flanking loop at the proximal side of the heme plane (residues 204–220) (Figure 4D). A side-specific mutagenesis study in DypB found that this proximal loop may have significant role in the heme stability (Rodrigues et al., 2021). This loop has also been implicated in the stabilization of the substrate owing to its flexibility thereby facilitating the substrate/product turnover by flipping in and out around the heme binding site (Liu et al., 2011).

Further, we used the MOLEonline tool (<https://mole.upol.cz/online>) to analyse the cavities and tunnels nearby the heme binding pocket and those in long-range distances (Supplementary Figure S3) (Sehna et al., 2013). Overall, 14 tunnels were identified, three of which are located next to the heme and perpendicular to each other with characteristics that might have an implication in the DdDyP catalysis—entry of substrates and exit of reaction products. These channels may serve as entry gates for H₂O₂ thereby facilitating the enzyme activation required for the oxidative catalysis (Figure 5A) (Chen et al., 2015; Yoshida et al., 2016; Habib et al., 2019). Two tunnels have average diameter of ~3.0 Å, which is sufficient to facilitate the entry of H₂O₂ and perhaps the exit of reaction products of similar size. This diameter is about twice the diameter of the substrate channels in the DdPoxA, which is located roughly in a similar position at the distal side (Nicolussi et al., 2018). This may imply variation on the nature and substrate sizes between the two classes of heme peroxidases, the DyP-type and the peroxidase-cyclooxygenase. All tunnels are lined with hydrophobic residues in the middle of the channel as well as several key catalytic residues in the distal and proximal sides of the heme plane. In particular, Arg239, Asp149, His222, Glu152, Ser241, and Thr226 in addition to several hydrophobic residues where found in two proximal channels (Supplementary Figure S3), which are converged to form a main channel with a length of 42 Å and a diameter of ~4.0 Å. The access gate of this channel is lined with charged residues as shown in Figures 5D, E, indicating its implication in the substrate entry. Further, we identified two major cavities at the distal side of the heme plane, of which one cavity (cavity 1) has a volume of 2,881 Å³, corresponding to 9.6% of the total surface of DdDyP and 4.7 times of the heme molecule. It is located at the heme binding pocket, accommodating the main channel at the binding pocket and extends to the proximal side of the heme plane, indicating a role for this cavity in the catalysis of DyP-peroxidases (Yoshida et al., 2011; Habib et al., 2019; Rai et al., 2021). The second cavity (cavity 2) with approximately half a volume of that of cavity 1 (1,411 Å³) is located at the N-terminal region distant from the heme binding pocket and in contact with cavity 2 near the molecular centre of DdDyP (Supplementary Figure S3). The presence of such cavities is important for accommodating wide-range of substrates thereby fulfilling the substrate broad specificity of DyP-type peroxidases (Pfanzagl et al., 2019; Silva et al., 2023).

4 Conclusion

In conclusion, we demonstrated the use of *E. coli* C43(DE3) strain for heterologous expression of DdDyP peroxidase, without the use of a heme precursor δ -ALA, heme chloride or iron supplement, to produce DdDyP holoprotein with a natively incorporated heme, relying primarily on the *E. coli* heme biosynthesis by benefiting from

the use of enriched medium and low temperature during expression, which yielded an R_Z value of ~ 1.0 and a holoprotein with sufficient stability. We further showed, by mean of X-ray crystallography, that the native DdDyP expressed in this condition has comparable heme geometry and binding properties. Our study also demonstrates that the natively incorporated heme is well stabilized via hydrogen bonds provided by nearby Arg239, Glu152 and water molecules in addition to van der Waals interactions between the porphyrin rings and surrounding residues within van der Waals distances. Two cavities occupying a total volume of $4,292 \text{ \AA}^3$, corresponding to 14.3% of the total monomeric volume ($29,951 \text{ \AA}^3$), were identified. Of which the main cavity (cavity 1) around the heme binding pocket was found to accommodate a large access channel that spans the heme binding pocket.

The high-quality crystals optimized in this work would be suitable for use as a model for metalloenzymes to study the dynamics and substrate binding kinetics during catalysis. This can be achieved by, for instance, the mixing-and-inject time-resolved serial femtosecond crystallography approach (Pandey et al., 2021), which enables tracking the formation of the reaction intermediates as well as the mechanism of substrate breakdown into products as demonstrated in other metalloproteins (Malla and Schmidt, 2022; Worrall and Hough, 2022). Our work provides a firm basis for future co-crystallization and ligand binding experiments with a range-range of substrates of different classes to investigate the molecular mechanism of the broad substrate-specificity in DyP-type peroxidases using spectroscopic, X-ray diffraction and theoretical methods.

Furthermore, the present work may contribute to the ongoing efforts in exploiting the catalytic activity of DyP-type peroxidases in combination with other enzymes such as laccase to enhance the catalytic properties (Permana et al., 2019), for examples, for the production of efficient gas/water permeable barrier materials or in the food packaging sectors by improving the mechanical and antioxidant properties of lignocellulosic composite films (Gerbin et al., 2020), or for biomedical and pharmaceutical applications, e.g., melanin decolorization, biosynthesis of bioactive natural products and pharmaceuticals degradation (Shin et al., 2019; Mohit et al., 2020; Cardullo et al., 2022).

Data availability statement

The datasets presented in this study can be found in online repositories. The names of the repository/repositories and accession number(s) can be found in the article/Supplementary Material.

Author contributions

Conceptualization, FK; experiments, ÖK, LB, HH, and FK; formal analysis and data interpretation, FK; Diffraction data

collection and processing, FK, ÖK, and SK; X-ray structural analysis, FK; contributed funding/reagents/analytic tools, RB and AM; supervised the project, FK; manuscript writing, FK with input from all authors. All authors contributed to the article and approved the submitted version.

Funding

This work was supported by the European XFEL GmbH internal operational budget for the SPB/SFX instrument.

Acknowledgments

We would like to thank the staff members of the SPB/SFX instrument of European XFEL GmbH for fruitful discussion during the conduction of this research. We are grateful to the staff members of the XBI Biolab at European XFEL GmbH for technical support. We acknowledge the use of the XBI Biolab at European XFEL GmbH, enabled by the XBI User Consortium. X-ray diffraction experiments at the P11/PETRA III beamline in DESY were carried out via the proposal no. BAG-20211047 acquired by Huijong Han and Kristina Lorenzen from European XFEL GmbH. We also thank the staff members of the P11/PETRA III beamline at DESY, Hamburg. We acknowledge European XFEL GmbH in Schenefeld, Germany, for provision of biochemistry and x-ray beamtimes at PETRA III/DESY.

Conflict of interest

The authors declare that the research was conducted in the absence of any commercial or financial relationships that could be construed as a potential conflict of interest.

Publisher's note

All claims expressed in this article are solely those of the authors and do not necessarily represent those of their affiliated organizations, or those of the publisher, the editors and the reviewers. Any product that may be evaluated in this article, or claim that may be made by its manufacturer, is not guaranteed or endorsed by the publisher.

Supplementary material

The Supplementary Material for this article can be found online at: <https://www.frontiersin.org/articles/10.3389/fchem.2023.1220543/full#supplementary-material>

References

- Afonine, P. V., Bunkoczi, G., Chen, V. B., Headd, J. J., McCoy, A. J., Moriarty, N. W., et al. (2012). Graphical tools for macromolecular crystallography in PHENIX. *J. Appl. Cryst.* 45, 581–586. doi:10.1107/S0021889812017293
- Burkhardt, A., Pakendorf, T., Reime, B., Meyer, J., Fischer, P., Stübe, N., et al. (2016). Status of the crystallography beamlines at PETRA III. *Eur. Phys. J. Plus* 131, 56. doi:10.1140/epjp/i2016-16056-0

- Bury, C. S., Brooks-Bartlett, J. C., Walsh, S. P., and Garman, E. F. (2018). Estimate your dose: RADDSE-3D. *Protein Sci.* 27, 217–228. doi:10.1002/pro.3302
- Cardullo, N., Muccilli, V., and Tringali, C. (2022). Laccase-mediated synthesis of bioactive natural products and their analogues. *RSC Chem. Biol.* 3, 614–647. doi:10.1039/D1CB00259G
- Chen, C., and Li, Tao. (2016). Bacterial dye-decolorizing peroxidases: Biochemical properties and biotechnological opportunities. *Phys. Sci. Rev.* 1, 20160051. doi:10.1515/psr-2016-0051
- Chen, C., Shrestha, R., Jia, K., Gao, P. F., Geisbrecht, B. V., Bossmann, S. H., et al. (2015). Characterization of dye-decolorizing peroxidase (DyP) from *thermomonomospora curvata* reveals unique catalytic properties of A-type DyPs. *J. Biol. Chem.* 290, 23447–23463. doi:10.1074/jbc.M115.658807
- Colpa, D. I., Fraaije, M. W., and van Bloois, E. (2014). DyP-Type peroxidases: A promising and versatile class of enzymes. *J. Ind. Microbiol. Biotechnol.* 41, 1–7. doi:10.1007/s10295-013-1371-6
- de Gonzalo, G., Colpa, D. I., Habib, M. H., and Fraaije, M. W. (2016). Bacterial enzymes involved in lignin degradation. *J. Biotechnol.* 236, 110–119. doi:10.1016/j.jbiotec.2016.08.011
- Denninger, J. W., Schelvis, J. P. M., Brandish, P. E., Zhao, Y., Babcock, G. T., and Marletta, M. A. (2000). Interaction of soluble guanylate cyclase with YC-1: Kinetic and resonance Raman studies. *Biochemistry* 39, 4191–4198. doi:10.1021/bi992332q
- Ebrahim, A., Moreno-Chicano, T., Appleby, M. V., Chaplin, A. K., Beale, J. H., Sherrell, D. A., et al. (2019). Dose-resolved serial synchrotron and XFEL structures of radiation-sensitive metalloproteins. *IUCr* 6, 543–551. doi:10.1107/S2052525219003956
- Emsley, P., Lohkamp, B., Scott, W. G., and Cowtan, K. (2010). Features and development of coot. *Acta Cryst. D.* 66, 486–501. doi:10.1107/S0907444910007493
- Fiege, K., Querebillo, C. J., Hildebrandt, P., and Frankenberg-Dinkel, N. (2018). Improved method for the incorporation of heme cofactors into recombinant proteins using *Escherichia coli* Nissle 1917. *Biochemistry* 57, 2747–2755. doi:10.1021/acs.biochem.8b00242
- Francis, D. M., and Page, R. (2010). Strategies to optimize protein expression in *E. coli*. *Curr. Protoc. Protein Sci.* 5 (1), 5241–52429. doi:10.1002/0471140864.ps0524s61
- Gan, J., Bilal, M., Li, X., Hussain Shah, S. Z., Mohamed, B. A., Hadibarata, T., et al. (2022). Peroxidases-based enticing biotechnological platforms for biodegradation and biotransformation of emerging contaminants. *Chemosphere* 307 (Pt3), 136035. doi:10.1016/j.chemosphere.2022.136035
- Ge, J., Wang, X., Bai, Y., Wang, Y., Wang, Y., Tu, T., et al. (2023). Engineering *Escherichia coli* for efficient assembly of heme proteins. *Microb. Cell Fact.* 22, 59. doi:10.1186/s12934-023-02067-5
- Gerbin, E., Frapart, Y.-M., Marcuello, C., Cottyn, B., Foulon, L., Pernes, M., et al. (2020). Dual antioxidant properties and organic radical stabilization in cellulose nanocomposite films functionalized by *in situ* polymerization of coniferyl alcohol. *Biomacromolecules* 21, 3163–3175. doi:10.1021/acs.biomac.0c00583
- Habib, M. H., Rozeboom, H. J., and Fraaije, M. W. (2019). Characterization of a new DyP-peroxidase from the alkaliphilic *Cellulomonas bogoriensis*. *Molecules* 24, 1208. doi:10.3390/molecules24071208
- Han, H., Round, E., Schubert, R., Gül, Y., Makroczyová, J., Meza, D., et al. (2021). The XBI BioLab for life science experiments at the European XFEL. *J. Appl. Crystallogr.* 54 (Pt 1), 7–21. doi:10.1107/S1600576720013989
- Henderson, R. (1990). Cryo-protection of protein crystals against radiation damage in electron and X-ray diffraction. *Proc. R. Soc. B Biol. Sci.* 241, 6–8. doi:10.1098/rspb.1990.0057
- Huang, C.-J., Peng, H.-L., Patel, A. K., Singhanian, R. R., Dong, C.-D., and Cheng, C.-Y. (2021). Effects of lower temperature on expression and biochemical characteristics of HCV NS3 antigen recombinant protein. *Catalysts* 11, 1297. doi:10.3390/catal11111297
- Kabsch, W. (2010). XDS. *Acta Crystallogr. D. Biol. Crystallogr.* 66 (Pt 2), 125–132. doi:10.1107/S0907444909047337
- Kim, S. J., and Shoda, M. (1999). Purification and characterization of a novel peroxidase from *Geotrichum candidum* dec 1 involved in decolorization of dyes. *Appl. Environ. Microbiol.* 65, 1029–1035. doi:10.1128/AEM.65.3.1029-1035.1999
- Koua, F. H., Umena, Y., Kawakami, K., and Shen, J.-R. (2013). Structure of Sr-substituted photosystem II at 2.1 Å resolution and its implications in the mechanism of water oxidation. *Proc. Natl. Acad. Sci. U. S. A.* 110, 3889–3894. doi:10.1073/pnas.1219922110
- Krainer, F. W., Capone, S., Jäger, M., Vogl, T., Gerstmann, M., Glieder, A., et al. (2015). Optimizing cofactor availability for the production of recombinant heme peroxidase in *Pichia pastoris*. *Microb. Cell Fact.* 14, 4. doi:10.1186/s12934-014-0187-z
- Krissinel, E., and Henrick, K. (2007). Inference of macromolecular assemblies from crystalline state. *J. Mol. Biol.* 372, 774–797. doi:10.1016/j.jmb.2007.05.022
- Layer, G., Reichelt, J., Jahn, D., and Heinz, D. W. (2010). Structure and function of enzymes in heme biosynthesis. *Protein Sci.* 19, 1137–1161. doi:10.1002/pro.405
- Lemon, C. M., and Marletta, M. A. (2021). Designer heme proteins: Achieving novel function with abiological heme analogues. *Acc. Chem. Res.* 54, 4565–4575. doi:10.1021/acs.accounts.1c00588
- Lessard, J. C. (2013). Growth media for *E. coli*. *Methods Enzymol.* 533, 181–189. doi:10.1016/B978-0-12-420067-8.00011-8
- Liu, X., Du, Q., Wang, Z., Zhu, D., Huang, Y., Li, N., et al. (2011). Crystal structure and biochemical features of EfeB/YcdB from *Escherichia coli* O157. *J. Biol. Chem.* 286, 14922–14931. doi:10.1074/jbc.M110.197780
- Malla, T. N., and Schmidt, M. (2022). Transient state measurements on proteins by time-resolved crystallography. *Curr. Opin. Struct. Biol.* 74, 102376. doi:10.1016/j.sbi.2022.102376
- Mogharrab, N., Ghourchian, H., and Amininasab, M. (2007). Structural stabilization and functional improvement of horseradish peroxidase upon modification of accessible lysines: Experiments and simulation. *Biophys. J.* 92, 1192–1203. doi:10.1529/biophysj.106.092858
- Mohit, E., Tabarzad, M., and Faramarzi, M. A. (2020). Biomedical and pharmaceutical-related applications of laccases. *Curr. Protein Pep. Sci.* 21, 78–98. doi:10.2174/1389203720666191011105624
- Nicolussi, A., Dunn, J. D., Mlynek, G., Bellei, M., Zamocky, M., Battistuzzi, G., et al. (2018). Secreted heme peroxidase from *Dictyostelium discoideum*: Insights into catalysis, structure, and biological role. *J. Biol. Chem.* 293, 1330–1345. doi:10.1074/jbc.RA117.000463
- Owen, R. L., Rudino-Pinera, E., and Garman, E. F. (2006). Experimental determination of the radiation dose limit for cryocooled protein crystals. *Proc. Natl. Acad. Sci. U. S. A.* 103, 4912–4917. doi:10.1073/pnas.0600973103
- Pandey, S., Calvey, G., Katz, A. M., Malla, T. N., Koua, F. H. M., Martin-Garcia, J. M., et al. (2021). Observation of substrate diffusion and ligand binding in enzyme crystals using high-repetition-rate mix-and-inject serial crystallography. *IUCr* 8, 878–895. doi:10.1107/s2052252521008125
- Park, Y.-J., and Kim, D.-M. (2021). Production of recombinant horseradish peroxidase in an engineered cell-free protein synthesis system. *Front. Bioeng. Biotechnol.* 9, 778496. doi:10.3389/fbioe.2021.778496
- Permana, D., Minamihata, K., Tatsuke, T., Lee, J. M., Kusakabe, T., Goto, M., et al. (2019). Polymerization of horseradish peroxidase by a laccase-catalyzed tyrosine coupling reaction. *Biotechnol. J.* 14, e1800531. doi:10.1002/biot.201800531
- Pfanzagl, V., Beale, J. H., Michlits, H., Schmidt, D., Gabler, T., Obinger, C., et al. (2020). X-ray-induced photoreduction of heme metal centers rapidly induces active-site perturbations in a protein-independent manner. *J. Biol. Chem.* 295 (39), 13488–13501. doi:10.1074/jbc.RA120.014087
- Pfanzagl, V., Bellei, M., Hofbauer, S., Laurent, C. V. F. P., Furtmüller, P. G., Oostenbrink, C., et al. (2019). Redox thermodynamics of B-class dye-decolorizing peroxidases. *J. Inorg. Biochem.* 199, 110761. doi:10.1016/j.jinorgbio.2019.110761
- Pranawidjaja, S., Choi, S. I., Lay, B. W., and Kim, P. (2015). Analysis of heme biosynthetic pathways in a recombinant *Escherichia coli*. *J. Microbiol. Biotechnol.* 25, 880–886. doi:10.4014/jmb.1411.11050
- Rai, A., Fedorov, R., and Manstein, D. J. (2014). Expression, purification and crystallization of a dye-decolorizing peroxidase from *Dictyostelium discoideum*. *Acta Crystallogr. Sect. F. Struct. Biol. Commun.* 70, 252–255. doi:10.1107/S2053230X14000545
- Rai, A., Klare, J. P., Reinke, P. Y. A., Englmaier, F., Fohrer, J., Fedorov, R., et al. (2021). Structural and biochemical characterization of a dye-decolorizing peroxidase from *Dictyostelium discoideum*. *Int. J. Mol. Sci.* 22, 6265. doi:10.3390/ijms22126265
- Rajhans, G., Sen, S. K., Barik, A., and Raut, S. (2020). Elucidation of fungal dye-decolorizing peroxidase (DyP) and ligninolytic enzyme activities in decolorization and mineralization of azo dyes. *J. Appl. Microbiol.* 129, 1633–1643. doi:10.1111/jam.14731
- Ramzi, A. B., Hyeon, J. E., and Han, S. O. (2015). Improved catalytic activities of a dye-decolorizing peroxidase (DyP) by overexpression of ALA and heme biosynthesis genes in *Escherichia coli*. *Proc. Biochem.* 50, 1272–1276. doi:10.1016/j.procbio.2015.05.004
- Rodrigues, C. F., Borges, P. T., Scocozza, M. F., Silva, D., Taborda, A., Brissos, V., et al. (2021). Loops around the heme pocket have a critical role in the function and stability of BsDyP from *Bacillus subtilis*. *Int. J. Mol. Sci.* 22, 10862. doi:10.3390/ijms221910862
- Sacquin-Mora, S., and Lavery, R. (2006). Investigating the local flexibility of functional residues in hemoproteins. *Biophys. J.* 90, 2706–2717. doi:10.1529/biophysj.105.074997
- Salvachúa, D., Prieto, A., Martínez, Á. T., and Martínez, M. J. (2013). Characterization of a novel dye-decolorizing peroxidase (DyP)-type enzyme from *Irpex lacteus* and its application in enzymatic hydrolysis of wheat straw. *Appl. Environ. Microbiol.* 79, 4316–4324. doi:10.1128/AEM.00699-13
- Scocozza, M. F., Martins, L. O., and Murgida, D. H. (2021). Direct electrochemical generation of catalytically competent oxoferryl species of classes I and P dye decolorizing peroxidases. *Int. J. Mol. Sci.* 22, 12532. doi:10.3390/ijms22212532
- Scocozza, M. F., Vieyra, F., Battaglini, F., Martins, L. O., and Murgida, D. H. (2023). Electrochemical actuation of a DyP peroxidase: A facile method for drastic improvement of the catalytic performance. *ACS Catal.* 13, 7437–7449. doi:10.1021/acscatal.3c01530
- Sehnal, D., Radka Svobodová, V., Berka, K., Pravda, L., Navrátilová, V., Pavel, B., et al. (2013). Mole 2.0: Advanced approach for analysis of biomacromolecular channels. *J. Bioinform.* 5, 39. doi:10.1186/1758-2946-5-39

- Shin, S. K., Hyeon, J. E., Joo, Y.-C., Jeong, D. W., You, S. K., and Han, S. O. (2019). Effective melanin degradation by synergistic laccase-peroxidase enzyme complex for skin whitening and other practical applications. *Int. J. Biol. Macromol.* 129, 181–186. doi:10.1016/j.ijbiomac.2019.02.027
- Shrestha, R., Chen, X., Ramyar, K. X., Hayati, Z., Carlson, E. A., Bossmann, S. H., et al. (2016). Identification of surface-exposed protein radicals and A substrate oxidation site in A-class dye-decolorizing peroxidase from thermomonospora curvata. *ACS Catal.* 6, 8036–8047. doi:10.1021/acscatal.6b01952
- Silva, D., Rodrigues, C. F., Lorena, C., Borges, P. T., and Martins, L. O. (2023). Biocatalysis for biorefineries: The case of dye-decolorizing peroxidases. *Biotechnol. Adv.* 65, 108153. doi:10.1016/j.biotechadv.2023.108153
- Singh, R., Grigg, J. C., Armstrong, Z., Murphy, M. E., and Eltis, L. D. (2012). Distal heme pocket residues of B-type dye-decolorizing peroxidase: Arginine but not aspartate is essential for peroxidase activity. *J. Biol. Chem.* 287, 10623–10630. doi:10.1074/jbc.M111.332171
- Strittmatter, E., Wachter, S., Liers, C., Ullrich, R., Hofrichter, M., Plattner, D. A., et al. (2013). Radical formation on a conserved tyrosine residue is crucial for DyP activity. *Arch. Biochem. Biophys.* 537, 161–167. doi:10.1016/j.abb.2013.07.007
- Sudhamsu, J., Kabir, M., Airola, M. V., Patel, B. A., Yeh, S.-R., Rousseau, D. L., et al. (2010). Co-expression of ferrochelatase allows for complete heme incorporation into recombinant proteins produced in *E. coli*. *Protein Expr. Purif.* 73, 78–82. doi:10.1016/j.pep.2010.03.010
- Sugano, Y., Muramatsu, R., Ichiyangi, A., Sato, T., and Shoda, M. (2007). DyP, a unique dye-decolorizing peroxidase, represents a novel heme peroxidase family: ASP171 replaces the distal histidine of classical peroxidases. *J. Biol. Chem.* 282, 36652–36658. doi:10.1074/jbc.M706996200
- Sugano, Y., Sasaki, K., and Shoda, M. (1999). cDNA cloning and genetic analysis of a novel decolorizing enzyme, peroxidase gene *dyp* from *Geotrichum candidum* Dec 1. *J. Biosci. Bioeng.* 87, 411–417. doi:10.1016/s1389-1723(99)80087-5
- Sugano, Y., and Yoshida, T. (2021). DyP-Type peroxidases: Recent advances and perspectives. *Int. J. Mol. Sci.* 22, 5556–5570. doi:10.3390/ijms22115556
- Umena, Y., Kawakami, K., Shen, J.-R., and Kamiya, N. (2011). Crystal structure of oxygen-evolving photosystem II at a resolution of 1.9 Å. *Nature* 473, 55–60. doi:10.1038/nature09913
- Vogel, K. M., Hu, Z., Spiro, T. G., Dierks, E. A., Yu, A. E., and Burstyn, J. N. (1999). Variable forms of soluble guanylyl cyclase: Protein-ligand interactions and the issue of activation by carbon monoxide. *J. Biol. Inorg. Chem.* 4, 804–813. doi:10.1007/s007750050354
- Woodard, S. I., and Dailey, H. A. (1995). Regulation of heme biosynthesis in *Escherichia coli*. *Arch. Biochem. Biophys.* 316, 110–115. doi:10.1006/abbi.1995.1016
- Worrall, J. A. R., and Hough, M. A. (2022). Serial femtosecond crystallography approaches to understanding catalysis in iron enzymes. *Curr. Opin. Struct. Biol.* 77, 102486. doi:10.1016/j.sbi.2022.10.2486
- Xu, L., Sun, J., Qaria, M. A., Gao, L., and Zhu, D. (2021). Dye decoloring peroxidase structure, catalytic properties and applications: Current advancement and futurity. *Catalysts* 11, 955. doi:10.3390/catal11080955
- Yoshida, T., Ogola, H., Amano, Y., Hisabori, T., Ashida, H., Sawa, Y., et al. (2016). *Anabaena* sp. DyP-type peroxidase is a tetramer consisting of two asymmetric dimers. *Proteins* 84, 31–42. doi:10.1002/prot.24952
- Yoshida, T., and Sugano, Y. (2023). Unexpected diversity of dye-decolorizing peroxidases. *Biochem. Biophys. Rep.* 33, 101401. doi:10.1016/j.bbrep.2022.101401
- Yoshida, T., Tsuge, H., Konno, H., Hisabori, T., and Sugano, Y. (2011). The catalytic mechanism of dye-decolorizing peroxidase DyP may require the swinging movement of an aspartic acid residue. *FEBS J.* 278, 2387–2394. doi:10.1111/j.1742-4658.2011.08161.x
- Zhang, J., Kang, Z., Chen, J., and Du, G. (2015). Optimization of the heme biosynthesis pathway for the production of 5-aminolevulinic acid in *Escherichia coli*. *Sci. Rep.* 5, 8584. doi:10.1038/srep08584
- Zubieta, C., Krishna, S. S., Kapoor, M., Kozbial, P., McMullan, D., Axelrod, H. L., et al. (2007). Crystal structures of two novel dye-decolorizing peroxidases reveal a beta-barrel fold with a conserved heme-binding motif. *Proteins* 69, 223–233. doi:10.1002/prot.21550



OPEN ACCESS

EDITED BY

Aram Rezaei,
Kermanshah University of Medical
Sciences, Iran

REVIEWED BY

Chao Wang,
The Scripps Research Institute,
United States
Wesley Wang,
The Scripps Research Institute,
United States

*CORRESPONDENCE

Yichun Wang,
✉ ywang65@nd.edu

RECEIVED 17 April 2023

ACCEPTED 24 July 2023

PUBLISHED 02 August 2023

CITATION

Jeon H, Zhu R, Kim G and Wang Y (2023),
Chirality-enhanced transport and drug
delivery of graphene nanocarriers to
tumor-like cellular spheroid.
Front. Chem. 11:1207579.
doi: 10.3389/fchem.2023.1207579

COPYRIGHT

© 2023 Jeon, Zhu, Kim and Wang. This is
an open-access article distributed under
the terms of the [Creative Commons
Attribution License \(CC BY\)](#). The use,
distribution or reproduction in other
forums is permitted, provided the original
author(s) and the copyright owner(s) are
credited and that the original publication
in this journal is cited, in accordance with
accepted academic practice. No use,
distribution or reproduction is permitted
which does not comply with these terms.

Chirality-enhanced transport and drug delivery of graphene nanocarriers to tumor-like cellular spheroid

Hyunsu Jeon, Runyao Zhu, Gaeun Kim and Yichun Wang*

Department of Chemical and Biomolecular Engineering, University of Notre Dame, Notre Dame, IN, United States

Chirality, defined as “a mirror image,” is a universal geometry of biological and nonbiological forms of matter. This geometry of molecules determines how they interact during their assembly and transport. With the development of nanotechnology, many nanoparticles with chiral geometry or chiroptical activity have emerged for biomedical research. The mechanisms by which chirality originates and the corresponding synthesis methods have been discussed and developed in the past decade. Inspired by the chiral selectivity in life, a comprehensive and in-depth study of interactions between chiral nanomaterials and biological systems has far-reaching significance in biomedicine. Here, we investigated the effect of the chirality of nanoscale drug carriers, graphene quantum dots (GQDs), on their transport in tumor-like cellular spheroids. Chirality of GQDs (*L/D*-GQDs) was achieved by the surface modification of GQDs with *L/D*-cysteines. As an *in-vitro* tissue model for drug testing, cellular spheroids were derived from a human hepatoma cell line (i.e., HepG2 cells) using the Hanging-drop method. Our results reveal that the *L*-GQDs had a 1.7-fold higher apparent diffusion coefficient than the *D*-GQDs, indicating that the *L*-GQDs can enhance their transport into tumor-like cellular spheroids. Moreover, when loaded with a common chemotherapy drug, Doxorubicin (DOX), via π - π stacking, *L*-GQDs are more effective as nanocarriers for drug delivery into solid tumor-like tissue, resulting in 25% higher efficacy for cancerous cellular spheroids than free DOX. Overall, our studies indicated that the chirality of nanocarriers is essential for the design of drug delivery vehicles to enhance the transport of drugs in a cancerous tumor.

KEYWORDS

chirality, graphene quantum dots, cellular spheroid, diffusion coefficient, drug delivery

1 Introduction

The left- or right-handedness of molecules (e.g., *L*- or *D*-), known as chirality, plays a crucial role in biological processes (Zhao et al., 2020; Shao et al., 2021). The interaction of biomolecules depends on their three-dimensional (3D) shape and spatial arrangement, while typically, one type of chiral molecules (i.e., enantiomers) is biologically active, constructing biopolymers as homochiral building blocks (Salam, 1991; Warning et al., 2021). This rule applies not only to natural molecules in living organisms [e.g., amino acids, nucleotides, sugars, their oligomers, and macromolecules (Powell et al., 2012)] but also to synthetic matters, including both small chemicals [i.e., drugs (Speirs, 1962; Du et al., 2020;

Yeom et al., 2020)] and bulk substances [i.e., biomaterials (Wang et al., 2019)]. With the development of nanotechnology, many nanoparticles (NPs) with chiral geometry or chiroptical activity have emerged for biomedical applications (Suzuki et al., 2016; Du et al., 2017; Jiang et al., 2017; Yeom et al., 2020; Peng et al., 2021; Wang et al., 2022b; Döring et al., 2022; Wu and Pauly, 2022). The origin of chirality and the associated synthesis techniques have been extensively explored and refined in previous studies (Suzuki et al., 2016; Jiang et al., 2017; Ma et al., 2017; Döring et al., 2022; Wu and Pauly, 2022). Drawing inspiration from the selectivity exhibited by chiral entities in biological systems, a thorough and rigorous investigation into the nanoscale interactions between chiral nanomaterials and biological systems have profound implications for biomedicine. Recent studies showed that the chiral interaction of NPs with protein and lipid membranes at bio-interfaces plays a key role in cell uptake (Shanker and Aschner, 2001; Shanker et al., 2001; Al-Hajaj et al., 2011) and tissue transport (Du et al., 2017; Huang et al., 2020a). For instance, phospholipid bilayers, the fundamental structure of the cell membrane, are enantio-selectively permeable to chiral nanomaterials due to their chiral interaction, which results in highly efficient cell uptake of right-handed (*D*-) NPs with nanocore-dominant chirality (Sarasij et al., 2007; Suzuki et al., 2016; Du et al., 2017; Yeom et al., 2020). Meanwhile, chiral NPs interacting with membrane proteins exhibit asymmetric active transport through cell membranes (Sarasij et al., 2007). Left-handed (*L*-) NPs with ligand-dominant chirality affect active cellular uptake in human cells as well as cellular efflux (Al-Hajaj et al., 2011). Lastly, the transport and distribution of NPs in tissues are strongly influenced by the dynamics of NPs interacting with the cell membrane and extracellular matrix (ECM) (Sherman and Fisher, 1986; Cooper, 2000; Ng and Pun, 2008; Chauhan et al., 2009; Hsu et al., 2012; Gao et al., 2013; Wang et al., 2015; Ziemys et al., 2018; Fulaz et al., 2019; Leedale et al., 2020; Lenzini et al., 2020; Koomullil et al., 2021). Engineering chirality of NPs can enhance their transport and uptake in the tissue microenvironment by altering the reaction-diffusion processes due to the nanocarrier-induced cell uptake and non-diffusive active transport due to the proteinaceous polyelectrolyte disassembly on the tissue ECM (Huang et al., 2020b). Hence, it is essential to consider the chirality of nanocarriers and understand their effect on the design of drug delivery systems (Zhao et al., 2021).

Graphene quantum dots (GQDs), a graphene-based NP, have emerged as a versatile and promising tool for biomedical applications in drug delivery (Yeom et al., 2020), biosensing (Hai et al., 2018), and bioimaging (Li et al., 2023), due to their unique properties, including high surface area-to-volume ratio (Tian et al., 2018), tunable optical properties (Hai et al., 2018), and excellent biocompatibility (Henna and Pramod, 2020). For example, GQDs emit strong, stable, and tunable fluorescence signals (Wang et al., 2016) for high-resolution imaging of biological structures (Biswas et al., 2021). They can be easily functionalized with specific biomolecules to enhance their biostability (Vázquez-Nakagawa et al., 2022), endow desired functionality (Suzuki et al., 2016; Sattari et al., 2021), target specific cells or tissues (Yao et al., 2017), or contain chemical drugs (Sawy et al., 2021). Notably, the planar plane of GQDs mainly consists of aromatic rings, which makes them well-suited for loading small aromatic molecules, such

as chemotherapy drugs (Askari et al., 2021; Mirzaei-Kalar et al., 2022), through aromatic stacking (i.e., π - π stacking) (Liu et al., 2009). This property enabled the development of GQDs as drug carriers for drug delivery that could effectively transport and release the loaded drugs to targeted cells or tissues with high selectivity and efficacy (Liu et al., 2009; Wo et al., 2016; Askari et al., 2021; Kiani Nejad et al., 2022; Mirzaei-Kalar et al., 2022). The edges of GQDs can be engineered to contain desired functional groups, which enables covalent modification with chiral molecules, endowing nanoscale chirality (Suzuki et al., 2016). Moreover, chiral matching with the cellular lipid membranes (Sarasij et al., 2007; Suzuki et al., 2016; Du et al., 2017; Yeom et al., 2020) enhanced the loading of chiral GQDs with embedded chemicals into extracellular vesicles for achieving advanced exosome engineering (Zhang et al., 2023).

This study investigated how the chirality of GQDs affected their transport in tumor-like cellular spheroids, a well-known 3D cell culture model (Figure 1). Compared to the traditional two-dimensional (2D) cell culture models, 3D cell culture mimics the *in vivo* tissue microenvironment morphologically and compositionally (Wang and Jeon, 2022) by replicating *in vivo* cell growth, proliferation, and differentiation *in vitro* (Charoen et al., 2014; Chen, 2016), providing insight into nanocarrier transport in native tissues (Gunti et al., 2021). The chirality of GQDs was obtained by surface modification with *L/D*-cysteines (Figure 1A), which gave a strong chiroptical activity of GQDs and indicated nanoscale chirality by the twist of the graphene nanosheets. (Wang et al., 2016; Zhang et al., 2023). The chiral GQDs were tested in the tumor-like cellular spheroids, which were derived from a human hepatoma cell line (HepG2) by Hanging-drop (i.e., 3-day-cultured cellular aggregates) (Timmins and Nielsen, 2007) followed by suspension culture (i.e., 10-day-cultured cellular spheroids) (Ryu et al., 2019) (Figure 1B). From the results, we found chirality-dependent phenomena in both cellular aggregates and spheroids: 1) while tested in cellular aggregates, *L/D*-GQDs interacted with the immature ECM of cellular aggregates differently, occurring distinct structural change (i.e., swelling) of cellular aggregates (Figure 1C); 2) we observed faster transport of *L*-GQDs into cellular spheroids compared to that of *D*-GQDs, representing significant differences in apparent diffusion coefficients in tumor-like tissue (Figure 1D). Accordingly, as a proof of concept for drug delivery application, DOX-loaded *L*-GQDs showed increased efficacy in tumor-like cellular spheroids compared to free DOX or DOX-loaded *D*-GQDs, conducting enhanced drug transport and delivery to the cancerous tissue model (Figure 1E). In summary, the chirality of GQDs influences their transport into tumor-like tissues, thus their delivery efficiency as nanocarriers, which indicates the importance and potential of chirality for designing and developing nanocarriers for drug delivery systems.

2 Materials and methods

2.1 Materials and agents

Carbon nanofibers (719803) were purchased from Sigma-Aldrich (MO), and sulfuric acid (95%–98%; BDH3068-500MLP) and nitric acid (69%–70%; BDH3044-500MLPC) were purchased

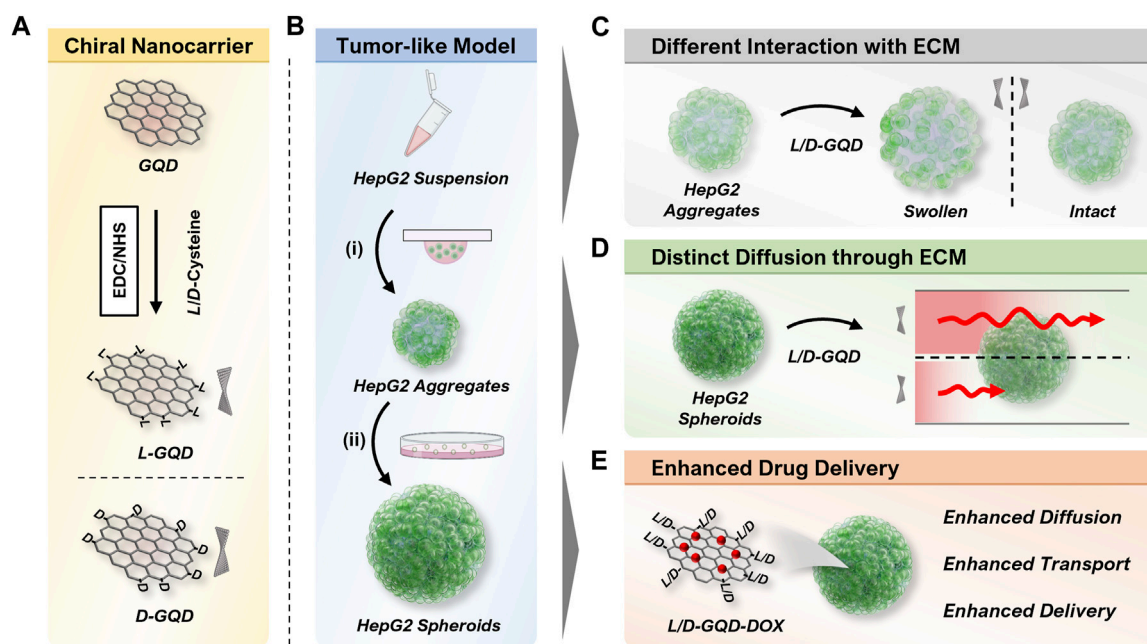


FIGURE 1

Illustration of overall workflow. (A) Scheme of the left- or right-handed graphene quantum dots (L/D-GQDs) preparation. (B) Scheme showing the human hepatoma (HepG2) cellular spheroid preparation. The cellular aggregates were prepared by (i) the Hanging drop method and matured to cellular spheroids by (ii) the suspension culture method. (C) Graphene quantum dots (GQDs) with chirality showed a distinct effect on the structure change of cellular aggregates (e.g., swelling). (D) Chiral GQDs showed distinct diffusivities in HepG2 cellular spheroids. (E) Chiral GQDs can serve as a nanocarrier for doxorubicin (DOX) with enhanced diffusion, transport, and delivery in tumor-like tissue.

from VWR (PA). The dialysis membrane tubing (MWCO: 1 kD; 20060186) was purchased from Spectrum Chemical Manufacturing Company (NJ). 1-ethyl-3-(3-dimethyl-aminopropyl) carbodiimide (EDC; 22980) was purchased from Thermofisher Scientific (MA). N-hydroxysuccinimide sodium salt (Sulfo-NHS; 56485) and L-cysteine (30089) were purchased from Sigma-Aldrich (MO). D-cysteine (A110205-011) was purchased from AmBeed (IL).

Minimum essential medium Eagle 1 X (MEM; 10-010-CV) and phosphate-buffered saline 1 X (PBS; 21-040-CM) were purchased from Corning (NY). Avantor Seradigm USDA-approved origin fetal bovine serum (FBS; 1300-500) was purchased from VWR (PA), kept at temperature of -20°C (e.g., without the heat inactivation). Antibiotic antimycotic (15240096) was purchased from Fisher Scientific (MA). Gibco™ Trypsin-EDTA (25200072) was purchased from Thermofisher Scientific (MA). 4% Paraformaldehyde in 0.1 M phosphate buffer (15735-50S) was purchased from Electron Microscopy Sciences (PA). Ethanol absolute (64-17-5) was purchased from VWR (PA). LIVE/DEAD™ Cell Imaging Kit (488/570) (R37601) was purchased from Thermofisher Scientific (MA).

2.2 GQD synthesis and functionalization

GQDs were prepared using a modified Hummers method (Peng et al., 2012). 0.45 g of carbon fiber was added into 90 mL of concentrated H_2SO_4 (98%) and stirred for 1.5 h in a 250 mL round bottom glass flask. After stirring, 30 mL of concentrated

HNO_3 (68%) was added to the mixture solution and sonicated for 1 h in a 250 mL round bottom glass flask. Then, the mixture reacted at 120°C for 20 h. Next, the solution was neutralized by a 5 M of sodium hydroxide solution. The final product was further dialyzed for 3 days in a dialysis bag with 1 K MWCO for purification.

The surface modification of GQDs with cysteines (e.g., L-GQDs and D-GQDs) was carried out using EDC/NHS coupling reaction (Suzuki et al., 2016; Park and Park, 2022). 1 mL of EDC with a concentration of 100 mM (in DI water) was mixed with 25 mL GQDs (0.25 mg mL^{-1} in DI water), followed by 30-min stirring. 1 mL of NHS (500 mM in DI water) was added into the mixture solution and stirred for 30 min. 1 mL of L/D-cysteines (100 mM in DI water) was added into the reaction, and the mixture reacted for 16 h. The product was purified by a dialysis bag with 1 K MWCO followed by filtration with VWR syringe filter ($0.22\text{ }\mu\text{m}$; 76479-010; VWR, PA). To load DOX to GQDs (e.g., L-GQD-DOX or D-GQD-DOX), 0.5 mg mL^{-1} of GQDs and $350\text{ }\mu\text{M}$ of DOX were prepared under a deionized water solution followed by room-temperature incubation for 30 min protected from light. The DOX loading efficiency test was performed by measuring the fluorescence intensity of $200\text{ }\mu\text{M}$ DOX loaded in a concentration range of L/D-GQDs (e.g., 0, 75, 150, 225, and $300\text{ }\mu\text{g mL}^{-1}$, respectively). The measurement was performed with Tecan Infinite 200Pro (Tecan, Männedorf, Switzerland) under 480 nm excitation for 600 nm emission. The loading efficiency was calculated by the following Eq. 1, where η is the loading efficiency, I_0 is fluorescence intensity from unquenched DOX, I_Q is fluorescence intensity from quenched

DOX, C is concentration of L/D -GQDs, and $I(C)$ is DOX fluorescence intensity as a function of GQD concentration (e.g., C).

$$\eta = 1 - \frac{I(C) - I_0}{I_Q - I_0} \times (100\%) \quad (1)$$

2.3 GQD characterization

The size and shape of L/D -GQDs were characterized by a transmission electron microscope (TEM; JEOL 2011; Joel, WA and Talos F200i; Thermo Fisher Scientific, MA). A 3- μ L droplet of the L/D -GQD solution (0.1 mg mL⁻¹) was placed on the carbon-coated copper TEM grid (CF200-Cu-25; Purchased from Electron Microscopy Sciences, PA) and allowed to dry in the air. The imaging was performed with a TEM instrument under an accelerating voltage of 200 kV. The size distribution of the GQDs was analyzed by using ImageJ software. The chemical composition of L/D -GQDs was estimated with Fourier-transform infrared (FTIR) spectroscopy, compared to the unmodified GQDs. Attenuated Total Reflectance (ATR)-FTIR analysis was performed using a Bruker Tensor 27 FTIR Spectrometer (Bruker Optics International Company, MA) with a diamond lens ATR module. 3 μ L of 2 mg mL⁻¹ GQDs was dried in the air, and each spectrum was measured as the accumulation of 64 scans at a spectral resolution of 2 cm⁻¹ within the range 4,000–700 cm⁻¹.

The absorbance and circular dichroism (CD) spectra of L/D -GQDs were evaluated with CD spectroscopy (Jasco J-1700 Spectrometer; Jasco International Company, MD) at 20°C. The L/D -GQD solution was diluted to 50 μ g mL⁻¹, followed by spectra scanning from 200 nm to 400 nm with 0.1 nm intervals, 5 nm bandwidth, and a scan speed of 50 nm min⁻¹. The fluorescence emission property of L/D -GQDs was measured by Tecan Infinite 200Pro (Tecan, Männedorf, Switzerland). The fluorescence profile of the L/D -GQD solution was measured throughout a range of emission wavelengths from 400 nm to 700 nm under the 365 nm excitation.

2.4 Cell culture and cellular spheroid fabrication

Hepatocellular carcinoma human cells (HepG2) [American Type Culture Collection (ATCC), VA] were maintained with MEM supplemented with 10% FBS and 1% Antibiotic-Antimycotic in a humidified incubator (MCO-15AC; Sanyo, Osaka, Japan) at 37°C with 5% CO₂. The cells were passaged routinely to maintain exponential growth (e.g., Passages 6–12). HepG2 cells were washed with PBS, trypsinized with trypsin-EDTA solution, and condensed at 3.4×10^4 cells mL⁻¹ in a fresh cell culture medium. 7- μ L droplets of cell suspension were gently arrayed on the lid of a 60 mm non-treated culture dish. The bottom of the dish was filled with 6 mL of PBS solution, followed by the droplet-arrayed lid covering. The culture dish was incubated for 72 h at 37°C with 5% CO₂. The cell aggregates were harvested with PBS, condensed with centrifugation, and cultured in a new 60 mm non-treated culture dish. The cell culture media was changed once in 48 h up to 7 days. The microscopic images were taken in suspension

culture every 48 h, and the ImageJ software collected the size of the cellular spheroids.

2.5 Cellular spheroid characterization and drug testing

For the field-emission scanning electron microscopic (FESEM) imaging, the spheroids were treated with 1 mL of 2% paraformaldehyde (20 mL⁻¹) for 1.5 h and washed with 1 mL of PBS three times. To dehydrate the spheroids, gradual ethanol concentrations (e.g., 25%, 50%, 70%, 90%, 100%, 100%, and 100%) were prepared and treated to the spheroids for 20 min each. The dehydrated spheroids were deposited onto the aluminum specimen mounts (75210; Electron Microscopy Sciences, PA) and dried overnight. The samples were coated with 3.5 nm Iridium by Cressington Vacuum Coating Systems 208HRD (Ted Pella International Company, CA) and imaged under 10.0 kV with a field-emission scanning electron microscopic (Magellan 400, FEI Company, OR).

For the Live/Dead assay, the LIVE/DEAD™ Cell Imaging Kit (488/570) (ThermoFisher Scientific, MA) was used following the manufacturer's instructions. 1 mL of spheroid suspensions (e.g., 3-day-cultured and 10-day-cultured spheroids; 20 mL⁻¹) were mixed with the staining solution containing both live cell indicator and dead cell indicator for 3 h followed by the 3 h fixation with 2% paraformaldehyde. The samples were kept in 2 mL PBS before imaging with A1R-MP Laser Scanning Confocal Microscopy (CLSM; Nikon, Tokyo, Japan). The images were processed for the maximum intensity projection using NIS-Elements software (Nikon, Tokyo, Japan).

For DOX dosage-dependent test, a range of DOX solutions was prepared (e.g., 0, 20, 40, 80, 160, and 320 μ M) in fresh cell culture media with a final volume of 1 mL. The 10-day-cultured cellular spheroids were incubated with the DOX-embedding media for 6 h (e.g., 20 mL⁻¹). Following two-time PBS washing, the spheroids were incubated with fresh cell culture media for 24 h. The spheroids were stained with a LIVE/DEAD™ Cell Imaging Kit and fixed with 2% paraformaldehyde using the same protocol and procedure as the Live/Dead assay. The microscopic images of cellular spheroids were collected using bright field microscopy for each concentration (e.g., 6-h treatment of 0, 20, 40, 80, 160, and 320 μ M DOX, respectively, followed by 24-h incubation with fresh cell culture media) and for each incubation time (e.g., 6-h treatment of 120 μ M DOX followed by 24, 72, 120, and 144 h of incubation with fresh cell culture media) to estimate the size change of cellular spheroids using the ImageJ software. For DOX-loaded GQD drug effect assay, L -GQD-DOX or D -GQD-DOX solutions (e.g., Prepared as GQD:DOX = 0.5 mg mL⁻¹:350 μ M; See Materials and Methods Section 2.2) were mixed with fresh cell culture media with the final concentration of DOX as 120 μ M with the final volume of 1 mL. The 10-day-cultured cellular spheroids were incubated with the L/D -GQD-DOX-containing media for 6 h (e.g., 20 mL⁻¹). Following two-time PBS washing, the spheroids were incubated with fresh cell culture media for 24 h. The spheroids were collected to perform two experiments: 1) luminescence-based cell viability assay and 2) fluorescence-based live/dead cell imaging. For luminescence-based cell viability assay, the spheroids were in a 96-well plate

(e.g., 1 well⁻¹ with 100 μ L fresh cell culture media) and mixed with 100 μ L reaction solution of CellTiter-Glo 3D cell viability assay kit (G9681; Promega, WI). The 96-well plate was gently rocked for 5 min and stabilized at room temperature for 30 min, following the manufacturer's instruction. The luminescence from the 96-well plate was measured with Tecan Infinite 200Pro (Tecan, Männedorf, Switzerland) and normalized with the control group. For fluorescence imaging, the spheroids were stained with a LIVE/DEAD™ Cell Imaging Kit and fixed with 2% paraformaldehyde using the same protocol and procedure as the Live/Dead assay.

2.6 Monitoring GQD transport into cellular spheroid

The effect of GQDs on early ECM was evaluated by treating *L/D*-GQDs to HepG2 aggregates (e.g., 3-day-cultured HepG2 cellular aggregates without suspension culture) or HepG2 spheroids (e.g., 10-day-cultured HepG2 cellular spheroids after suspension culture) under CLSM imaging. The 3-day-cultured cellular aggregate suspension (e.g., 20 mL⁻¹; 0.9 mL) or the 10-day-cultured cellular spheroid suspension (e.g., 20 mL⁻¹; 0.9 mL) and *L/D*-GQDs (1 mg mL⁻¹) were prepared. As GQDs were treated to cellular aggregates/spheroids, the images were collected under Capturing Time Series Images function (e.g., 12 recurring cycles; 1 cycle refers to Capturing Z Series Images for aggregates). The bright-field images, including respective temporal information, were collected throughout the aggregate region. The size distribution of aggregates/spheroids was collected using ImageJ software from bright-field channel images for each time point.

GQD transports into 3-day-cultured cellular aggregates and 10-day-cultured cellular spheroids were evaluated by CLSM imaging. The 3-day-cultured cellular aggregates, the 10-day-cultured cellular spheroid suspension (e.g., 20 mL⁻¹; 0.9 mL), and *L/D*-GQDs (1 mg mL⁻¹; 0.1 mL) were prepared. Under Capturing Time Series Images function (e.g., 12 recurring cycles; 1 cycle refers to Capturing Z Series Images for aggregates/spheroids) on the A1R-MP CLSM, 100 μ L of GQD solutions were treated gently into 15 mm glass bottom dish (801002, NEST Biotech, Wuxi, China) embedding 0.9 mL of the aggregate/spheroid suspension (e.g., Total 1 mL; 18 aggregates/spheroids; 0.1 mg GQDs). The total GQD intensity within cellular aggregates and spheroids was collected from the maximum intensity projection images from NIS-Elements software and estimated with ImageJ software. The time-lapse spatiotemporal information of the GQD transport was collected and processed with the maximum intensity projection using NIS-Elements software. ImageJ software collected and quantified the spatiotemporal information from GQD-channel images for respective time points, processing them to select the spheroid outline and quantify GQD transport.

2.7 Image processing and quantification

The oversaturation in image contrast followed by color inversion made the bright-field images into the masking layer for isolating the GQD signals only for the spheroid region. The outlined GQD channel images in the spheroid regions were quantified with

further image processing for three approaches: Integrated intensity analysis, radially-averaged intensities, and time-dependent intensities at a fixed radial position. First, the integrated intensity analysis was performed with the following Eq. 2, where $I(x,y)$ is the intensity of the GQD signal in x and y coordinates inside the spheroid region, S is the set of points inside the outlined region of a cellular spheroid, and A_s is an area of the cellular spheroid. Second, the radially-averaged intensities of the *L/D*-GQDs were quantified with the spheroid region-masked GQD channel images by using Radial Profile Angle plugin in ImageJ software. Third, the time-dependent intensities at a fixed radial position were collected from the radially-averaged intensities with fixed relative radius (e.g., $\bar{r} = 0.5$ and $\bar{r} = 1$ where \bar{r} denotes relative radii to the whole spheroid radius).

$$\bar{I}_{total}(t) = \frac{1}{A_s} \sum_{(x,y) \in S} I(x,y,t) \quad (2)$$

A simple diffusion equation was introduced to determine apparent diffusion coefficients, as shown in the following Eqs. 3, 4 with dimensionless parameters $\bar{r} = r/r_{max}$, $\bar{t} = t/t_{eq}$, and $\bar{C}_i = C_i/C_{i,eq}$, where r_{max} stands for the radius having the maximum intensity from the radially-averaged plot, t_{eq} stands for the observed time that intensity reaches a plateau, and $C_{i,eq}$ stands for the concentration or intensity of GQDs when intensity reaches a plateau. Here, D_i , the apparent diffusion coefficients of *L/D*-GQDs (e.g., D_L or D_D), is a function of \bar{r} and it could be extracted by using the following Eq. 5, where r_{max} is spheroid radius and t_{eq} is the time that intensity reaches a plateau in the time-dependent intensities at a fixed radial position. To quantify the drug effect of DOX, the area of dead cells in the Z-projected CLSM image was collected and normalized with those of live area from each spheroid (e.g., extracted from the Calcein-AM channel).

$$\frac{\partial C_i}{\partial t} = \frac{D_i}{r} \frac{\partial}{\partial r} \left(r \frac{\partial C_i}{\partial r} \right) \quad (3)$$

$$\frac{1}{t_{eq}} \frac{\partial \bar{C}_i}{\partial \bar{t}} = \frac{D_i}{\bar{r} (r_{max})^2} \frac{\partial}{\partial \bar{r}} \left(\bar{r} \frac{\partial \bar{C}_i}{\partial \bar{r}} \right) \quad (4)$$

$$D_i = \frac{(r_{max})^2}{t_{eq}} \quad (5)$$

3 Result and discussion

Chiral GQDs were derived by the same procedure as our previous work (i.e., EDC/NHS reaction) (Suzuki et al., 2016) from as-synthesized GQDs by a modified Hummers method (Peng et al., 2012). In brief, the edges of as-synthesized GQDs were functionalized with *L*-cysteines (i.e., *L*-GQDs) or *D*-cysteines (i.e., *D*-GQDs) under EDC/NHS reaction, aiming the amide bond between the carboxylic acid group on GQDs (i.e., -COOH) and amine group in both cysteines (i.e., -NH₂) (Suzuki et al., 2016; Zhu et al., 2022a; Zhang et al., 2023). The sizes of *L*-GQDs and *D*-GQDs are similar to as-synthesized GQDs (Figure 2A and Supplementary Figure S1). The frequency distribution analysis for the TEM images showed that the average size of *L*-GQDs was 7.88 \pm 2.11 nm, while *D*-GQDs was 7.99 \pm 2.03 nm (Figure 2B and Supplementary Figure S2), which confirmed that *L*-GQDs and *D*-GQDs had a similar size.

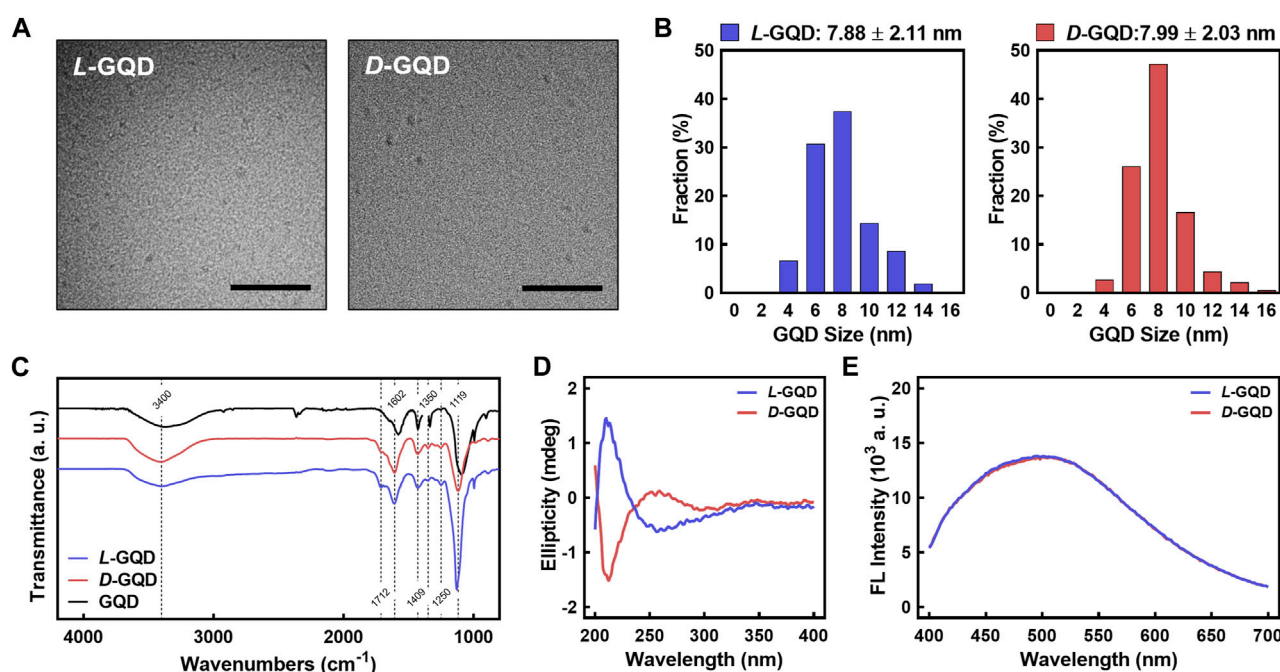


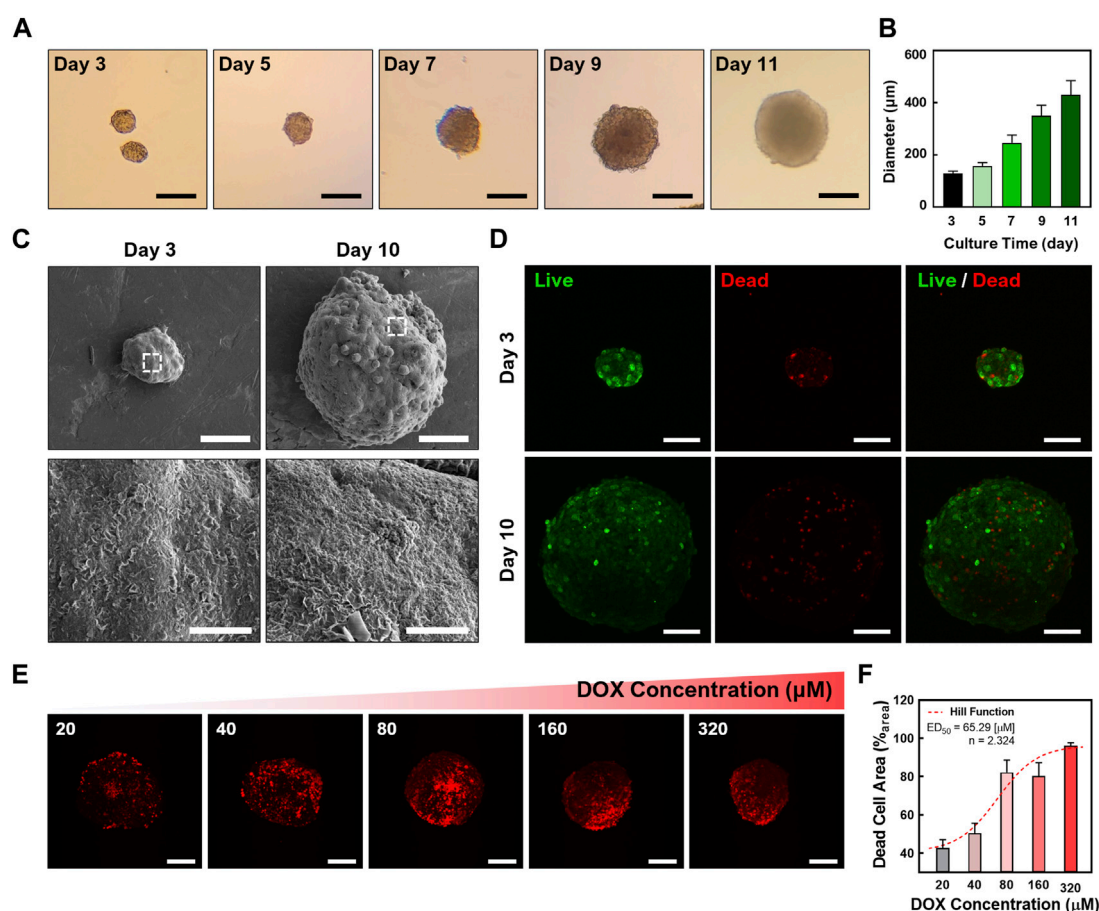
FIGURE 2

Characterizations of *L/D*-GQDs. (A) Transmission electron microscopic (TEM) images of *L*-GQDs (left) and *D*-GQDs (right) (Scale bar: 100 nm). (B) Size distributions of *L*-GQDs (left) and *D*-GQDs (right). The distributions were collected and analyzed from TEM images. (C) Fourier-transform infrared (FTIR) spectra of *L/D*-GQDs compared to the unmodified GQDs (blue: *L*-GQDs, red: *D*-GQDs, black: GQDs). (D) Circular Dichroism (CD) spectra of *L/D*-GQDs (blue: *L*-GQDs, red: *D*-GQDs). (E) Emitted fluorescent intensity of *L/D*-GQDs excited at 365 nm (blue: *L*-GQDs, red: *D*-GQDs).

The FTIR analysis (Figure 2C) verified the chemical modification of the *L/D*-GQDs compared to the unmodified GQDs. Both *L*- and *D*-GQDs have the featured bonds in as-synthesized *L/D*-GQDs (i.e., 3,400, 1409, and 1350 cm^{-1} for -OH group; 1712 cm^{-1} for -C=O group; 1602 cm^{-1} for C=C group; 1119 cm^{-1} for C-O group), as well as the *L/D*-cysteines related peak at 1250 cm^{-1} (i.e., C-N group) (Supplementary Table S1). This result demonstrated the successful chiral modification of GQDs with *L/D*-cysteines. CD spectra of *L/D*-GQDs displayed ellipticity peaked at the same wavelengths of 213 nm and 258 nm with opposite signs (Figure 2D) without significant differences in absorbance (Supplementary Figure S3), confirming the successful chiral modification of GQDs. Excited at 365 nm wavelength, both *L/D*-GQDs showed significant emission at ~ 500 nm, regardless of the chiral modification on the particles (Figure 2E).

To investigate the transport of chiral GQDs in cancerous tissues, tumor-like cellular spheroids were derived from HepG2 cells using the Hanging-drop method for 3 days (i.e., immature cellular aggregates) (Timmins and Nielsen, 2007) followed by the suspension culture for 7 days (i.e., mature cellular spheroids) (Ryu et al., 2019). The serial microscopic imaging of the spheroids showed the proliferation of the cells in spheroids under the suspension culture (Figure 3A). The diameter of the spheroids was around 170 μm on Day 3 (i.e., cellular aggregates using the Hanging-drop method) while showing linear growth in suspension culture step up to 400 μm until Day 11 (i.e., cellular spheroids; Figure 3B). This result implies an optimal growth rate of the cells inside the spheroids. Under FESEM images (Figure 3C),

characteristic comparisons between immature cellular aggregates and mature cellular spheroids were performed by observing ECM structure on the surface of cellular spheroids. Mature cellular spheroids (i.e., 10-day-cultured cellular spheroids with 7-day suspension culture after 3-day Hanging drop culture) showed denser polymeric structure on their surface than immature cellular aggregates (i.e., 3-day-cultured cellular aggregates derived from 3-day Hanging drop culture), implying the formation of more ECM that mimic the native microenvironment in matured cellular spheroids. Moreover, cellular aggregates and spheroids showed a high ratio of live cells (e.g., the green signal from Calcein-AM) to dead cells (e.g., the red signal from BOBO-3 Iodide) using Live/Dead assay, demonstrating their high cell viability (Figure 3D). A common chemotherapy drug, DOX, was administered into cellular spheroids to determine the dose-dependent effect of DOX on cellular spheroids. CLSM images of HepG2 spheroids stained with the Live/Dead assay (Figure 3E) showed an increasing portion of dead cells (i.e., Red signal from BOBO-3 iodide) in cellular spheroids as DOX concentrations increased. This result was further analyzed by the area quantification from image processing (Figure 3F), demonstrating a DOX dosage-responsive effect on cellular spheroids. A Fitting Hill Function estimated the effective dose at 50% death (ED_{50}) as 65.29 μM , similar to the previous test of the dose-responsive effect of DOX on HepG2 cellular spheroids (Zhu et al., 2022b). Accordingly, the size of the cellular spheroids decreased as the DOX dosage increased, showing 20% shrinkage of their diameter with the 320 μM DOX treatment and 24-h incubation (Supplementary

**FIGURE 3**

Characterizations of cellular spheroids. **(A)** Time-lapse microscopic images of the cellular spheroids in suspension culture (Scale bar: 200 μm) and **(B)** sizes of the cellular spheroid at each time point. **(C)** Field-emission scanning electron microscopic (FESEM) images of the cellular aggregates and cellular spheroids. **(D)** Confocal laser scanning microscopic (CLSM) images showing the cellular aggregates and spheroids with Live/Dead staining (Green: Calcein-AM, live cell indicator; Red channel: BOBO-3 Iodide, dead cell indicator; Scale bar: 100 μm; Z-projected maximum intensity images). **(E)** CLSM images showing a DOX dosage-dependent treatment in cellular spheroids. The dead cells in cellular spheroids were stained with BOBO-3 Iodide (Scale bar: 200 μm; Z-projected maximum intensity images). **(F)** Quantitative analysis of DOX concentration-dependent response of cellular spheroids. A Hill Function was plotted to determine ED_{50} (65.29 μM).

Figure S4A). Moreover, increasing incubation time after the DOX treatment resulted in further size decrease of cellular spheroids, implying the effective drug response (Supplementary Figure S4B). These results indicated the cellular spheroids are a reliable 3D culture model *in vitro* for evaluation of nanocarriers.

To investigate how the chirality of nanocarrier chiral GQDs impacts tumor tissue, we added *L/D*-GQDs into the immature/mature HepG2 cellular aggregates/spheroids (e.g., 3/10-day-cultured) and observed their size change using CLSM time-lapse imaging (Figures 4A, B). As a result, *L*-GQDs induced significant swelling of cellular aggregates within 20 min, while the size of cellular aggregates treated by *D*-GQDs did not change significantly (Figure 4A). The size estimation by quantitative analysis revealed that *L*-GQDs-driven swelling of cellular aggregates was about a 20% increase in diameter (Figure 4B). In comparison, only a 2.5% diameter change was observed for *D*-GQD-treated cellular aggregates, indicating that *L*-GQDs induced a 1.41-fold structural volume change compared to *D*-GQDs. This phenomenon indicated the different chirality of GQDs induced

distinct interaction between GQDs and ECM of cellular aggregates, consistent with the integrated intensity analysis (See Supplementary Result Section 1.1; Supplementary Figure S5). In contrast, mature cellular spheroids showed no significant size change after being treated with chiral GQDs (Figures 4C, D). These results implied chiral GQDs interacted distinctively with the immature ECM structure in cell aggregates, while not affecting the structural stability of the cellular spheroids due to the complete formation of ECM (See Figure 3C).

To study the effect of nanocarrier's chirality on their transport into cancerous tissue, we monitored the distribution of chiral GQDs in tumor-like cellular spheroids (e.g., 10-day-cultured cellular spheroids) throughout the time-lapse CLSM images (i.e., TRITC-filtered red channel). We continuously image the process with a 12-step protocol starting from 0 min (i.e., after adding *L/D*-GQDs to cellular spheroids), spanning less than 80 min. The GQD signals in the fluorescent images (Figure 5A and Supplementary Figure S6A, B) showed significant changes in the spheroid region as a function of time. The interface of the spheroids and solutions were

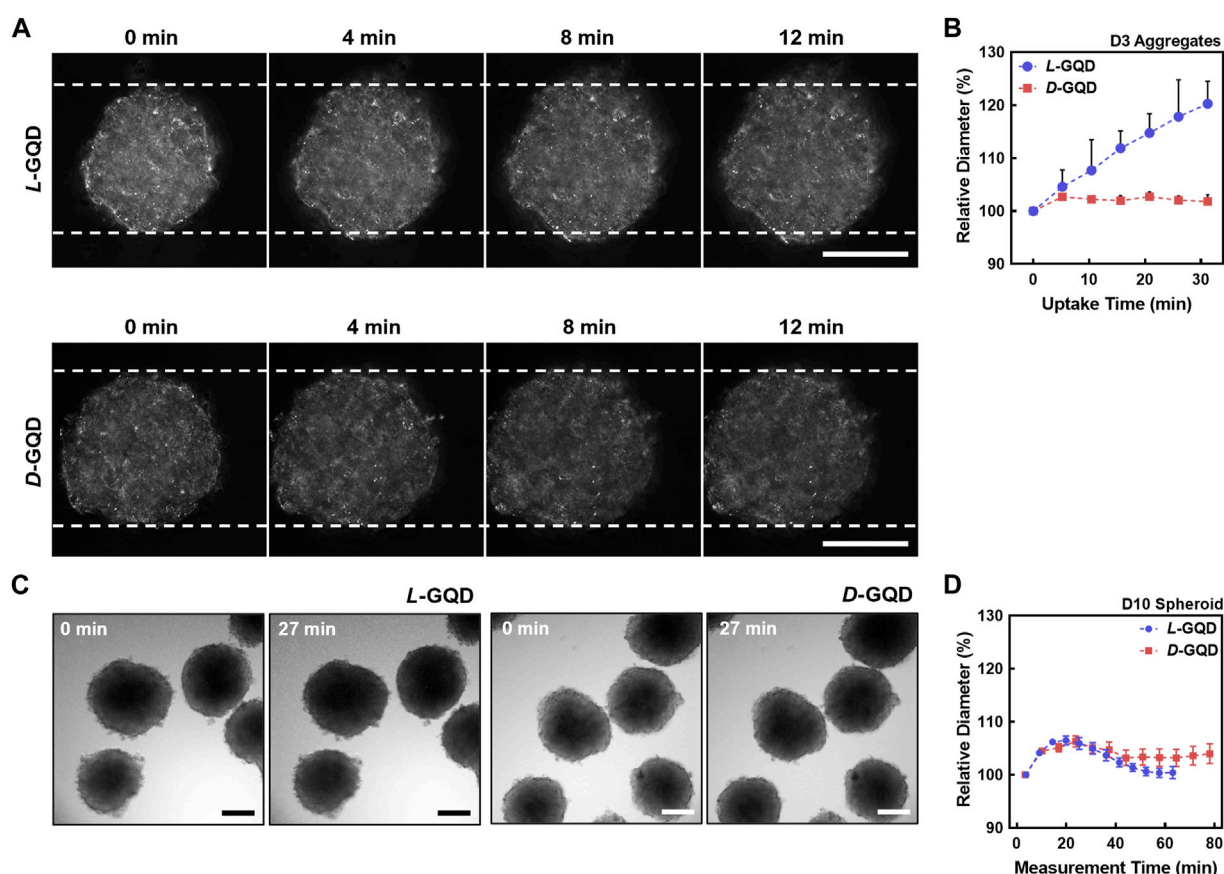


FIGURE 4

The effects of chiral GQDs on the swelling of cellular aggregates and spheroids. The bright field images were taken with CLSM under the chiral GQD treatment to cellular aggregates and spheroids. (A) Bright-field images showing size changes of the cellular aggregates under the *L/D*-GQD treatment (*L*-GQDs: top, *D*-GQDs: bottom, Scale bar: 100 μ m). White dashed lines indicated the initial width of aggregates. (B) Size changes of the spheroids under the *L/D*-GQD treatments (*L*-GQDs: blue curve, *D*-GQDs: red curve; $N = 5$). (C) Bright-field images showing the size change of the cellular spheroids under the *L/D*-GQD treatment (*L*-GQDs: left, *D*-GQDs: right; Scale bar: 100 μ m). (D) Size changes of the cellular spheroids under the *L/D*-GQD treatment (*L*-GQDs: blue curve, *D*-GQDs: red curve; $N = 5$).

distinguishable right after adding GQDs (i.e., 0 min images in Figure 5A and Supplementary Figure S6A, B), while the interface between the spheroid and the solution turned into red signals gradually over time (i.e., >0 min images in Figure 5A and Supplementary Figure S6A, B). This phenomenon demonstrated that both *L*- and *D*-GQDs diffused into the cellular spheroid. Notably, GQD diffusion mainly occurred at the very early stage of the treatment (e.g., Intensities in the spheroid region changed between 0 min and 27 min images in Figure 5A) and reached a plateau later than 40 min images (See Supplementary Figure S6A, B).

To quantitatively study the transport of chiral GQDs in cellular spheroids (Figures 5B, C), we further analyzed the GQD distribution over time by image processing (Supplementary Figure S7) based on the CLSM images (See Figure 5A and Supplementary Figure S6A, B; 10-day-cultured cellular spheroids). The radially averaged intensity plots were formed by averaging the intensity of GQDs from the radius of each spheroid, facilitating the GQD-signal analysis with spatial and temporal coordinates (i.e., $\bar{I}(r, t)$; See Materials and Methods Section 2.7) (Supplementary Figure S8). Based on the analysis,

L-GQDs exhibited 1.5-fold higher plateau intensities than *D*-GQDs at the edge of the cellular spheroid while showing a shorter time to reach a plateau at r_{max} than *D*-GQDs. This result implies that *L*-GQDs diffuse into the cellular spheroids more effectively and efficiently than *D*-GQDs, consistent with the integrated intensity analysis (See Supplementary Result Section 1.1; Supplementary Figure S9).

To evaluate the chirality-induced effect of GQD transport precisely, time-dependent intensities at a fixed radial position were collected from the spatiotemporal distribution (See Supplementary Figure S8) and represented with relative radii: the outer shell of the spheroids (i.e., $\bar{r} = 1$; \bar{r} denotes relative radii to the whole spheroid radius) and half of the radius (i.e., $\bar{r} = 0.5$) (Figure 5B). The plots from the outer shell showed the intensity saturation at specific times, t_{eq} (i.e., $\bar{r} = 1$ for both *L*-GQDs and *D*-GQDs; solid lines in Figure 5B), while intensities from the half radius were increasing throughout the measurement (i.e., $\bar{r} = 0.5$ for both *L*-GQDs and *D*-GQDs; dotted lines in Figure 5B). The t_{eq} values were estimated as 22.6 ± 1.2 min for *L*-GQDs and 31.4 ± 3.7 min for *D*-GQDs, implying *L*-GQDs have a higher apparent diffusion coefficient (i.e., D_l) than *D*-GQDs. These estimations

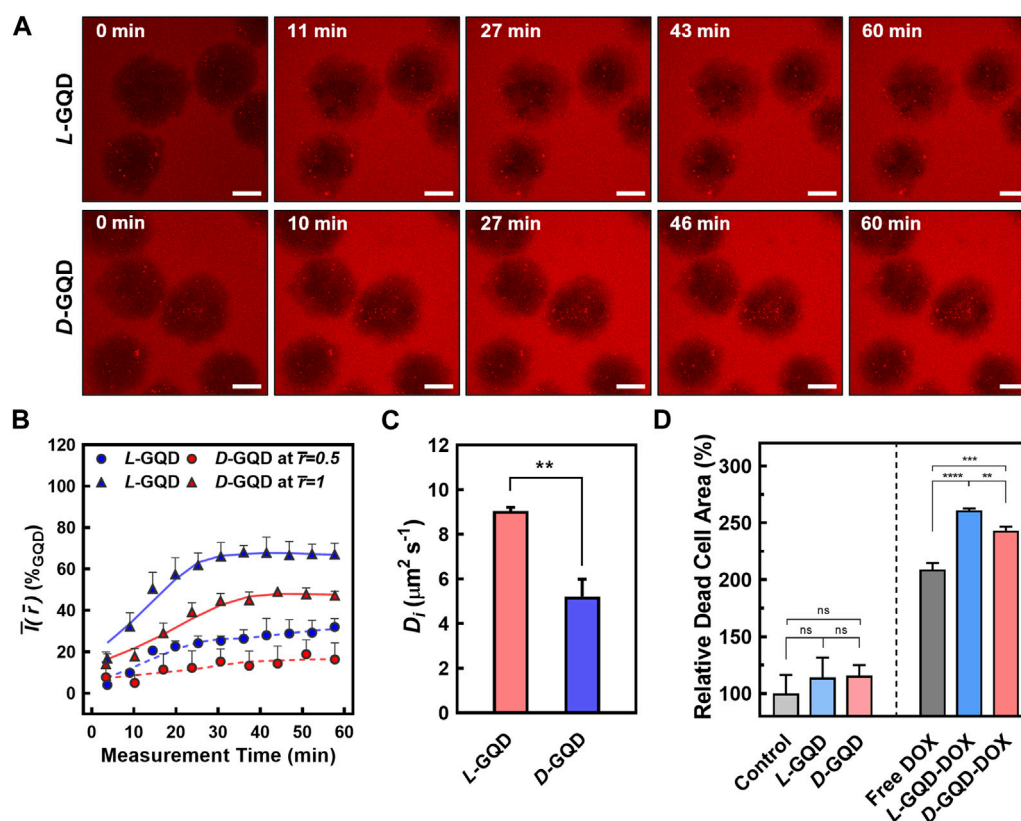


FIGURE 5

The comparison of chiral GQD diffusion to cellular spheroids. (A) Time-lapse CLSM images showing the transport of the GQDs into the spheroids (Red channel: GQDs; L-GQDs: top; D-GQDs: bottom; Scale bar: 100 μm ; Z-projected maximum intensity images). (B) Time-dependent intensity plots at a fixed radial position. Solid lines showed the intensities in maximum radius ($\bar{r} = 1$) while dotted lines showed the intensities in half radius ($\bar{r} = 0.5$). (C) Evaluated apparent diffusion coefficients for L/D-GQDs (**: $p < 0.01$). (D) Quantitative analysis of dead cell area under DOX-loaded L/D-GQD treatment to cellular spheroids (ns: not significant, **: $p < 0.01$, ***: $p < 0.001$, ****: $p < 0.0001$).

suggested that the transport of L-GQDs in cellular spheroids is much faster than that of D-GQDs.

To estimate the D_i values of L/D-GQDs in tumor-like tissue (i.e., D_L or D_D), a simple diffusion model was introduced as shown in Eqs. 3, 4 (See Materials and Methods Section 2.7). The $\partial \bar{C}_i / \partial \bar{t}$ term is negligible (i.e., $\partial \bar{C}_i / \partial \bar{t} = 1$; Due to the dimensionless form) and it can be assumed that the radially-averaged plots are linear (i.e., $\partial \bar{C}_i / \partial \bar{r} = 1$; See Supplementary Figure S8). Hence, D_i is the function of \bar{r} and could be extracted by using Eq. 5: $D_i = (r_{\max})^2 / t_{eq}$, where i denotes L or D for L/D-GQDs (i.e., D_L or D_D). Extracted D_L was $9.04 \mu\text{m}^2 \text{s}^{-1}$ and D_D was $5.20 \mu\text{m}^2 \text{s}^{-1}$ (Figure 5C), showing statistically significant differences. Notably, D_L was 1.7-fold higher than D_D , indicating again that L-GQDs are more favorable to diffuse into the cellular spheroid. Interestingly, the values of D_L and D_D are much smaller than the diffusivity calculated from the Stokes-Einstein equation (e.g., $62.3 \mu\text{m}^2 \text{s}^{-1}$ for 7 nm NP dispersed in water at 25°C) (Rudiyak, 2016), similar to the diffusivity of 44 ± 1 nm-sized NPs (e.g., $7.31 \pm 0.4 \mu\text{m}^2 \text{s}^{-1}$ dispersed in water at 25°C) (Mun et al., 2014). This fact implies NP diffusion was hindered by the densely packed ECM structures of cancerous cellular spheroids. In summary, our studies on chiral GQD diffusion through cellular spheroids showed enhanced transport of L-GQDs compared to those of D-GQDs, implying chiral

modification of NPs can enhance their diffusion and potentially improve drug delivery efficiency in tumor-like tissue.

As a proof-of-concept, we employed chiral GQDs as nanocarriers for small chemotherapy drugs (e.g., DOX) and investigated their delivery efficiency into tumor-like tissue. Due to its planar anthraquinone structure, chiral GQDs can be loaded with DOX via the π - π stacking (Supplementary Figure S10) (Liu et al., 2009; Wo et al., 2016; Askari et al., 2021; Sawy et al., 2021; Kiani Nejad et al., 2022; Mirzaei-Kalar et al., 2022). Two drug-loaded nanocarriers, L-GQD-DOX and D-GQD-DOX, were tested in mature cellular spheroids and compared to the controls (e.g., Non-treated, L-GQD-treated, and D-GQD-treated groups as negative controls; free DOX-treated group as a positive control). As a result, both nanocarrier groups loaded with DOX (i.e., L-GQD-DOX and D-GQD-DOX groups) show significant increases in the ratio of dead cells than all negative controls in the CLSM images with Live/Dead staining (Supplementary Figure S11 and Figure 5D). Compared to the positive control, free DOX group, the L/D-GQD-DOX groups showed a higher ratio of dead cells: 25% increase with L-GQD-DOX and 16% increase with D-GQD-DOX showing a statistical significance (Figure 5D). Moreover, L-GQD-induced enhanced delivery of DOX led to a lower living cell activity as the cell viability in Supplementary Figure S12, showing a

statistical significance between free DOX and *L*-GQD-DOX groups. Combining all, these facts demonstrate that the chirality of nanocarriers can improve the delivery efficiency of drugs by enhanced transport through ECM.

4 Conclusion

Our study successfully developed chiral nanocarriers, *L*- and *D*-GQDs and evaluated their transport in tumor-like cellular spheroids. We discovered that left-handed chiral nanocarrier, *L*-GQDs, induced structural swelling of cellular aggregates with 15% in their diameter while *D*-GQDs as nanocarriers showed limited effect, indicating the distinct interactions of the chiral GQDs with the immature ECM structure. Moreover, we demonstrated the impact of nanocarrier chirality on its transport and diffusion in tumor-like cellular spheroids: a 1.7-fold higher D_i of *L*-GQDs than that of *D*-GQDs. Furthermore, we conducted a proof-of-concept design for enhanced DOX delivery, *L*-GQD-DOX, based on the unique feature of *L*-GQDs, leading to a 25% increase in drug effect compared to free DOX. Overall, our work indicated the importance to consider chirality when designing drug carriers, as it is promising to enhance the transport and delivery of small drugs in 3D tumor-like tissue.

Data availability statement

The original contributions presented in the study are included in the article/**Supplementary Material**, further inquiries can be directed to the corresponding author.

Author contributions

HJ and YW conceptualized and designed the study and all the experiments. YW supervised overall conceptualization, validation, and data analysis. RZ synthesized and characterized chiral GQDs. GK synthesized and characterized DOX-loaded chiral GQDs. HJ performed cell culture-related works and fabricated 3D cellular spheroids. HJ performed cell-related imaging and image processing. HJ wrote the original draft, and YW supervised all the work. All authors contributed to the article and approved the submitted version.

References

- Al-Hajaj, N. A., Moquin, A., Neibert, K. D., Soliman, G. M., Winnik, F. M., and Maysinger, D. (2011). Short ligands affect modes of QD uptake and elimination in human cells. *ACS Nano* 5, 4909–4918. doi:10.1021/nn201009w
- Askari, E., Naghib, S. M., Zahedi, A., Seyfoori, A., Zare, Y., and Rhee, K. Y. (2021). Local delivery of chemotherapeutic agent in tissue engineering based on gelatin/graphene hydrogel. *J. Mater. Res.* 12, 412–422. doi:10.1016/j.jmrt.2021.02.084
- Biswas, M. C., Islam, M. T., Nandy, P. K., and Hossain, M. M. (2021). Graphene quantum dots (GQDs) for bioimaging and drug delivery applications: A review. *ACS Mater. Lett.* 3, 889–911. doi:10.1021/acsmaterialslett.0c00550
- Charoen, K. M., Fallica, B., Colson, Y. L., Zaman, M. H., and Grinstaff, M. W. (2014). Embedded multicellular spheroids as a biomimetic 3D cancer model for evaluating drug and drug-device combinations. *Biomater* 35, 2264–2271. doi:10.1016/j.biomaterials.2013.11.038
- Chauhan, V. P., Lanning, R. M., Diop-Frimpong, B., Mok, W., Brown, E. B., Padera, T. P., et al. (2009). Multiscale measurements distinguish cellular and interstitial hindrances to diffusion *in vivo*. *Biophys. J.* 97, 330–336. doi:10.1016/j.bpj.2009.03.064
- Chen, C. S. (2016). 3D biomimetic cultures: The next platform for cell Biology. *Trends Cell Biol.* 26, 798–800. doi:10.1016/j.tcb.2016.08.008
- Cooper, G. M. (2000). "Transport of small molecules," in *The cell: A molecular approach*. 2nd edition (United States: Sinauer Associates).
- Döring, A., Ushakova, E., and Rogach, A. L. (2022). Chiral carbon dots: Synthesis, optical properties, and emerging applications. *Light Sci. Appl.* 11, 75. doi:10.1038/s41377-022-00764-1
- Du, X., Zhou, J., Wang, J., Zhou, R., and Xu, B. (2017). Chirality controls reaction-diffusion of nanoparticles for inhibiting cancer cells. *ChemNanoMat* 3, 17–21. doi:10.1002/cnma.201600258
- Du, Z., Liu, C., Song, H., Scott, P., Liu, Z., Ren, J., et al. (2020). Neutrophil-membrane-directed bioorthogonal synthesis of inflammation-targeting chiral drugs. *Chem* 6, 2060–2072. doi:10.1016/j.chempr.2020.06.002

Funding

We acknowledge funding from an American Cancer Society Institutional Research Grant (ACS IRG-17-182-04) and the National Science Foundation Industry- University Cooperative Research Center (The Center for Bioanalytic Metrology). This research was funded in part by a Summer Graduate Research Fellowship from the Berthiaume Institute for Precision Health at the University of Notre Dame.

Acknowledgments

All the CLSM imaging was carried out in part in the Notre Dame Integrated Imaging Facility, University of Notre Dame, using A1R-MP Laser Scanning Confocal Microscopy. We thank Sara Cole for the knowledge and expertise as well as time towards this research.

Conflict of interest

The authors declare that the research was conducted in the absence of any commercial or financial relationships that could be construed as a potential conflict of interest.

Publisher's note

All claims expressed in this article are solely those of the authors and do not necessarily represent those of their affiliated organizations, or those of the publisher, the editors and the reviewers. Any product that may be evaluated in this article, or claim that may be made by its manufacturer, is not guaranteed or endorsed by the publisher.

Supplementary material

The Supplementary Material for this article can be found online at: <https://www.frontiersin.org/articles/10.3389/fchem.2023.1207579/full#supplementary-material>

- Fulaz, S., Vitale, S., Quinn, L., and Casey, E. (2019). Nanoparticle–biofilm interactions: The role of the EPS matrix. *Trends Microbiol.* 27, 915–926. doi:10.1016/j.tim.2019.07.004
- Gao, Y., Li, M., Chen, B., Shen, Z., Guo, P., Wientjes, M. G., et al. (2013). Predictive models of diffusive nanoparticle transport in 3-dimensional tumor cell spheroids. *AAPS J.* 15, 816–831. doi:10.1208/s12248-013-9478-2
- Gunti, S., Hoke, A. T. K., Vu, K. P., and London, N. R. (2021). Organoid and spheroid tumor models: Techniques and applications. *Cancers* 13, 874. doi:10.3390/cancers13040874
- Hai, X., Feng, J., Chen, X., and Wang, J. (2018). Tuning the optical properties of graphene quantum dots for biosensing and bioimaging. *J. Mater. Chem. B* 6, 3219–3234. doi:10.1039/C8TB00428E
- Henna, T. K., and Pramod, K. (2020). “Biocompatibility of graphene quantum dots and related materials,” in *Handbook of biomaterials biocompatibility woodhead publishing Series in biomaterials*. Editor M. Mozafari (United States: Woodhead Publishing), 353–367. doi:10.1016/B978-0-08-102967-1.00017-7
- Hsu, Y.-H., Moya, M. L., Abiri, P., Hughes, C. C. W., George, S. C., and Lee, A. P. (2012). Full range physiological mass transport control in 3D tissue cultures. *Lab. Chip* 13, 81–89. doi:10.1039/C2LC40787F
- Huang, Y., Fu, Y., Li, M., Jiang, D., Kuttyreff, C. J., Engle, J. W., et al. (2020a). Chirality-driven transportation and oxidation prevention by chiral selenium nanoparticles. *Angew. Chem.* 132, 4436–4444. doi:10.1002/ange.201910615
- Huang, Y., Fu, Y., Li, M., Jiang, D., Kuttyreff, C. J., Engle, J. W., et al. (2020b). Chirality-driven transportation and oxidation prevention by chiral selenium nanoparticles. *Angew. Chem. Int. Ed. Engl.* 59, 4406–4414. doi:10.1002/anie.201910615
- Jiang, S., Chekini, M., Qu, Z.-B., Wang, Y., Yeltik, A., Liu, Y., et al. (2017). Chiral ceramic nanoparticles and peptide catalysis. *J. Am. Chem. Soc.* 139, 13701–13712. doi:10.1021/jacs.7b01445
- Kiani Nejad, Z., Akbar Khandar, A., and Khatamian, M. (2022). Graphene quantum dots based MnFe₂O₄@SiO₂ magnetic nanostructure as a pH-sensitive fluorescence resonance energy transfer (FRET) system to enhance the anticancer effect of the drug. *Int. J. Pharm.* 628, 122254. doi:10.1016/j.jpharm.2022.122254
- Koomullil, R., Tehrani, B., Goliwas, K., Wang, Y., Ponnazhagan, S., Berry, J., et al. (2021). Computational simulation of exosome transport in tumor microenvironment. *Front. Med.* 8, 643793. doi:10.3389/fmed.2021.643793
- Leedale, J. A., Kyffin, J. A., Harding, A. L., Colley, H. E., Murdoch, C., Sharma, P., et al. (2020). Multiscale modelling of drug transport and metabolism in liver spheroids. *Interface Focus* 10, 20190041. doi:10.1098/rsfs.2019.0041
- Lenzini, S., Bargi, R., Chung, G., and Shin, J.-W. (2020). Matrix mechanics and water permeation regulate extracellular vesicle transport. *Nat. Nanotechnol.* 15, 217–223. doi:10.1038/s41565-020-0636-2
- Li, G., Liu, Z., Gao, W., and Tang, B. (2023). Recent advancement in graphene quantum dots based fluorescent sensor: Design, construction and bio-medical applications. *Coord. Chem. Rev.* 478, 214966. doi:10.1016/j.ccr.2022.214966
- Liu, Z., Fan, A. C., Rakhra, K., Sherlock, S., Goodwin, A., Chen, X., et al. (2009). Supramolecular stacking of doxorubicin on carbon nanotubes for *in vivo* cancer therapy. *Angew. Chem. Int. Ed. Engl.* 48, 7668–7672. doi:10.1002/anie.200902612
- Ma, W., Xu, L., de Moura, A. F., Wu, X., Kuang, H., Xu, C., et al. (2017). Chiral inorganic nanostructures. *Chem. Rev.* 117, 8041–8093. doi:10.1021/acs.chemrev.6b00755
- Mirzaei-Kalar, Z., Kiani Nejad, Z., and Khandar, A. A. (2022). New ZnFe₂O₄@SiO₂@graphene quantum dots as an effective nanocarrier for targeted DOX delivery and CT-DNA binder. *J. Mol. Liq.* 363, 119904. doi:10.1016/j.molliq.2022.119904
- Mun, E. A., Hannell, C., Rogers, S. E., Hole, P., Williams, A. C., and Khutoryanskiy, V. V. (2014). On the role of specific interactions in the diffusion of nanoparticles in aqueous polymer solutions. *Langmuir* 30, 308–317. doi:10.1021/la4029035
- Ng, C. P., and Pun, S. H. (2008). A perfusable 3D cell–matrix tissue culture chamber for *in situ* evaluation of nanoparticle vehicle penetration and transport. *Biotechnol. Bioeng.* 99, 1490–1501. doi:10.1002/bit.21698
- Park, H., and Park, S. Y. (2022). Enhancing the alkaline hydrogen evolution reaction of graphene quantum dots by ethylenediamine functionalization. *ACS Appl. Mater. Interfaces* 14, 26733–26741. doi:10.1021/acsami.2c04703
- Peng, J., Gao, W., Gupta, B. K., Liu, Z., Romero-Aburto, R., Ge, L., et al. (2012). Graphene quantum dots derived from carbon fibers. *Nano Lett.* 12, 844–849. doi:10.1021/nl2038979
- Peng, Z., Yuan, L., XuHong, J., Tian, H., Zhang, Y., Deng, J., et al. (2021). Chiral nanomaterials for tumor therapy: Autophagy, apoptosis, and photothermal ablation. *J. Nanobiotechnology* 19, 220. doi:10.1186/s12951-021-00965-7
- Powell, M. E., Evans, C. D., Bull, S. D., James, T. D., and Fordred, P. S. (2012). “Spectroscopic analysis: Diastereomeric derivatization for spectroscopy,” in *Comprehensive chirality*. Editors E. M. Carreira and H. Yamamoto (London, U. K. Elsevier), 571–599. doi:10.1016/B978-0-08-095167-6.00845-4
- Rudiyak, V. Ya. (2016). “Diffusion of nanoparticles in gases and liquids,” in *Handbook of nanoparticles*. Editor M. Aliofkhaezai (Berlin, Germany: Springer International Publishing), 1193–1218. doi:10.1007/978-3-319-15338-4_54
- Ryu, N.-E., Lee, S.-H., and Park, H. (2019). Spheroid culture system methods and applications for mesenchymal stem cells. *Cells* 8, 1620. doi:10.3390/cells8121620
- Salam, A. (1991). The role of chirality in the origin of life. *J. Mol. Evol.* 33, 105–113. doi:10.1007/BF02193624
- Sarasij, R. C., Mayor, S., and Rao, M. (2007). Chirality-induced budding: A raft-mediated mechanism for endocytosis and morphology of caveolae? *Biophys. J.* 92, 3140–3158. doi:10.1529/biophysj.106.085662
- Sattari, S., Adeli, M., Beyranvand, S., and Nemati, M. (2021). Functionalized graphene platforms for anticancer drug delivery. *Int. J. Nanomedicine* 16, 5955–5980. doi:10.2147/IJN.S249712
- Sawy, A. M., Barhoum, A., Abdel Gaber, S. A., El-Hallouty, S. M., Shousha, W. G., Maarouf, A. A., et al. (2021). Insights of doxorubicin loaded graphene quantum dots: Synthesis, DFT drug interactions, and cytotoxicity. *Mater. Sci. Eng. C* 122, 111921. doi:10.1016/j.msec.2021.111921
- Shanker, G., Allen, J. W., Mutkus, L. A., and Aschner, M. (2001). The uptake of cysteine in cultured primary astrocytes and neurons. *Brain Res.* 902, 156–163. doi:10.1016/S0006-8993(01)02342-3
- Shanker, G., and Aschner, M. (2001). Identification and characterization of uptake systems for cysteine and cysteine in cultured astrocytes and neurons: Evidence for methylmercury-targeted disruption of astrocyte transport. *J. Neurosci. Res.* 66, 998–1002. doi:10.1002/jnr.10066
- Shao, Y., Yang, G., Lin, J., Fan, X., Guo, Y., Zhu, W., et al. (2021). Shining light on chiral inorganic nanomaterials for biological issues. *Theranostics* 11, 9262–9295. doi:10.7150/thno.64511
- Sherman, I. A., and Fisher, M. M. (1986). Hepatic transport of fluorescent molecules: *In vivo* studies using intravital TV microscopy. *Hepatology* 6, 444–449. doi:10.1002/hep.1840060321
- Speirs, A. L. (1962). Thalidomide and congenital abnormalities. *Lancet* 279, 303–305. doi:10.1016/S0140-6736(62)91248-5
- Suzuki, N., Wang, Y., Elvati, P., Qu, Z.-B., Kim, K., Jiang, S., et al. (2016). Chiral graphene quantum dots. *ACS Nano* 10, 1744–1755. doi:10.1021/acsnano.5b06369
- Tian, P., Tang, L., Teng, K. S., and Lau, S. P. (2018). Graphene quantum dots from Chemistry to applications. *Mater. Today Chem.* 10, 221–258. doi:10.1016/j.mtchem.2018.09.007
- Timmins, N. E., and Nielsen, L. K. (2007). “Generation of multicellular tumor spheroids by the hanging-drop method,” in *Tissue engineering methods in molecular medicine™*. Editors H. Hauser and M. Fussenegeger (Totowa, NJ: Humana Press), 141–151. doi:10.1007/978-1-59745-443-8_8
- Vázquez-Nakagawa, M., Rodríguez-Pérez, L., Martín, N., and Herranz, M. A. (2022). Supramolecular assembly of edge functionalized top-down chiral graphene quantum dots. *Angew. Chem. Int. Ed. Engl.* 61, e202211365. doi:10.1002/anie.202211365
- Wang, S., Cole, I. S., Zhao, D., and Li, Q. (2016). The dual roles of functional groups in the photoluminescence of graphene quantum dots. *Nanoscale* 8, 7449–7458. doi:10.1039/C5NR07042B
- Wang, X., Wu, B., Zhang, Y., and Feng, C. (2022b). Chiral graphene-based supramolecular hydrogels toward tumor therapy. *Polym. Chem.* 13, 1685–1694. doi:10.1039/D1PY01724A
- Wang, Y., Bahng, J. H., Che, Q., Han, J., and Kotov, N. A. (2015). Anomalous fast diffusion of targeted carbon nanotubes in cellular spheroids. *ACS Nano* 9, 8231–8238. doi:10.1021/acsnano.5b02595
- Wang, Y., and Jeon, H. (2022). 3D cell cultures toward quantitative high-throughput drug screening. *Trends Pharmacol. Sci.* 43, 569–581. doi:10.1016/j.tips.2022.03.014
- Wang, Y., Jiang, Z., Xu, W., Yang, Y., Zhuang, X., Ding, J., et al. (2019). Chiral polypeptide thermogels induce controlled inflammatory response as potential immunoadjuvants. *ACS Appl. Mater. Interfaces* 11, 8725–8730. doi:10.1021/acsami.9b01872
- Warning, L. A., Miandashti, A. R., McCarthy, L. A., Zhang, Q., Landes, C. F., and Link, S. (2021). Nanophotonic approaches for chirality sensing. *ACS Nano* 15, 15538–15566. doi:10.1021/acsnano.1c04992
- Wo, F., Xu, R., Shao, Y., Zhang, Z., Chu, M., Shi, D., et al. (2016). A multimodal system with synergistic effects of magneto-mechanical, photothermal, photodynamic and chemo therapies of cancer in graphene-quantum dot-coated hollow magnetic nanospheres. *Theranostics* 6, 485–500. doi:10.7150/thno.13411
- Wu, W., and Pauly, M. (2022). Chiral plasmonic nanostructures: Recent advances in their synthesis and applications. *Mater. Adv.* 3, 186–215. doi:10.1039/D1MA00915J
- Yao, C., Tu, Y., Ding, L., Li, C., Wang, J., Fang, H., et al. (2017). Tumor cell-specific nuclear targeting of functionalized graphene quantum dots *in vivo*. *Bioconjug Chem.* 28, 2608–2619. doi:10.1021/acs.bioconjchem.7b00466

- Yeom, J., Guimaraes, P. P. G., Ahn, H. M., Jung, B.-K., Hu, Q., McHugh, K., et al. (2020). Chiral supraparticles for controllable nanomedicine. *Adv. Mater.* 32, 1903878. doi:10.1002/adma.201903878
- Zhang, Y., Zhu, Y., Kim, G., Wang, C., Zhu, R., Lu, X., et al. (2023). Chiral graphene quantum dots enhanced drug loading into small extracellular vesicles. *bioRxiv* 2023, 10191–10205. doi:10.1021/acsnano.3c00305
- Zhao, B., Yang, S., Deng, J., and Pan, K. (2021). Chiral graphene hybrid materials: Structures, properties, and chiral applications. *Adv. Sci.* 8, 2003681. doi:10.1002/advs.202003681
- Zhao, X., Zang, S.-Q., and Chen, X. (2020). Stereospecific interactions between chiral inorganic nanomaterials and biological systems. *Chem. Soc. Rev.* 49, 2481–2503. doi:10.1039/D0CS00093K
- Zhu, R., Makwana, K. M., Zhang, Y., Rajewski, B. H., Valle, J. R. D., and Wang, Y. (2022a). Inhibition and disassembly of tau aggregates by engineered graphene quantum dots. *bioRxiv* 2022, 522245. doi:10.1101/2022.12.29.522245
- Zhu, R., Wu, Q., He, Y., Gao, M., Li, Y., Peng, W., et al. (2022b). Fabrication of size-controllable and arrangement-orderly HepG2 spheroids for drug screening via decellularized liver matrix-derived micropattern array chips. *ACS Omega* 7, 2364–2376. doi:10.1021/acsomega.1c06302
- Ziemys, A., Kojic, M., Milosevic, M., Schrefler, B., and Ferrari, M. (2018). Multiscale models for transport and biodistribution of therapeutics in cancer. *Comput. Aided Chem. Eng.* 42, 209–237. doi:10.1016/B978-0-444-63964-6.00007-6



OPEN ACCESS

EDITED BY

Rongsheng (Ross) Wang, Temple University, United States

REVIEWED BY

Utoomporn Surayot,
Chiang Mai University, Thailand
Chao Cai,
Ocean University of China, China
Wei Zeng,
Zhejiang Agriculture and Forestry University, China
Xiaolu Jiang,
Marine Biomedical Research Institute of Qingdao, China

*CORRESPONDENCE

Hairong Cheng,
✉ chenghr893@nenu.edu.cn

RECEIVED 23 May 2023

ACCEPTED 21 July 2023

PUBLISHED 07 August 2023

CITATION

Geng J, Wang G, Guo J, Han X, Qu Y, Zhou Y, Tai G, Sun L and Cheng H (2023), Preparation and structural analysis of fucomannogalactan and β -1,6-glucan from *Grifola frondosa* mycelium. *Front. Chem.* 11:1227288. doi: 10.3389/fchem.2023.1227288

COPYRIGHT

© 2023 Geng, Wang, Guo, Han, Qu, Zhou, Tai, Sun and Cheng. This is an open-access article distributed under the terms of the [Creative Commons Attribution License \(CC BY\)](https://creativecommons.org/licenses/by/4.0/). The use, distribution or reproduction in other forums is permitted, provided the original author(s) and the copyright owner(s) are credited and that the original publication in this journal is cited, in accordance with accepted academic practice. No use, distribution or reproduction is permitted which does not comply with these terms.

Preparation and structural analysis of fucomannogalactan and β -1,6-glucan from *Grifola frondosa* mycelium

Jie Geng¹, Guining Wang¹, Jiao Guo¹, Xiao Han¹, Yunhe Qu², Yifa Zhou¹, Guihua Tai¹, Lin Sun¹ and Hairong Cheng^{1*}

¹Jilin Province Key Laboratory on Chemistry and Biology of Changbai Mountain Natural Drugs, Glycoconjugate Engineering Research Center of the Ministry of Education, School of Life Sciences, Northeast Normal University, Changchun, China, ²Central Laboratory, Changchun Normal University, Changchun, China

Introduction: Polysaccharides, key components present in *Grifola frondosa*, can be divided into those derived from fruiting bodies, mycelium, and fermentation broth based on their source. The structure of *G. frondosa* fruiting body-derived polysaccharides has been fully characterized. However, the structure of *G. frondosa* mycelium-derived polysaccharides remains to be elucidated.

Methods: In this study, we obtained mycelia from *G. frondosa* by liquid fermentation and extracted them with water and alkaline solution. Then, the mycelia were isolated and purified to obtain homogeneity and systematically characterized by methylation and FT infrared (FT-IR) and nuclear magnetic resonance (NMR) spectroscopy.

Results and discussion: Structural analysis showed that two neutral fractions (WGFP-N-a and AGFP-N-a₁) have a common backbone composed of α -1,6-D-Me-Galp and α -1,6-D-Galp that were substituted at O-2 by 1,2-Manp, α -1,3-L-Fucp, and α -T-D-Manp and thus are identified as fucomannogalactans. WGFP-A-a, AGFP-A-b, and AGFP-A-c are β -1,6-glucans with different molecular weights and are branched with β -1,3-D-Glcp and T-D-Glcp at the O-3 of Glc. Our results provide important structural information about *G. frondosa* mycelium-derived polysaccharides and provide the basis for their further development and application.

KEYWORDS

Grifola frondosa, mycelium, fucomannogalactan, glucan, structure analysis

1 Introduction

Grifola frondosa belongs to the subphylum Basidiomycota, class Laminaria, order Aphyllum, family Polyporaceae, and genus Trichomycota. *Grifola frondosa* is an edible and medicinal mushroom, with significant developmental and research value. It is very popular in China, Japan, and other Asian countries because of its flavor and nutritional value. *Grifola frondosa* has many active ingredients, such as polysaccharides (especially β -1,6-glucans and β -1,3-glucans), glycoproteins, ergosterol, polyphenol yellow, and fungal SOD enzyme (Švagelj et al., 2008; Wu et al., 2021). These polysaccharides can be divided into those derived from fruiting bodies, mycelium, and fermentation broth based on their source (Santos Arteiro et al., 2012). The structure of *G. frondosa* fruiting body-derived

polysaccharides has been fully characterized. However, the structure of *G. frondosa* mycelium-derived polysaccharides remains to be elucidated. Recently, polysaccharides from *G. frondosa* mycelium have received considerable attention due to their anti-tumor, immune regulatory, antioxidant, and other properties (Zhuang et al., 1994; Nie et al., 2006; Cui et al., 2007; Zhao et al., 2016; Wu et al., 2021).

Given that *G. frondosa* mycelium-derived polysaccharides display numerous pharmacological activities, analyzing their structures is crucial for their development and utilization. Available reports have provided limited information about the structural characteristics of *G. frondosa* mycelium-derived polysaccharides. Iino et al. (1985) were the first to extract the Grifolan component from *G. frondosa* mycelium under cold alkaline conditions. Grifolan is a β -1,3-glucan with 1,6-Glcp branches. Adachi et al. (1994) extracted a purified fungal β -1,3-D-glucan with 0.5% citrate buffer from *G. frondosa* mycelium. An α -configuration proteoglycan GFPS1b with a molecular weight of 21 kDa was obtained from *G. frondosa* mycelium and found to be composed of Glc, Gal, and arabinose (Ara) at a molar ratio of 4:2:1. GFPS1b has a backbone consisting of α -1,4-Galp and α -1,3-Glcp (Cui et al., 2007). Zhao et al. (2016) extracted the mycelium of *G. frondosa* with hot water at 80°C to obtain a polysaccharide GRP1 with a molecular weight of 40.5 kDa. Moreover, during the process of liquid fermentation, many factors, such as the source of bacteria, fermentation duration, medium selection, and polysaccharide extraction method, may impact the structure of the polysaccharide.

To fully characterize polysaccharides from *G. frondosa* mycelium, we prepared and investigated a series of water-soluble and alkali-soluble polysaccharides. Our results will enhance the structural information about *G. frondosa* mycelium-derived polysaccharides and provide direction for the development and application of *G. frondosa* mycelium-derived polysaccharides as functional food.

2 Materials and methods

2.1 Materials

The *Grifola frondosa* CTS8 strain was purchased from BNCC (Henan, China). DEAE-cellulose was purchased from Shanghai Chemical Reagent Research Institute (Shanghai, China). Sepharose CL-6B was purchased from GE healthcare (Pittsburgh, United States). Bio-Gel P-2 was purchased from Bio-Rad (California, United States). β -1,3-Glucanase and α -glucoamylase were purchased from Megazyme (Ireland). All other chemicals used were of analytical grade and commercially available or produced in China.

2.2 Liquid fermentation culture

Strain activation and preservation: The prepared PDA culture was sterilized at 115°C for 30 min. After cooling, the slanted strains of *G. frondosa* were kept under aseptic conditions, and two pieces (~0.5 cm \times 0.5 cm) were cut. The blocks were inoculated on the

PDA plate medium, placed in an incubator maintained at a constant temperature of 25°C for 14 days, and transferred to 4°C for storage after the medium surface was completely covered by mycelia.

For liquid seed culture, the prepared medium was dispensed into 2-L conical flasks which were filled with 1 L of liquid. The flasks were sterilized at 115°C for 30 min, and then each flask was inoculated under aseptic conditions. Each Erlenmeyer flask was connected to 25 activated *G. frondosa* flat plates (~1 cm \times 1 cm) and placed them in a shaker maintained at a constant temperature of 25°C. The flasks were cultured at 160 rpm for 7 days to obtain a large number of uniform-sized mycelium balls.

The fermentation culture was carried out in a 5-L fermenter containing 3 L of the sterilized fermentation medium, which had been prepared and cooled under aseptic conditions (115°C for 30 min). The *G. frondosa* seed solution was inoculated with 10% of the inoculum and cultivated for 6 days while being fed in batches. Real-time monitoring for the pH value and dissolved oxygen value was conducted, and ventilation volume and stirring speed were controlled.

2.3 Polysaccharide extraction and purification

After drying, the mycelium was extracted with distilled water (material/dH₂O, w/v, 1:20) twice at 100°C for 3 h. Extracts were concentrated under vacuum at 60°C and precipitated using four volumes of 95% ethanol at 4°C for 12 h. After centrifugation (4,000 rpm, 15 min), the precipitate was collected, redissolved in dH₂O, frozen at -80°C for 30 min, and freeze-dried using an Alpha 2-4 LD plus freeze dryer (Christ, Germany). A water-soluble polysaccharide (WGFP) was obtained, and mycelium residues after water extraction were obtained with 0.5 M of NaOH solution (material/alkali, w/v, 1:25) three times at 80°C for 3 h. After neutralization, the extract was concentrated *in vacuo* at 60°C and precipitated at 4°C using four volumes of 95% ethanol for 12 h. After centrifugation (4,000 rpm, 15 min), the precipitate was collected and re-dissolved in water, followed by dialysis and lyophilization. The alkali-soluble polysaccharide AGFP was obtained.

WGFP and AGFP were dissolved in distilled water, applied on a DEAE-cellulose column (8.0 \times 20 cm, Cl⁻), and eluted with distilled water and 0.3 M NaCl, yielding a neutral polysaccharide and an acidic polysaccharide fraction, respectively. All fractions were further purified using a Sepharose CL-6B column, resulting in homogeneous neutral and acidic polysaccharide fractions.

2.4 General methods

The total carbohydrate content was determined by the phenol-sulfuric acid protocol with glucose as the standard (DuBois et al., 1956). The uronic acid content was determined by using the colorimetric method proposed by Filisetti-Cozzi and Carpita (1991) with glucuronic acid as the standard. The protein content was determined by using the Bradford assay with bovine serum albumin (BSA) as the standard (Sedmak Jj Fau - Grossberg and Grossberg, 1977).

The ash content was determined by using the muffle furnace burning method. A glycogen-like polysaccharide was detected by the I_2 -KI assay (Wang et al., 2010). Molecular weights were determined by high-performance gel-permeation chromatography (HPGPC). HPGPC was carried out at 40°C using a TSK-gel G-3000PW_{XL} column (7.8 × 300 mm, Tosoh, Japan) connected to a Shimadzu high-performance liquid chromatography (HPLC) system. The column was pre-calibrated with dextrans as the standard. Polysaccharide samples (5 mg/mL) were dissolved in 0.2 M NaCl at a flow rate of 0.6 mL/min and monitored using a refractive index RID-10A detector (Shimadzu, Tokyo, Japan).

2.5 Monosaccharide composition analysis

Monosaccharide composition was analyzed by using an external standard method. According to the retention time of nine monosaccharide standards, the monosaccharide composition of polysaccharide samples was determined. The content of each monosaccharide was determined based on the peak area.

A polysaccharide sample (2 mg) was hydrolyzed first with anhydrous methanol containing 1 M HCl at 80°C for 16 h and then with 2 M TFA at 120°C for 1 h. Hydrolyzed monosaccharides and nine monosaccharide standards were derived using 1-phenyl-3-methyl-5-pyrazolone (PMP) and analyzed by HPLC as previously described (Wang et al., 2023). The column temperature was 35°C, and the detection wavelength was 245 nm. The flow rate was 1.0 mL/min, and the injection volume was 10.0 μ L. The mobile phase was 80.8% PBS (0.1 M, pH 7.0) and 19.2% acetonitrile (v/v), and the detector used was an SPD-20A ultraviolet detection system.

2.6 Fourier transform infrared spectroscopy

The polysaccharide sample was ground with spectroscopic grade KBr and then pressed into a powder to form a pellet. Fourier transform infrared spectroscopy (FT-IR) spectra were obtained on the PerkinElmer Spectrum Two FT-IR spectrometer (PerkinElmer, United States) in the wavenumber range of 4,000–400 cm^{-1} .

2.7 Methylation analysis

Methylation analysis was carried out according to the method proposed by Needs and Selvendran (1993). In brief, the polysaccharide sample (10 mg) was dissolved in DMSO (1.5 mL) and methylated with a suspension of NaOH/DMSO (1.5 mL) and iodomethane (2.0 mL). The reaction mixture was extracted with dichloromethane (CH_2Cl_2), and then the solvent was removed by vacuum evaporation. Complete methylation was confirmed by the disappearance of the -OH band (3,200–3,400 cm^{-1}) in the FT-IR spectrum. The per-O-methylated polysaccharide was hydrolyzed subsequently using HCOOH (85%, 1 mL) for 4 h at 100°C and then with CF_3COOH (2 M, 1 mL) for 6 h at 100°C. The partially methylated sugars in the hydrolyzate were reduced by NaBH_4 and then acetylated. The resulting alditol acetates were analyzed by

GC-MS (7890B-5977B, Agilent, United States) using an HP-5ms capillary column (30 m × 0.32 mm × 0.25 mm). The oven temperature was programmed from 120°C (hold for 1 min) to 210°C (hold for 2 min) at a rate of 3 °C/min and then up to 260°C (hold for 4 min) at a rate of 10 °C/min. The temperature of both the inlet and the detector was set at 300°C. Helium was used as a carrier gas. The mass scan range was 50–500 m/z.

2.8 Congo Red experiment

Congo Red binds to polysaccharides that have a three-helix structure, thus exhibiting a characteristic redshift (Liu et al., 2011). Various concentrations of NaOH solutions were prepared: 0, 0.1, 0.2, 0.4, 0.6, and 0.8 M. Congo Red was dissolved in a solution of 80 μ M. Polysaccharide samples were prepared at a concentration of 2 mg/mL, and 2.5 mL of 80 μ M Congo Red was added to this solution followed by the addition of distilled water. Finally, 3 mL NaOH solution of various concentrations was added to make the final concentration 0–0.4 M. The solution was equilibrated at room temperature for 1 h and analyzed using an UV spectrophotometer covering the wavelength range of 400–700 nm to identify the maximum absorption wavelength.

2.9 NMR spectroscopy

^1H and ^{13}C NMR spectra were recorded at 20°C on a Bruker Avance 600 MHz spectrometer (Germany) with a Bruker 5 mm broadband probe, operating at 600 MHz for ^1H NMR and 150 MHz for ^{13}C NMR. Samples (20 mg) were dissolved in D_2O (0.5 mL) and centrifuged to remove any undissolved substances. Data were analyzed using the standard Bruker software.

2.10 Enzymatic hydrolysis analysis

A measure of 20 mg AGFP-N-b was added with 4 mL dH_2O to obtain a reaction substrate with a concentration of 5 mg/mL. When the sample was fully dissolved, saccharification enzyme was added at a rate of 1 U and allowed for a reaction period of 24 h at 37°C. At the end of 100°C for 10 min, the reaction mixture was centrifuged at 12,000 rpm for 10 min. The supernatant was collected after concentration and freeze-dried. Finally, the lyophilized sample was applied on the Bio-Gel P-2 gel column (1.6 × 100 cm). The eluate was ddH_2O , and the elution flow rate was 0.15 mL/min. The elution peaks were detected by using the phenol-sulfuric acid method, the two main elution peaks were collected and freeze-dried. Then, the monosaccharide composition and methylation analysis were performed.

3 Results

3.1 Liquid fermentation culture

Maitake mycelium showed a dense white hyphae morphology on the solid-activated medium, as shown in Supplementary Figure

TABLE 1 Yield, molecular weight, I₂-KI chromogenicity, and monosaccharide composition of WGFP, AGFP, WGFP-N-a, WGFP-A-a, AGFP-N-a, AGFP-A-b, AGFP-A-c, AGFP-N-a₁, and AGFP-N-a₂.

Fraction	Yield (%)	Mw (kDa)	I ₂ -KI	Monosaccharide composition (mol%)						
				Glc	Gal	Man	Fuc	Me-Gal	GlcA	Xyl
WGFP	5.1	—	-	51.6	4.2	22.6	7.1	10.2	2.6	1.7
AGFP	19.4	—	+	65.9	4.0	9.6	7.5	8.3	2.6	2.1
WGFP-N-a	52.5 ^a	28.9	-	4.6	9.3	33.6	26.8	25.7	—	—
WGFP-A-a	73.2 ^b	5.0	-	80.2	1.7	11.8	—	—	6.3	—
AGFP-N-a	75.5 ^a	28.6	+	27.6	4.3	24.3	18.5	22.3	—	3.0
AGFP-A-b	14.4 ^b	19.9	-	91.4	—	2.7	1.3	1.4	3.2	—
AGFP-A-c	63.3 ^b	4.1	-	91.6	—	4.2	—	—	4.2	—
AGFP-N-a ₁	—	28.7	-	4.1	4.3	33.3	24.6	30.2	—	3.5
AGFP-N-a ₂	—	—	+	100.0	—	—	—	—	—	—

^aYield represents the yield of the neutral polysaccharide homogeneous fraction relative to the neutral polysaccharide loading.

^bYield represents the yield of the acidic polysaccharide homogeneous fraction relative to the acidic polysaccharide loading.

S1A. After inoculation in a triangular vial for approximately 3 days, fine uniform bacterial bulbs developed, and in approximately 7 days hyphal bulbs were visibly denser (~2 mm in diameter), and the bacterial liquid became acidic, as shown in **Supplementary Figure S1B**. The seed solution was inoculated in a 5-L fermentation tank (3 L of liquid loading) according to the inoculation amount of 10% (v/v), and sterility was maintained. The bacterial growth process can generally be seen in the stagnation period, linear growth period, stabilization period, and senescence period. The growth of mycelium was slow in approximately 0–2 days during the early stage of fermentation; the growth rate of mycelium was fast in 3–4 days; then, the mycelium biomass increased rapidly, while the pH decreased. The growth was slow, yet stable, in 5–6 days. The fermentation liquid gradually became viscous, and the fermentation was stopped. The mycelium morphology of the fermentation tank culture is shown in **Supplementary Figure S1C**.

The liquid fermentation culture product of the fermenter was collected, and the dried *G. frondosa* mycelium was obtained by centrifugation, washing, and drying. A single liquid fermentation process took 13 days, and 22.8 g of the dried mycelium was obtained per 3 L of culture. The mycelium biomass yield was 7.6 g/L.

3.2 Extraction of polysaccharides

The total polysaccharide content from *G. frondosa* mycelium termed WGFP (10.2 g) was obtained by boiling water extraction of 200 g dried *G. frondosa* mycelium. The extraction yield was 5.1%. Then, the residue was extracted by alkali solution to obtain the polysaccharide (AGFP). The yield was 19.4%.

The components of WGFP and AGFP were determined, and the results are shown in **Supplementary Table S1**. The sugar content (40.0%–50.0%) of WGFP and AGFP was similar, and they both contained low amounts of uronic acid (<5.0%) and high protein content (~20.0%). WGFP also contained high ash (33.0%). After deproteinization of WGFP and AGFP, the protein content of WGFP

decreased from 18.9% to 3.2%, and the protein content of AGFP decreased from 28.8% to 4.1%.

After complete acid hydrolysis and derivatization, HPLC was used to determine monosaccharide composition. The results are shown in **Table 1**. The monosaccharide molar ratio of WGFP was Glc:Man:Me-Gal:Fuc:Gal:GlcA:Xyl = 51.6:22.6:10.2:7.1:4.2:2.6:1.7. WGFP mainly contains Glc, Man, and Me-Gal. The monosaccharide molar ratio of AGFP was Glc:Man:Me-Gal:Fuc:Gal:GlcA:Xyl = 65.9:9.6:8.3:7.5:4.0:2.6:2.1. AGFP is mainly composed of Glc, with a small amount of Man, Me-Gal, and Fuc.

3.3 Fractionation of polysaccharides

WGFP and AGFP were both initially fractionated by anion-exchange chromatography. The neutral fraction was eluted with distilled water, and the acidic fraction was eluted with 0.3 M NaCl. These fractions were further separated by gel-permeation chromatography (**Figure 1**). Following separation, two purified neutral polysaccharide fractions (WGFP-N and AGFP-N) and two purified acid polysaccharide fractions (WGFP-A and AGFP-A) were obtained from different polysaccharides (**Figure 1**).

The weight-averaged molecular weights of WGFP-N, WGFP-A, AGFP-N, and AGFP-A were determined by HPGPC (**Figure 1**). The molecular weights of the two neutral polysaccharides, WGFP-N and AGFP-N, were 27 and 28.6 kDa, respectively. The molecular weights of the two acidic polysaccharides were low. The weight-averaged molecular weight of WGFP-A was ~5 kDa, and the distribution range was wide. The molecular weight of AGFP-A was ~1.9 kDa; however, the distribution range was not homogeneous. The Sephadex G-75 gel column was used for WGFP-N, AGFP-N, and AGFP-A to prepare polysaccharide fractions with homogeneous molecular weights. A Sephadex G-50 gel column was used for WGFP-A to prepare a polysaccharide fraction with a homogeneous molecular weight. This resulted in the preparation of five homogeneous polysaccharide fractions, WGFP-N-a, WGFP-A-a, AGFP-N-a, AGFP-A-b, and AGFP-A-c.

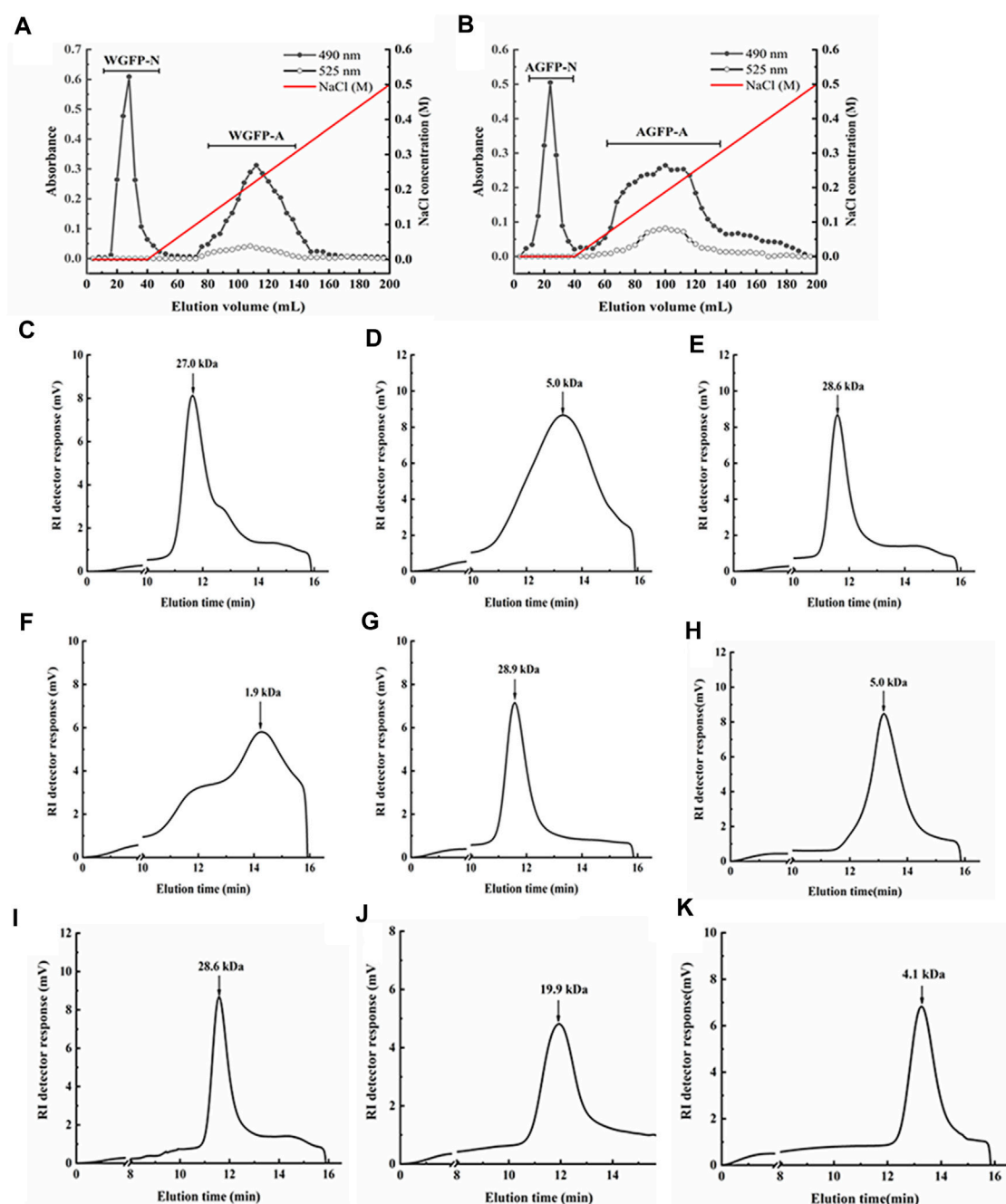


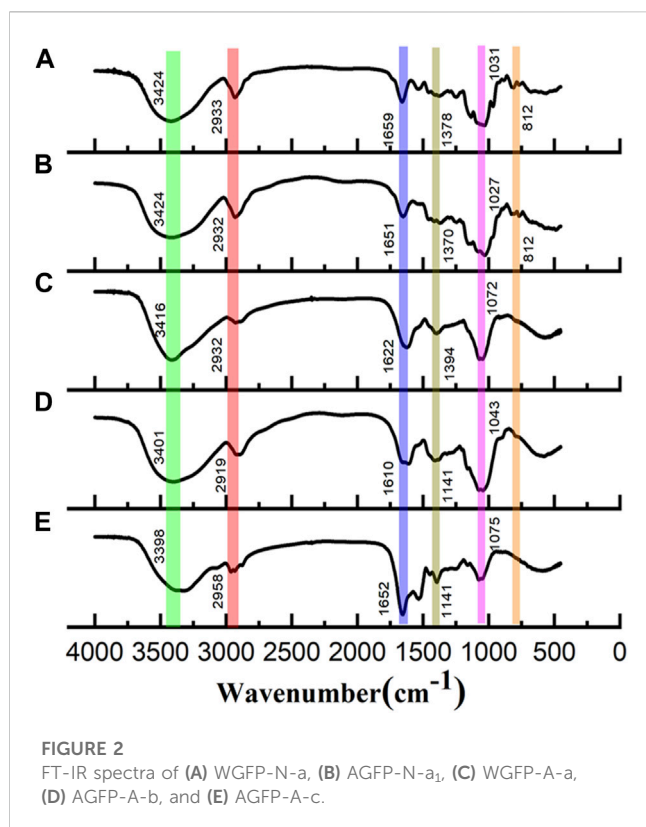
FIGURE 1

Elution profiles of (A) WGFP and (B) AGFP on the DEAE-cellulose column, eluted by a 547 linear gradient of NaCl, respectively (-●-, total sugar; -○-, uronic acid). The elution profiles of the polysaccharide fractions on HPGPC: (C) WGFP-N, (D) WGFP-A, (E) AGFP-N, (F) AGFP-A, (G) WGFP-N-a, (H) WGFP-A-a, (I) AGFP-N-a, (J) AGFP-A-b, and (K) AGFP-A-c.

Monosaccharide compositions were determined by HPLC as shown in Table 1. The yields of WGFP-N-a and AGFP-N-a were 52.5% and 75.5%, with molecular weights of 28.9 and 28.6 kDa (Figure 1), respectively. WGFP-N-a and AGFP-N-a both mainly contained Man, Me-Gal, and Fuc, whereas AGFP-N-a also contained a small amount of Glc. The yields of WGFP-A-a, AGFP-A-b, and AGFP-A-c were 73.2%, 14.4%, and 63.3%, respectively, and their molecular weights were 5, 19.9, and

4.1 kDa (Figure 1), respectively. Monosaccharide composition showed that all fractions were mainly composed of Glc.

In addition to the results from the iodine chromogenic assay, saccharification enzyme was used to enzymatically hydrolyze AGFP-N-a to remove glucans. After enzymolysis, the sample was separated on a Bio-Gel P-2 gel column. The elution curve is shown in Supplementary Figure S3. Elution peaks were collected, and the initial elution peaks were named AGFP-N-a₁ and AGFP-



N-a₂. The results of the monosaccharide composition analysis for AGFP-N-a, AGFP-N-a₁, and AGFP-N-a₂ are shown in Table 1. The content of Glc decreased from 27.6% to 4.1%, following enzymatic hydrolysis. The molecular weight distributions of AGFP-N-a and AGFP-N-a₁ are shown in Supplementary Figure S4. The molecular weight distribution did not change after enzymolysis. Therefore, we assume that 27.6% of Glc was present as galactan.

3.4 FT-IR spectra analysis

FT-IR spectra were used to characterize the primary functional groups in these polysaccharides and are shown in Figure 2. All polysaccharides showed the characteristic bands of carbohydrate compounds. The intense absorption band near 3,400 cm⁻¹ (3,394 cm⁻¹ or 3,374 cm⁻¹) is associated with the stretching vibration of O-H, a characteristic of polysaccharides. The weak band observed at approximately 2,930 cm⁻¹ (2,929 cm⁻¹ or 2,927 cm⁻¹) was attributed to C-H stretching of CH₂ groups (Li and Shah, 2014). In addition, there was no significant absorption peak at 1730 cm⁻¹, suggesting that all the polysaccharide fractions did not contain uronic acid (Zhang et al., 2023). Bands observed at 1,143 cm⁻¹ are typical of C-O-C stretching vibrations (Zhang et al., 2015). The asymmetrical stretching bands observed at approximately 1,650 cm⁻¹ (1,648 cm⁻¹ or 1,645 cm⁻¹) and the weaker symmetric stretching

TABLE 2 Types and ratios of glycosidic bonds of WGFP-N-a and AGFP-N-a₁.

Methylated sugar	Linkage	Molar ratio (%)		Mass fragment (m/z)
		WGFP-N-a	AGFP-N-a ₁	
2,3,4-Me ₃ -Fucp	T-	2.2	2.7	72,89,101,117,131,161,175
2,4-Me ₂ -Fucp	1,3-	20.1	23.1	89,101,117,131,159,173,233
2,3,4-Me ₃ -Galp	1,6-	13.1	13.8	87,101,117,129,161,173,189,233
3,4-Me ₂ -Galp	1,2,6-	26.1	27.0	99,113,129,159,189,233
2,3,4,6-Me ₄ -Manp	T-	28.1	28.8	101,117,129,145,161,205
3,4,6-Me ₃ -Manp	1,2-	10.4	4.6	87,101,129,145,161,189

TABLE 3 Types and ratios of glycosidic bonds of WGFP-A-a, AGFP-A-b, and AGFP-A-c.

Methylated sugar	Linkage	Molar ratio (%)			Mass fragment (m/z)
		WGFP-A-a	AGFP-A-b	AGFP-A-c	
2,3,4,6-Me ₄ -Glc p	T-	8.2	17.9	18.3	101,117,129,145,161,205
2,4,6-Me ₃ -Glc p	1,3-	19.5	23.3	23.3	87,101,117,129,161,233
2,3,6-Me ₃ -Glc p	1,4-	8.4	7.5	4.9	58,101,117,129,161,233
2,3,4-Me ₃ -Glc p	1,6-	42.1	28.3	33.4	87,101,117,129,161,233
2,4-Me ₂ -Glc p	1,3,6-	14.2	20.8	20.1	87,117,129,139,189,233
2,3,4,6-Me ₄ -Manp	T-	7.6	2.2	—	101,117,129,145,161,205

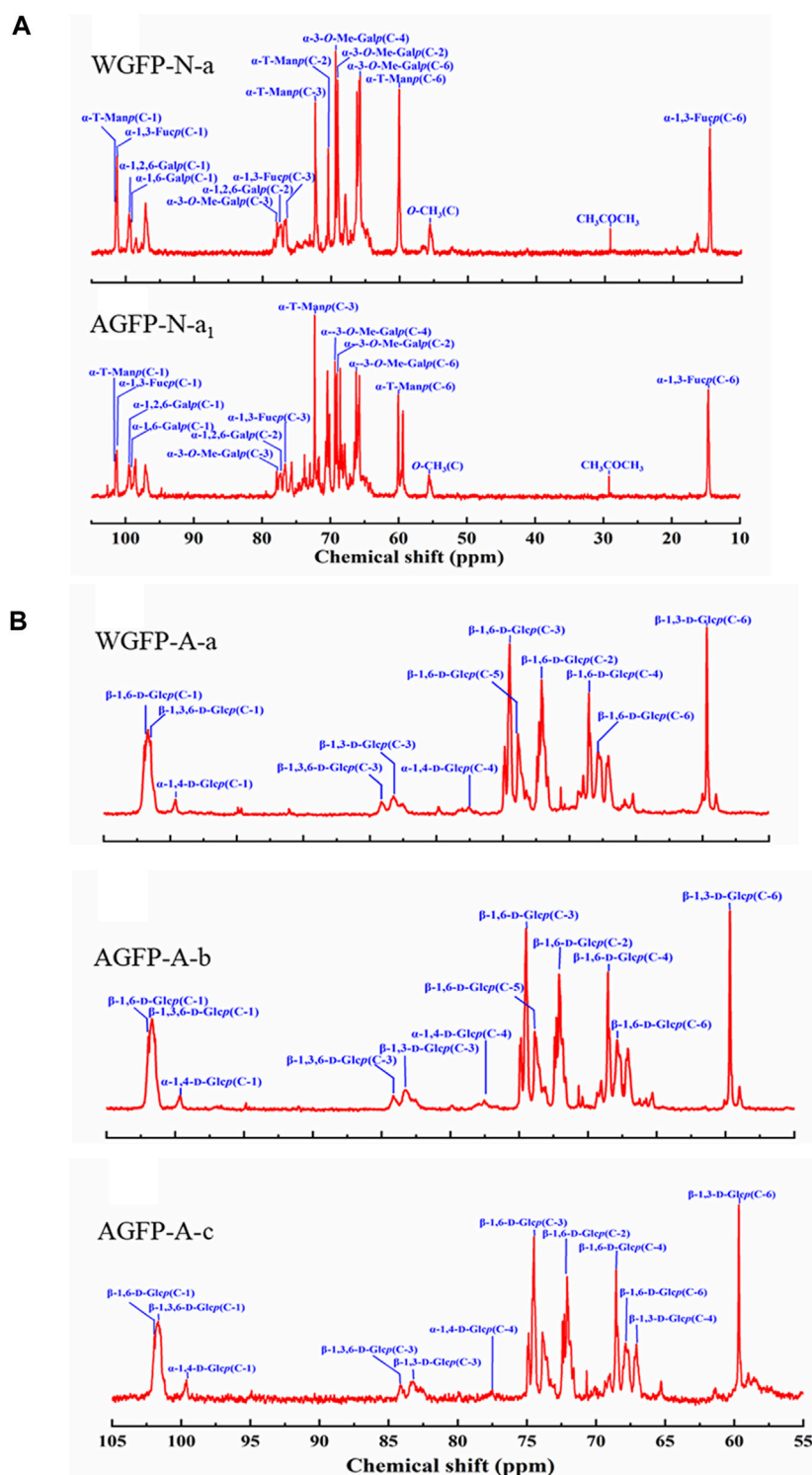


FIGURE 3

¹³C-NMR spectra of (A) WGFP-N-a and AGFP-N-a₁; (B) WGFP-A-a, AGFP-A-b, and AGFP-A-c.

bands at approximately 1,409 cm⁻¹ are attributed to asymmetric and symmetric stretching of C=O, respectively. The band observed at approximately 1,080 cm⁻¹ (1,082 cm⁻¹ or 1,075 cm⁻¹) is the characteristic stretching vibration peak of pyran ring C-O-C,

indicating the presence of the pyranose ring (Yan et al., 2019). Weak bands observed at approximately 858 cm⁻¹ and 896 cm⁻¹ indicate the presence of α -linked and β -linked glycosyl residues, respectively (Ning et al., 2021).

TABLE 4 ^{13}C -NMR spectral assignments of WGFP-N-a, AGFP-N-a₁, WGFP-A-a, AGFP-A-b, and AGFP-A-c.

Fraction	Linkage type	C-1	C-2	C-3	C-4	C-5	C-6	O-CH ₃
WGFP-N-a	α -1,6-D-Galp	99.30	69.05	68.55	69.38	67.96	65.90	—
	α -1,2,6-D-Galp	99.51	77.32	68.43	67.90	67.83	65.81	—
	α -1,6-D-Me-Galp	98.48	69.05	77.91	69.36	67.90	65.76	55.57
	α -T-Manp	101.41	70.44	72.32	69.30	74.71	60.07	—
	α -1,3-L-Fucp	101.27	70.69	76.65	73.10	67.17	14.76	—
AGFP-N-a ₁	α -1,6-D-Galp	99.29	69.04	68.55	69.31	67.96	66.26	—
	α -1,2,6-D-Galp	99.49	77.27	68.42	67.90	67.71	66.07	—
	α -1,6-D-Me-Galp	98.93	69.04	77.88	69.31	67.92	65.90	55.59
	α -T-Manp	101.42	70.42	72.30	69.27	74.71	60.09	—
	α -1,3-L-Fucp	101.29	70.68	76.62	73.00	67.16	14.73	—
WGFP-A-a	β -1,6-D-Glcp	101.85	72.09	74.49	68.54	73.87	67.70	—
	β -1,3,6-D-Glcp	101.47	72.31	84.13	68.45	74.86	67.84	—
	β -1,3-D-Glcp	101.68	71.62	83.22	67.07	74.49	59.67	—
	α -1,4-D-Glcp	99.61	71.63	73.39	77.54	71.38	60.48	—
AGFP-A-b	β -1,6-D-Glcp	101.94	72.00	74.49	68.55	73.87	67.70	—
	β -1,3,6-D-Glcp	101.69	72.28	84.25	68.46	74.87	67.84	—
	β -1,3-D-Glcp	101.78	71.62	83.24	67.10	74.49	59.68	—
	α -1,4-D-Glcp	99.67	71.64	73.37	77.53	71.36	60.32	—
AGFP-A-c	β -1,6-D-Glcp	101.94	72.09	74.51	68.54	73.87	67.70	—
	β -1,3,6-D-Glcp	101.52	72.28	84.17	68.46	74.87	67.88	—
	β -1,3-D-Glcp	101.67	71.83	83.23	67.10	74.49	59.67	—
	α -1,4-D-Glcp	99.56	71.63	73.36	77.54	71.38	60.48	—

3.5 Structural analysis of polysaccharides

3.5.1 Methylation analysis

The total ion chromatogram and fragment ion peaks from methylation are shown in [Supplementary Figures S7, S8](#), and the results of glycosidic bond types and ratios are shown in [Table 2](#). The structures of WGFP-N-a and AGFP-N-a₁ are rather similar. Me-Gal and Gal exist in the form of 1,6-Gal and 1,2,6-Gal, respectively. Man residues mainly exist in the form of T-Man, and a small amount of 1,2-Man was also detected. Moreover, there was some 1,3-Fuc observed in the fraction. Based on this, we propose that both WGFP-N-a and AGFP-N-a₁ are mainly composed of 1,6-Me-Galp with a small amount of 1,6-Galp to form the main chain, with some substitutions at O-2. T-Manp, 1,3-Fucp, and 1,2-Manp are present as side chains. The branching degrees of WGFP-N-a and AGFP-N-a₁ are 66.6% and 66.2%, respectively.

In WGFP-A-a, Glc is mostly present as 1,6-Glc with additional contributions from 1,3-Glc, 1,3,6-Glc, 1,4-Glc, and T-Glc. The branching degree was found to be 25.2%. In addition to Glc, Man was present in the form of T-Man. We propose that WGFP-A-a contains a branched 1,6-glucan linked with T-Manp

and T-Glcp at the O-3 position, whereas a small amount of 1,3-linked Glc may be present in either the side chains or main chain. In AGFP-A-b and AGFP-A-c, there are differences in the amount of Glc, which can exceed 90%. Glc mostly exists in the form of 1,6-linked. Additionally, Glc is also present in 1,3-, T-, and 1,4-linkages with degrees of branching of 42.3% and 37.6%. We suggest that AGFP-A-b and AGFP-A-c constitute a branched 1,6-glucan containing T-Glcp as side chains, whereas a small amount of 1,3-linked Glc is present in side chains or in the main chain ([Table 3](#)).

3.5.2 NMR spectra

^{13}C -NMR spectra of WGFP-N-a and AGFP-N-a₁ are shown in [Figure 3A](#), with chemical shift assignments presented in [Table 4](#). Anomeric carbon signals of α -T-Manp in WGFP-N-a and AGFP-N-a₁ were observed at 101.41 ppm and 101.42 ppm, while those of α -1,3-L-Fucp were detected at 101.27 and 101.42 ppm, respectively. In addition, anomeric carbon signals of α -1,6-Me-D-Galp, α -1,6-D-Galp, and α -1,2,6-D-Galp of WGFP-N-a appeared at 98.48, 99.30, and 99.51 ppm, while those of AGFP-N-a₁ were found at 98.93, 99.29, and 99.49 ppm. In WGFP-N-a and AGFP-N-a₁, signals from O-CH₃ were observed at 55.58 ppm, whereas the presence of two

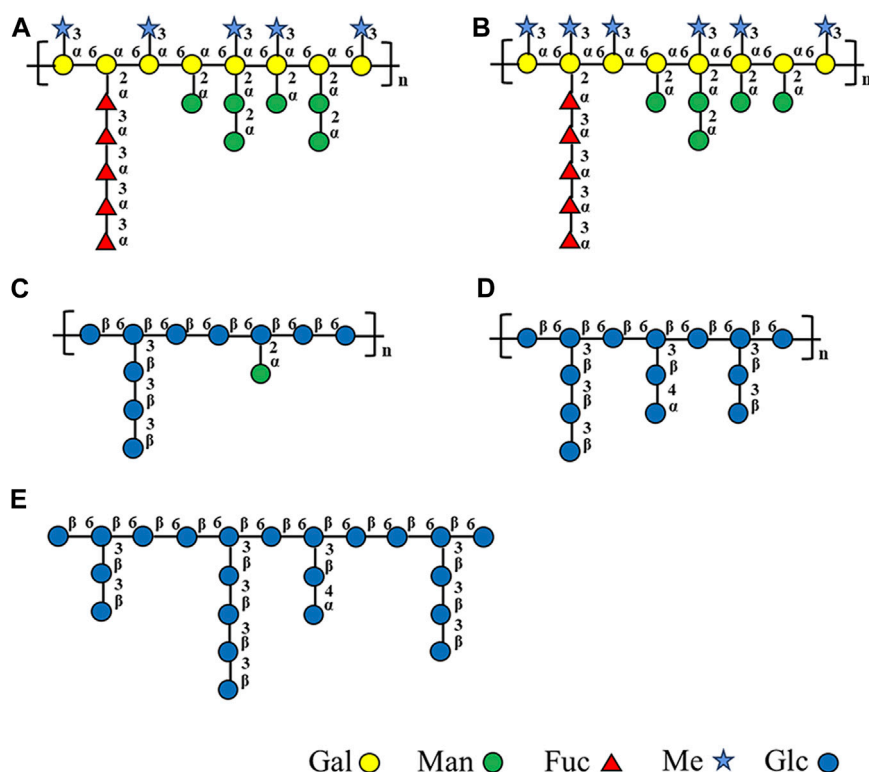


FIGURE 4

Structural models of (A) WGFP-N-a, (B) AGFP-N-a₁, (C) WGFP-A-a, (D) AGFP-A-b, and (E) AGFP-A-c.

signals near 77.90 ppm suggested that O-CH₃ was connected to the O-3 position of Gal. The existence of Me-Gal was confirmed, which is consistent with the monosaccharide composition detected by HPLC. Taken together with methylation results, we propose that WGFP-N-a and AGFP-N-a₁ primarily consist of α -1,6-D-Me-Galp as their main chains with a small amount of α -1,6-D-Galp branched at the O-2 position. α -1,3-L-Fucp and α -T-Manp are likely present at the side chains. Therefore, these polysaccharides can be called fucomannogalactan.

¹³C-NMR spectra of WGFP-A-a, AGFP-A-b, and AGFP-A-c are shown in Figure 3B, and their chemical shifts are provided in Table 4. In WGFP-A-a, AGFP-A-b, and AGFP-A-c, anomeric carbon signals from β -1,6-D-Glcp are observed at 101.85, 101.94, and 101.94 ppm, respectively. Anomeric carbon signals from β -1,3,6-D-Glcp appeared at 101.47 ppm, 101.69, and 101.52 ppm, whereas those from α -1,4-D-Glcp are found at 99.61, 99.67, and 99.56 ppm, respectively. The structures of these three polysaccharides are similar and are consistent with our methylation results. We concluded that WGFP-A-a, AGFP-A-b, and AGFP-A-c are composed of β -1,6-D-Glcp as the main chain that is substituted at O-3 position. β -1,3-D-Glcp may exist in side chains or in the main chain.

¹H-NMR also showed the same results similar to the ¹³C-NMR spectra, which further confirmed the structure of polysaccharides. More detailed analysis of ¹H-NMR spectra of WGFP-N-a, AGFP-N-a₁, WGFP-A-a, AGFP-A-b, and AGFP-A-c is shown in the Supplementary Material (Supplementary Results; Supplementary Figure S9; Supplementary Table S2).

Based on monosaccharide composition, methylation, FT-IR, and NMR, Figure 4 illustrates structural models of the homogeneous fractions of these five polysaccharides.

4 Discussion

Grifola frondosa is a valuable, medicinal fungus, with a rich nutritional value. Polysaccharides are one of the most bioactive substances derived from *G. frondosa* (He et al., 2017; Wu et al., 2021), yet this fungus is limited in nature and difficult to cultivate. This limits the amount of fruiting bodies that can be obtained to process large quantities of its polysaccharides. However, the use of submerged cultures of this fungus offers a promising alternative as it is rapid, cost-effective, easy to control, and free from heavy metal contamination. Here, *G. frondosa* mycelium-derived polysaccharides were extracted by alkylation, acidification, or simply by using water. Iino et al. (1985) were the first to extract Grifolan from *G. frondosa* mycelium under cold alkaline conditions. Adachi et al. (1994) extracted β -1,3-D-glucan from *G. frondosa* mycelium using 0.5% citrate buffer. Zhao et al. (2016) extracted polysaccharide GRP1 using hot water. It has been reported that different extraction methods resulted in different Mw compositions and structures of polysaccharides (Ren et al., 2023). However, there is no report on the extraction of polysaccharides from mycelium residues by alkaline solution after hot water extraction of polysaccharides from *G. frondosa* mycelium. In the present study, we used this

approach for the first time to thoroughly extract *G. frondosa* mycelium-derived polysaccharides.

Previous reports showed that *G. frondosa* mycelium-derived polysaccharides are mainly composed of α -1,3-Glcp, α -1,6-Glcp, and α -1,4-Galp as the main chains. Similar structured polysaccharides (termed WGFP-A-a, AGFP-A-b, and AGFP-A-c) were obtained in this study. These are composed of β -1,6-D-Glcp and β -1,3-D-Glcp, with T-D-Glcp likely present in the side chains to form β -1,6-glucan. The molecular weights of these three polysaccharides ranged from 4.1 kDa to 19.9 kDa, similar to GFPS1b with a molecular weight of 21 kDa extracted by Cui et al. (2007) and smaller than GRP1 (40.5 kDa) extracted by Zhao et al. (2016).

Zhang et al. (2023) extracted an acidic polysaccharide GFP-A from the fruiting bodies of *G. frondosa*. The molecular weight of GFP-A was reported to be ~1,100 kDa, making it much larger than the mycelium-derived polysaccharide identified in this study. GFP-A is mainly composed of Glc with α -type glycosidic linkages, whereas WGFP-A-a, AGFP-A-b, and AGFP-A-c are mainly composed of β -Glcp. Glucan GFPA (~5,570 kDa) was extracted from the fruiting bodies of *G. frondosa* (Li et al., 2022) and has an α -1,4-D-Glcp backbone with β -1,4,6-D-Glcp and T- β -Glcp as side chains. The mycelium glucans found in this study have lower molecular weights (4.1 kDa to ~19.9 kDa) and are composed of a β -1,6-D-Glcp backbone with branched side chains of β -1,3-D-Glcp and T-D-Glcp residues at O-3 of the Glcp residues.

It is noteworthy that two novel polysaccharides WGFP-N-a and AGFP-N-a₁ are reported here. These are primarily composed of α -1,6-D-Me-Galp and α -1,6-D-Galp as main chains. WGFP-N-a and AGFP-N-a₁ are fucomannogalactan because they contain Fuc and Man as side chains. This structure has been reported in *G. frondosa* fruiting bodies but was not yet found in *G. frondosa* mycelia (Wang et al., 2014). Our present research provides the basis for extracting fucomannogalactan and β -1,6-glucans from *G. frondosa* mycelium.

5 Conclusion

In this study, we have isolated polysaccharides from *G. frondosa* mycelium and analyzed five homogeneous fractions that are divided into two types of structures: fucomannogalactan and β -1,6-glucans. WGFP-N-a and AGFP-N-a₁ mainly consist of α -1,6-D-Me-Galp, with a small amount of α -1,6-D-Galp as the main chain and with α -1,3-L-Fucp, α -1,2-D-Manp, and α -T-D-Manp as side chains branched at the O-2 position of Me-Gal and Gal, to form fucomannogalactan. WGFP-A-a, AGFP-A-b, and AGFP-A-c are mainly composed of β -1,6-D-Glcp branched at O-3 of Glc. β -1,3-D-Glcp and T-D-Glcp may exist as side chains to form β -1,6-glucan. To the best of our knowledge, this is the first study that has characterized polysaccharides derived from *G. frondosa* mycelium.

References

Adachi, Y., Okazaki M Fau - Ohno, N., Ohno N Fau - Yadomae, T., and Yadomae, T. (1994). Enhancement of cytokine production by macrophages stimulated with (1,3,6)- β -D-Glucan, grifolan (GRN), isolated from *Grifola frondosa*. *Biol. Pharm. Bull.* 17 (12), 1554–1560. doi:10.1248/bpb.17.1554

Data availability statement

The original contributions presented in the study are included in the article/Supplementary Material; further inquiries can be directed to the corresponding author.

Author contributions

HC and YZ designed and conceived the study. JGE, GW, and JGU performed the experiments. XH and YQ analyzed the data. YZ, HC, and JGE wrote and edited the manuscript. All authors contributed to the article and approved the submitted version.

Funding

This work was supported by the National Natural Science Foundation of China (no. 22007011), Jilin Provincial Science and Technology Department Program (no. YDZJ202101ZYTS088), and Jilin Province Development and Reform Commission (no. 2022C042-8).

Acknowledgments

The authors thank Dr. Kevin H. Mayo for editing this manuscript.

Conflict of interest

The authors declare that the research was conducted in the absence of any commercial or financial relationships that could be construed as a potential conflict of interest.

Publisher's note

All claims expressed in this article are solely those of the authors and do not necessarily represent those of their affiliated organizations, or those of the publisher, the editors, and the reviewers. Any product that may be evaluated in this article, or claim that may be made by its manufacturer, is not guaranteed or endorsed by the publisher.

Supplementary material

The Supplementary Material for this article can be found online at: <https://www.frontiersin.org/articles/10.3389/fchem.2023.1227288/full#supplementary-material>

Cui, F. J., Tao, W. Y., Xu, Z. H., Guo, W. J., Xu, H. Y., Ao, Z. H., et al. (2007). Structural analysis of anti-tumor heteropolysaccharide GFPS1b from the cultured mycelia of *Grifola frondosa* GF9801. *Bioresour. Technol.* 98, 395–401. doi:10.1016/j.biortech.2005.12.015

- Dubois, M., Gilles, K. A., Hamilton, J. K., Rebers, P. A., and Smith, F. (1956). Colorimetric method for determination of sugars and related substances. *Anal. Chem.* 28, 350–356. doi:10.1021/ac60111a017
- Filiseti-Cozzi, T. M. C. C., and Carpita, N. C. (1991). Measurement of uronic acids without interference from neutral sugars. *Anal. Biochem.* 197, 157–162. doi:10.1016/0003-2697(91)90372-z
- He, X., Wang, X., Fang, J., Chang, Y., Ning, N., Guo, H., et al. (2017). Polysaccharides in *Grifola frondosa* mushroom and their health promoting properties: A review. *Int. J. Biol. Macromol.* 101, 910–921. doi:10.1016/j.ijbiomac.2017.03.177
- Iino, K., Ohno, N., Suzuki, I., Miyazaki, T., Yadomae, T., Oikawa, S., et al. (1985). Structural characterisation of a neutral antitumour β -D-glucan extracted with hot sodium hydroxide from cultured fruit bodies of *Grifola frondosa*. *Carbohydr. Res.* 141, 111–119. doi:10.1016/s0008-6215(00)90760-2
- Li, Q., Zhu, L., Qi, X., Zhou, T., Li, Y., Cai, M., et al. (2022). Immunostimulatory and antioxidant activities of the selenized polysaccharide from edible *Grifola frondosa*. *Food. Sci. Nutr.* 10, 1289–1298. doi:10.1002/fsn3.2764
- Li, S., and Shah, N. P. (2014). Antioxidant and antibacterial activities of sulfated polysaccharides from *Pleurotus eryngii* and *Streptococcus thermophilus* ASCC 1275. *Food. Chem.* 165, 262–270. doi:10.1016/j.foodchem.2014.05.110
- Liu, J., Zhang, C., Wang, Y., Yu, H., Liu, H., Wang, L., et al. (2011). Structural elucidation of a heteroglycan from the fruiting bodies of *Agaricus blazei* Murill. *Int. J. Biol. Macromol.* 49, 716–720. doi:10.1016/j.ijbiomac.2011.07.003
- Needs, P. W., and Selvendran, R. R. (1993). Avoiding oxidative degradation during sodium hydroxide/methyl iodide-mediated carbohydrate methylation in dimethyl sulfoxide. *Carbohydr. Res.* 245, 1–10. doi:10.1016/0008-6215(93)80055-j
- Nie, X., Shi, B., Ding, Y., and Tao, W. (2006). Preparation of a chemically sulfated polysaccharide derived from *Grifola frondosa* and its potential biological activities. *Int. J. Biol. Macromol.* 39, 228–233. doi:10.1016/j.ijbiomac.2006.03.030
- Ning, X., Liu, Y., Jia, M., Wang, Q., Sun, Z., Ji, L., et al. (2021). Pectic polysaccharides from *Radix Sophorae Tonkinensis* exhibit significant antioxidant effects. *Carbohydr. Polym.* 262, 117925. doi:10.1016/j.carbpol.2021.117925
- Ren, B., Wei, S., and Huang, H. (2023). Recent advances in *Grifola frondosa* polysaccharides: Production, properties, and bioactivities. *Curr. Opin. Food Sci.* 49, 100946. doi:10.1016/j.cofs.2022.100946
- Santos Arteiro, J. M., Rosário Martins, M., Salvador, C., Fátima Candeias, M., Karmali, A., and Teresa Caldeira, A. (2012). Protein-polysaccharides of *Trametes versicolor*: Production and biological activities. *Med. Chem. Res.* 21, 937–943. doi:10.1007/s00044-011-9604-6
- Sedmak Jj Fau - Grossberg, S. E., and Grossberg, S. E. (1977). A rapid, sensitive, and versatile assay for protein using Coomassie brilliant blue G250. *Anal. Biochem.* doi:10.1016/0003-2697(77)90428-6
- Švagelj, M., Berović, M., Boh, B., Menard, A., Simčič, S., and Wraber, B. (2008). Solid-state cultivation of *Grifola frondosa* (dicks: Fr) S.F. Gray biomass and immunostimulatory effects of fungal intra- and extracellular β -polysaccharides. *N. Biotechnol.* 25, 150–156. doi:10.1016/j.nbt.2008.08.006
- Wang, J., Li, Y., Tian, Y., Xu, X., Ji, X., Cao, X., et al. (2010). A novel triple-wavelength colorimetric method for measuring amylose and amylopectin contents. *Starke.* 62, 508–516. doi:10.1002/star.200900242
- Wang, J., Zhou, Y., Yu, Y., Wang, Y., Xue, D., Zhou, Y., et al. (2023). A ginseng-derived rhamnogalacturonan I (RG-I) pectin promotes longevity via TOR signalling in *Caenorhabditis elegans*. *Carbohydr. Polym.* 312, 120818. doi:10.1016/j.carbpol.2023.120818
- Wang, Y., Shen, X., Liao, W., Fang, J., Chen, X., Dong, Q., et al. (2014). A heteropolysaccharide, 1-fuco-d-manno-1,6- α -d-galactan extracted from *Grifola frondosa* and antiangiogenic activity of its sulfated derivative. *Carbohydr. Polym.* 101, 631–641. doi:10.1016/j.carbpol.2013.09.085
- Wu, J.-Y., Siu, K.-C., and Geng, P. (2021). Bioactive ingredients and medicinal values of *Grifola frondosa* (maitake). *Foods* 10, 95. doi:10.3390/foods10010095
- Yan, J., Zhu, L., Qu, Y., Qu, X., Mu, M., Zhang, M., et al. (2019). Analyses of active antioxidant polysaccharides from four edible mushrooms. *Int. J. Biol. Macromol.* 123, 945–956. doi:10.1016/j.ijbiomac.2018.11.079
- Zhang, G., Yin, Q., Han, T., Zhao, Y., Su, J., Li, M., et al. (2015). Purification and antioxidant effect of novel fungal polysaccharides from the stroma of *Cordyceps kyushuensis*. *Ind. Crops. Prod.* 69, 485–491. doi:10.1016/j.indcrop.2015.03.006
- Zhang, H., Dong, X., Ji, H., Yu, J., and Liu, A. (2023). Preparation and structural characterization of acid-extracted polysaccharide from *Grifola frondosa* and antitumor activity on S180 tumor-bearing mice. *Int. J. Biol. Macromol.* 234, 123302. doi:10.1016/j.ijbiomac.2023.123302
- Zhao, C., Gao, L., Wang, C., Liu, B., Jin, Y., and Xing, Z. (2016). Structural characterization and antiviral activity of a novel heteropolysaccharide isolated from *Grifola frondosa* against enterovirus 71. *Carbohydr. Polym.* 144, 382–389. doi:10.1016/j.carbpol.2015.12.005
- Zhuang, C., Mizuno, T., Ito, H., Shimura, K., Sumiya, T., and Kawade, M. (1994). Fractionation and antitumor activity of polysaccharides from *Grifola frondosa* mycelium. *Biosci. Biotechnol. Biochem.* 58 (51), 185–188. doi:10.1271/bbb.58.185



OPEN ACCESS

EDITED BY

Dongdong Zeng,
Shanghai University of Medicine and
Health Sciences, China

REVIEWED BY

Saumya Nigam,
Michigan State University, United States
Bing Chen,
Fujian Medical University, China

*CORRESPONDENCE

Yao Luo,
✉ luoyao@scu.edu.cn
Zhiping Deng,
✉ dengzp1016@163.com

[†]These authors have contributed equally
to this work and share first authorship

RECEIVED 03 July 2023

ACCEPTED 29 August 2023

PUBLISHED 07 September 2023

CITATION

Li W, Li M, Huang Q, He X, Shen C, Hou X,
Xue F, Deng Z and Luo Y (2023),
Advancement of regulating cellular
signaling pathways in NSCLC target
therapy via nanodrug.
Front. Chem. 11:1251986.
doi: 10.3389/fchem.2023.1251986

COPYRIGHT

© 2023 Li, Li, Huang, He, Shen, Hou, Xue,
Deng and Luo. This is an open-access
article distributed under the terms of the
[Creative Commons Attribution License](#)
(CC BY). The use, distribution or
reproduction in other forums is
permitted, provided the original author(s)
and the copyright owner(s) are credited
and that the original publication in this
journal is cited, in accordance with
accepted academic practice. No use,
distribution or reproduction is permitted
which does not comply with these terms.

Advancement of regulating cellular signaling pathways in NSCLC target therapy via nanodrug

Wenqiang Li^{1†}, Mei Li^{2†}, Qian Huang³, Xiaoyu He³, Chen Shen²,
Xiaoming Hou², Fulai Xue², Zhiping Deng^{1*} and Yao Luo^{1,2*}

¹Zigong First People's Hospital, Zigong, Sichuan, China, ²West China Hospital, Sichuan University, Chengdu, Sichuan, China, ³Sichuan North Medical College, Nanchong, Sichuan, China

Lung cancer (LC) is one of the leading causes of high cancer-associated mortality worldwide. Non-small cell lung cancer (NSCLC) is the most common type of LC. The mechanisms of NSCLC evolution involve the alterations of multiple complex signaling pathways. Even with advances in biological understanding, early diagnosis, therapy, and mechanisms of drug resistance, many dilemmas still need to face in NSCLC treatments. However, many efforts have been made to explore the pathological changes of tumor cells based on specific molecular signals for drug therapy and targeted delivery. Nano-delivery has great potential in the diagnosis and treatment of tumors. In recent years, many studies have focused on different combinations of drugs and nanoparticles (NPs) to constitute nano-based drug delivery systems (NDDS), which deliver drugs regulating specific molecular signaling pathways in tumor cells, and most of them have positive implications. This review summarized the recent advances of therapeutic targets discovered in signaling pathways in NSCLC as well as the related NDDS, and presented the future prospects and challenges.

KEYWORDS

nanodrug, signaling pathways, non-small cell lung cancer, drug resistance, targeted therapy

1 Introduction

Cancer is the main cause of death worldwide, and lung cancer (LC) is the disease with the highest mortality rate (Ferlay et al., 2018; Ferlay et al., 2019). According to histology, LC is generally divided into two categories: small cell lung cancer (SCLC) and non-small cell lung cancer (NSCLC). Here, NSCLC is the most common type of LC (85%), with high incidence rate and high mortality (Ferlay et al., 2019). Moreover, the average survival rate of patients is 10%–20% (Ferlay et al., 2018). Nowadays, targeted drugs for gene mutations and immune loci have become the preferred option for NSCLC patients, but the current clinical route of drug delivery still has major drawbacks, such as low drug utilization and significant side effects, which reduce the survival benefits for clinical patients (Hirsch et al., 2017; de Scordilli et al., 2022). In addition, there are many problems inherent in the traditional route of drug delivery. The bioavailability of oral and intravenous dosing is low, and these systemic dosing regimens can cause a variety of toxic reactions in the body, including severe vomiting, seizures, vasculitis, and even death, clearly doing more harm than good in low-risk stage IA NSCLC (NSCLC Meta-analysis Collaborative Group, 2014; Argilés et al., 2023). Therefore,

developing new therapeutic interventions which focus on more microscopic and detailed levels like the signaling pathways of disease onset to overcome these limitations is of great significance. Scientists have done a great deal of work in exploring the evolution of tumor cells based on specific molecular signals for drug treatment and targeted delivery. Targeted therapy has become a hot term in tumor treatment with a broad meaning that includes not only the targeting of drugs but also the precise delivery of drugs.

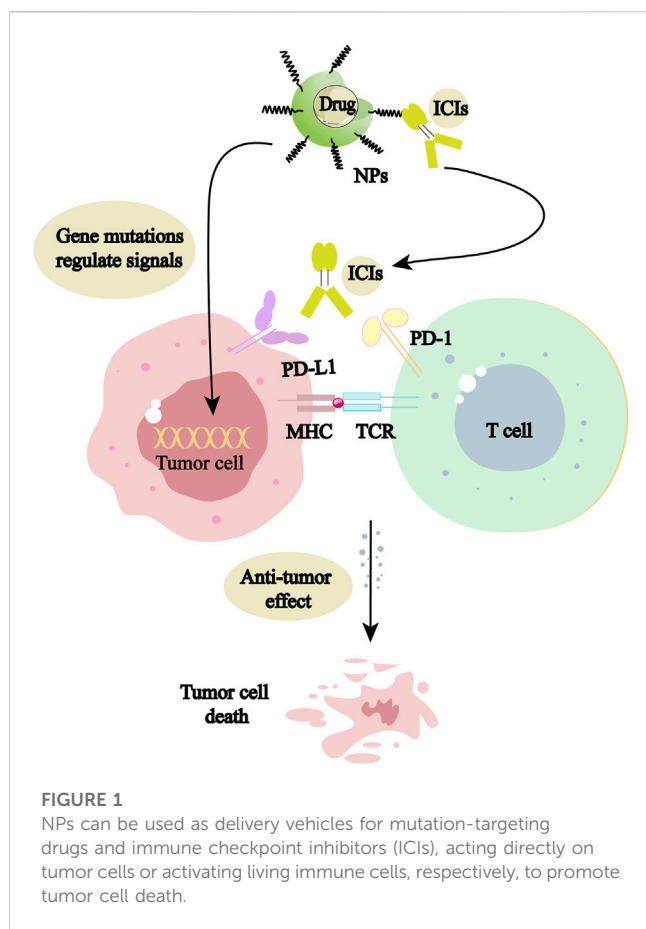
For the proliferation and invasion process of LC cells, abnormal cell signaling pathways, which exist complex regulatory mechanisms, are closely related to genetic mutations. Mutations of RAS gene are common in NSCLC, and most of them are KRAS mutations (Punekar et al., 2022). Mitogen-activated protein kinase (MAPK) is one of the major signals stimulated by RAS (Ferlay et al., 2018; Ferlay et al., 2019). The RAS rapid fibrosarcoma (RAF)-MAPK-extracellular signal-regulated kinase (ERK) pathway and phosphatidylinositol 3-kinase (PI3K)-protein kinase B (AKT) pathway control cell survival and proliferation in NSCLC (Ferlay et al., 2019). *Epidermal growth factor receptor (EGFR)* gene mutations are important in the development of NSCLC. It can increase EGFR expression when mutations in kinase, resulting in the functional upregulation of the EGFR pathway and uncontrolled proliferation of mutant tumor cells (Passaro et al., 2021). In malignant cells, vascular endothelial growth factor (VEGF) and VEGF receptor (VEGFR) promote cell proliferation, survival, and angiogenesis in, and inhibition of VEGF and VEGFR retards tumor growth (Niu et al., 2022). Also important in cell differentiation, proliferation, and cancer progression are the pathways NTRK/ROS1 and JAK-STAT (Lai and Johnson, 2010; Song et al., 2023). In summary, molecular signaling has a strong connection with tumor progression, which is also can modulate drug resistance. To fully understand the functions of these pathways, it is necessary to examine their upstream and downstream node. As evidence accumulates, strategies that target these pathways may hold promise for NSCLC treatment. However, the complexity of signaling makes it difficult to understand the complete regulatory pathway of a particular signaling target in tumor cells. At the same time, all mutated genes may become therapeutic targets, while there are still many unknown mutated genes, so that continuing in-depth screening of mutated genes has a positive effect on drug development.

Accompanied by the discovery of more and more signaling pathways, a great victory has been achieved in the precise molecular therapy of NSCLC, which established in regulating signaling pathways to overcome the drug resistance. For example, activation of NF- κ B/Bcl-2/Snail pathway increases chemotherapy resistance in NSCLC, and thus targeted drug delivery of this pathway would behave with good specificity and pharmacokinetic characteristics which could inhibit tumor cell proliferation (McCubrey et al., 2008; Chen et al., 2015; Asati et al., 2016). Targeted drugs can reduce resistance to chemotherapy drugs, but are prone to cause new genetic mutations during treatment, leading to resistance to targeted drugs (Cabanos and Hata, 2021). Targeting EGFR tyrosine kinase inhibitors (EGFR-TKIs) for NSCLC promotes the emergence of acquired drug resistance, a major barrier to EGFR-targeted therapy (Johnson et al., 2022). EGFR resistance mechanisms are mainly classified as dependent resistance and

non-dependent resistance. Dependent resistance mechanisms include T790M mutation, C797 mutation and G796R mutation, while non-dependent resistance mechanisms are divided into mesenchymal-epithelial transition (MET) factor amplification, (human epidermal growth factor receptor 2) HER2 amplification and gene fusion (Passaro et al., 2021; Nie et al., 2022). Apart from that, the PI3K/AKT/mTOR signaling pathway can activate EGFR and mutate among various malignant tumors, including leukemia and NSCLC (Yan et al., 2021; Chen et al., 2022). Studies have confirmed that the knockdown of *miR-126*, *miR-203*, and *miR-34a* genes can regulate drug resistance through PI3K/AKT signaling pathway (Zhong et al., 2010; Garofalo et al., 2011). It has to be acknowledged that some unknown signaling pathways may have direct or indirect effects of the drug resistance.

In addition to the drug resistance of cancer cells, the positive and negative role of the signaling molecules in the immune system in drug therapy is also being paid attention to. Immune-related regulators play key roles in autoimmunity, self-tolerance, and the malignant microenvironment, such as the co-suppressor receptor programmed death 1 (PD-1) and its ligand (PD-L1) (Reck et al., 2022). Furthermore, there is substantial evidence that cancer cells may use these immunomodulatory factors to evade the immune response (Muenst et al., 2015). PD-1/PD-L1 pathway immunologic drugs have been widely used in the treatment of NSCLC (Suresh et al., 2018; Reck et al., 2022). At the same time, immunotherapeutic drugs, when applied to the human body, are distributed to various tissues and organs throughout the body and cannot achieve precise focal targeting, thus causing a series of immune-related adverse reactions, which greatly hinders their clinical application potential (Jing et al., 2021; Zhou et al., 2023). To overcome these problems and improve patient outcomes, nanoparticles (NPs) with penetrating and slow release properties have been proposed to successfully treat drug-resistant cancer cells of NSCLC *in vitro* or *in vivo* models (Palazzolo et al., 2018; Patra et al., 2018; Wang et al., 2018). The results of these studies have stimulated the interest of researchers in nanomaterials, and more research is still in progress.

The emergence of drug resistance and apparent toxicity is currently an important reason for the unsustainable treatment of NSCLC patients. NPs are endowed with special functions due to their microstructure, which bring more hope to address these problems. In particular, the modified NPs have the advantage of targeting and carrying multiple drugs. Nanotechnology requires multidisciplinary cooperation, involving various types of NPs as well as new nanodevices and applications of nanomaterials in different fields (Molina et al., 2008; Sung et al., 2021). NPs have a wide surface area and can be modified by bonding or encapsulation (Rosell et al., 2020). As carriers of antineoplastic drugs, NPs have greatly improved efficacy, safety, stability and pharmacokinetics of drugs (Naylor et al., 2016; Stater et al., 2021; Haider et al., 2022; Tian et al., 2022; Detappe et al., 2023; Fang et al., 2023; Nguyen et al., 2023). The researches on tumor targeted therapy via NPs focus on the size and the impact of encapsulation techniques on the bioavailability of drugs *in vivo* (Raju et al., 2021; Ezhilarasan et al., 2022; Huang et al., 2022). Biocompatible nanocarriers can be tailored to tumor characteristics to improve their physical and chemical properties, permeability, and metabolism, such as the smaller structures can penetrate tissue barriers more easily (Seeta Rama Raju et al., 2015). Furthermore, researchers can limit the uptake of drugs in healthy tissues by wrapping appropriate NPs to enhance



drug targeting, thereby shield normal cells from the cytotoxic effects of anticancer drugs, and reduce adverse drug reaction (Kalyane et al., 2019; Haider et al., 2020; Duan et al., 2022; Haider et al., 2022).

Nano-based drug delivery systems (NDDS) formed by NPs have become a hot issue for research. NDDS has a wide range of promising applications in NSCLC treatment and has the potential to save patients' lives. Targeted therapy aiming at mutated genes and immune targets is of epoch-making significance in NSCLC treatment. So far, the abundant studies on signaling targets based on NDDS have performed well in the delivery of targeted and immune drugs, and the mechanism is shown in Figure 1. NDDS is a new therapeutic concept, which is theoretically well synergistic with the drug itself, providing benefits to patients, and makes the goal of long-term coexistence with malignancy the technical and theoretical basis. It will break through the limitations of traditional treatments and promotes NSCLC patients to live longer.

In this paper, we summarize the results achieved in recent years regarding the discovery of therapeutic targets in signaling pathways of NSCLC and related NDDS, and present the future prospects and challenges.

2 Strengths of nanodrug in NSCLC treatment

The pathogenesis of NSCLC is mediated by multiple intercellular molecular signaling pathways, and the targeted therapeutically relevant signaling targets are also receiving more attention. Gene-targeted

therapy is widely used in the treatment of NSCLC, where EGFR classical mutations and KRAS G12C/D/V occur more frequently, while ROS1 rearrangements, RET rearrangements, NTRK fusions, MET14 exon skipping mutation, BRAF V600E mutations are relatively infrequent. They can be classified as "rare" mutations, but all of them have corresponding targeted drugs and should not be ignored (Harada et al., 2023). However, the physicochemical properties of these targeted drugs are always poor. Besides, the complex multi-order biological barriers in the body often lead to treatment that does not achieve the desired efficacy and also brings certain side effects on the organism (Boolell et al., 2015). More seriously, some side effects can even hasten the patient's death.

In the immune system, T cell-mediated cellular immunity is the "main legion" for tumor eradication, where T cell activation is required to exert anti-tumor effects (Tanaka and Sakaguchi, 2017; Liu et al., 2020). But some "cunning" tumor cells can bypass immune surveillance and grow uncontrollably, thus endangering the health of the body. These tumor cells manipulate the immune cells by using the characteristics of immune checkpoints, and express PD-L1 protein on the surface, which causes T cells to lose the activity of killing tumor cells, thus realizing the immune escape (Jiang et al., 2019; Kim et al., 2019; Liu Z. et al., 2021). Immune checkpoint inhibitors (ICIs) can effectively overcome tumor immune evasion, and antagonists targeting immune checkpoint ligands can effectively activate tumor-specific T cells (Zhang et al., 2020; Liu et al., 2022). But traditional immune checkpoint blockade therapies have disadvantages, such as low immunogenicity, weak targeting, easy drug resistance, and accidental cytokine storms (Vincent et al., 2022). NDDS can effectively enhance ICIs' blocking efficiency. At the same time, it can achieve synergistic tumor treatment in combination with other therapeutic tools (Vincent et al., 2022).

NDDS can control the distribution and metabolic behavior at different levels of tissues, cells, and organelles by improving the stability and physicochemical properties of drugs, as well as by overcoming multi-level biological barriers (Chen et al., 2014; Wang J. et al., 2021). Similarly, it has significant implications for the regulation of drug resistance (Vincent et al., 2022). Based on the anatomical and pathophysiological differences between normal and tumor cells, the NPs have strong enhanced permeability and retention (EPR) effect, as shown in Figure 2 (Ikeda-Imafuku et al., 2022; Wu et al., 2023). Nanocarriers can be divided into natural polymer and synthetic polymer materials, most of which have excellent biocompatibility, stability, safety, non-toxicity and modifiability, mainly including virus-like particles, poly lactic glycolic acid (PLGA), liposomes, dendrimers, metal organic framework compounds, as shown in Figure 3 (Guo and Jiang, 2020; Ji et al., 2023). Meanwhile, many biomaterials are inherently targeted, so that nanomaterial delivery systems are always partnered with nucleic acid drugs (Zhang et al., 2013). Due to the emergence of drug resistance, targeting related signaling pathways based on nanomaterials has become a new direction to treat NSCLC in recent years, as shown in Table 1.

3 Nanodrug targeted epidermal growth factor receptor in NSCLC

The EGFR is one of the most common mutation driver oncogenes. Among Asian female nonsmokers with NSCLC, the

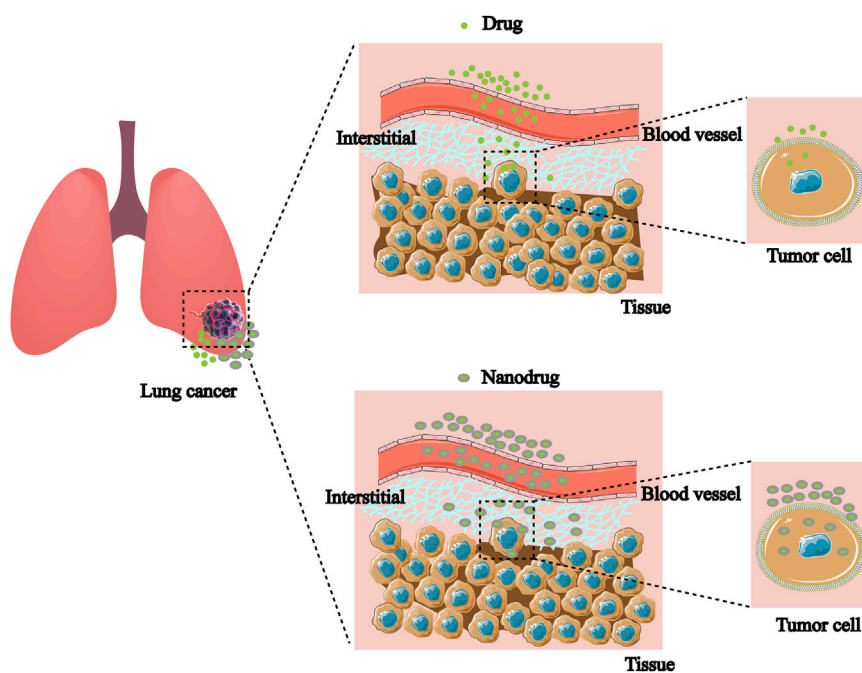


FIGURE 2

Nanodrugs are more likely to break through cellular and tissue barriers to accumulate in target cells than non-nanodrugs.

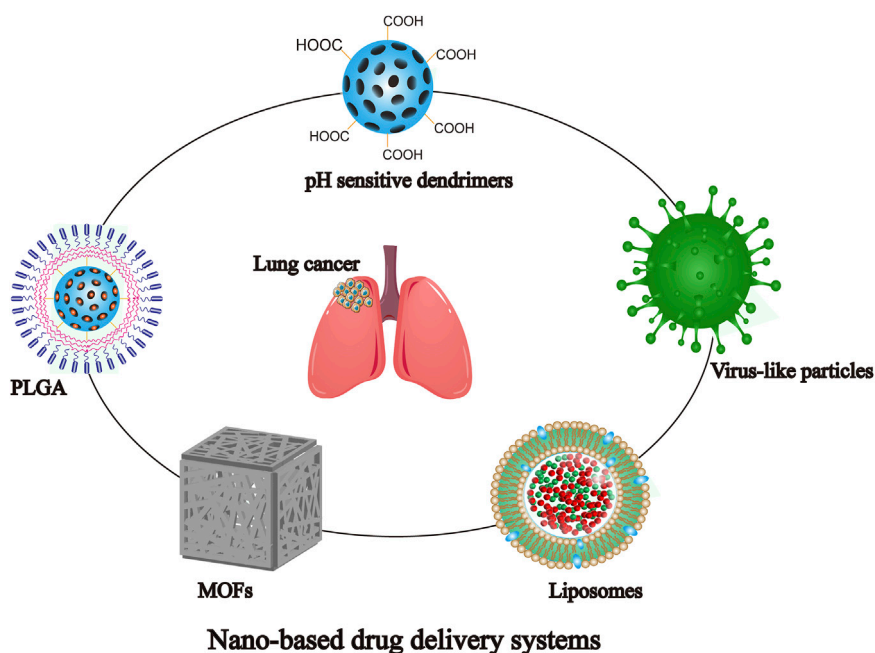


FIGURE 3

Different types of nanomaterials commonly used for NDDS.

mutation rate was as high as 59.4%, with exon 19 deletions and L858R point mutations located in the receptor tyrosine kinase (RTK) domain accounting for 90% of mutations (Li et al., 2016; Bilek et al., 2019). The stimulation of MAPK and PI3K is highly associated with increased cancer risk, and the downstream signaling

pathways are associated with cell proliferation, metastasis, and drug resistance (Villaruz et al., 2013; Ciuffreda et al., 2014). Drugs targeting the EGFR have been developed rapidly, such as gefitinib, afatinib, and osimertinib (Yang et al., 2020; Lai-Kwon et al., 2021; Li et al., 2022; Liam et al., 2023). Despite the significant

TABLE 1 Examples of targeted signaling pathways based on nanomaterials for the treatment of NSCLC.

Nanocarriers	Drugs	Mechanisms	Results	Ref
Magnetic lentivirus	RNAi	Microscale RNAi was achieved by EGFR silencing	Leading to EGFR-TKIs resistant H19750 cell apoptosis	Arrieta et al. (2012)
HA-6-(2-nitroimidazole) hexylamine-LOX	AAV2	Activation and release of lactate lead to specific delivery in tumor for virotherapy	Promoting cell apoptosis and inhibiting proliferation	Tseng et al. (2018)
PEGHis0.5-PEG-Glu0.5	—	Activating the p53 mediated apoptosis signaling pathway and inducing the production of light induced ROS in NSCLC cells	Suppressing cell growth and resensitizing cancer cells	Li et al. (2016)
RNA NPs	siRNA	Silencing anti-apoptotic factor Survivin	Chemotherapy sensitization and tumor regression	Li et al. (2021)
FITC-AEYLR	—	FITC-AEYLR has high EGFR targeting ability, enhancing cell specific uptake <i>in vitro</i>	—	Han et al. (2013)
apt-CL-E	erlotinib	Promoting the uptake of erlotinib in EGFR mutated cancer cells	Causing cell cycle arrest and apoptosis	Li et al. (2017)
PEG-PLA	CsA/Gef	CsA formed in NPs is inactivated through the STAT3/Bcl-2 signaling pathway	Sensitizing Gef resistant cells and drug-resistant tumors to Gef therapy	Han et al. (2018)
NP-DUAL	Gefitinib	Adjusting STAT3/miR-21/AKT/PTEN/HIF-1 α axis to restore MET	Sensitizing drug-resistant cells again	Upadhyay et al. (2021)
PVI	siRNA	Silencing VEGF in cancer cells	Inhibiting cell proliferation and metastasis	Kandasamy et al. (2020)
QDs	—	Collaborative PTT/PDT	Inhibiting NSCLC without significant toxicity	Kuo et al. (2018)
QDs	NIR	Promoting the production of reactive oxygen species by regulating the PI3K/AKT pathway	Triggering cell death	Liu et al. (2021b)
Carboxymethyl chitosan	siRNA	Resulting in a significant decrease in STAT3 expression	Increasing cell apoptosis rate and inhibiting proliferation	Chen et al. (2020)
LNPs	siRNA	Silencing STAT3 and HIF-1 α	Causing an increase in macrophage levels and increasing anti-tumor efficacy	Shobaki et al. (2020)
SLNs	RNAi	Downregulating STAT3	Sensitizing cancer cells resistant to cisplatin	Kotmakçı et al. (2017)
PLA	Erlotinib/fedratinib	Downregulating expression of p-EGFR, p-JAK2, p-STAT3, and Survivin in the JAK2/STAT3 signaling pathway	Reversing ELTN resistance and synergistic anti-cancer effect	Chen et al. (2018)
RBCm-OM/PLGA	OM	Reducing the expression level of Bcl-2, promoting the release of cell c in the cytoplasm, and activating Caspase-3	Reducing cancer cell proliferation <i>in vitro</i> , inducing apoptosis <i>in vivo</i> , and inhibiting tumor growth	Chen et al. (2020)
PVP-b-PCL	Tet	Up-regulating the expression of TIMP-3, Bcl-2 and Bcl-xl, down-regulating the expression of MMP2 and MMP9	Enhancing cell apoptosis, and inhibiting cell migration and invasion	Xu et al. (2014)
Cationic immunoliposo-me	Plasmid DNA	Downregulation of immunosuppressive molecules and addition of cytotoxic T cell activity	Restoring effective immune response to lung cancer cells	Kim et al. (2022)
Chlorin e6-encapsulated fluorinated dendrimer	CRISPR/Cas9	F-PC/pHCP under 660 nm laser activated the HSP70 promoter and enabled the specific expression of the Cas9 protein to disrupt the <i>PD-L1</i> gene, and prevent immune escape	Inducing immunogenic cell death of tumor cells, and inhibiting tumor growth	Zhao L. et al. (2022)
ZnPP@MSN	RGDyK	Integrin $\beta 3$ ($\beta 3$ -int) is strongly upregulated in NSCLC-SM. Its inhibitor RGDyK promotes PD-L1 ubiquitination	Reversing the immune escape of cancer cells	Zhou et al. (2022)
Nanodiamond-dox	Orubicin	Induction of PD-L1 as well as NF- κ B-dependent RAGE expression in tumor cells	Inhibiting tumor cell growth	Xu et al. (2021)

(Continued on following page)

TABLE 1 (Continued) Examples of targeted signaling pathways based on nanomaterials for the treatment of NSCLC.

Nanocarriers	Drugs	Mechanisms	Results	Ref
		via the RAGE/NF- κ B pathway enhances the role of HMGB1's		

Abbreviations: Ref.: references; EGFR: epidermal growth factor receptor; EGFR-TKIs: EGFR, tyrosine kinase inhibitors; HA: hexylamine acid; LOX: lactate oxidase; AAV2: adeno-associated virus serotype 2; PEG: polyethylene glycol; His: histidine; Glu: glutamic acid; ROS: reactive oxygen species; NSCLC: non-small cell lung cancer; NPs: nanoparticles; siRNA: small interfering RNA; FITC: fluorescein isothiocyanate; Apt-CL-E: Apt-Cs-anchored liposomal complexes; PLA: poly (D,L-lactic acid); CsA: cyclosporin A; Gef: Gefitinib; NP-DUAL: transferrin modified poly lactic glycolic acid thymidine nanoparticle combined with gefitinib; MET: mesenchymal-epithelial transition factor; PVI: poly (1-vinylimidazole); QDs: quantum dots; PTT: photothermal therapy; PDT: photodynamic therapy; NIR: Near-infrared; LNPs: lipid nanoparticles; SLNs: solid lipid nanoparticles; ELTN: erlotinib; RBCm-OM/PLGA: combination of polylactic acid glycolic acid (PLGA) and red blood cell membrane (RBCm) to wrap obatok mesylate (OM); PVP-b-PCL: poly (N-vinylpyrrolidone) block poly (ϵ -Caprolactone); Tet: tetrandrine; CRISPR: clustered regularly interspaced short palindromic repeats; PD-L1: programmed cell death 1 ligand 1; ZnPP: zinc protoporphyrin; MSN: mesoporous silica nanoparticles; RAGE: receptor for advanced glycation endproducts; TAMs: tumor-associated macrophages.

effect of initial treatment, patients often develop acquired resistance after a period of time, by mechanisms including dependence or non-dependence on the EGFR pathway (Taniguchi et al., 2019; Chmielecki et al., 2023). To solve these problems, NPs with special properties such as slow release have been shown initial success (Huang et al., 2022).

The latest monotherapies to address resistance to EGFR-TKIs mainly include nanoconjugates viral delivery, nucleic acid therapy, and targeted EGFR-TKIs loaded in nanostructures. Viruses as natural carrier materials take advantage of the biochemical and physical properties, such as solubility and nanometer size, making them an important choice for NDDS (Sainsbury and Steinmetz, 2023). Arrieta's team constructed a novel type of magnetic lentivirus that can infect EGFR-TKIs-resistant cells in the model and realize microscale RNA interference (RNAi) by inhibiting EGFR expression, causing apoptosis of drug-resistant cells (Song et al., 2009; Li et al., 2021). In addition, pH affects the effect of nanocarriers mainly by microenvironment/nanomaterial surface charge interconversion, tumor penetration size, and swelling or disintegration upon drug release (Song et al., 2008). The lactate accumulation method was used to design lactate-responsive vectors containing lactate oxidase (LOX) and AAV2, which reduced pH and viral infection, as well as increased apoptosis when both LOX and lactate were presented in the formulation (Tseng et al., 2018).

Nanocarriers can carry nucleic acids through the phospholipid bilayer of cell membranes, which promotes easier drug accumulation within the target cells (Bishop et al., 2015). Li et al. reported that exosomes loaded with small interfering RNA (siRNA) were used for the suppression of NSCLC (Li et al., 2021). Cholesterol is used to anchor ligands targeting EGFR onto secretions that load siRNA to silence the anti-apoptotic factor survivin. Cytoplasmic delivery of siRNA resolves the problem of endosomal capture and leads to effective gene knockdown, chemosensitization and tumor regression. In NSCLC patients, the knockdown of expression of selected appropriate targets restores sensitivity to EGFR-targeted drugs (Li et al., 2021). Thereby, the progress has been made in combining RNA nanotechnology with exon-delivery platforms, which can improve the targeting of cancer therapies.

The discovery of ligands that bind specifically to cancer cells is essential for NDDS delivery, and peptide binding to liposomes has been used to selectively deliver drugs to kill tumor cells with EGFR mutations (Song et al., 2008; Song et al., 2009). The study was performed by small peptides with phosphorylation sites (AEYLR, EYINQ, and PDYQQD), which were labeled with fluorescein isothiocyanate (FITC), in tumor cells of NSCLC with or without

EGFR expression. It showed that AEYLR recognizes EGFR protein with high selectivity (Han et al., 2013). This confirmed that NDDS bound to AEYLR can accumulate more easily in tumor cells. Li et al. prepared lipid-containing NPs loaded with anti-EGFR DNA aptamer, which can make NDDS reach the target cells more easily by exploiting the specific binding of EGFR DNA aptamer, thus increasing the drug concentration and exerting better anti-tumor efficacy of targeted drugs (Li et al., 2017). Additionally, Han et al. loaded cyclosporine A and targeted drugs in a nanostructured poly (ethylene glycol)-poly (lactic acid) (PEG-PLA) and found a significant effect of cyclosporine A in reversing resistance to EGFR-TKIs (Han et al., 2018). Compared to EGFR-TKIs alone, NPs loaded with EGFR TKI not only reduce systemic toxicity but also improve intracellular delivery and increase bioavailability (Ahlawat et al., 2022). Upadhyay et al. demonstrated the efficiency of transferrin-modified PLGA thymoquinone NPs combined with gefitinib (NP-DUAL-3) in treating resistant NSCLC cells for the first time (Upadhyay et al., 2021). The results indicated that NP-DUAL-3 may restore the MET phenomenon, thereby making drug-resistant NSCLC cells re-sensitive to gefitinib. Therefore, the combination of NPs and gefitinib may be effective in treating NSCLC patients in the future.

4 Nanodrug targeted vascular endothelial growth factor receptor in NSCLC

VEGF is mainly secreted by vascular endothelial cells, as well as tumor microenvironment (TME) cells, such as tumor-associated macrophages (TAMs) (Hwang et al., 2020), tumor-associated neutrophils (TANs) (Guimarães-Bastos et al., 2022), mast cells (MCs) (Komi et al., 2020), myelogenous suppressor cells (MDSCs) (Mortezaee, 2021) and natural killer cells (NKs) (Eisinger et al., 2020). VEGF is the main mediator of tumor microangiogenesis and closely associated with the development and progression of NSCLC. In addition, VEGF stimulates regulatory immune cells by inhibiting antigen presentation, thus promoting immunosuppression of the TME. It is an important manifestation of VEGF's involvement in immune regulation (Zhao Y. et al., 2022).

The binding of VEGF ligands to VEGFR-2 and the PI3K/AKT signaling pathway control the survival of endothelial cells (Wang et al., 2022). The activation of endothelial nitrogen monoxide (NO) synthase by c-Src and phospholipase C1 (PLC1), and the activation

of prostacyclin synthase by Raf1-MEK1/2/ERK1/2 lead to an increase of NO and PGI₂ in endothelial cells, respectively (Socinski et al., 2018). This pathway is the core of endothelial cell proliferation. The upregulation of NO induced by VEGF may also participate in the generation and mobilization of endothelial progenitor cells (Aicher et al., 2003).

Kandasamy et al. explored the efficiency of poly (1-vinyl imidazole) (PVI) as an effective siRNA carrier for VEGF gene silencing (Kandasamy et al., 2020). They found that the individual PVI polymer was safe to the cells, and the polymer exhibited good internalization and effectively escaped the inner body, indicating that the vector may be a biocompatible system for gene therapy. In terms of silencing VEGF in tumors, the polymerase is more effective than free siRNA, and the silencing of VEGF leads to changes in the gene expression responsible for cancer cell proliferation and metastasis. Peptide silencing of VEGF can enhance the cytotoxicity of chemotherapy drug 5-fluorouracil, suggesting that it could be used as an adjuvant treatment strategy for cancer. Meanwhile, VEGF-targeted RNAi using poly-siRNA/tGC NPs in combination with chemotherapeutic agents can control tumor growth by increasing anti-angiogenic efficacy while minimizing toxicity and drug resistance (Kwak et al., 2017). Chemically polymerized siRNAs complexed with thiolated-glycol chitosan (psi (VEGF)/tGC) NPs mediated suppression of VEGF which exerted anti-tumor effects. Furthermore, the combination of bevacizumab can better perform the drug's efficacy (Kim et al., 2017).

5 Nanodrug regulated PI3K/AKT/mTOR signaling pathway in NSCLC

The PI3K/AKT/mTOR pathway is vital in regulating cell growth and metabolism, which is significantly activated in NSCLC (50%–73%) (Papadimitrakopoulou, 2012). Meanwhile, persistent activation of this pathway can contribute to the development of resistance to anticancer therapy. PI3K is regulated by numerous upstream factors, such as HER2 (Tan, 2020). Under stress or ligand binding, AKT is readily activated to regulate the phosphorylation of phosphatidylinositol 4,5-bisphosphate (PIP₂) to phosphatidylinositol 3,4,5-trisphosphate (PIP₃) (Papadimitrakopoulou, 2012). Activation of AKT will cause changes in downstream signaling molecules, which can inhibit Bcl-2-associated death promoter (BAD) and Bcl-2-associated X protein (BAX), members of the Bcl-2 family, and promote apoptosis (Cantley, 2002). Activation of nuclear factor-κB (NF-κB) light chain enhancer plays a role in immune regulation and biological behavior (Sonenshein, 1997). Another important downstream pathway is the activation of protein kinase mTOR. The mTOR can cause activation of the eukaryotic translation initiation factor 4 complex, which subsequently promotes tumor development, regulates cell cycle, and inhibits cell apoptosis (Engelman et al., 2006).

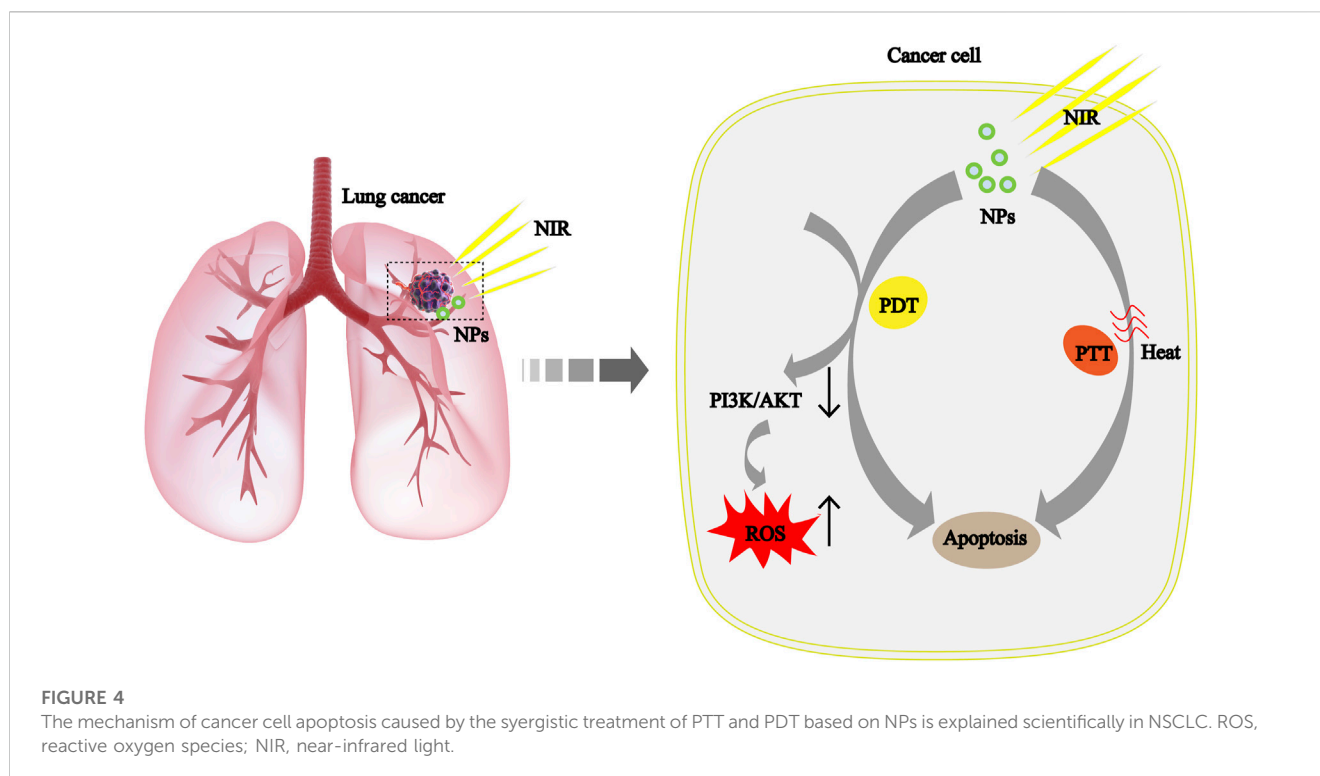
In recent years, photothermal therapy (PTT) and photodynamic therapy (PDT) based on nanomaterials have made remarkable progress as an anticancer strategy, as shown in Figure 4 (Hou et al., 2020; Sun et al., 2020). Quantum dots (QDs) have good biocompatibility, solubility, excellent photostability, and easy

surface functionalization properties, making them new promising nanomaterials (McHugh et al., 2018; Fan et al., 2019). Kuo et al. improved the efficiency of PDT by functionalizing nitrogen doped QDs with amino molecules (Kuo et al., 2018). Liu's team has constructed a novel CoFe₂O₄ with excellent synergistic PTT/PDT properties, which can effectively inhibit NSCLC without significant toxicity. In addition, CoFe₂O₄ treatment also increases reactive oxygen species by regulating the PI3K/AKT pathway, thereby triggering cell death (Liu J. et al., 2021). Based on the current results, the safe, non-toxic NPs may have a positive effect on NSCLC treatment.

6 Nanodrug regulated JAK2/STAT3 signaling pathway in NSCLC

Janus kinase (JAK) is a non-receptor tyrosine kinase that mediates the cascade activation of signaling molecules after cytokine and receptor binding (Johnson et al., 2018). The JAK family consists of four members (JAK1-3 and TYK2) (Lin et al., 2018). Abnormal JAK2 signaling plays an important role in solid tumors (Lee et al., 2006). The signal transducer and activator of transcription (STAT) protein family consists of seven members (STAT1-4, STAT5a, STAT5b, and STAT6) (Fang et al., 2017). STAT3 is a transcription factor that has been extensively studied in cancer. Generally, the JAK2/STAT3 pathway mediates signal transduction through a variety of cytokine receptors, such as interleukin-6 (IL-6) (Zhong et al., 1994) or granulocyte colony-stimulating factor (G-CSF) (Thorn et al., 2016), and EGFR (Shi and Kehrl, 2004), which makes JAK2 phosphorylate on its tyrosine residues (called autophosphorylation) and activate its kinase domain. This signaling pathway regulates not only different cancer cell biological habits, including oncogenesis, proliferation, and distant transfer, but also the development and maintenance of tumor stem cells (CSCs). Phosphorylation levels of STAT3 are associated with poor prognosis in NSCLC, and aberrant STAT3 activity has been observed in malignant cells of other tumors. Therefore, there is a broad prospect of the STAT3 signaling pathway in the treatment of NSCLC. NPs are up-and-coming delivery systems for small-molecule drugs and nucleic acid. Consequently, the nanodrugs targeted signaling pathways are more conducive to uptake and utilization.

The TME contains a vast array of TAMs, which are classified into M1 (anti-tumor) and M2 (tumor-promoting) phenotypes (Mills, 2012; Sica and Mantovani, 2012; Komohara et al., 2016). The activation of STAT3 enhances M2-type polarization, and contributes to the formation of tumor-related phenotypes (Kortylewski et al., 2009). Chen et al. developed dual-targeting delivery system by using siRNA to target both tumor cells and M2 macrophages to silence STAT3 (Chen et al., 2020). The dual targeting system used for siRNA packaging was constructed through electronic self-assembly, consisted of carboxymethyl chitosan, and coupled with folic acid. Compared with non-targeted NPs, the dual-targeted delivery system led to a significant decrease in expression of STAT3, with a successful transition of macrophages from the M2 phenotype to the M1 phenotype, while increased apoptosis and inhibited proliferation of LC cells. In addition, Shobaki's group used a lipid NPs (LNPs) to targeted deliver siRNA to TAMs, which



can silence STAT3 and hypoxia-inducible factor 1 α (HIF-1 α) (Shobaki et al., 2020). It led to an increase of M1 macrophages, thus obtaining well anti-tumor therapeutic effects. On the whole, the novel nanodrugs targeting macrophages and STAT3 behave with good clinical and pharmaceutical application prospects.

RNAi is a powerful tool to downregulate the level of STAT3, which can make drug-resistant cancer cells re-sensitive (Alshamsan et al., 2011; Kotmakçı et al., 2017). To deliver RNAi-mediated plasmid DNA, Kotmakçı et al. developed and evaluated a kind of cationic solid lipid NPs (SLNs). It showed that the expression level of STAT3 mRNA decreased by approximately five-fold while cisplatin-resistant cancer cells were re-sensitive after SLNs treatment (Kotmakçı et al., 2017). Chen et al. used the PEG-PLA NPs to deliver small molecule drugs (Chen et al., 2018). The results showed a synergistic anti-tumor effect on resistant NSCLC *in vitro*. The nanodrug significantly downregulated the level of biomolecules in signaling pathways, such as p-JAK2, which can cause drug resistance. In summary, the NPs-mediated drug co-delivery method can overcome drug resistance by regulating specific signaling pathways.

7 Nanodrug induced p53 and Bax/Bcl-2 pathway Dysfunction in NSCLC

As a well-known tumor suppressor, p53 can inhibit cell proliferation and promote apoptosis (Cui and Guo, 2016). Dysfunction of the p53 pathway is particularly common, accounting for approximately 68% of NSCLC patients (Kong et al., 2019). A variety of downstream signal molecules are regulated by p53 in tumor, such as B-cell lymphoma 2 protein (Bcl-2) and Bcl-2 related X protein (Bclx). P53 can downregulate the

anti-apoptosis factor Bcl-2 and upregulate the pro-apoptosis factor Bclx (Rasheduzzaman et al., 2018).

The main problems with the application of Bcl-2 antagonists in cancer treatment are their poor water solubility and toxicity to normal cells (Schimmer et al., 2008; Paik et al., 2010). NPs can be used to improve the solubility of drugs to enhance anti-tumor efficiency (Li et al., 2018). Chen et al. prepared RBCm-OM/PLGA NPs by combining PLGA with red blood cell membrane (RBCm) to wrap obatok mesylate (OM) (Chen S et al., 2020). The results showed that their NDDS could effectively stop the growth of malignant tumor cells *in vitro* and *in vivo* by inducing apoptosis related to the high accumulation of nanodrugs. Similarly, tetrandrine (Tet) was used to make NPs (Tet NPs), which can enhance cell apoptosis by down-regulating the expression of Bcl-2. What's more, Tet NPs can inhibit cell migration and invasion more effectively than free Tet by down-regulating matrix metalloproteinases 2 (MMP2) and matrix metalloproteinases 9 (MMP9), and upregulating tissue inhibitor of metalloproteinase-3 (TIMP-3) (Xu et al., 2014). The above results indicate that uniting anti-Bcl-2 drugs and NPs might have good prospects in the field of NSCLC treatment by improving the anti-cancer efficiency.

8 Nanodrug remodeled tumor immune microenvironment in NSCLC

During the process of cell differentiation and proliferation, the immunogenicity of tumor cells is reduced, which leads to immune escape (Guo et al., 2022). ICIs can influence the activation and depletion of T cells by interacting with PD-1 or PD-L1, and ultimately inhibit the occurrence of tumor immune escape. (Gordon et al., 2017). This kind of drugs have the potential to

improve the survival rate of cancer patients, which are regarded as a desirable choice for the tumor treatment.

To improve the response rate of ICIs therapies, Zhao et al. successfully constructed a nanodrug consisting of fluorinated dendrimer and HSP70 promoter-driven CRISPR/Cas9 (Zhao L. et al., 2022). In this system, the activated HSP70 promoter facilitated the expression of Cas9 protein, leading to permanent genomic destruction of PD-L1. Consequently, it effectively hindered the immune escape of tumor cells. In another study, Zhou et al. found that integrin $\beta 3$ ($\beta 3$ -INT) is highly expressed in NSCLC and further observed that the inhibitor RGDyK facilitates the process of PD-L1 ubiquitination (Zhou et al., 2022). Based on this, their group prepared RGDyK-modified mesoporous silica NPs loaded with zinc protoporphyrin (ZnPP@MSN-RGDyK). This nanodrug showed high photodynamic treatment efficiency and good immunotherapeutic effect by precisely targeting $\beta 3$ -INT to weaken the function of PD-L1 in preclinical tumor models.

NSCLC patients often develop drug resistance in ICIs monotherapy (Dempke et al., 2018). Kim's team constructed an investigational tumor-targeted nanodrug named SGT-53 (Kim et al., 2022). They found that SGT-53 can restore an effective immune response to tumor cells by modulating immunosuppressive cells, including T cells and macrophages, and downregulate the expression of immunosuppressive molecule Galectin-1. Furthermore, the study revealed that the intensity of macrophage infiltration was highly correlated with the emergence of ICIs resistance (Cui et al., 2020; Kim et al., 2020; Zhu et al., 2020). Besides, Xu et al. bound nano-diamond doxorubicin conjugate (Nano-DOX) to a PD-L1 blocking agent named BMS-1, which can effectively reactivate the M1-type macrophages to kill tumor cells and inhibit tumor growth (Xu et al., 2021).

In summary, the combination of NPs and ICIs can not only help in the precise targeting of drugs, but also restore the immune surveillance function.

9 Challenges and prospects of nanodrug in targeted NSCLC therapy

Targeted therapies and immunotherapies have been widely used in clinical practice. These drugs improve the prognosis of patients with a variety of advanced cancers. However, most of the targeted drugs are unable to achieve the expected therapeutic effects due to their low solubility, low bioavailability and severe adverse reactions (de Scordilli et al., 2022). Furthermore, systemic administration of immunotherapy can also cause immune damage to respiratory and cardiovascular systems or other systems, and can even be life-threatening (Lahiri et al., 2023). Nanotechnology is a rapidly evolving field that offers new strategies related to drug delivery. Here, the modifiability and micro-size properties enable nanomaterials to play a synergistic therapeutic role with drugs. From this, NDDS can regulate the drug concentration of target cells by controlling the release rate, which eventually overcome the shortcomings of anti-cancer drugs, including the drug resistance, systemic toxicity and rapid metabolism (Abdelaziz et al., 2018; Wang X. et al., 2021). The intersection of disciplines brings a broader prospect for the development of nanomedicine.

Despite the encouraging successes, there are still many problems that remain to be solved, which seem impossible to accomplish in a short period of time. Currently, many studies are dedicated to develop safe and effective nanodrugs in NSCLC, but very few drugs can pass clinical trials (Liao et al., 2020). There are still many unknown metabolic pathways of nanodrugs in the human body, which may bring unpredictable drug side effects (Abdelaziz et al., 2018). They are easily absorbed by healthy cells through active transport because the nanodrugs have small size, which may cause damage on normal histiocytes (Ferrari, 2005; Wang X. et al., 2021). There is still a long way to go for nanodrugs to enter clinical treatment, which requires close cooperation between disciplines. For example, multi-radionuclide imaging can personalize treatment by stratifying patients, and the use of artificial intelligence algorithms can help select specific nano parameters in these highly complex cases to improve the biological function (Arrieta et al., 2012; Mahmoud et al., 2020). Nanodrug plays an active role in the regulation of various signaling pathways in tumors. Many signaling pathways in TME have been shown to play important roles in tumor cell growth, and it is necessary to develop specific drug and delivery devices for these signaling pathways (Wang F. et al., 2021; Lei et al., 2022).

In summary, both nanotechnology and signaling pathway-regulated drugs are ushering in a new era of disease treatment, and their synergistic effects have broad clinical application prospects. However, there are still many problems need to be solved. Accordingly, it is necessary to combine the advantages of complementary multidisciplinary to solve these problems, and this will bring benefits to tumor patients as soon as possible.

10 Conclusion and future prospects

In recent years, the global incidence of NSCLC is the highest among all cancer incidence rates. Currently, precision molecular therapy for NSCLC has been widely used, and many drugs have entered the clinic, but more signal-regulated pathways of tumor development are still unclear. It is the goal of medical development to find more effective and safer therapeutic targets. NDDS brings more convenience to drug therapy, but the defects of the nanodrug itself still need to be overcome. The most important problems come from the stability, effectiveness, and safety of the nanomaterials themselves, in addition to the type of carrier material, preparation technology, and cost issues (Ji et al., 2022). At present, the pharmacokinetic behaviors of more nanodrugs are unclear, which is also an important reason for the low success rate of clinical transformation (Cao and Chen, 2022). Multidisciplinary intersection brings the advantage of solving these problems, and therefore the exchange of new technologies among various disciplines needs to be enhanced (Boehnke et al., 2022; Xu C. et al., 2023). Besides, studies on the regulation of signaling pathways by nanodrugs are mostly conducted *in vitro* or in animal models. Due to the heterogeneity of cancers in animal models and clinical patients, the therapeutic effects of nanodrugs have large differences between the preclinical therapy and clinical trials, which reduces their clinical application (Xu W. et al., 2023). Therefore, it will be beneficial to improve clinical feasibility of nanodrugs by developing humanized animal models (May, 2018).

Meanwhile, we need clinical trials to validate and evaluate their efficacy and safety.

The combination of drugs and nanomaterials will provide hope for patient survival (Van der Meel et al., 2019; Jia et al., 2023). Multi-drug combination is one of the important means to improve anti-cancer efficacy, and it is also a general trend in the field of drug research and development (Detappe et al., 2023). Exploring more therapeutic targets for molecular signaling is also an important prerequisite for promoting multi-drug combination therapy (You et al., 2023). Nanocarriers provide a safe, fast and effective platform for multi-drug combination therapy (Yang et al., 2023). Hence, NDDS combined with multi-target drugs synergistic therapy may be the focus of future research.

Designing efficient and safe nanodrugs and exhaustively investigating their pharmacokinetics *in vivo* are key to their application and development. The development of humanised animal models will also greatly improve the success rate of clinical translation of novel nanodrugs. Exploring more molecular signalling targets and multi-target combination therapy based on nanocarriers are important research directions. With the development of nanotechnology, NPs will also be updated, and their obvious advantages as drug carriers will be played more in practical applications. Eventually, they will become powerful tools for patients to overcome NSCLC. For the next phase of research on nanodrug, researchers should spend more time and effort to provide clear evidence for existing mechanisms rather than creating many new and complex nanocarriers for similar concepts as a way to advance the clinical translation of nanomedicines.

In conclusion, the research of nanodrugs in regulating signaling pathways is still in its infancy, and many practical problems still need to be solved.

Author contributions

YL and ZD designed this study. WL, ML, XHe, and QH drafted the manuscript. WL performed drawing and organization of figures. ML, CS, XH, FX, and YL revised the manuscript. All authors contributed to the article and approved the submitted version.

References

- Abdelaziz, H. M., Gaber, M., Abd-Elwakil, M. M., Mabrouk, M. T., Elgohary, M. M., Kamel, N. M., et al. (2018). Inhalable particulate drug delivery systems for lung cancer therapy: nanoparticles, microparticles, nanocomposites and nanoaggregates. *J. Control Release* 269, 374–392. doi:10.1016/j.jconrel.2017.11.036
- Ahlawat, P., Phutela, K., Bal, A., Singh, N., and Sharma, S. (2022). Therapeutic potential of human serum albumin nanoparticles encapsulated actinonin in murine model of lung adenocarcinoma. *Drug Deliv.* 29 (1), 2403–2413. doi:10.1080/10717544.2022.2067600
- Aicher, A., Heeschen, C., Mildner-Rihm, C., Urbich, C., Ihling, C., Technau-Ihling, K., et al. (2003). Essential role of endothelial nitric oxide synthase for mobilization of stem and progenitor cells. *Nat. Med.* 9 (11), 1370–1376. doi:10.1038/nm948
- Alshamsan, A., Hamdy, S., Haddadi, A., Samuel, J., El-Kadi, A. O., Uludağ, H., et al. (2011). STAT3 knockdown in B16 melanoma by siRNA lipopolyplexes induces bystander immune response *in vitro* and *in vivo*. *Transl. Oncol.* 4 (3), 178–188. doi:10.1593/tlo.11100
- Argilés, J. M., López-Soriano, F. J., and Stemmler Bbusquets, S. (2023). Cancer-associated cachexia - understanding the tumour macroenvironment and microenvironment to improve management. *Nat. Rev. Clin. Oncol.* 20 (4), 250–264. doi:10.1038/s41571-023-00734-5
- Arrieta, Ó., Medina, L. A., Estrada-Lobato, E., Hernández-Pedro, N., Villanueva-Rodríguez, G., Martínez-Barrera, L., et al. (2012). First-line chemotherapy with liposomal doxorubicin plus cisplatin for patients with advanced malignant pleural mesothelioma: phase II trial. *Br. J. Cancer* 106 (6), 1027–1032. doi:10.1038/bjc.2012.44
- Asati, V., Mahapatra, D. K., and Bharti, S. K. (2016). PI3K/Akt/mTOR and Ras/Raf/MEK/ERK signaling pathways inhibitors as anticancer agents: structural and pharmacological perspectives. *Eur. J. Med. Chem.* 109, 314–341. doi:10.1016/j.ejmech.2016.01.012
- Bilek, O., Holánek, M., Berkovcová, J., Horký, O., Kazda, T., Čoupková, H., et al. (2019). Uncommon EGFR mutations in non-small cell lung cancer and their impact on the treatment. *Klin. Onkol.* 32 (3), 6–12. doi:10.14735/amko2019386
- Bishop, C. J., Kozielski, K. L., and Green, J. J. (2015). Exploring the role of polymer structure on intracellular nucleic acid delivery via polymeric nanoparticles. *J. Control Release* 219, 488–499. doi:10.1016/j.jconrel.2015.09.046
- Boehnke, N., Straehla, J. P., Safford, H. C., Kocak, M., Rees, M. G., Ronan, M., et al. (2022). Massively parallel pooled screening reveals genomic determinants of nanoparticle delivery. *Science* 377 (6604), eabm5551. doi:10.1126/science.abm5551
- Boolell, V., Alamgeer, M., Watkins, D. N., and Ganju, V. (2015). The evolution of therapies in non-small cell lung cancer. *Cancers (Basel)* 7 (3), 1815–1846. doi:10.3390/cancers7030864
- Cabano, H. F., and Hata, A. N. (2021). Emerging insights into targeted therapy-tolerant persister cells in cancer. *Cancers (Basel)* 13 (11), 2666. doi:10.3390/cancers13112666
- Cantley, L. C. (2002). The phosphoinositide 3-kinase pathway. *Science* 296 (5573), 1655–1657. doi:10.1126/science.296.5573.1655

Funding

This work was funded by the Zigong Academy of Medical Sciences 2022, Nos ZGYKY22KF008, ZGYKY22KF009, and ZGYKY22KF005; the National Natural Science Foundation of China, No. 82003262; the Key R&D Program of Sichuan Provincial Department of Science and Technology (Major Science and Technology Project), No. 2022YFS0095; China Postdoctoral Science Foundation, Nos 2019TQ0221 and 2019M663517; Post-Doctor Research Project, West China Hospital, Sichuan University, Nos 2019HXBH059 and 2021HXBH009; Sichuan University Postdoctoral Interdisciplinary Innovation Fund.

Acknowledgments

The authors would like to gratefully acknowledge Dr. Yi Li (West China Hospital), Dr. Quan Yuan and Dr. Youli Wen (Zigong First People's Hospital) for their instructive suggestions to refine the manuscript.

Conflict of interest

The authors declare that the research was conducted in the absence of any commercial or financial relationships that could be construed as a potential conflict of interest.

Publisher's note

All claims expressed in this article are solely those of the authors and do not necessarily represent those of their affiliated organizations, or those of the publisher, the editors and the reviewers. Any product that may be evaluated in this article, or claim that may be made by its manufacturer, is not guaranteed or endorsed by the publisher.

- Cao, M., and Chen, C. (2022). Bioavailability of nanomaterials: bridging the gap between nanostructures and their bioactivity. *Natl. Sci. Rev.* 9 (10), nwac119. doi:10.1093/nsr/nwac119
- Chen, D., Zhang, F., Wang, J., He, H., Duan, S., Zhu, R., et al. (2018). Biodegradable nanoparticles mediated Co-delivery of erlotinib (ELTN) and fedratinib (FDTN) toward the treatment of ELTN-resistant non-small cell lung cancer (NSCLC) via suppression of the JAK2/STAT3 signaling pathway. *Front. Pharmacol.* 9, 1214. doi:10.3389/fphar.2018.01214
- Chen, J., Dou, Y., Tang, Y., and Zhang, X. (2020). Folate receptor-targeted RNAi nanoparticles for silencing STAT3 in tumor-associated macrophages and tumor cells. *Nanomedicine* 25, 102173. doi:10.1016/j.nano.2020.102173
- Chen, N., Wei, M., Sun, Y., Li, F., Pei, H., Li, X., et al. (2014). Self-assembly of polyadenine-tailed CpG oligonucleotide-gold nanoparticle nanoconjugates with immunostimulatory activity. *Small* 10 (2), 368–375. doi:10.1002/sml.201300903
- Chen, P. M., Cheng, Y. W., Wu, T. C., Chen, C. Y., and Lee, H. (2015). MnSOD overexpression confers cisplatin resistance in lung adenocarcinoma via the NF- κ B/Snail/Bcl-2 pathway. *Free Radic. Biol. Med.* 79, 127–137. doi:10.1016/j.freeradbiomed.2014.12.001
- Chen, Q., Lai, Q., Jiang, Y., Yao, J., Chen, Q., Zhang, L., et al. (2022). Anlotinib exerts potent antileukemic activities in Ph chromosome negative and positive B-cell acute lymphoblastic leukemia via perturbation of PI3K/AKT/mTOR pathway. *Transl. Oncol.* 25, 101516. doi:10.1016/j.tranon.2022.101516
- Chen, S. S., Ren, Y., and Duan, P. (2020). Biomimetic nanoparticle loading obatoclax mesylate for the treatment of non-small-cell lung cancer (NSCLC) through suppressing Bcl-2 signaling. *Biomed. Pharmacother.* 129, 110371. doi:10.1016/j.biopha.2020.110371
- Chmielecki, J., Mok, T., Wu, Y. L., Han, J. Y., Ahn, M. J., Ramalingam, S. S., et al. (2023). Analysis of acquired resistance mechanisms to osimertinib in patients with EGFR-mutated advanced non-small cell lung cancer from the AURA3 trial. *Nat. Commun.* 14 (1), 1071. doi:10.1038/s41467-023-35962-x
- Ciuffreda, L., Incani, U. C., Steelman, L. S., Abrams, S. L., Falcone, I., Curatolo, A. D., et al. (2014). Signaling intermediates (MAPK and PI3K) as therapeutic targets in NSCLC. *Curr. Pharm. Des.* 20 (24), 3944–3957. doi:10.2174/13816128113196660763
- Cui, X., Ma, C., Vasudevaraja, V., Serrano, J., Tong, J., Peng, Y., et al. (2020). Dissecting the immunosuppressive tumor microenvironments in Glioblastoma-on-a-Chip for optimized PD-1 immunotherapy. *Elife* 9, 52253. doi:10.7554/eLife.52253
- Cui, Y., and Guo, G. (2016). Immunomodulatory function of the tumor suppressor p53 in host immune response and the tumor microenvironment. *Int. J. Mol. Sci.* 17 (11), 1942. doi:10.3390/ijms17111942
- de Scordilli, M., Michelotti, A., Bertoli, E., De Carlo, E., and Del Conte Abearz, A. (2022). Targeted therapy and immunotherapy in early-stage non-small cell lung cancer: current evidence and ongoing trials. *Int. J. Mol. Sci.* 23 (13), 7222. doi:10.3390/ijms23137222
- Dempke, W. C. M., Fenchel, K., and Dale, S. P. (2018). Programmed cell death ligand-1 (PD-L1) as a biomarker for non-small cell lung cancer (NSCLC) treatment—are we barking up the wrong tree? *Transl. Lung Cancer Res.* 7 (3), S275–S279. doi:10.21037/tlcr.2018.04.18
- Detappe, A., Nguyen, H. V., Jiang, Y., Agius, M. P., Wang, W., Mathieu, C., et al. (2023). Molecular bottlebrush prodrugs as mono- and triplex combination therapies for multiple myeloma. *Nat. Nanotechnol.* 18 (2), 184–192. doi:10.1038/s41565-022-01310-1
- Duan, Y., Shen, C., Zhang, Y., and Luo, Y. (2022). Advanced diagnostic and therapeutic strategies in nanotechnology for lung cancer. *Front. Oncol.* 12, 1031000. doi:10.3389/fonc.2022.1031000
- Eisinger, S., Sarhan, D., Boura, V. F., Ibarlucea-Benitez, I., Tyystjarvi, S., Oliynyk, G., et al. (2020). Targeting a scavenger receptor on tumor-associated macrophages activates tumor cell killing by natural killer cells. *Proc. Natl. Acad. Sci. U. S. A.* 117 (50), 32005–32016. doi:10.1073/pnas.2015343117
- Engelman, J. A., Luo, J., and Cantley, L. C. (2006). The evolution of phosphatidylinositol 3-kinases as regulators of growth and metabolism. *Nat. Rev. Genet.* 7 (8), 606–619. doi:10.1038/nrg1879
- Ezhilarasan, D., Lakshmi, T., and Mallineni, S. K. (2022). Nano-based targeted drug delivery for lung cancer: therapeutic avenues and challenges. *Nanomedicine (Lond)* 17 (24), 1855–1869. doi:10.2217/nnm-2021-0364
- Fan, H. Y., Yu, X. H., Wang, K., Yin, Y. J., Tang, Y. J., Tang, Y. L., et al. (2019). Graphene quantum dots (GQDs)-based nanomaterials for improving photodynamic therapy in cancer treatment. *Eur. J. Med. Chem.* 182, 111620. doi:10.1016/j.ejmech.2019.111620
- Fang, R. H., Gao, W., and Zhang, L. (2023). Targeting drugs to tumours using cell membrane-coated nanoparticles. *Nat. Rev. Clin. Oncol.* 20 (1), 33–48. doi:10.1038/s41571-022-00699-x
- Fang, X., Hong, Y., Dai, L., Qian, Y., Zhu, C., Wu, B., et al. (2017). CRH promotes human colon cancer cell proliferation via IL-6/JAK2/STAT3 signaling pathway and VEGF-induced tumor angiogenesis. *Mol. Carcinog.* 56 (11), 2434–2445. doi:10.1002/mc.22691
- Ferlay, J., Colombet, M., Soerjomataram, I., Dyba, T., Randi, G., Bettio, M., et al. (2018). Cancer incidence and mortality patterns in Europe: estimates for 40 countries and 25 major cancers in 2018. *Eur. J. Cancer* 103, 356–387. doi:10.1016/j.ejca.2018.07.005
- Ferlay, J., Colombet, M., Soerjomataram, I., Mathers, C., Parkin, D. M., Piñeros, M., et al. (2019). Estimating the global cancer incidence and mortality in 2018: GLOBOCAN sources and methods. *Int. J. Cancer* 144 (8), 1941–1953. doi:10.1002/ijc.31937
- Ferrari, M. (2005). Cancer nanotechnology: opportunities and challenges. *Nat. Rev. Cancer* 5 (3), 161–171. doi:10.1038/nrc1566
- Garofalo, M., Romano, G., Di Leva, G., Nuovo, G., Jeon, Y. J., Nganheu, A., et al. (2011). Retracted article: EGFR and MET receptor tyrosine kinase-altered microRNA expression induces tumorigenesis and gefitinib resistance in lung cancers. *Nat. Med.* 18 (1), 74–82. doi:10.1038/nm.2577
- Gordon, S. R., Maute, R. L., Dulken, B. W., Hutter, G., George, B. M., McCracken, M. N., et al. (2017). PD-1 expression by tumour-associated macrophages inhibits phagocytosis and tumour immunity. *Nature* 545 (7655), 495–499. doi:10.1038/nature22396
- Guimarães-Bastos, D., Frony, A. C., Barja-Fidalgo, C., and Moraes, J. A. (2022). Melanoma-derived extracellular vesicles skew neutrophils into a pro-tumor phenotype. *J. Leukoc. Biol.* 111 (3), 585–596. doi:10.1002/jlb.3a0120-050rr
- Guo, Q., and Jiang, C. (2020). Delivery strategies for macromolecular drugs in cancer therapy. *Acta Pharm. Sin. B* 10 (6), 979–986. doi:10.1016/j.apsb.2020.01.009
- Guo, Y., Xie, Y., and Luo, Y. (2022). The role of long non-coding RNAs in the tumor immune microenvironment. *Front. Immunol.* 13, 851004. doi:10.3389/fimmu.2022.851004
- Haider, M., Abidin, S. M., Kamal, L., and Orive, G. (2020). Nanostructured lipid carriers for delivery of chemotherapeutics: a review. *Pharmaceutics* 12 (3), 288. doi:10.3390/pharmaceutics12030288
- Haider, M., Zaki, K. Z., El Hamshary, M. R., Hussain, Z., and Orive Gibrabhim, H. O. (2022). Polymeric nanocarriers: a promising tool for early diagnosis and efficient treatment of colorectal cancer. *J. Adv. Res.* 39, 237–255. doi:10.1016/j.jare.2021.11.008
- Han, C. Y., Yue, L. L., Tai, L. Y., Zhou, L., Li, X. Y., Xing, G. H., et al. (2013). A novel small peptide as an epidermal growth factor receptor targeting ligand for nanodelivery in vitro. *Int. J. Nanomedicine* 8, 1541–1549. doi:10.2147/ijn.S43627
- Han, W., Shi, L., Ren, L., Zhou, L., Li, T., Qiao, Y., et al. (2018). A nanomedicine approach enables co-delivery of cyclosporin A and gefitinib to potentiate the therapeutic efficacy in drug-resistant lung cancer. *Signal Transduct. Target Ther.* 3, 16. doi:10.1038/s41392-018-0019-4
- Harada, G., Yang, S. R., Cocco, E., and Drilon, A. (2023). Rare molecular subtypes of lung cancer. *Nat. Rev. Clin. Oncol.* 20 (4), 229–249. doi:10.1038/s41571-023-00733-6
- Hirsch, F. R., Scagliotti, G. V., Mulshine, J. L., Kwon, R., Curran, W. J., Jr., Wu, Y. L., et al. (2017). Lung cancer: current therapies and new targeted treatments. *Lancet* 389 (10066), 299–311. doi:10.1016/s0140-6736(16)30958-8
- Hou, Y. J., Yang, X. X., Liu, R. Q., Zhao, D., Guo, C. X., Zhu, A. C., et al. (2020). Pathological mechanism of photodynamic therapy and photothermal therapy based on nanoparticles. *Int. J. Nanomedicine* 15, 6827–6838. doi:10.2147/ijn.S269321
- Huang, J., Zhuang, C., Chen, J., Chen, X., Li, X., Zhang, T., et al. (2022). Targeted drug/gene/photodynamic therapy via a stimuli-responsive dendritic-polymer-based nanococktail for treatment of EGFR-TKI-resistant non-small-cell lung cancer. *Adv. Mater.* 34 (27), e2201516. doi:10.1002/adma.202201516
- Hwang, I., Kim, J. W., Ylaya, K., Chung, E. J., Kitano, H., Perry, C., et al. (2020). Tumor-associated macrophage, angiogenesis and lymphangiogenesis markers predict prognosis of non-small cell lung cancer patients. *J. Transl. Med.* 18 (1), 443. doi:10.1186/s12967-020-02618-z
- Ikeda-Imafuku, M., Wang, L. L., Rodrigues, D., Shaha, S., Zhao, Z., and Mitragotri, S. (2022). Strategies to improve the EPR effect: a mechanistic perspective and clinical translation. *J. Control Release* 345, 512–536. doi:10.1016/j.jconrel.2022.03.043
- Ji, D., Zhang, Y., Sun, J., Zhang, B., Ma, W., Cheng, B., et al. (2023). An engineered influenza virus to deliver antigens for lung cancer vaccination. *Nat. Biotechnol.* 2023, 01796. doi:10.1038/s41587-023-01796-7
- Ji, X., Li, Q., Song, H., and Fan, C. (2022). Protein-mimicking nanoparticles in biosystems. *Adv. Mater.* 34 (37), e2201562. doi:10.1002/adma.202201562
- Jia, Y., Jiang, Y., He, Y., Zhang, W., Zou, J., Magar, K. T., et al. (2023). Approved nanomedicine against diseases. *Pharmaceutics* 15 (3), 774. doi:10.3390/pharmaceutics15030774
- Jiang, X., Wang, J., Deng, X., Xiong, F., Ge, J., Xiang, B., et al. (2019). Role of the tumor microenvironment in PD-L1/PD-1-mediated tumor immune escape. *Mol. Cancer* 18 (1), 10. doi:10.1186/s12943-018-0928-4
- Jing, Y., Zhang, Y., Wang, J., Li, K., Chen, X., Heng, J., et al. (2021). Association between sex and immune-related adverse events during immune checkpoint inhibitor therapy. *J. Natl. Cancer Inst.* 113 (10), 1396–1404. doi:10.1093/jnci/djab035
- Johnson, D. E., O'Keefe, R. A., and Grandis, J. R. (2018). Targeting the IL-6/JAK/STAT3 signalling axis in cancer. *Nat. Rev. Clin. Oncol.* 15 (4), 234–248. doi:10.1038/nrclinonc.2018.8
- Johnson, M., Garassino, M. C., Mok, T., and Mitsudomi, T. (2022). Treatment strategies and outcomes for patients with EGFR-mutant non-small cell lung cancer resistant to EGFR tyrosine kinase inhibitors: focus on novel therapies. *Lung Cancer* 170, 41–51. doi:10.1016/j.lungcan.2022.05.011

- Kalyane, D., Raval, N., Maheshwari, R., Tambe, V., Kalia, K., and Tekade, R. K. (2019). Employment of enhanced permeability and retention effect (EPR): nanoparticle-based precision tools for targeting of therapeutic and diagnostic agent in cancer. *Mater Sci. Eng. C Mater Biol. Appl.* 98, 1252–1276. doi:10.1016/j.msec.2019.01.066
- Kandasamy, G., Danilovtseva, E. N., Annenkov, V. V., and Krishnan, U. M. (2020). Poly(1-vinylimidazole) polyplexes as novel therapeutic gene carriers for lung cancer therapy. *Beilstein J. Nanotechnol.* 11, 354–369. doi:10.3762/bjnano.11.26
- Kim, D. H., Kim, H., Choi, Y. J., Kim, S. Y., Lee, J. E., Sung, K. J., et al. (2019). Exosomal PD-L1 promotes tumor growth through immune escape in non-small cell lung cancer. *Exp. Mol. Med.* 51 (8), 1–13. doi:10.1038/s12276-019-0295-2
- Kim, M. G., Jo, S. D., Yhee, J. Y., Lee, B. S., Lee, S. J., Park, S. G., et al. (2017). Synergistic anti-tumor effects of bevacizumab and tumor targeted polymerized VEGF siRNA nanoparticles. *Biochem. Biophys. Res. Commun.* 489 (1), 35–41. doi:10.1016/j.bbrc.2017.05.103
- Kim, S. S., Harford, J. B., Moghe, M., Doherty, C., and Chang, E. H. (2022). A novel P53 nanomedicine reduces immunosuppression and augments anti-PD-1 therapy for non-small cell lung cancer in syngeneic mouse models. *Cells* 11 (21), cells11213434. doi:10.3390/cells11213434
- Kim, Y. J., Won, C. H., Lee, M. W., Choi, J. H., Chang, S. E., and Lee, W. J. (2020). Correlation between tumor-associated macrophage and immune checkpoint molecule expression and its prognostic significance in cutaneous melanoma. *J. Clin. Med.* 9 (8), 2500. doi:10.3390/jcm9082500
- Komi, D. E. A., Khomtchouk, K., and Santa Maria, P. L. (2020). A review of the contribution of mast cells in wound healing: involved molecular and cellular mechanisms. *Clin. Rev. Allergy Immunol.* 58 (3), 298–312. doi:10.1007/s12016-019-08729-w
- Komohara, Y., Fujiwara, Y., Ohnishi, K., and Takeya, M. (2016). Tumor-associated macrophages: potential therapeutic targets for anti-cancer therapy. *Adv. Drug Deliv. Rev.* 99, 180–185. doi:10.1016/j.addr.2015.11.009
- Kong, N., Tao, W., Ling, X., Wang, J., Xiao, Y., Shi, S., et al. (2019). Synthetic mRNA nanoparticle-mediated restoration of p53 tumor suppressor sensitizes p53-deficient cancers to mTOR inhibition. *Sci. Transl. Med.* 11 (523), eaaw1565. doi:10.1126/scitranslmed.aaw1565
- Kortylewski, M., Swiderski, P., Herrmann, A., Wang, L., Kowolik, C., Kujawski, M., et al. (2009). *In vivo* delivery of siRNA to immune cells by conjugation to a TLR9 agonist enhances antitumor immune responses. *Nat. Biotechnol.* 27 (10), 925–932. doi:10.1038/nbt.1564
- Kotmakçı, M., Çetintaş, V. B., and Kantarcı, A. G. (2017). Preparation and characterization of lipid nanoparticle/pDNA complexes for STAT3 downregulation and overcoming chemotherapy resistance in lung cancer cells. *Int. J. Pharm.* 525 (1), 101–111. doi:10.1016/j.ijpharm.2017.04.034
- Kuo, W. S., Shao, Y. T., Huang, K. S., Chou, T. M., and Yang, C. H. (2018). Antimicrobial amino-functionalized nitrogen-doped graphene quantum dots for eliminating multidrug-resistant species in dual-modality photodynamic therapy and bioimaging under two-photon excitation. *ACS Appl. Mater. Interfaces* 10 (17), 14438–14446. doi:10.1021/acsami.8b01429
- Kwak, G., Jo, S. D., Kim, D., Kim, H., Kim, M. G., Kim, K., et al. (2017). Synergistic antitumor effects of combination treatment with metronomic doxorubicin and VEGF-targeting RNAi nanoparticles. *J. Control Release* 267, 203–213. doi:10.1016/j.jconrel.2017.08.015
- Lahiri, A., Maji, A., Potdar, P. D., Singh, N., Parikh, P., Bisht, B., et al. (2023). Lung cancer immunotherapy: progress, pitfalls, and promises. *Mol. Cancer* 22 (1), 40. doi:10.1186/s12943-023-01740-y
- Lai, S. Y., and Johnson, F. M. (2010). Defining the role of the JAK-STAT pathway in head and neck and thoracic malignancies: implications for future therapeutic approaches. *Drug Resist Update* 13 (3), 67–78. doi:10.1016/j.drup.2010.04.001
- Lai-Kwon, J., Tiu, C., Pal, A., Khurana, S., and Minchom, A. (2021). Moving beyond epidermal growth factor receptor resistance in metastatic non-small cell lung cancer - a drug development perspective. *Crit. Rev. Oncol. Hematol.* 159, 103225. doi:10.1016/j.critrevonc.2021.103225
- Lee, J. W., Soung, Y. H., Kim, S. Y., Nam, S. W., Park, W. S., Lee, J. Y., et al. (2006). Absence of JAK2 V617F mutation in gastric cancers. *Acta Oncol.* 45 (2), 222–223. doi:10.1080/02841860500341223
- Lei, R., Zhou, M., Zhang, S., Luo, J., Qu, C., Wang, Y., et al. (2022). Potential role of PRKCSH in lung cancer: bioinformatics analysis and a case study of nano ZnO. *Nanoscale* 14 (12), 4495–4510. doi:10.1039/d1nr08133k
- Li, F., Mei, H., Xie, X., Zhang, H., Liu, J., Lv, T., et al. (2017). Aptamer-Conjugated chitosan-anchored liposomal complexes for targeted delivery of erlotinib to EGFR-mutated lung cancer cells. *Aaps J.* 19 (3), 814–826. doi:10.1208/s12248-017-0057-9
- Li, H. S., Wang, S. Z., Xu, H. Y., Yan, X., Zhang, J. Y., Lei, S. Y., et al. (2022). Afatinib and dacomitinib efficacy, safety, progression patterns, and resistance mechanisms in patients with non-small cell lung cancer carrying uncommon EGFR mutations: a comparative cohort study in China (afanda study). *Cancers (Basel)* 14 (21), cancers14215307. doi:10.3390/cancers14215307
- Li, R., He, Y., Zhang, S., Qin, J., and Wang, J. (2018). Cell membrane-based nanoparticles: a new biomimetic platform for tumor diagnosis and treatment. *Acta Pharm. Sin.* B 8 (1), 14–22. doi:10.1016/j.apsb.2017.11.009
- Li, C., Hu, J., Li, W., Song, G., and Shen, J. (2016). Combined bortezomib-based chemotherapy and p53 gene therapy using hollow mesoporous silica nanospheres for p53 mutant non-small cell lung cancer treatment. *Biomater. Sci.* 5 (1), 77–88. doi:10.1039/c6bm00449k
- Li, S., Choi, Y. L., Gong, Z., Liu, X., Lira, M., Kan, Z., et al. (2016). Comprehensive characterization of oncogenic drivers in asian lung adenocarcinoma. *J. Thorac. Oncol.* 11 (12), 2129–2140. doi:10.1016/j.jtho.2016.08.142
- Li, Z., Yang, L., Wang, H., Binzel, D. W., Williams, T. M., and Guo, P. (2021). Non-small-cell lung cancer regression by siRNA delivered through exosomes that display EGFR RNA aptamer. *Nucleic Acid. Ther.* 31 (5), 364–374. doi:10.1089/nat.2021.0002
- Liam, C. K., Ahmad, A. R., Hsia, T. C., Zhou, J., Kim, D. W., Soo, R. A., et al. (2023). Randomized trial of tepotinib plus gefitinib versus chemotherapy in EGFR-mutant NSCLC with EGFR inhibitor resistance due to MET amplification: INSIGHT final analysis. *Clin. Cancer Res.* 29 (10), 1879–1886. doi:10.1158/1078-0432.CCR-22-3318
- Liao, Z., Wong, S. W., Yeo, H. L., and Zhao, Y. (2020). Smart nanocarriers for cancer treatment: clinical impact and safety. *Nanolimpact* 20, 100253. doi:10.1016/j.nimpact.2020.100253
- Lin, T. E., HuangFu, W. C., Chao, M. W., Sung, T. Y., Chang, C. D., Chen, Y. Y., et al. (2018). A novel selective JAK2 inhibitor identified using pharmacological interactions. *Front. Pharmacol.* 9, 1379. doi:10.3389/fphar.2018.01379
- Liu, B., Hu, X., Feng, K., Gao, R., Xue, Z., Zhang, S., et al. (2022). Temporal single-cell tracing reveals clonal revival and expansion of precursor exhausted T cells during anti-PD-1 therapy in lung cancer. *Nat. Cancer* 3 (1), 108–121. doi:10.1038/s43018-021-00292-8
- Liu, J., Shi, X., Zhang, R., Zhang, M., He, J., Chen, J., et al. (2021b). CoFe(2)O(4)-Quantum dots for synergistic photothermal/photodynamic therapy of non-small-cell lung cancer via triggering apoptosis by regulating PI3K/AKT pathway. *Nanoscale Res. Lett.* 16 (1), 120. doi:10.1186/s11671-021-03580-5
- Liu, Q., Sun, Z., and Chen, L. (2020). Memory T cells: strategies for optimizing tumor immunotherapy. *Protein Cell* 11 (8), 549–564. doi:10.1007/s12328-020-00707-9
- Liu, Z., Wang, T., She, Y., Wu, K., Gu, S., Li, L., et al. (2021a). N(6)-methyladenosine-modified circIGF2BP3 inhibits CD8(+) T-cell responses to facilitate tumor immune evasion by promoting the deubiquitination of PD-L1 in non-small cell lung cancer. *Mol. Cancer* 20 (1), 105. doi:10.1186/s12943-021-01398-4
- Mahmoud, M. E., Allam, E. A., El-Sharkawy, R. M., Soliman, M. A., Saad, E. A., and El-Khatib, A. M. (2020). Nano-manganese oxide-functionalized-oleyl amine as a simple and low cost nanosorbent for remediation of Zn(II)/Co(II) and their radioactive nuclides (65)Zn and (60)Co from water. *Appl. Radiat. Isot.* 159, 108989. doi:10.1016/j.apradiso.2019.108989
- May, M. (2018). Cancer research with a human touch. *Nature* 556 (7700), 259–261. doi:10.1038/d41586-018-04161-w
- McCubrey, J. A., Steelman, L. S., Abrams, S. L., Bertrand, F. E., Ludwig, D. E., Basecke, J., et al. (2008). Targeting survival cascades induced by activation of Ras/Raf/MEK/ERK, PI3K/PDEN/Akt/mTOR and Jak/STAT pathways for effective leukemia therapy. *Leukemia* 22 (4), 708–722. doi:10.1038/leu.2008.27
- McHugh, K. J., Jing, L., Behrens, A. M., Jayawardena, S., Tang, W., Gao, M., et al. (2018). Biocompatible semiconductor quantum dots as cancer imaging agents. *Adv. Mater.* 30 (18), e1706356. doi:10.1002/adma.201706356
- Mills, C. D. (2012). M1 and M2 macrophages: oracles of health and disease. *Crit. Rev. Immunol.* 32 (6), 463–488. doi:10.1615/critrevimmunol.v32.i6.10
- Molina, J. R., Yang, P., Cassivi, S. D., Schild, S. E., and Adjei, A. A. (2008). Non-small cell lung cancer: epidemiology, risk factors, treatment, and survivorship. *Mayo Clin. Proc.* 83 (5), 584–594. doi:10.4065/83.5.584
- Mortezaei, K. (2021). Myeloid-derived suppressor cells in cancer immunotherapy-clinical perspectives. *Life Sci.* 277, 119627. doi:10.1016/j.lfs.2021.119627
- Muenst, S., Soysal, S. D., Tzankov, A., and Hoeller, S. (2015). The PD-1/PD-L1 pathway: biological background and clinical relevance of an emerging treatment target in immunotherapy. *Expert Opin. Ther. Targets* 19 (2), 201–211. doi:10.1517/14728222.2014.980235
- Naylor, E. C., Desani, J. K., and Chung, P. K. (2016). Targeted therapy and immunotherapy for lung cancer. *Surg. Oncol. Clin. N. Am.* 25 (3), 601–609. doi:10.1016/j.soc.2016.02.011
- Nguyen, P. H. D., Jayasinghe, M. K., Le, A. H., Peng, B., and Le, M. T. N. (2023). Advances in drug delivery systems based on red blood cells and their membrane-derived nanoparticles. *ACS Nano* 17 (6), 5187–5210. doi:10.1021/acsnano.2c11965
- Nie, M., Chen, N., Pang, H., Jiang, T., Jiang, W., Tian, P., et al. (2022). Targeting acetylcholine signaling modulates persistent drug tolerance in EGFR-mutant lung cancer and impedes tumor relapse. *J. Clin. Invest.* 132 (20), jci160152. doi:10.1172/jci160152
- Niu, Z., Jin, R., Zhang, Y., and Li, H. (2022). Signaling pathways and targeted therapies in lung squamous cell carcinoma: mechanisms and clinical trials. *Signal Transduct. Target Ther.* 7 (1), 353. doi:10.1038/s41392-022-01200-x
- NSCLC Meta-analysis Collaborative Group (2014). Preoperative chemotherapy for non-small-cell lung cancer: a systematic review and meta-analysis of individual participant data. *Lancet* 383 (9928), 1561–1571. doi:10.1016/s0140-6736(13)61259-5

- Paik, P. K., Rudin, C. M., Brown, A., Rizvi, N. A., Takebe, N., Travis, W., et al. (2010). A phase I study of obatoclax mesylate, a Bcl-2 antagonist, plus topotecan in solid tumor malignancies. *Cancer Chemother. Pharmacol.* 66 (6), 1079–1085. doi:10.1007/s00280-010-1265-5
- Palazzolo, S., Bayda, S., Hadla, M., Caligiuri, I., Corona, G., Toffoli, G., et al. (2018). The clinical translation of organic nanomaterials for cancer therapy: a focus on polymeric nanoparticles, micelles, liposomes and exosomes. *Curr. Med. Chem.* 25 (34), 4224–4268. doi:10.2174/0929867324666170830113755
- Papadimitrakopoulou, V. (2012). Development of PI3K/AKT/mTOR pathway inhibitors and their application in personalized therapy for non-small-cell lung cancer. *J. Thorac. Oncol.* 7 (8), 1315–1326. doi:10.1097/JTO.0b013e31825493eb
- Passaro, A., Jänne, P. A., Mok, T., and Peters, S. (2021). Overcoming therapy resistance in EGFR-mutant lung cancer. *Nat. Cancer* 2 (4), 377–391. doi:10.1038/s43018-021-00195-8
- Patra, J. K., Das, G., Fraceto, L. F., Campos, E. V. R., Rodriguez-Torres, M. D. P., Acosta-Torres, L. S., et al. (2018). Nano based drug delivery systems: recent developments and future prospects. *J. Nanobiotechnology* 16 (1), 71. doi:10.1186/s12951-018-0392-8
- Punekar, S. R., Velcheti, V., Neel, B. G., and Wong, K. K. (2022). The current state of the art and future trends in RAS-targeted cancer therapies. *Nat. Rev. Clin. Oncol.* 19 (10), 637–655. doi:10.1038/s41571-022-00671-9
- Raju, G. S. R., Dariya, B., Mungamuri, S. K., Chalikonda, G., Kang, S. M., Khan, I. N., et al. (2021). Nanomaterials multifunctional behavior for enlightened cancer therapeutics. *Semin. Cancer Biol.* 69, 178–189. doi:10.1016/j.semcancer.2019.08.013
- Rasheduzzaman, M., Jeong, J. K., and Park, S. Y. (2018). Resveratrol sensitizes lung cancer cell to TRAIL by p53 independent and suppression of Akt/NF- κ B signaling. *Life Sci.* 208, 208–220. doi:10.1016/j.lfs.2018.07.035
- Reck, M., Remon, J., and Hellmann, M. D. (2022). First-Line immunotherapy for non-small-cell lung cancer. *J. Clin. Oncol.* 40 (6), 586–597. doi:10.1200/jco.21.01497
- Rosell, R., Karachaliou, N., and Arrieta, O. (2020). Novel molecular targets for the treatment of lung cancer. *Curr. Opin. Oncol.* 32 (1), 37–43. doi:10.1097/CCO.0000000000000590
- Sainsbury, F., and Steinmetz, N. F. (2023). Nanotechnology meets virology. *Virology* 581, 56–57. doi:10.1016/j.virol.2023.02.015
- Schimmer, A. D., O'Brien, S., Kantarjian, H., Brandwein, J., Cheson, B. D., Minden, M. D., et al. (2008). A phase I study of the pan bcl-2 family inhibitor obatoclax mesylate in patients with advanced hematologic malignancies. *Clin. Cancer Res.* 14 (24), 8295–8301. doi:10.1158/1078-0432.Ccr-08-0999
- Seeta Rama Raju, G., Benton, L., Pavitra, E., and Yu, J. S. (2015). Multifunctional nanoparticles: recent progress in cancer therapeutics. *Chem. Commun. (Camb)* 51 (68), 13248–13259. doi:10.1039/c5cc04643b
- Shi, C. S., and Kehl, J. H. (2004). Pyk2 amplifies epidermal growth factor and c-Src-induced Stat3 activation. *J. Biol. Chem.* 279 (17), 17224–17231. doi:10.1074/jbc.M311875200
- Shobaki, N., Sato, Y., Suzuki, Y., Okabe, N., and Harashima, H. (2020). Manipulating the function of tumor-associated macrophages by siRNA-loaded lipid nanoparticles for cancer immunotherapy. *J. Control Release* 325, 235–248. doi:10.1016/j.jconrel.2020.07.001
- Sica, A., and Mantovani, A. (2012). Macrophage plasticity and polarization: *in vivo* veritas. *J. Clin. Invest.* 122 (3), 787–795. doi:10.1172/jci59643
- Socinski, M. A., Jotte, R. M., Cappuzzo, F., Orlandi, F., Stroyakovskiy, D., Nogami, N., et al. (2018). Atezolizumab for first-line treatment of metastatic nonsquamous NSCLC. *N. Engl. J. Med.* 378 (24), 2288–2301. doi:10.1056/NEJMoa1716948
- Sonenshein, G. E. (1997). Rel/NF-kappa B transcription factors and the control of apoptosis. *Semin. Cancer Biol.* 8 (2), 113–119. doi:10.1006/scbi.1997.0062
- Song, H., Wu, J., Tang, Y., Dai, Y., Xiang, X., Li, Y., et al. (2023). Diverse rescue potencies of p53 mutations to ATO are predetermined by intrinsic mutational properties. *Sci. Transl. Med.* 15 (690), eabn9155. doi:10.1126/scitranslmed.abn9155
- Song, S., Liu, D., Peng, J., Deng, H., Guo, Y., Xu, L. X., et al. (2009). Novel peptide ligand directs liposomes toward EGF-R high-expressing cancer cells *in vitro* and *in vivo*. *Faseb J.* 23 (5), 1396–1404. doi:10.1096/fj.08-117002
- Song, S., Liu, D., Peng, J., Sun, Y., Li, Z., Gu, J. R., et al. (2008). Peptide ligand-mediated liposome distribution and targeting to EGFR expressing tumor *in vivo*. *Int. J. Pharm.* 363 (1–2), 155–161. doi:10.1016/j.ijpharm.2008.07.012
- Stater, E. P., Sonay, A. Y., Hart, C., and Grimm, J. (2021). The ancillary effects of nanoparticles and their implications for nanomedicine. *Nat. Nanotechnol.* 16 (11), 1180–1194. doi:10.1038/s41565-021-01017-9
- Sun, Y., Zhang, Y., Gao, Y., Wang, P., He, G., Blum, N. T., et al. (2020). Six birds with one stone: versatile nanoporphyrim for single-laser-triggered synergistic phototheranostics and robust immune activation. *Adv. Mater.* 32 (48), e2004481. doi:10.1002/adma.202004481
- Sung, H., Ferlay, J., Siegel, R. L., Laversanne, M., Soerjomataram, I., Jemal, A., et al. (2021). Global cancer statistics 2020: GLOBOCAN estimates of incidence and mortality worldwide for 36 cancers in 185 countries. *CA Cancer J. Clin.* 71 (3), 209–249. doi:10.3322/caac.21660
- Suresh, K., Naidoo, J., Lin, C. T., and Danoff, S. (2018). Immune checkpoint immunotherapy for non-small cell lung cancer: benefits and pulmonary toxicities. *Chest* 154 (6), 1416–1423. doi:10.1016/j.chest.2018.08.1048
- Tan, A. C. (2020). Targeting the PI3K/Akt/mTOR pathway in non-small cell lung cancer (NSCLC). *Thorac. Cancer* 11 (3), 511–518. doi:10.1111/1759-7714.13328
- Tanaka, A., and Sakaguchi, S. (2017). Regulatory T cells in cancer immunotherapy. *Cell Res.* 27 (1), 109–118. doi:10.1038/cr.2016.151
- Taniguchi, H., Yamada, T., Wang, R., Tanimura, K., Adachi, Y., Nishiyama, A., et al. (2019). AXL confers intrinsic resistance to osimertinib and advances the emergence of tolerant cells. *Nat. Commun.* 10 (1), 259. doi:10.1038/s41467-018-08074-0
- Thorn, M., Guha, P., Cunetta, M., Espot, N. J., Miller, G., Junghans, R. P., et al. (2016). Tumor-associated GM-CSF overexpression induces immunoinhibitory molecules via STAT3 in myeloid-suppressor cells infiltrating liver metastases. *Cancer Gene Ther.* 23 (6), 188–198. doi:10.1038/cgt.2016.19
- Tian, Y., Gao, Z., Wang, N., Hu, M., Ju, Y., Li, Q., et al. (2022). Engineering poly(ethylene glycol) nanoparticles for accelerated blood clearance inhibition and targeted drug delivery. *J. Am. Chem. Soc.* 144 (40), 18419–18428. doi:10.1021/jacs.2c06877
- Tsang, S. J., Kempson, I. M., Huang, K. Y., Li, H. J., Fa, Y. C., Ho, Y. C., et al. (2018). Targeting tumor microenvironment by bioreduction-activated nanoparticles for light-triggered virotherapy. *ACS Nano* 12 (10), 9894–9902. doi:10.1021/acsnano.8b02813
- Upadhyay, P., Ghosh, A., Basu, A., Pranati, P. A., Gupta, P., Das, S., et al. (2021). Delivery of gefitinib in synergism with thymoquinone via transferrin-conjugated nanoparticle sensitizes gefitinib-resistant non-small cell lung carcinoma to control metastasis and stemness. *Biomater. Sci.* 9 (24), 8285–8312. doi:10.1039/d1bm01148k
- Van der Meel, R., Sulheim, E., Shi, Y., Kiessling, F., and Mulder Wjmlammers, T. (2019). Smart cancer nanomedicine. *Nat. Nanotechnol.* 14 (11), 1007–1017. doi:10.1038/s41565-019-0567-y
- Villaluz, L. C., Burns, T. F., Ramfidis, V. S., and Socinski, M. A. (2013). Personalizing therapy in advanced non-small cell lung cancer. *Semin. Respir. Crit. Care Med.* 34 (6), 822–836. doi:10.1055/s-0033-1358552
- Vincent, M. P., Navidzadeh, J. O., Bobbala, S., and Scott, E. A. (2022). Leveraging self-assembled nanobiomaterials for improved cancer immunotherapy. *Cancer Cell* 40 (3), 255–276. doi:10.1016/j.ccell.2022.01.006
- Wang, F., Chen, X., Cheng, H., Song, L., Liu, J., Caplan, S., et al. (2021). MICAL2PV suppresses the formation of tunneling nanotubes and modulates mitochondrial trafficking. *EMBO Rep.* 22 (7), e52006. doi:10.15252/embr.202052006
- Wang, H. J., Ran, H. F., Yin, Y., Xu, X. G., Jiang, B. X., Yu, S. Q., et al. (2022). Catalpol improves impaired neurovascular unit in ischemic stroke rats via enhancing VEGF-PI3K/AKT and VEGF-MEK1/2/ERK1/2 signaling. *Acta Pharmacol. Sin.* 43 (7), 1670–1685. doi:10.1038/s41401-021-00803-4
- Wang, J., Ni, Q., Wang, Y., Zhang, Y., He, H., Gao, D., et al. (2021). Nanoscale drug delivery systems for controllable drug behaviors by multi-stage barrier penetration. *J. Control Release* 331, 282–295. doi:10.1016/j.jconrel.2020.08.045
- Wang, X., Zhong, X., Li, J., Liu, Z., and Cheng, L. (2021). Inorganic nanomaterials with rapid clearance for biomedical applications. *Chem. Soc. Rev.* 50 (15), 8669–8742. doi:10.1039/d0cs00461h
- Wang, Z., Liu, W., Shi, J., Chen, N., and Fan, C. (2018). Nanoscale delivery systems for cancer immunotherapy. *Mater. Horizons* 5 (3), 344–362. doi:10.1039/c7mh00099g
- Wu, D., Zhang, Z., Li, X., Zhu, T., Wang, J., and Hu, Q. (2023). Supramolecular theranostic nanomedicine for *in situ* self-boosting cancer photochemotherapy. *Biomacromolecules* 24 (2), 1022–1031. doi:10.1021/acs.biomac.2c01469
- Xu, C., Ji, X., Zhou, Y., Cheng, Y., Guo, D., Li, Q., et al. (2023). Slimming and reinvigorating tumor-associated dendritic cells with hierarchical lipid rewiring nanoparticles. *Adv. Mater.* 35 (30), e2211415. doi:10.1002/adma.202211415
- Xu, H., Hou, Z., Zhang, H., Kong, H., Li, X., Wang, H., et al. (2014). An efficient Trojan delivery of tetrandrine by poly(N-vinylpyrrolidone)-block-poly(ϵ -caprolactone) (PVP-b-PCL) nanoparticles shows enhanced apoptotic induction of lung cancer cells and inhibition of its migration and invasion. *Int. J. Nanomedicine* 9, 231–242. doi:10.2147/ijn.S55541
- Xu, H. Z., Li, T. F., Wang, C., Ma, Y., Liu, Y., Zheng, M. Y., et al. (2021). Synergy of nanodiamond-doxorubicin conjugates and PD-L1 blockade effectively turns tumor-associated macrophages against tumor cells. *J. Nanobiotechnology* 19 (1), 268. doi:10.1186/s12951-021-01017-w
- Xu, W., Yang, S., Lu, L., Xu, Q., Wu, S., Zhou, J., et al. (2023). Influence of lung cancer model characteristics on tumor targeting behavior of nanodrugs. *J. Control Release* 354, 538–553. doi:10.1016/j.jconrel.2023.01.026
- Yan, S., Zhang, B., Feng, J., Wu, H., Duan, N., Zhu, Y., et al. (2021). FGFC1 selectively inhibits erlotinib-resistant non-small cell lung cancer via elevation of ROS mediated by the EGFR/PI3K/Akt/mTOR pathway. *Front. Pharmacol.* 12, 764699. doi:10.3389/fphar.2021.764699
- Yang, C. Y., Yang, J. C., and Yang, P. C. (2020). Precision management of advanced non-small cell lung cancer. *Annu. Rev. Med.* 71, 117–136. doi:10.1146/annurev-med-051718-013524
- Yang, Z., Gao, D., Zhao, J., Yang, G., Guo, M., Wang, Y., et al. (2023). Thermal immuno-nanomedicine in cancer. *Nat. Rev. Clin. Oncol.* 20 (2), 116–134. doi:10.1038/s41571-022-00717-y

- You, M., Xie, Z., Zhang, N., Zhang, Y., Xiao, D., Liu, S., et al. (2023). Signaling pathways in cancer metabolism: mechanisms and therapeutic targets. *Signal Transduct. Target Ther.* 8 (1), 196. doi:10.1038/s41392-023-01442-3
- Zhang, M., Yang, W., Wang, P., Deng, Y., Dong, Y. T., Liu, F. F., et al. (2020). CCL7 recruits cDC1 to promote antitumor immunity and facilitate checkpoint immunotherapy to non-small cell lung cancer. *Nat. Commun.* 11 (1), 6119. doi:10.1038/s41467-020-19973-6
- Zhang, Y., Wang, Z., and Gemeinhart, R. A. (2013). Progress in microRNA delivery. *J. Control Release* 172 (3), 962–974. doi:10.1016/j.jconrel.2013.09.015
- Zhao, L., Li, D., Zhang, Y., Huang, Q., Zhang, Z., Chen, C., et al. (2022). HSP70-Promoter-Driven CRISPR/Cas9 system activated by reactive oxygen species for multifaceted anticancer immune response and potentiated immunotherapy. *ACS Nano* 16 (9), 13821–13833. doi:10.1021/acsnano.2c01885
- Zhao, Y., Guo, S., Deng, J., Shen, J., Du, F., Wu, X., et al. (2022). VEGF/VEGFR-targeted therapy and immunotherapy in non-small cell lung cancer: targeting the tumor microenvironment. *Int. J. Biol. Sci.* 18 (9), 3845–3858. doi:10.7150/ijbs.70958
- Zhong, M., Ma, X., Sun, C., and Chen, L. (2010). MicroRNAs reduce tumor growth and contribute to enhance cytotoxicity induced by gefitinib in non-small cell lung cancer. *Chem. Biol. Interact.* 184 (3), 431–438. doi:10.1016/j.cbi.2010.01.025
- Zhong, Z., Wen, Z., and Darnell, J. E., Jr (1994). Stat3: a STAT family member activated by tyrosine phosphorylation in response to epidermal growth factor and interleukin-6. *Science* 264 (5155), 95–98. doi:10.1126/science.8140422
- Zhou, L., Liang, H., Ge, Y., Ding, W., Chen, Q., Zhang, T., et al. (2022). Precisely targeted nano-controller of PD-L1 level for non-small cell lung cancer spinal metastasis immunotherapy. *Adv. Healthc. Mater* 11 (20), e2200938. doi:10.1002/adhm.202200938
- Zhou, Y., Chen, H., Tang, L., Feng, Y., Tao, Y., Huang, L., et al. (2023). Association of immune-related adverse events and efficacy in advanced non-small-cell lung cancer: a systematic review and meta-analysis. *Immunotherapy* 15 (3), 209–220. doi:10.2217/imt-2022-0028
- Zhu, Z., Zhang, H., Chen, B., Liu, X., Zhang, S., Zong, Z., et al. (2020). PD-L1-Mediated immunosuppression in glioblastoma is associated with the infiltration and M2-polarization of tumor-associated macrophages. *Front. Immunol.* 11, 588552. doi:10.3389/fimmu.2020.588552

Frontiers in Chemistry

Explores all fields of chemical science across the periodic table

Advances our understanding of how atoms, ions, and molecules come together and come apart. It explores the role of chemistry in our everyday lives - from electronic devices to health and wellbeing.

Discover the latest Research Topics

[See more →](#)

Frontiers

Avenue du Tribunal-Fédéral 34
1005 Lausanne, Switzerland
frontiersin.org

Contact us

+41 (0)21 510 17 00
frontiersin.org/about/contact

